PERGAMON

Quaternary Science Reviews 20 (2001) 1475–1560

QSR

# Terrestrial in situ cosmogenic nuclides: theory and application

John C. Gosse[a,*], Fred M. Phillips[b]

[a]Department of Geology, 120 Lindley Hall, University of Kansas, Lawrence, KS 66045, USA
[b]Department of Earth & Environmental Science, New Mexico Tech, Socorro, NM 87801, USA

**Abstract**

The cosmogenic nuclide exposure history method is undergoing major developments in analytical, theoretical, and applied areas. The capability to routinely measure low concentrations of stable and radioactive cosmogenic nuclides has led to new methods for addressing long-standing geologic questions and has provided insights into rates and styles of surficial processes. The different physical and chemical properties of the six most widely used nuclides: $^{3}$He, $^{10}$Be, $^{14}$C, $^{21}$Ne, $^{26}$Al, and $^{36}$Cl, make it possible to apply the surface exposure dating methods on rock surfaces of virtually any lithology at any latitude and altitude, for exposures ranging from $10^{2}$ to $10^{7}$ years. The terrestrial in situ cosmogenic nuclide method is beginning to revolutionize the manner in which we study landscape evolution. Single or multiple nuclides can be measured in a single rock surface to obtain erosion rates on boulder and bedrock surfaces, fluvial incision rates, denudation rates of individual landforms or entire drainage basins, burial histories of rock surfaces and sediment, scarp retreat, fault slip rates, paleoseismology, and paleoaltimetry. Ages of climatic variations recorded by moraine and alluvium sediments are being directly determined. Advances in our understanding of how cosmic radiation interacts with the geomagnetic field and atmosphere will improve numerical simulations of cosmic-ray interactions over any exposure duration and complement additional empirical measurements of nuclide production rates. The total uncertainty in the exposure ages is continually improving. This article presents the theory necessary for interpreting cosmogenic nuclide data, reviews estimates of parameters, describes strategies and practical considerations in field applications, and assesses sources of error in interpreting cosmogenic nuclide measurements. 

## TABLE OF CONTENTS



* Corresponding author. Tel.: +1-785-864-4974; fax: +1-785-864-5276.
*E-mail address:* gosse@ukans.edu (J.C. Gosse).

0277-3791/01/$ - see front matter 
PII: S0277-3791(00)00171-2

## 1. Introduction

For many years after its discovery in 1912 by Austrian physicist Victor Hess, cosmic radiation was studied mainly for the insights it could provide into fundamental particle physics. Since particle accelerators were not yet invented, cosmic-rays provided a unique source of high-energy subatomic particles for physics experimentation. In 1934 A.V. Grosse suggested that cosmic radiation could produce radioactive nuclides at the surface of the earth and gave such (hypothetical) species the name "cosmic radio-elements". The realization by Libby in 1949 that cosmic radiation produced easily measurable amounts of $^{14}C$ through interaction with the atmosphere opened the new possibility of applications to the earth sciences. In 1955 Raymond Davis and Oliver Schaffer proposed that cosmogenic nuclides produced within minerals at the surface of the earth could be applied to geological problems. Starting in the 1950s, interactions of cosmic rays with rock materials was studied in meteorites, and in lunar samples since 1969 (Reedy et al., 1983), but much lower production rates inhibited similar measurements in terrestrial rocks. A theoretical foundation for such studies was laid by Lal and Peters (1967). In spite of these visionary early efforts, terrestrial in situ cosmogenic nuclide applications languished until the mid-1980s because available analytical instrumentation was not capable of routinely measuring the exceedingly low concentrations of most cosmogenic nuclides produced at earth-surface altitudes. The production rates in surficial rocks are commonly several orders of magnitude less than average rates in the atmosphere. (In this paper we refer to cosmogenic nuclides produced within rocks or minerals at, or close to, the surface of the earth as "terrestrial in situ cosmogenic nuclides" (TCN), and describe nuclides produced in the atmosphere as "meteoric" or "atmospheric" to distinguish them from TCN.)

In the early-1980s two new types of geochemical instrumentation were applied: accelerator mass spectrometry (AMS) and highly sensitive conventional noble-gas mass spectrometry. With these analytical advances the new earth-science investigation techniques proposed by the early pioneers could become a reality. In the 15 years since the publication of the first papers demonstrating that these analytical methods were practical for routine measurement of TCN, the annual numbers of publications applying TCN to earth-science problems has grown exponentially. However, we feel that one factor still limiting the range and number of applications is the lack of readily available information on the theory and practice of TCN techniques. Although several publications on TCN methods exist, there is no single reference to refer for a complete overview. The objective of this review is to provide such a reference. It is intended mainly for those potentially interested in the TCN methods, those starting to apply them, or for those who wish to evaluate TCN applications by others. We attempt to provide sufficient detail on theory and parameters to enable the reader to compute TCN ages and erosion rates, as well as practical advice on field strategies and sampling. We also analyze the sensitivity of the TCN method to chemical, physical, and geological factors which affect the interpretation of TCN data for solving geologic problems. This paper does not attempt to provide anything but cursory reviews of analytical methods, previous earth-science applications, cosmic-ray physics, or instructions for statistically treating the uncertainty in interpretations of TCN data. References to other articles that treat these topics in detail are given. We hope that this article will stimulate new ideas for applying and advancing TCN methods.

### 1.1. Development of the TCN methods

The development of the TCN exposure history methods can be summarized in four distinct phases: (1) the realization of the utility of TCN for determining surface exposure ages; (2) the development of a means to estimate the secondary cosmic-ray flux at different sites of any latitude and elevation; (3) the development of AMS and highly sensitive noble-gas mass spectrometry; and (4) the continuing refinement of TCN techniques. As described above, Raymond Davis and Oliver Schaeffer (1955) were the first to attempt to apply TCN to geological problems. They measured the concentration of an in situ cosmogenic nuclide ($^{36}Cl$) in a sample of mafic rock from below the limit of late Pleistocene glaciation in the Rocky Mountains using a screen-wall beta counter similar to that employed for radiocarbon dating by Libby in 1949. Using an estimate of the half life of radioactive $^{36}Cl$

determined by the Chalk River Laboratory in Canada ($t_{1/2}$ $^{36}Cl = 3.01 \times 10^5$ yr), the thermal neutron cross section of chlorine ( $\sim$ 32 barns), the neutron absorption rate (derived by others) at sea level and mountain (3000 m) elevations, and the absorption mean free path in water (140 g cm$^{-2}$), they calculated an exposure age for a pre-Wisconsinan surface on a phonolite from Cripple Creek, Colorado to be 24,000 years (with a 10% analytical uncertainty), while the $^{36}Cl$ activity of a Wisconsinan-ice-covered syenite surface near sea level in New Hampshire was below the detection limits of the counter (modern recalculation of the Cripple Creek sample gives an age in excess of 200,000 years, due to a reduction in the value used for the neutron flux). Despite the promising results of their experiments, exposure dating was not pursued by others because of the limitations of beta counting (for example, even though the Cripple Creek phonolite had an exceptional Cl content of 3500 ppm, their analysis nevertheless required the extraction of 13 g of chlorine from more than 4 kg of rock) and the uncertainty of the production rates of $^{36}Cl$ and other TCN. Using high-sensitivity noble gas mass spectrometry 20 years later, Srinivasan (1976) determined that two Archean barite samples contained spallogenic $^{126}Xe$ produced from interactions with secondary cosmic radiation. Srinivasan calculated a "surface residence time" of 270,000 to 120,000 years for the sedimentary barite sample from Fig Tree group of South Africa. The different ages resulted from the uncertainty in scaling the decrease in the cosmic-ray flux with depth through the atmosphere.

The next milestone was marked by the contributions of physicists in the late 1950s and early 1960s who attempted to derive models describing the interaction between cosmic radiation and the complex geomagnetic field and atmosphere. The rate of in situ (and atmospheric) production of cosmogenic nuclides increases with altitude and latitude (the reasons for this are discussed in Sections 3.1 and 3.7.1 below). Unfortunately, the scaling factors for spatial and temporal variations in the particle flux above the surface of the Earth are difficult to derive. This is because (i) the rate of change in cosmic-ray flux (and disintegration rate) with depth in the atmosphere is not constant with latitude, (ii) the atmosphere does not comprise a homogeneous or simple layered shell, (iii) the Earth's geomagnetic field cannot always be considered a geocentric dipole, and (iv) high-altitude outermost neutrons may escape back to space before slowing. D. Lal (1958), Lal et al. (1958, 1960), and Lal and Peters (1967) produced syntheses of data on nuclear disintegrations in the stratosphere and troposphere. This spatial model for star production rates in the atmosphere was verified empirically by Lal et al. (1960) at high elevation at 51°N latitude and could be used to normalize production rates on the surface of the Earth (Lal and Peters, 1967). ("Stars" are multi-pronged tracks on photo emulsions that record the paths of several particles emitted during reactions of cosmic rays with atomic nuclei.) Although additional verification is needed over geological time scales (see below) the majority of TCN studies have used Lal's global star production model (most recently presented in Lal, 1991) to normalize production rates.

The third phase of development of the TCN surface exposure dating method came 30 years after Davis and Schaeffer's landmark work. Although the possibility of using cosmic-ray-derived nuclides produced in rocks to date the exposure time was recognized, measurement of the rare radionuclides with sufficiently long half lives in most surficial rocks was not routinely practical with existing mass spectrometers or counting methods because of their extremely low concentrations. The development of AMS in the early 1980s and subsequent refinements (Klein et al., 1982; Elmore and Phillips, 1987) rendered possible the measurement of isotopic ratios as low as $10^{-15}$, with total analytical reproducibility as low as $< 3\%$. Several groups were responsible for the rejuvenation of the TCN exposure dating method in the mid-1980s. Originally concerned with $^{36}Cl$ contributions to groundwater recharge from surficial production, F. Phillips (New Mexico Tech) and D. Elmore and others (University of Rochester, now at Purdue University) realized the production could be used for surface dating and used AMS to measure $^{36}Cl$ concentrations from independently dated lava flows (Phillips et al., 1986). The second group (L. Brown at Carnegie Institution of Washington, and J. Klein and R. Middleton at University of Pennsylvania) accidentally arrived at the use of in situ products for exposure chronology during their pioneering work on using atmospherically derived $^{10}Be$ to trace subducted sediments through magmatic arc volcanoes (Brown et al., 1982). They postulated that a significant component of $^{10}Be$ measured in Columbia River basalt flows was derived from in situ production. The University of Pennsylvania group subsequently sought to empirically determine the production rate of $^{10}Be$ and $^{26}Al$ in quartz, together with K. Nishiizumi, Lal, and Arnold (Nishiizumi et al., 1986). The first application of terrestrial $^{10}Be$ was to determine the surface exposure history of Libyan Desert Glass from western Egypt (Klein et al., 1986a). Concurrently with the $^{10}Be$ and $^{36}Cl$ developments, Kurz et al. (1985), (Kurz, 1986a, b), and then Craig and Poreda (1986), demonstrated that, due to its relatively high cosmogenic production rate and nuclear stability, natural concentrations of cosmogenic $^{3}He$ could be measured with a conventional mass spectrometer and could therefore also be useful for exposure dating. Subsequent investigations (cited below) improved the sample strategies, sample processing and analysis, and modeling aspects of TCN exposure dating, and the use of two additional in situ produced nuclides, $^{21}Ne$ (Graf et al., 1991; Staudacher and Allégre, 1991; Poreda and Cerling, 1992) and $^{14}C$ (Jull et al., 1992, 1994a, b; Lifton et al., submitted as two papers in 2000). Better

isolation of the muonic contribution to TCN production on and below earth's surface has been an important recent development (e.g. Heisinger et al., 1997). Although more confirmation is needed, their data support the premise that the muogenic production at the surface is less than assumed by the most widely used scaling model for $^{10}$Be and $^{26}$Al, and provides a means to explain the discrepancy among production rate measurements at calibration sites with different altitudes (proposed by J. Stone, 1999).

We are just beginning the fourth major phase of TCN development: the refinement of cosmogenic nuclide production scaling models that reliably incorporate second-order physical processes that influence in-situ production (e.g., work by Lifton et al., submitted; Stone, in press; Masarik and Beer, 1999). These effects include the influence of non-dipole components of the geomagnetic field, temporal and spatial variations in the paleo-atmosphere and surface elevation, and improvements in the mean absorption free path of different particles at and below earth's surface at different latitudes and altitudes. Although many of these effects have been individually measured or predicted, it is clear that the development of a single encompassing model will require the agglomeration of resources from experts in many different fields.

### *1.2. Applications of TCN exposure methods*

Published applications of TCN exposure history methods are already far too numerous to completely list. Instead, we list some prominent examples of various applications based on our own reading. TCN methods have been used to reconstruct Quaternary ice volume fluctuations from continental (Nishiizumi et al., 1991a; Gosse et al., 1993; McCarroll and Nesje, 1993; Brook et al., 1995a, b, 1996a, b; Ivy-Ochs et al., 1995; Steig et al., 1998; Ackert et al., 1999; Bierman et al., 1999; Davis et al., 1999; Zreda et al., 1999; Marsella et al., in press) and mountain (Phillips et al., 1990; Gosse et al., 1995a, c; Phillips, 1996; Jackson et al., 1997; Briner and Swanson, 1998; Moscariello et al., 1998; Ivy-Ochs et al., 1999) moraine and glacial erosion records. Several of these have pushed the precision of the method to apparently resolve short-lived events such as the Younger Dryas or ice rafting events in the North Atlantic (Gosse et al., 1995a; Phillips et al., 1996a; Ivy-Ochs et al., 1999). Neotectonic applications include the dating of volcanic events (Marti and Craig, 1987; Cerling, 1990; Kurz et al., 1990; Nishiizumi et al., 1990, 1994; Trull et al., 1991, 1995; Anthony and Poths, 1992; Poreda and Cerling, 1992; Staudacher and Allégre, 1993; Zreda et al., 1993; Cerling and Craig, 1994a; Laughlin et al., 1994; Phillips et al., 1994; Sheppard et al., 1995; Wells et al., 1995; Gosse et al., 1996c; Poths et al., 1996; Ackert et al., 1998; Cerling et al., 1999; Licciardi et al., 1999), time control on paleoseismic events (Bierman and Gillespie, 1994; Gosse et al., 1996b; Siame et al., 1997; Ayarbe et al., 1998; Bell et al., 1998; Brown et al., 1998a; Van der Woerd et al., 1998; Zreda and Noller, 1998), and surface uplift rates, rock uplift rates, and incision rates (Brook et al., 1995a; Burbank et al., 1996; Seidl et al., 1997; Small et al., 1997; Gosse et al., 1998; Leland et al., 1998; Gosse and Stone, submitted) (see Morris et al., submitted, for discussion). Several geologic anomalies have been dated by cosmogenic nuclides, including a revealing exposé of Libyan Glass (Klein et al., 1986b) and the timing of the famous Cañon Diablo meteorite impact which excavated Meteor Crater at approximately 49,000 years ago (Nishiizumi et al., 1991c; Phillips et al., 1991). Because the concentration of cosmogenic nuclides is sensitive to surface erosion and depth below the surface, the in situ methods have made significant breakthroughs in establishing the rates and styles of local and large-scale erosion, soil development, and landscape evolution (Nishiizumi et al., 1986, 1991a; Dockhorn et al., 1991; Albrecht et al., 1993; Bierman, 1994; Cerling and Craig, 1994b; Stone et al., 1994, 1998a; Zreda et al., 1994; Bierman et al., 1995a; Bierman and Turner, 1995; Brown et al., 1995b, 1998b; Gillespie and Bierman, 1995; Wells et al., 1995; Granger et al., 1996, 1997; Lal, 1996; Heimsath et al., 1997, 1999; Seidl et al., 1997; Small and Anderson, 1998; Ballantyne et al., 1998; Phillips et al., 1998; Small et al., 1997, 1999; Cerling et al., 1999; Fleming et al., 1999). The method can be applied to study surficial processes over the full range of climate settings (Brook and Kurz, 1993; Brook et al., 1993; Brown et al., 1995a, b, 1998b), with a wide range of lithologies and mineralogy (quartz, plagioclase, pyroxene, amphibole, olivine, and others, and whole rock analyses can be used for $^{36}$Cl). Depending on the surface preservation and exposure history, the dating technique has an effective range from the Pliocene ($>2.65$ Ma) (Nishiizumi et al., 1991a; Brook et al., 1995b; Ivy-Ochs et al., 1995; Schaefer et al., 1999) to the late Holocene (the Holocene is $<10$ ka) (Kurz et al., 1990; Cerling and Craig, 1994a; Laughlin et al., 1994; Ballantyne et al., 1998; Van der Woerd et al., 1998; Cerling et al., 1999).

The rapid and wide acceptance of these techniques (utilizing $^{3}$He, $^{10}$Be, $^{14}$C, $^{21}$Ne, $^{26}$Al, and $^{36}$Cl) is not only due to their wide applicability to problems in surficial geology but also to the reproducibility exhibited by many of the early results. The precision of multiple measurements from a single landform (better than $\sim 5\%$, e.g. Gosse et al., 1995a, c) has approached the limit of the analytical methods. Many valuable lessons have been learned over the past decade of technique development and testing, including improvements in chemical methodologies (Kohl and Nishiizumi, 1992; Ochs and Ivy-Ochs, 1997; Stone, 1998; Lifton et al., submitted) and refinements in the effective production rates of the individual isotope-target systems (Cerling and Craig, 1994a; Clark et al., 1995; Larsen et al., 1995; Gosse and Klein, 1996; Phillips et al., 1996b; Stone et al., 1996, 1998b; Kubik et al., 1998; Licciardi et al., 1999; Stone, 1999).

### 1.3. Previous reviews

In addition to the articles describing detailed applications above, there have been several comprehensive publications on the nature of TCN and utility of TCN methods to address geomorphic and geochronological questions. In his reviews of in-situ cosmogenic nuclides, Lal (1988, 1991) summarized previous work by himself and others to provide fundamental data (including production rate estimates, parameters for altitude and latitude production rate adjustments, and the relationship between geomagnetic field intensity and production rates on Earth's surface) and strategies for using single and multiple nuclides to determine erosion rates. McHargue and Damon (1991) provided a thorough examination of the global $^{10}$Be cycle in which the natural sources and sinks of $^{10}$Be in the Earth's cryosphere, biosphere, hydrosphere, and atmosphere were evaluated. Morris (1991) reviewed the applications of both atmospheric and in situ $^{10}$Be as a chronometer, climate indicator, solar modulation monitor, and subduction zone tracer. Cerling and Craig (1994b) provided an excellent review of prior TCN applications and caveats regarding the application of TCN exposure methods and showed how stable nuclides could be useful for chronologies of $10^3$–$10^7$ yr. We highly recommend their review to anyone interested in the geomorphologic applications of terrestrial cosmogenic nuclides. Bierman (1994) and Bierman and Steig (1996) summarized the basics of TCN calculations for certain geomorphic applications, and offered ideas for applying TCN to obtain boundary conditions for landscape evolution modeling. Gillespie and Bierman (1995) evaluated the precision and limitations of using single or multiple TCN measurements to determine surface erosion rate and or exposure age. The issue of the difficulty in simultaneously solving erosion and exposure duration was discussed later by Lal (1996). A workshop summary by Gosse et al. (1996a, d) provides a recent review of the status of TCN production rates and compiled a list of information that the meeting participants suggested should be included in publications involving the interpretations of new TCN measurements. Morris et al. (submitted) summarized the developments in subduction zone processes, paleomagnetism, and active tectonics with atmospheric and in situ cosmogenic $^{10}$Be. In addition, several reviews of the utility of AMS in earth science have included worthwhile summaries of applications of the TCN methods (e.g., Tuniz and Klein, 1989; Finkel and Suter, 1993). A number of books published between 1960 and 1990 are still fundamental resources on cosmic-ray physics. Rossi's (1964) book is one of the most useful from both a historical and cosmic ray physics point of view. The book by Allkofer and Grieder (1984) includes more than 200 figures and is the most complete single collection of cosmic-ray (primary and secondary) data available. For geomagnetism and paleomagnetism, we find the recent book by Merrill et al. (1996) extremely helpful. We found other books useful for general cosmic-ray theory and history (e.g. Wolfendale, 1963; Pomerantz, 1971; Friedlander, 1989).

## 2. Glossary

### 2.1. Terminology

*Allochthonous*: describes rocks that have been transported from their place of origin (in the geomorphic sense) and subsequently deposited. Glacial erratics and clasts in alluvial fans, colluvium, gelifluction lobes, alluvium, loess, and till are here considered allochthonous.

*Attenuation length ($\Lambda$)*: the thickness of a slab of rock or other mass (air, water, sediment, snow) required to attenuate the intensity of the energetic cosmic-ray flux by a factor of $e^{-1}$ due to scattering and absorption processes (absorption mean free path or *e*-folding length). Units: $g\,cm^{-2}$. Values for typically range from 121 to $> 170\,g\,cm^{-2}$ (45 to $> 65$ cm in solid rock of bulk density $2.7\,g\,cm^{-3}$; see Table 3). $\Lambda$ varies with altitude and latitude, mostly because geomagnetic field and atmosphere effects change the energy spectrum (or 'hardness') of the incident radiation.

*Autochthonous*: rocks that have remained at or near their site of formation. Here, this term includes all bedrock and lava, tuff, authigenic vein filling in soils, and clasts in regolith or felsenmeer blocks which have not been significantly translated or rotated.

*Cross section [elemental] ($\sigma_i$)*: a measure of the probability of a given incident particle (fast or slow neutron, muon) interacting with a target atom of a particular element. Cross section can be interpreted geometrically by imagining a circle centered around the target nucleus with the radius proportional to the likelihood of interaction. Cross sections are particular to each particle/target interaction. Units: $cm^2$ or barns ($1\,barn = 10^{-24}\,cm^2$).

*Cross section [macroscopic] ($\Sigma$)*: a measure of the probability of a given incident particle interacting with any atom in a unit mass of rock or other material. The macroscopic cross section is the sum of the cross sections of all the atoms in the unit mass multiplied by Avogadro's number and divided by the mean atomic weight. Units: $cm^2\,g^{-1}$.

*Erosion*: the dynamic processes of transportation and removal of material from one site to another, regardless of the mechanism. The rate and style of erosion of a rock surface will influence the reliability of the TCN method used to determine its exposure duration. Weathered rock surfaces tend to erode more readily than non-weathered surfaces. It is useful to specify the surface that is being eroded to avoid ambiguity; i.e. a boulder on a moraine and the moraine ridge can both erode.

*Galactic cosmic radiation (GCR)*: energetic particles ($\sim 0.1$ to 10 GeV nucleon$^{-1}$), composed primarily of protons (83%) and a small fraction of α-particles (13%), heavier nuclei(1%), and electrons(3%) (Smart and Shea, 1985). Most of the GCR responsible for TCN production is incident from outside the solar system and thought to mainly originate within our galaxy. Higher energy particles (up to $> 10^{20}$ eV), probably from extra-Milky Way sources, have been detected but are less abundant (Gaisser, 1990; Gaisser and Stanev, 1998).

*Geomagnetic latitude*: angular distance on the Earth's surface measured between the north and south geomagnetic poles. It is analogous to geographic latitude, but with a coordinate system based on the geomagnetic pole rather than rotational pole.

*Inheritance:* refers to the retention of remnant cosmogenic nuclides from a previous episode of exposure. For example, a rock sampled on an alluvial fan surface may contain some residual TCN inherited from a time that the rock was exposed on a cliff face prior to deposition on the fan.

*Isobars*: families of nuclides possessing a common mass number.

*Isotopes*: families of nuclides possessing a common atomic number.

*Momentum (p)*: Approximated by classical (Newtonian) mechanics as the (rest) mass $m_0$ of a particle moving at velocity $v$, ($p = m_0 v$), it is correctly defined relativistically as $p = (m_0/\sqrt{1 - v^2/c})\, v$, where $c$ is the speed of light in a vacuum.

*Muon [negative] ($\mu^-$)*: negative muons are short-lived energetic lepton particles with a decay lifetime of about $10^{-6}$ s. Due to their relatively weak propensity for interaction with atoms, they can penetrate greater thicknesses of matter than strongly interacting particles such as protons, neutrons, and pions. Muonic production of cosmogenic nuclides therefore decreases with depth more slowly than the other important production pathways (e.g. by secondary neutrons).

*Muon capture reactions [negative]:* negative muons may fall into the electron shells of atoms and then be captured by the nucleus, resulting in the production of a cosmogenic nuclide. The probability that a muon captured by an atom will interact (captured by the nucleus to form a TCN) depends on the cross section of the nucleus and the lifetime of the muon. Because muons (a type of meson) are weakly attenuated relative to the nucleonic (e.g. protons and neutrons) component, the muon-capture component of TCN production becomes relatively more important at deeper rock depths (Kurz, 1986b; Fabryka-Martin, 1988).

*Nucleogenic nuclides:* nuclides that are produced in situ in earth materials as a result of nuclear reactions induced by daughter particles of the decay of non-cosmogenic radioactive elements within the material (Reedy et al., 1994b, p. 338). For example, alpha decay and spontaneous fission of U in rocks can result in the production of low-energy neutrons (indirectly, in the case of alpha decay) that can be absorbed by $^{35}$Cl to produce nucleogenic $^{36}$Cl. Nucleogenic contributions can potentially form a significant portion of the nuclide inventory for $^{21}$Ne, $^{36}$Cl, $^{41}$Ca and $^{26}$Al.

*Nuclide*: an atomic species that is characterized by a unique combination of atomic number and neutron number (e.g., $^{10}$Be, consisting of four protons and six neutrons).

*Production rate*: the rate at which a specific nuclide is produced from a specified element or in a mineral. Production rates may include separate terms for spallogenic, muonic, and thermal neutron capture interactions. Production rates for all TCN vary spatially and appear to have varied temporally. They are often reported as normalized to sea level and high latitude. Units: atoms (g target material)$^{-1}$ yr$^{-1}$ or atoms (mole target material)$^{-1}$ yr$^{-1}$.

*Rigidity:* The momentum of a particle per charge, or the product BR of the radius of curvature $R$ due to the deflection of a charged particle through a magnetic field, $B$. Each cosmic particle trajectory azimuth and zenith angle has a cutoff rigidity ($\mathfrak{R}$), or threshold rigidity, which is the minimum rigidity of an approaching particle of a given charge required to penetrate the magnetic field and interact with upper atmosphere nuclei. The vertical cutoffs refer to the rigidity of vertically approaching particle trajectories. The 'effective cutoff rigidity' (Shea et al., 1965, 1987) considers that the trajectories that project back to Earth are not allowed (protons and neutrons cannot penetrate through earth). At latitudes higher than about 58°, the cutoff rigidity drops lower than the minimum necessary momentum of the primaries required for in situ TCN (i.e. all particles with sufficient energy to produce in situ TCN are permitted through the magnetic field so production rates do not vary with magnetic field influences above this latitude).

*Secondary neutrons*: here, cosmic-ray neutrons (mostly $0.1 < E < 500$ MeV, with average $E = 1$ MeV; (Yamashita et al., 1966; O'Brien et al., 1978; Lal, 1988) that are products of the interaction of primary galactic cosmic radiation with atoms in the Earth's atmosphere and subsurface.

*Spallation reactions:* a nuclear reaction resulting from the collision of a highly energetic nucleon (usually a secondary cosmic-ray neutron of energy $> 10$ MeV in the case of in situ TCN) with a target nucleus (Templeton, 1953). Spallation reactions differ from fission reactions because they typically release multiple particles (protons, neutrons, and clusters of these nucleons) leaving a residual spallogenic nuclide with less mass than the original target nucleus. The mechanics of spallation involves two steps: (1) shattering of the target nucleus resulting from an initial collision, from which the primary particle may escape but with reduced momentum, and (2) an

immediate subsequent wave of nucleus disintegration that continues until the nucleus energy falls below the binding energy of individual nucleons.

*Standard atmosphere:* To calculate the pressure variation in the atmosphere due to barometric effects (e.g. adiabatic cooling), a model which describes the general decrease in air pressure with altitude has been used as a standard to which cosmic ray and other pressure-dependent processes can be scaled. The present model, which is a static isothermal model for which complete mixing is assumed, approximates the pressure in dry air up to about 11,000 m for mean annual conditions in mid-latitude regions (CRC Handbook, Lide, 1999–2000): It does not consider regional temperature and pressure anomalies and may not apply well to pressure regimes outside the mid-latitudes (Stone, in press).

*Terrestrial cosmogenic nuclide (TCN):* a nuclide produced by the interaction of secondary cosmic radiation with exposed target atoms in earth-surface materials. We use the term "TCN" to refer only to those cosmogenic nuclides that are produced in situ in minerals, not to those that are produced in the atmosphere and subsequently incorporated into sediment or rock (e.g., by absorption from meteoric water into soils or by the inclusion of atmospherically derived nuclides in seawater into magmatic arc rocks) nor those produced in situ in minerals by nuclear reactions arising from radioactive elements (see "Nucleogenic nuclides"). Although products of the cosmic-ray interactions yield a wide range of nuclides, here we use TCN primarily to refer to the six in situ-produced nuclides that are commonly used in geological applications ($^{3}$He, $^{10}$Be, $^{14}$C, $^{21}$Ne, $^{26}$Al, and $^{36}$Cl).

*Thermal neutron:* neutrons characterized by energy levels in the range imparted by thermal vibrations of the matrix ($E \approx 0.025$ eV), here referring specifically to those secondary neutrons produced in the atmosphere and rock. Thermal neutrons are produced when fast secondary neutrons collide repeatedly with atoms in the atmosphere and rock and subsequently lose energy. Typically, tens to hundreds of collisions are required to reduce neutron energies from the 1 MeV range to thermal energies.

*Thermal neutron absorption:* the capture of thermal neutrons by nuclei in rock, water, and air. Thermal neutron absorption reactions are most important the top few meters of the solid earth.

## 2.2. Notation

| | |
|---|---|
| $A_{(tg)}$ | mass number of a target nucleus |
| $A_a$ | average atomic weight of atmosphere ($14.5\,g\,mol^{-1}$) |
| $A_i$ | average atomic mass of material $i$ ($g\,mol^{-1}$) [Eq. (3.18)] |
| $C_k$ | mass concentration of element $k$ (g of $k$ $(g\,rock)^{-1}$) |
| $D_{eth}$ | epithermal neutron diffusion coefficient ($g\,cm^{-2}$) [Eq. (3.16)] |
| $D_{th}$ | thermal neutron diffusion coefficient ($g\,cm^{-2}$) [Eq. (3.33)] |
| $e^+$ | positron (Fig. 3.1b) |
| $e^-$ | electron (Fig. 3.1b) |
| $E$ | average long-term catchment erosion rate ($g\,cm^{-2}\,yr^{-1}$) |
| $E_k$ | kinetic energy |
| $f_{c,k}$ | fraction of stopped negative muons that are captured by element $k$ ("chemical compound factor") (unitless) [Eq. (3.41)] |
| $f_{d,k}$ | fraction of stopped muons captured by element $k$ that are absorbed into the nucleus before decay (unitless) [Eq. (3.41)] |
| $f_{eth,m}$ | fraction of epithermal neutron flux absorbed by elements that produce nuclide $m$ (unitless) [Eq. (3.12)] |
| $f_{i,k}$ | abundance of the isotope of element $k$ that produces nuclide $m$ subsequent to slow muon capture (unitless) [Eq. (3.41)] |
| $f_{n,k,m}$ | fraction of slow muon captures by element $k$ that produce nuclide $m$ (unitless) [Eq. (3.41)] |
| $f_{th,m}$ | fraction of thermal neutron flux absorbed by elements that produce nuclide $m$ (unitless) [Eq. (3.29)] |
| $F$ | cosmic-ray intensity (particles $cm^{-2}\,s^{-1}\,sr^{-1}$) [Eq. (3.7)] |
| $F_0$ | cosmic-ray intensity in the vertical direction (particles $cm^{-2}\,s^{-1}\,sr^{-1}$) [Eq. (3.53)] |
| $(F\Delta\Phi)^*_{eth}$ | parameter governing epithermal neutron flux near the land/atmosphere interface [Eq. (3.25)] |
| $(\Im\Delta\Phi)^*_{eth}$ | parameter governing thermal neutron flux near the land/atmosphere interface [Eq. (3.36)] |
| $(\Im\Delta\Phi)^*_{th}$ | parameter governing thermal neutron flux near the land/atmosphere interface [Eq. (3.37)] |
| $G$ | acceleration due to gravity ($9.80665\,m\,s^{-2}$) [Eq. (6.2)] |
| $H$ | horizontal component of the geomagnetic field (IGRF model or local measurement) |
| $I_{a,k}$ | dilute resonance integral for absorption of epithermal neutrons by element $k$ ($barn = 10^{-24}\,cm^{-2}$) |
| $I_{eff}$ | effective (macroscopic) resonance integral for absorption of epithermal neutrons ($cm^{-2}\,g^{-1}$) [Eq. (3.4)] |
| $J_q$ | production rate coefficients (atoms $g^{-1}\,yr^{-1}$) [Eq. (3.78)] |
| $J_q^Q$ | production rate coefficients corrected for sample thickness (atoms $g^{-1}\,yr^{-1}$) [Eq. (3.87)] |
| $\kappa$ | kaon (Fig. 1) |

$L_{eth}$ epithermal neutron diffusion length ($g\,cm^{-2}$) [Eq. (3.21)]
$L_{th}$ thermal neutron diffusion length ($g\,cm^{-2}$) [Eq. (3.34)]
$m$ particle mass (g)
$m_a$ mean molar mass of air ($g\,mol^{-1}$) [Eq. (6.2)]
$m_c$ mass of carrier added to sample (g)
$m_{ps}$ mass of purified sample (g)
$M$ geomagnetic dipole moment
$M_0$ present-day geomagnetic dipole moment
$n$ neutron (Fig. 3.1b)
$N_A$ Avogadros number ($6.02214 \times 10^{23}$ atoms $mol^{-1}$)
$N_k$ atomic concentration of element $k$ (atoms $g^{-1}$)
$N_m^{cont}$ concentration of nuclide $m$ from contamination sources (atoms $g^{-1}$)
$N_m^{inh}$ concentration of nuclide $m$ inherited from exposure prior to the event of interest(atoms $g^{-1}$)
$N_m^{meas}$ measured concentration of nuclide $m$ (atoms $g^{-1}$)
$N_m^n$ concentration of nuclide $m$ accumulated from nucleogenic reactions (atoms $g^{-1}$)
$N_m^t$ concentration of nuclide $m$ accumulated during and since the geological event of interest (atoms $g^{-1}$)
$N_m^*$ concentration of nuclide $m$ produced by radioactive decay reactions (atoms $g^{-1}$)
$P$ momentum ($g\,cm\,s^{-1}$); or proton (Fig. 3.1b)
$P_{eth,m}$ production rate of nuclide $m$ by epithermal neutron absorption reactions (atoms $g^{-1}\,yr^{-1}$) [Eq. (3.11)]
$P_f$ production rate of epithermal neutrons (from fast neutron flux) in atmosphere (neutrons $g^{-1}\,yr^{-1}$) [Eq. 3.9)]
$P_{\mu,m}$ production rate of nuclide $m$ by muon absorption reactions (atoms $g^{-1}\,yr^{-1}$) [Eq. (3.40)]
$P_{n,f\mu}$ production rate by absorption of neutrons arising from photodisintegration reactions induced by fast muons (atoms $g^{-1}\,yr^{-1}$) [Eq. (3.40)]
$P_{n,s\mu}$ production rate by absorption of neutrons arising from slow muon capture reactions (atoms $g^{-1}\,yr^{-1}$) [Eq. (3.40)]
$P_{s,m}$ production rate of nuclide $m$ by spallation reactions (atoms $g^{-1}\,yr^{-1}$) [Eq. (3.5)]
$P_{th,m}$ production rate of nuclide $m$ by thermal neutron absorption reactions (atoms $g^{-1}\,yr^{-1}$)
$P_{t,m}$ total production rate of nuclide $m$ (atoms $g^{-1}\,yr^{-1}$) [Eq. (3.5)]
$p(E_{th})$ resonance escape probability of a neutron from the epithermal energy range (unitless) [Eq. (3.3)]
$Q_{eth}$ ratio of production rate integrated over the thickness of a sample to the surface production rate, due to epithermal neutron absorption (unitless) [Eq. (3.75)]
$Q_s$ ratio of production rate integrated over the thickness of a sample to the surface production rate, due to spallation (unitless) [Eq. (3.74)]
$Q_{th}$ ratio of production rate integrated over the thickness of a sample to the surface production rate, due to thermal neutron absorption (unitless) [Eq. (3.76)]
$Q_\mu$ ratio of production rate integrated over the thickness of a sample to the surface production rate due, to muon absorption (unitless) [Eq. (3.77)]
$R_0$ gas constant, $83.144\,cm^3\,bar\,K^{-1}\,mol^{-1}$ or $8.3144\,J\,mol^{-1}\,K$ or $287.05\,J\,kg^{-1}\,K^{-1}$ [Eq. (6.2)]
$R_{eth,ss}$ ratio of epithermal neutron production in subsurface to that in atmosphere (unitless) [$R_{eth,a} = 1$] [Eq. (3.19)]
$R_{th,ss}$ ratio of thermal neutron production in subsurface to that in atmosphere (unitless) [$R_{th,a} = 1$] [Eq. (3.31)]
$R_{m/n}$ ratio of the concentrations of nuclides $m$ and $n$ (unitless) [Eq. (3.98)]
$R_\mu$ ratio of muon production rate to epithermal neutron production rate (unitless) [Eq. (3.49)]
$R'_\mu$ ratio of muon production rate to thermal neutron production rate (unitless) [Eq. (3.49)]
$\mathfrak{R}_0$ present-day geomagnetic cutoff rigidity
$\mathfrak{R}_\lambda$ geomagnetic cutoff rigidity
$S_{el}$ scaling factor for nucleonic production as a function of elevation and latitude [Eq. (3.5)]
$S_{L,eth}$ scaling factor for excess diffusion of epithermal neutrons out of objects of irregular geometry (unitless) [Eq. (3.5)]
$S_{L,th}$ scaling factor for excess diffusion of thermal neutrons out of objects of irregular geometry (unitless) [Eq. (3.5)]
$S_\mu$ scaling factor for muonic production as a function of elevation and latitude (unitless) [Eq. (3.5)]
$S_s$ scaling factor for shielding of a sample surface by snow, soil, or other material (unitless) [Eq. (3.72)]
$S_t$ scaling factor for shielding of a horizontal sample by surrounding topography (unitless) [Eq. (3.67)]
$S_T$ total scaling factor for shielding of a sample of arbitrary orientation by surrounding topography (unitless) [Eq. (3.70)]
$Y_s$ average neutron yield per stopped negative muon (n (stopped negative muon)$^{-1}$)

$Y_{\Sigma k,m}$ total production coefficient for nuclide $m$ from absorption of slow negative muons (atoms (stopped muon)$^{-1}$) [Eq. (3.41)]
$z$ linear distance (cm)
$Z$ mass distance (g cm$^{-2}$) [Eq. (3.6)]
$Z_s$ sample thickness (g cm$^{-2}$)
$Z_{(tg)}$ atomic number of a target nucleus
$\Delta\Phi^*_{eth}$ difference in equilibrium epithermal neutron fluxes between atmosphere and subsurface (n cm$^{-2}$ yr$^{-1}$) [Eq. (3.26)]
$\Delta\Phi^*_{th}$ difference in equilibrium thermal neutron fluxes between atmosphere and subsurface (n cm$^{-2}$ yr$^{-1}$) [Eq. (3.38)]
$\varepsilon$ mass erosion rate (g cm$^{-2}$ yr$^{-1}$)
$\gamma(\phi)$ angle between the normal to a surface and an incoming cosmic-ray particle from any arbitrary angle $\phi$ [Eq. (3.55)]
$\gamma$ gamma ray or photon [Fig. 3.1b]
$\Gamma_{eth}$ absorption rate of epithermal neutrons (n g$^{-1}$ yr$^{-1}$) [Eq. (3.11)]
$\Gamma_{th}$ absorption rate of thermal neutrons (n g$^{-1}$ yr$^{-1}$) [Eq. (3.28)]
$\lambda_{geo}$ geomagnetic latitude (deg)
$\lambda_{pdgeo}$ present-day geomagnetic latitude (deg)
$\lambda_{paleo}$ paleo-geomagnetic latitude (deg)
$\lambda_p$ geographic latitude of past geomagnetic pole position (deg)
$\lambda_m$ decay constant for nuclide $m$ (yr$^{-1}$)
$\lambda_s$ geographic latitude of a sample site (deg)
$\Lambda_{eth}$ attenuation length for absorption and moderation of epithermal neutron flux (g cm$^{-2}$) [Eq. (3.13)]
$\Lambda_{f,e}$ effective attenuation length for cosmic-ray flux through a surface of arbitrary orientation and shielding (g cm$^{-2}$) [Eq. (3.68)]
$\Lambda_{f,p}$ particle attenuation length for fast nucleonic particles (g cm$^{-2}$) [Eq. (3.7)]
$\Lambda_f$ apparent attenuation length for cosmic ray flux received from entire unobstructed sky through a horizontal surface (g cm$^{-2}$) [Eq. (3.59)]
$\Lambda_{th}$ attenuation length for absorption of thermal neutron flux (g cm$^{-2}$) [Eq. (3.32)] inclination angle, measured from the vertical
$\phi$ slope of a sample surface, in the downward direction (deg)
$\phi_n$ inclination of the normal to a surface (deg)
$\phi_p$ geographic longitude of past geomagnetic pole position (deg)
$\phi_s$ geographic longitude of a sample site (deg)
$\phi_{f\mu_x}$ fast muon flux (μ cm$^{-2}$ yr$^{-1}$)
$\Phi_{eth}$ epithermal neutron flux [concentration] (n cm$^{-2}$ yr$^{-1}$)
$\Phi_{th}$ thermal neutron flux [concentration] (n cm$^{-2}$ yr$^{-1}$)
$\Phi_f$ cosmic-ray flux received from entire unobstructed sky through a horizontal surface (particles cm$^{-2}$ yr$^{-1}$) [Eq. (3.9)]
$\Phi^*_{eth}$ epithermal neutron flux at land/atmosphere interface that would be observed if interface were not present (n cm$^{-2}$ yr$^{-1}$) [Eq. (3.22)]
$\Phi^*_{th}$ thermal neutron flux at land/atmosphere that would be observed if interface were not present (n cm$^{-2}$ yr$^{-1}$) [Eq. (3.35)]
$\mu$ muon [Eq. (3.2)]
$\nu$ neutrino [Eq. (3.2)]
$\rho_\beta$ bulk density of solid, liquid, or air (g cm$^{-3}$)
$\theta$ azimuth angle (deg)
$\theta_s$ strike of a sample surface (deg)
$\theta_n$ azimuth of the normal to a surface (deg)
$\sigma_{sc,k}$ elemental neutron scattering cross section for element $k$ (barn $= 10^{-24}$ cm$^{-2}$)
$\sigma_{th,k}$ elemental thermal neutron absorption cross section for element $k$ (barn $= 10^{-24}$ cm$^{-2}$)
$\Sigma_{eth}$ macroscopic absorption and moderation cross section for epithermal neutrons (cm$^2$ g$^{-1}$) [Eq. (3.13)]
$\Sigma_{sc}$ macroscopic neutron scattering cross section (cm$^2$ g$^{-1}$) [Eq. (3.17)]
$\Sigma_{th}$ macroscopic thermal neutron absorption cross section (cm$^2$ g$^{-1}$) [Eq. (3.1)]
$\Psi_{\mu-}$ stopping rate of slow negative muons ((stopped $\mu^-$) g$^{-1}$ yr$^{-1}$)
$\Psi_{m,k}$ production rate of nuclide $m$ by spallation of element $k$ (atoms (g target element) yr$^{-1}$)
$\xi$ dry air adiabatic lapse rate
$\xi_k$ average log decrement of energy loss per collision for element $k$ (dimensionless)
$\overline{\xi}_i$ mean macroscopic log decrement of energy loss per collision for element $k$ in material $i$ (dimensionless)

*Subscripts*

* radiogenic
a atmosphere; or absorption
c chemical; or carrier
cont contaminated
d decay
e effective
el elevation-latitude
eth epithermal
f fast
geo geomagnetic
i individual unit of material, a particle, or single event entity
inh inherited
$k$ element $k$
$m$ nuclide $m$
$n$ nucleogenic; or nuclide $n$
meas measured

| | |
|---|---|
| o | surface; or vertical; or present-day |
| p, paleo | past |
| pd | present day |
| s | slow; or spallation; or stopped; or site |
| sc | neutron scattering |
| ss | subsurface |
| *t* | time; or topography |
| T | total |
| th | thermal |
| tg | target |
| $\mu$ | muon |

## 3. Principles

### 3.1. Introduction

In a search for an analogy to teach his geomorphology class about terrestrial cosmogenic nuclide dating, professor Edward Evenson used the clever imagery of measuring the degree of redness on a person's skin to estimate the duration of exposure to sunlight. Although the analogy is not direct, it is effective because many of the same principles, factors, and uncertainties that apply to the suntan clock also apply to the TCN technique. Solar radiation varies depending on elevation and latitude, and temporally, and so does the secondary cosmic-ray flux. A tan will gradually wear away and cosmogenic radionuclides decay. Suntan lotion and hats will shield skin from solar radiation, while the atmosphere, snow, and mountains shield a landform from cosmic radiation. Not everybody tans to the same degree of redness and TCN production rates vary in different minerals. The change in the color of a sunburned epidermis after peeling may result in an overestimate or underestimate of the total sunlight exposure time, while erosion may result in an overestimate or underestimate of cosmic-ray exposure time. If returning for a second day of tanning, the person will begin partially tanned from the previous exposure, just as cosmogenic isotopes may be inherited from exposures prior to the present duration. In the next section we provide an outline of how primary cosmic radiation initiate the production of cosmogenic nuclides in rock on Earth.

#### 3.1.1. Source of the primary radiation

The galactic cosmic radiation (GCR) of interest regarding the production of terrestrial cosmogenic nuclides is largely composed of high-energy nucleons, mostly protons, which have sufficient energy ($\sim 1\,\mathrm{GeV} < E < \sim 10^{10}\,\mathrm{GeV}$) to produce nuclear disintegrations in the upper atmosphere. In this energy range, most of the primary cosmic radiation incident upon the Earth originates within the Milky Way galaxy, including the lower energy particles from our sun (Lingenfelter and Flamm, 1964). A small component (with ultrahigh energies up to $10^{20}\,\mathrm{eV}$) originates from sources outside our galaxy.

After spiraling through the interplanetary and terrestrial magnetic fields, inelastic interactions of the primaries with nuclei of atoms in the atmosphere produce a cascade of particles and reactions, with net energy being lost to the atmosphere and ultimately the materials of the Earth's surface (Fig. 1). The effects of the magnetic field on primary GCR are discussed in the next two sections. The particles produced from the initial interactions form what is traditionally referred to as 'secondary radiation'. Because collision cross section (probability for interaction of incident particle and target nuclei) is essentially independent of energy at the high energies ($> 100\,\mathrm{MeV}$), the secondary nucleons (e.g. protons and neutrons) and mesons (e.g. kaons and muons) produced in the top of the atmosphere (above $100\,\mathrm{g\,cm^{-2}}$) have essentially the same properties as the primary (Fig. 1b). As a result, the particle flux reaches a maximum at a depth corresponding to about one collision cross section ($\sim 80$–$90\,\mathrm{g\,cm^{-2}}$). This pile up is referred to as the Pfotzer Maximum after its discoverer in 1935 (Rossi, 1964, p. 167; Hayakawa, 1969, p. 8; Allkofer and Grieder, 1984, p. 4). Below this depth, the hadron flux (Fig. 1b) declines as the hadronic cascade loses energy to successive collisions (atmospheric depth corresponds to about 13 collision lengths). The hadron flux drops off with the cumulative mass traversed by the cosmic-ray beam in a fashion analogous to the exponential decrease of light intensity with depth into an absorbing medium (such as the atmosphere or rock), as described by Beer's Law. Cascading causes the drop off to be slower than uncollided primaries attenuate, so the actual curve describing the flux is not exactly exponential.

#### 3.1.2. Effects of the geomagnetic field on GCR

Theoretical study of the influence of a dipole field on charged particle trajectories had begun even before Hess' discovery of cosmic rays. In his effort to explain ionization effects observed in aurorae, Norwegian geophysicist C. Stormer calculated the trajectories of suspected solar particles through a geomagnetic dipole field. Appreciate that these complicated differential equations were first numerically integrated by Stormer and his students without a computer, and early attempts required over about 5000 h between 1904 and 1907 (Stormer, 1935). Although subsequently found inadequate for auroral processes (cf. Rossi, 1964), Stormer's theories provide the basis to all subsequent models of cosmic rays through a geomagnetic dipole field. Specifically, they provide a means to evaluate the minimum momentum required of a particle to pass through the geomagnetic (dipole) field of a given strength.

*Cosmic-ray intensity flux measurements.* In 1927, using a ship-mounted ionization chamber, Dutch physicist J. Clay detected a slight decrease in cosmic-ray intensity around the Suez Canal enroute from Amsterdam to Java. His results, among several unsuccessful contemporary

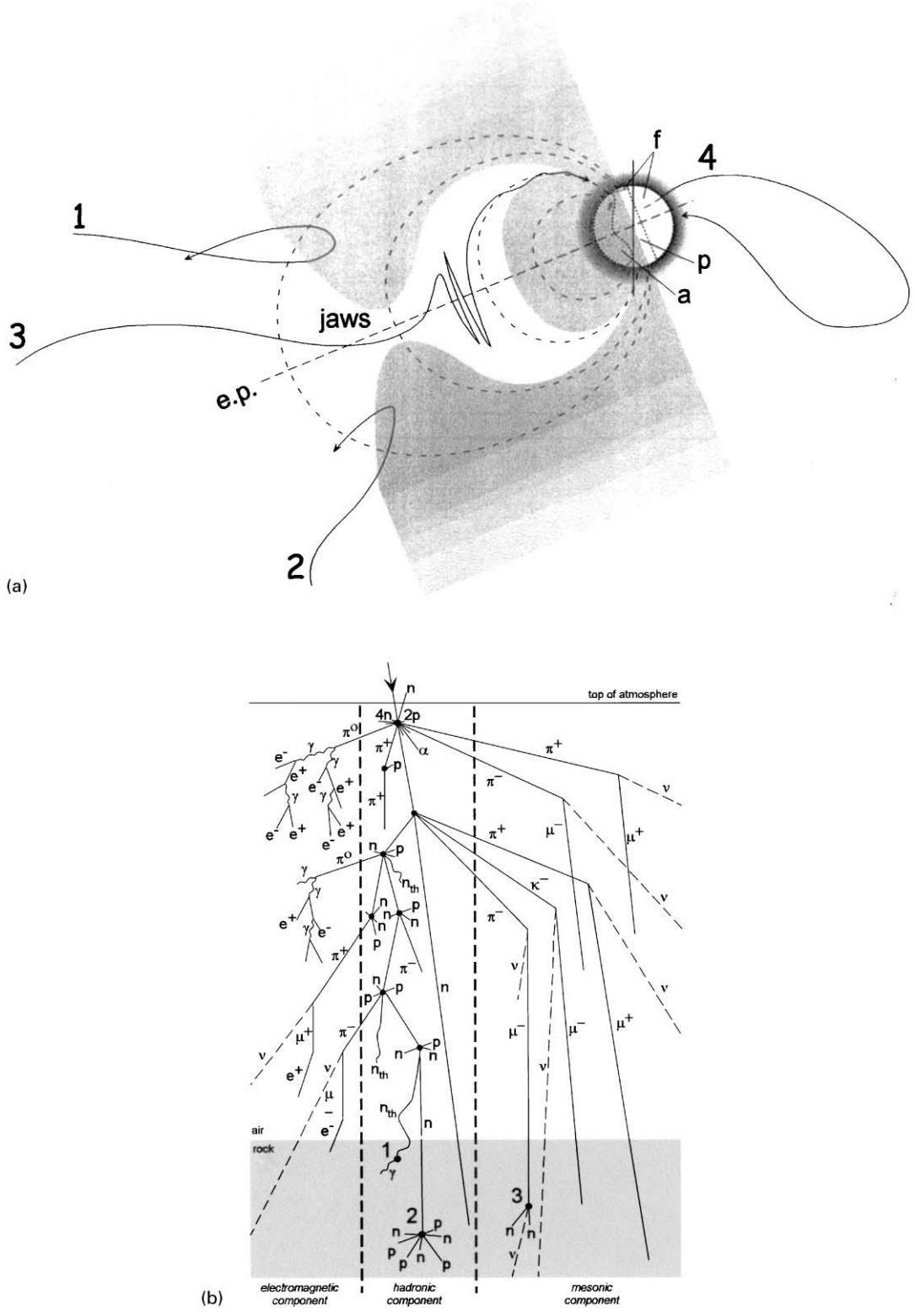


Fig. 1. Fate of a primary charged galactic cosmic ray particle 'a'. Influence on a proton trajectory of a geomagnetic dipole field that is tilted 22° from Earth's spin axis shown as the western half of the field in a meridian plane, compiled from Rossi (1964) and (Quenby and Wenk, 1962). 'e.p.' is equatorial plane. According to Stormer theory (see text), outer shaded region is forbidden to particles of a given insufficient rigidity. Trajectories 1, 2, and 3 of rigidity equivalent to the vertical threshold rigidity, arriving from infinity, must pass through the jaws into inner allowed region and ultimately follow a dipole field line down the horn to atmosphere. Trajectory 4 is impossible due to the opacity of the earth. Distribution of allowed main cone 'a', Stormer and shadow forbidden cones 'f', and the penumbra 'p' are approximated from Pomerantz (1971) for a 10 GV positively charged particle at mid-latitude. (b). The major components of a cosmic-ray extensive air shower (cascade), showing secondary particle production in the atmosphere and rock (modified from Allkofer and Grieder, 1984; Clay and Dawson, 1997). Particle symbols are given in the notation list. Numbers refer to examples of in situ cosmogenic nuclide interactions: (1) $^{35}Cl(n_{th}, \gamma)^{36}Cl$; (2) $^{16}O(n, 4p3n)^{10}Be$; (3) $^{28}Si(n,p2n)^{26}Al$. Vertical scale not linear.

attempts by others (particularly those at high latitudes), established that at least some primary cosmic rays were charged particles because their flux was modulated by the magnetic field. With more sophisticated equipment, the latitude shift ('knee' where the change in flux was greatest) was later found to be between about 41° (Millikan and Neher, 1936) and 25° in both hemispheres at sea level. It was later observed that the lowest cosmic-ray intensity did not occur along a single latitude, but varied longitudinally, indicating that the geomagnetic field was more complicated than a simple dipole field model. Compton (1933) convincingly showed that the cosmic-ray flux intensity variations were directly proportional to the horizontal component ($H$) of the geomagnetic field.

Subsequent measurements of the atmospheric distribution of both fast proton and fast neutron fluxes and star production (e.g. Simpson et al., 1951, 1956; Simpson and Fagot, 1953; Rose et al., 1956; Soberman, 1956; Lal, 1958; McDonald and Webber, 1959; Light et al., 1973; Merker et al., 1973) were made worldwide at different altitudes with shipmounted equipment and with airborne (balloon and jet) equipment to shallow depths in the atmosphere. It takes a depth between 80 and 200 g cm$^{-2}$ in the atmosphere (roughly 15,000 m asl, although this elevation is above of the effective limit of the Standard Atmosphere model) for the fast neutron flux to reach its maximum, because at shallower depths there are insufficient targets to produce the secondary neutrons, because the secondaries produced in the first cascade have properties similar to the primaries, and because the secondary neutrons tend to diffuse out of the atmosphere into space (Fig. 1b). Toward the base of the atmosphere the flux is attenuated rapidly with increasing depth as it is consumed in interactions with the atmospheric nuclei (Fig. 1b). It was recognized that below 200 g cm$^{-2}$ the attenuation lengths of fast neutrons and protons were similar to the attenuation lengths for star producing radiations (determined from emulsions) in air at different latitudes and altitudes (Simpson et al., 1951; Treiman, 1952). This suggested that the high-energy flux below 200 g cm$^{-2}$ was in approximate equilibrium with the flux of secondary low-to-medium energy particles (cf. O'Brien and Burke, 1973), and counts of star productions could be used to describe spatial variability of the cosmic-ray intensity in the atmosphere (e.g. Lal and Peters, 1967).

*Magnetic field effects on incident GCR.* Particle theory and cosmic-ray intensity measurements were soon combined. Lemaitre and Vallarta (1933) used Stormer's theory to reproduce the latitudinal variations in measured cosmic-ray intensities. They also proposed a means to determine the sign of the charge by determining the direction of incidence of the majority of the flux (a charged particle traversing a magnetic field will be deflected normal to both the direction of motion and the field, the direction of deflection depending on sign of the charge). Using the east–west asymmetry effect (the forbidden Stormer cones will face east for positive particles, Fig. 1a), they and Rossi independently determined from particle flux measurements that the majority of particles were positively charged. Notably, Stormer (1934) argued the Lemaitre and Vallarta (1933) calculations incorrectly oversimplified his trajectory models and lacked the precision necessary to map the intensity distribution.

Subsequent papers revealed the inadequacy of a geocentric geomagnetic dipole field model to explain more refined geographic distributions of the cosmic-ray intensity (Simpson et al., 1956; Pomerantz et al., 1960). The intensity records had clear evidence of local magnetic fields as well as possible external fields (Quenby, 1966), and showed longitudinal patterns that were not consistent with a simple dipole model. To avoid unsolvable complexities in the integration of differential equations, models incorporating non-dipole components of the magnetic field must be relatively simple. An eccentric dipole-quadrapole model that accommodates observed magnetic field secular variations was employed (e.g. Gall, 1960).

### *3.1.3. Trajectory models and models of secondary nuclide production rates*

Cosmogenic nuclide dating requires a reliable means to determine the production rate at any given latitude, altitude, depth below the ground surface, and time period. The goal is to produce a secondary cosmogenic nuclide production model that (1) explains the modern cosmic-ray flux distribution at different positions in the atmosphere or on land (e.g. Yamashita et al., 1966), (2) accommodates influences of secular changes in dipole intensity, dipole axis position, non-dipole effects, and distant changes due to the rotation of a tilted dipole through a highly ionized interplanetary gas (cf. Simpson et al., 1956), and (3) can yield reliable results for any duration in the past (e.g. Lingenfelter, 1963). In this section we begin with a discussion of the fundamental aspects of these models and end with a review of modern transport codes of cosmic-ray fluxes.

A charged GCR particle following a trajectory deflected toward earth through the interplanetary fields will begin feeling the effects of the dipole magnetic field long before it reaches the atmosphere or is influenced by second-order magnetic effects. As Rossi (1964) points out, above 32 km there is less than 1% of the total atmosphere, but even at 1600 km above earth the geomagnetic field is at one half of its strength at sea level (see Section 3.5.4 for atmospheric effects that must be simultaneously considered). The terrestrial geomagnetic field inhibits low-energy, charged, primaries from penetrating the atmosphere near the equator and deflects much of the radiation away from the earth. This is essentially because field lines are perpendicular to average incident cosmic-ray trajectories, which would cause the greatest deflection. The net effect is that a harder (higher average

energy) flux penetrates the upper atmosphere at the magnetic equator, and that higher latitudes receive a wider spectrum of energies. This is an oversimplification which will now be discussed in more detail.

The deflection of the trajectories of the incident cosmic rays can be studied by calculating the trajectory backwards from a position on earth using Stormer's equations (which were designed to track particles from the sun). The radius, $R$, of the deflection is proportional to the particle momentum, $p$, but inversely proportional to the magnitude of the charge of the particle (Ze) and the magnitude of the field intensity ($B$). So,

$$\frac{pc}{\mathrm{Ze}} = BR = \Re \tag{3.1}$$

and the product $BR$ is the magnetic rigidity, $\Re$, of the particle. The proportional relation between particle kinetic energy (eV) and rigidity (g cm) is approximately $E_k = 300\Re$, as shown graphically by Rossi (1964, his Fig. 5.3).

For any position on earth, a charged particle spiraling through a magnetic field will have allowed rigidities, forbidden rigidities, and an intermediate penumbra in which slight differences in trajectory may be allowed or forbidden (Fig. 1a). Models of particle trajectories can be run in reverse with increasing momentum until they escape the magnetic field. Any reverse approaches that returned to earth would be impossible. As determined by the east–west effect, trajectories of protons with sufficient momentum could arrive from any direction from the west of vertical. However, easterly trajectories of positively charged particles were allowed only if the trajectory extended up from the surface with a sufficiently vertical angle and radius to avoid projection back to the opaque earth (see Rossi, 1964, his Fig. 5.8). This meant that the final portion of a predominantly easterly trajectory of a proton must be able to curl and enter from the west or vertical.

Earlier, Stormer showed that certain other trajectories below a certain threshold vertical (cutoff) rigidity were impossible ('forbidden') to the particle because they would be bounded along dipole field lines or otherwise deflected, according to

$$\Re = \frac{M}{R_e^2}\left[\frac{1-\sqrt{1-\sin\theta\cos^3\lambda_{geo}}}{\sin\theta\cos\lambda_{geo}}\right]^2, \tag{3.2}$$

where $M$ is the dipole moment, $R_e$ is the radius of earth, and $\lambda_{geo}$ is the geomagnetic latitude of the top of the atmosphere, and $\theta$ is the angle between the velocity vector of the particle and the meridian plane (plane containing the particle and the dipole). For vertical arrival, $\sin\theta = 0$, Eq. (3.2) simplifies to

$$\Re = \frac{M}{4R_e}\cos^4\lambda_{geo} \quad (\mathrm{GV}). \tag{3.3}$$

Quenby and Webber (1959) derived Eq. (3.3) from Stormer theory and demonstrated that it was appropriate for latitudes above geomagnetic latitude 40°. From any position on the surface of Earth, a (Stormer) cone containing the forbidden trajectories by positively charged particles extends eastwards from the meridian plane (Fig. 1a). (The actual point of reference is not on the surface of Earth, but approximately 5.5 km height into the atmosphere (Quenby and Wenk, 1962, p. 1461)). Cutoffs up to 60 GeV may be experienced by positively charged particles approaching a dipole field from the east along the equatorial plane. Considering only the dipole field effect, the trajectory of a particle at vertical cutoff rigidity would enter from infinity an outer allowed zone and be required to penetrate through a slit ('jaws' of the forbidden zone, Fig. 1a). The width of the jaws depends on the particle rigidity, latitude, and the dipole strength, and can be estimated from the true (dipole and non-dipole) horizontal component of the field (Quenby and Webber, 1959; their Eq. (20)). Next, the particle would perform tight loops in an inner allowed region inside the jaws, and ultimately closely follow dipole field lines into the atmosphere (Fig. 1a). Also, depicted on Fig. 1a are the positions of allowed and forbidden regions (Stormer and shadow) for a 10 GV particle at mid-latitude (30°N, zones approximated from Pomerantz, 1971, p. 73).

Below 40° latitude where the jaws of the forbidden zone are much closer to the atmosphere and non-dipole effects become important, the particles of near threshold rigidity do not follow the dipole field lines, and Eq. (3.3) becomes invalid. The effect of the oversimplification is compounded by the increasing importance of off-vertical cutoffs with higher cutoff rigidities (equatorward). That Eq. (3.3) is invalid at lower latitudes is important because it is this equation that is that basis of several later articles, such as Elsasser et al. (1956), who attempted to express the variation in $^{14}C$ production in the atmosphere due to short-term variations in magnetic field intensity. For instance, below 20° a more appropriate expression for vertical cutoff rigidity would include the non-dipole field effects:

$$\Re = \frac{\bar{M}}{4R_e^2}\cos^4\bar{\lambda}_{geo} \tag{3.4}$$

with

$$\bar{M} = M\left[1 + 0.6\left(\frac{\Delta H}{H_D}\right)\right], \tag{3.5}$$

where $\bar{\lambda}_{geo}$ is a modification of the geomagnetic dipole latitude corrected for non-dipole-induced changes in inclination, and $\Delta H$ is the difference between the horizontal component of the dipole field $H_D$ and the horizontal component attributed to non-dipole (quadrapole) effects. Between latitudes 20 and 40° some combination of the two equations was proposed (Quenby and Webber, 1959)

and subsequent more rigid models have been computed (Quenby and Wenk, 1962). The effects of non-dipole field distortions are increasingly important at lower latitudes, where the jaws (Fig. 1b) are narrower for a given rigidity. For discussion of error of the use of trajectory mapping, the reader is referred to Quenby and Webber (1958, p. 103), and Stormer (1955). The influences of the non-dipole field on in situ production rates are specifically treated in Section 3.5.3.

Eqs. (3.3) and (3.4) neglect the penumbral correction for forbidden trajectories which would intersect earth before arrival. Penumbral trajectories are completely forbidden below geomagnetic latitude 25° (dipole field) and may amount to 1.5 GV in places, especially between 20 and 30°. With increasing latitude the region is composed of a decreasing ratio of forbidden : allowed rigidities, because slight disturbances, such as non-dipole field anomalies, can alter trajectory that would be otherwise forbidden in a dipole field. Quenby and Wenk (1962) proposed a means to evaluate the non-dipole influences and the penumbral correction for given rigidities. With the aid of high-speed computers, understanding the geomagnetic effects on cosmic radiation was enhanced by making repeated trajectory traces to determine the maximum $\Re_U$ (the rigidity value for the highest allowed/forbidden transition) and minimum $\Re_L$ (rigidity value for the lowest allowed/forbidden transition) possible for a given latitude, longitude, altitude, zenith angle, azimuth angle, and magnetic field model (Shea et al., 1987). Where the penumbra is transparent $\Re_u = \Re_L$, otherwise the difference between the two reflects the magnitude of the penumbra effect. They calculate an *effective* cutoff rigidity to include the penumbra effect.

### 3.1.4. Recent numerical models of GCR particle production

Even with computers, it was considered impractical (Shea et al., 1987) to model all of these variables for every position on earth, and only vertical cutoff values are generally reported (but see Bland and Cioni (1968) for non-vertical cutoffs). Advanced rigidity models and cascade transport codes (e.g. Lingenfelter, 1963; Light et al., 1973; Merker et al., 1973; O'Brien, 1979; Gaisser, 1990; Masarik and Reedy, 1996; Masarik and Beer, 1999) compare favorably with experimental data (K. O'Brien, pers. comm., 2000). Many of the atmospheric transport codes of cosmic radiation employ Monte Carlo simulations of the interactions of particles in a magnetic field that are governed by the Botzmann equation, which helps describe the production of particles of given energy considering the speed, direction, mean life, and collisional cross sections (O'Brien et al., 1978; O'Brien, 1979). These models account for higher-order field effects by calculating the dipole strength that would give the actual cutoff rigidity at a given location (see Quenby and Webber, 1959, p. 95; Quenby and Wenk, 1962, p. 1459).

Models of cosmic-ray distributions were also derived by fitting star or neutron flux data to model secondary particle production at different atmospheric altitudes and geomagnetic latitudes (Lal and Peters, 1967) and even different times in the past (Lingenfelter, 1963). The model developed by Lal (1991) has been the standard means of scaling in situ TCN production rates for any given site and depth, with an approximate uncertainty of $> 10\%$ (D. Lal, personal communication). Dunai (2000) recently proposed that inclination could serve as a proxy for magnetic intensity at a given site, in lieu of latitude. The proposed improvement was greater sensitivity to higher pole effects (e.g. longitudinal effects due to non-dipole field components). However, these models were based thermal neutron counting (or star production) data from the atmosphere. The models are based on data influenced by a magnetic field that incorporates short-term ($< 10^0$–$10^2$ yr) magnetic field anomalies due to non-axial position of the dipole and non-dipole field (Dunai, 2000). The applicability of these models is therefore limited by (1) the capacity of the magnetic field data upon which they are based to represent the integrated field over arbitrary exposure durations; (2) the inability of geomagnetic latitude-based models to incorporate paleo-longitudinal anomalies (e.g. Lal, 1991); and (3) inconsistencies between site magnetic inclination from a degree $> 2$ harmonic geomagnetic reference field model and the actual intensity field of the earth (Dunai, 2000). Lifton et al. (submitted) are proposing a new approach for in situ production that returns to the trajectory rigidity methods, with the advantage that the effective cutoff rigidity transport models are able to predict both longitudinal and latitudinal perturbations of cosmic-ray flux due to non-dipole and other effects.

Using a Monte Carlo approach (cf. Armstrong et al., 1973; Masarik and Reedy, 1996) to model the cosmic-ray flux through the atmosphere, Masarik and Beer (1999) have performed the most recent coupled cosmogenic nuclide production-transport simulations for the atmosphere. Unfortunately, they did not extend their model to include in situ production in rocks. Masarik and Reedy (1996) simulated production of specific atmospheric and in situ cosmogenic nuclides based on Monte Carlo codes that predict particle production and transport according to the present understanding of relevant physical processes and conditions (e.g. nuclear cross sections). Their results were generally consistent with empirical data (production rates, isotopic production ratios, attenuation lengths). The next step logical would be to couple the atmospheric and in situ transport codes to a variable magnetic field model.

Most of these models use the Standard Atmosphere model to determine how the cosmic-ray flux will travel through the atmosphere. Although a reasonable first-order approximation, the Standard Atmosphere does not incorporate significant long-term second-order

anomalies that will contribute to the misfit of the observed cosmic-ray flux data and geomagnetic field based models. For instance, Stone (in press) points out that persistent pressure deviations over Siberia and Iceland depart from the Standard Atmosphere by $\pm$ 4.4 hPa at sea level, which would directly correspond to about a $\pm$ 3–4% change in TCN production rates (presently within the uncertainty of the nuclide production models for any site). However, he points out that in situ production rates in Antarctica would be 25–30% higher than rates for the same latitude in the Arctic (Stone, in press). Clearly, we are approaching a point in the development of the TCN method when the secondary spatial (e.g. atmospheric, magnetic) variations must be accurately incorporated into the numerical scaling models of cosmic ray flux and TCN production.

### 3.1.5. *Nuclide production from primary GCR*

As the cascade of reactions propagates down through the atmosphere and eventually the upper few meters of the Earth's crust, the composition of the nuclear particle flux tends to become dominated by neutrons (Fig. 1b). This is because they have a higher probability of being emitted from stimulated nuclei, and because, being electrically neutral, they are not slowed by ionization energy losses to atoms they encounter. In addition to the secondary neutron radiation, a relatively smaller number of $\pi^{\pm}$ and $K^{\pm}$ mesons are produced ($E \sim 400$ MeV), resulting in a flux of short-lived muons which also contributes to TCN production (cf. Section 3.1.8) (Fig. 1b). The secondary fast nucleons (and minor mesonic flux) continue to produce cosmogenic nuclides in the atmosphere, hydrosphere, and lithosphere by breaking apart target atoms through spallation interactions. As energy is lost due to successive reactions, down to the 1–5 MeV range, the neutrons are no longer capable of causing spallation reactions and their remaining energy is dissipated mainly by momentum transfer during elastic scattering off incident nuclei. The neutrons pass through the epithermal energy range (between $\sim$ 0.1 MeV and 0.5 eV) down to the level dictated by the thermal energy of the gas or solid within which the neutron resides. Such neutrons are referred to as "thermal neutrons" and are characterized by a kinetic energy of approximately 0.025 eV per neutron. In this state, their paths are described by Brownian motion, due to random collisions with atomic nuclei in the medium. Ultimately these neutrons are absorbed by the nuclei of atoms they encounter, resulting in the formation of "thermal-neutron-produced cosmogenic nuclides". By far, the most important of these is $^{14}C$, produced in the atmosphere by thermal neutron absorption into $^{14}N$ (the reaction $^{14}N(n,p)^{14}C$). In minerals at the Earth's surface, the most important thermal-neutron produced cosmogenic nuclides are $^{36}Cl$ (produced mainly by the reaction $^{35}Cl(n,\gamma)^{36}Cl$) and $^{41}Ca$ (produced by the reaction $^{40}Ca(n,\gamma)^{41}Ca$). Due to the different types of cosmic-ray reactions involved, the pattern of TCN production with depth by spallation reactions differs from that of thermal-neutron-absorption reactions. This can be illustrated by comparing the depth-dependence of the production of $^{10}Be$ in a quartz arenite (Fig. 2a) and $^{36}Cl$ in a limestone (Fig. 2b). These reactions are discussed in detail below.

All TCN exposure history methods are based on the production of rare nuclides from a small portion of the interactions between secondary cosmic radiation

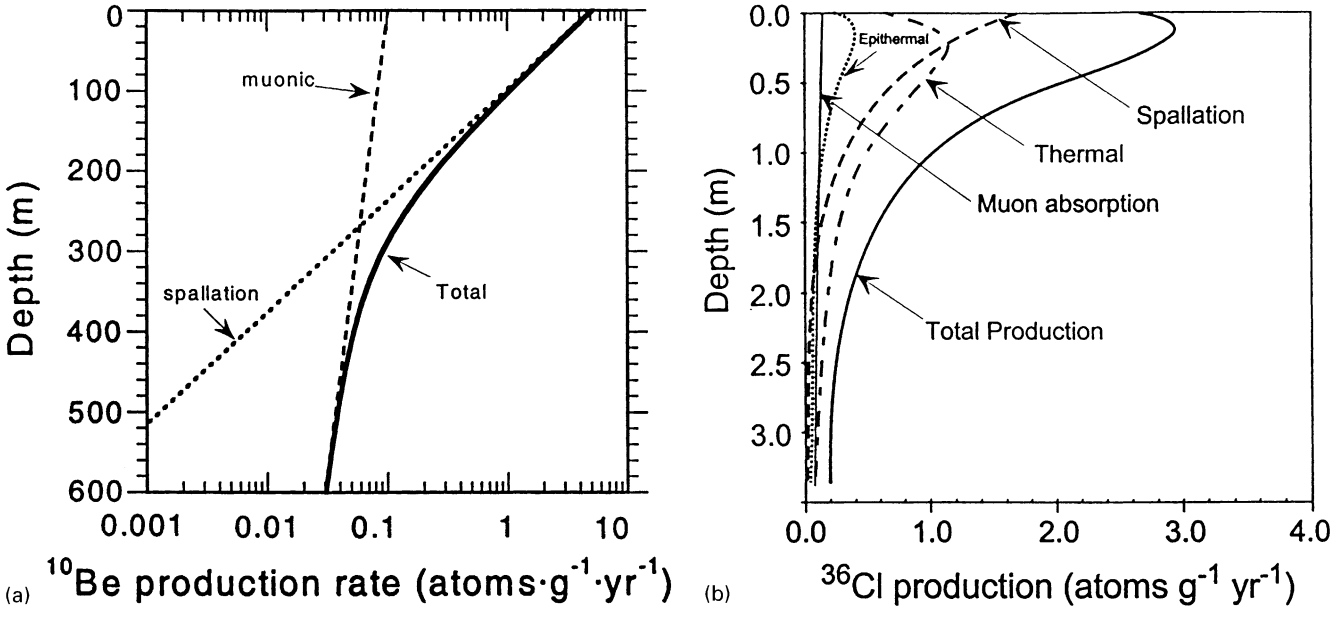


Fig. 2. Variation of the production of TCN with depth in rock at high latitude and sea level: (a) $^{10}Be$ in quartz arenite; (b) $^{36}Cl$ in an ultramafic rock. Average ultramafic rock composition from Fabryka-Martin (1988) was used, but Cl concentration was reduced to 10 ppm.

of different energies and atoms in an exposed mineral. In the following sections, we do not distinguish between minerals in rocks and unconsolidated sediment because the major differences between rocks and unconsolidated sediment is with regard to geomorphic processes, not the fundamental principles of TCN methods. Specific treatment of unconsolidated materials is discussed in Sections 3.11, 4.4 and 5.2.

*3.1.6. TCN production by energetic nucleons*

Most of the secondary high-energy ($> \sim 10$ MeV) nucleonic radiation at mountaintop elevations is composed of neutrons. A spallation reaction is a high-incident energy process in which a neutron (or other nucleon) collides with a target nucleus (e.g., a silicon atom) and breaks from the target nucleus several (typically 3–10) lighter particles, leaving a lighter residual nucleus (e.g. $^{21}$Ne) (Templeton, 1953). Spallogenic reduction of the nucleus mass occurs in two phases: (1) shattering of the target nucleus resulting from an initial collision, from which the primary particle may escape but with reduced momentum, and (2) a consequent spalling of individual or clusters of nucleons induced by the energy dissipation throughout the nucleus until the energy falls below the binding energy of individual nucleons. The product mass distribution is bimodal and favors product masses that are either slightly less than the target mass (the residual nucleus of the target atom) or much lighter particles such as protons and neutrons. For example, when a $^{28}$Si is the target of a spallation reaction, it is much more probable that nuclides with masses of 27–25 and 1–3 will be produced than two nuclides with a mass of 14. This is partly why spallogenic $^{26}$Al has a greater production rate in quartz than $^{10}$Be does, even though $^{10}$Be can be produced from both $^{28}$Si and $^{16}$O. The spallogenic TCN concentration profiles in the upper 2 m of rock are characterized approximately by an exponential curve with *e*-folding length that is similar to the attenuation profile of fast neutrons in air (Fig. 2a). However, a numerical simulation of neutron flux with depth below a rock surface at sea level and high latitudes by Reedy and Masarik (1995) showed an initial flat region to a depth of 12 g cm$^{-2}$ (roughly 4.4 cm) which was not seen with earlier transport models (e.g. O'Brien et al., 1978). The flattening was also apparent in measured profiles (Dep, 1995). If this flattening is ignored (presently it is ignored), it would result in an underestimation of near surface production rates by up to 3.7%. It suggests that a different production rate adjustment be made to shallow surface samples ($< 4$ cm) for spallogenic or muogenic cosmogenic nuclides.

*3.1.7. TCN production by low-energy neutron*

In general, the epithermal and thermal neutron fluxes are in equilibrium with the cosmogenic neutron production rate by energetic cosmic radiation and hence follow the exponential dependence of flux with cumulative mass below the top of the atmosphere. However, the atmosphere/land surface interface constitutes an abrupt discontinuity in material properties that produces a corresponding perturbation in the spatial distribution of the low-energy neutron fluxes. The most important of these properties are the macroscopic thermal and epithermal neutron absorption cross sections ($\Sigma_{\text{th}}$ and $I_{\text{eff}}$). The macroscopic epithermal neutron absorption cross section is also referred to as the effective resonance integral for absorption of epithermal neutrons. These parameters describe the propensity of a heterogeneous (in terms of elemental composition) bulk material to absorb neutrons through nuclear reaction. The macroscopic thermal neutron absorption cross section is given by

$$\sum_{\text{th}} = \sum_{k} \sigma_{\text{th},k} N_k, \tag{3.6}$$

where $\sigma_{\text{th},k}$ is the elemental thermal neutron cross-section of the $k_{\text{th}}$ element and $N_k$ is the concentration of that element (in atoms g$^{-1}$ or mol g$^{-1}$). The elemental thermal neutron cross section is usually expressed in barns, where one barn is equal to $10^{-24}$ cm$^2$ (understood as per atom in this case). The macroscopic thermal neutron is therefore usually expressed in cm$^2$ g$^{-1}$ or barn mol g$^{-1}$.

The macroscopic thermal neutron cross section of the atmosphere is 0.0602 cm$^2$ g$^{-1}$, while that of common types of rock ranges from about 0.004 to 0.008 cm$^2$ g$^{-1}$ (Fabryka-Martin, 1988; Liu et al., 1994). The approximately one-order-of magnitude greater absorption by the atmosphere is due to the large thermal neutron cross section of nitrogen, 1.9 barns. As a result, the thermal neutron flux in the atmosphere above the land surface is much less than in the solid earth below. The change in thermal neutron flux at the atmosphere/land interface is not abrupt, however, because the gas-like properties of thermal neutrons allow net upward diffusion of neutrons thermalized in the solid earth (cf. O'Brien et al., 1978).

The diffusive behavior of thermal neutrons therefore produces a thermal neutron flux profile that smoothly increases downward below the land surface to a depth of approximately 50 g cm$^{-2}$, then reverses and decreases with additional depth, a characteristic shape that we refer to as the thermal neutron "bulge" (Fig. 2b). This profile is in marked contrast to that of energetic cosmic radiation, which decreases exponentially with depth. This divergence in the depth dependence of the production rates of thermal-neutron produced and spallation produced cosmogenic nuclides can be used to advantage in studies of surficial materials that may have had complex exposure histories. However, such use requires the ability to quantify the depth dependence of the thermal neutron flux.

*3.1.8. TCN production by muons*

The sections above have described the production of cosmogenic nuclides by reactions of terrestrial atoms with neutrons, protons, and occasionally with heavier nuclear fragments. These particles, due to their strong nuclear interactions and often high energies, are quite reactive. Most of them are therefore absorbed in the atmosphere and the top few meters of the solid earth. In sharp contrast, large numbers of very low-mass particles such as neutrinos can pass through the entire earth with so few reactions resulting that they are not useful for geological applications. Muons occupy an intermediate position.

Primary cosmic-ray reactions in the upper atmosphere produce unstable $\pi^{\pm}$ and $K^{\pm}$ mesons. If they do not interact quickly with atmospheric nuclei these particles can decay to muons, with mass 207 times that of the electron, before reaching the land surface. At ground level approximately half the cosmic-ray flux consists of energetic muons. Although muons decay rapidly (lifetime $\sim 10^{-6}$ s), like other leptons they do not undergo strong (nuclear force) reactions with other particles. Thus reactivity is low, so the muons penetrate much deeper than the hadronic (i.e. meson and baryon particles that participate in the strong interaction) component of the cosmic-ray flux. Such muons are lost due to either spontaneous decay (to electrons and neutrinos) or due to slowing by ionization and capture (in the case of negative muons) by positively charged nuclei. Muonic interactions producing TCN mainly involve the capture of slow negative muons ($\mu^-$) by charged nuclei, although coulombic interactions of fast muons also contribute (Lal, 1988). Interactions with a target of mass number $A_{(tg)}$ and atomic number $Z_{(tg)}$ induced by stopping slow negative muons to produce TCN take on the general form

$$\mu^-(A_{tg}, Z_{tg}) \rightarrow (A_{tg} - x, Z_{tg} - 1) + (x)n_i + v_\mu \qquad (3.7)$$

leading to a reduction of at least 1 in $A_{(tg)}$ (or in $Z_{(tg)}$ if, for example, $x = 0$). Here $n$ refers to neutrons and $v$ to neutrinos. Reaction of the muon with a nuclear proton releases large amounts of energy and particles (including neutrinos) are ejected from the excited nucleus (Charalambus, 1971). Negative muon reactions on various target nuclei can produce $^{10}$Be, $^{26}$Al, $^{36}$Cl and other nuclides. They can also indirectly release neutrons, through a variety of reactions, which can in turn generate nuclides such as $^{36}$Cl through low-energy neutron absorption (Stone et al., 1998b). Highly energetic muons can also interact spallogenically.

It is difficult to precisely isolate the contribution of muon capture mechanisms to TCN production at the surface because neutron spallation reactions can also produce any muon-produced ('muogenic') product. However, the muogenic component can be isolated from the fast nucleon component because muons have the capacity to penetrate more deeply into rocks. An interesting dilemma has developed over the relative contribution of muons to the total production of TCN in rocks near the surface. Hampel et al. (1975) interpreted cosmogenic $^{26}$Al in silicate rock at $\sim 1.8$ m depth as being completely produced by muonic interactions. Measurements of $^{26}$Al at depths of 10 m below the rock surface by Middleton and Klein (1987) led them to predict that $\sim 10\%$ of the surface production of TCN at sea level was through muon capture by $^{28}$Si. Other evidence suggests that 10% is too high and the value is probably closer to 1–3% at the surface (Brown et al., 1992a, 1995a; Heisinger et al., 1997; Stone et al., 1998b). In the case of using cosmogenic $^{26}$Al and $^{10}$Be, it is not critical to know the exact muogenic component because fortunately the $^{26}$Al/$^{10}$Be muonic production ratio ($7.0 \pm 0.4$, Reedy et al. (1994a); $7.2 \pm 1.2$, Heisinger et al. (1997)) is approximately the same as the $^{26}$Al/$^{10}$Be neutron spallogenic production ratio ($\sim 6.0$ in quartz, Nishiizumi et al. (1989), and 7.1 in synthetic $SiO_2$ targets, Reedy et al. (1994a)). On the other hand, recent preliminary results of Kim et al. (1999) show that the muon-dominated $^{26}$Al/$^{10}$Be less than $4.4 \pm 0.1$. This is lower than the neutron-dominated $^{26}$Al/$^{10}$Be production ratio and is lower than the estimates from simulations and experiment. The magnitude of the muogenic production will affect both the spatial scaling of production and the effects of erosion on the rate of TCN buildup.

Muogenic nuclides are potentially very useful for a variety of earth-science applications. The sensitivity of nuclide concentrations to erosion rate decreases as the attenuation length for production increases (e.g., a nuclide produced mainly in the top few centimeters will be "reset" by quite shallow erosion, whereas one whose production is spread over several meters of depth will be much less affected). The attenuation length for muon production (which does not adhere closely to an exponential profile; Stone et al., 1998b) is about 1500 g cm$^{-2}$ (Brown et al., 1995a), an order of magnitude longer than for neutron and proton production. The muon flux actually decreases more slowly with depth than an exponential relation would predict. Used in combination with a nuclide produced by a shorter attenuation length reaction, muogenic nuclides offer the potential to determine both the exposure age and erosion rate of rapidly eroding landforms (Stone et al., 1998b).

Several deep profiles of $^{36}$Cl (Kubik et al., 1984; Dockhorn et al., 1991; Stone et al., 1998b), and $^{10}$Be and $^{26}$Al (Nishiizumi et al., 1994; Brown et al., 1995a) that record muogenic production have been measured. In spite of these efforts, and laboratory investigations of muon reactions as well, the systematics of muon reactions in geological materials are poorly quantified compared to the major hadronic reactions. This is partially a result of the complexity of muon reactions. Neutron and proton reactions are essentially colligative, that is, they occur in proportion to the abundance of the target element in the

rock. Negative muons, however, first interact with the electron shells of the target atoms in a fashion analogous to electrons and thus the reaction parameters are dependent on the chemical properties of the rock. This additional complexity makes field calibration of the reaction parameters a difficult and involved task. These parameters have been established for muon production of $^{36}$Cl in the relatively simple case of pure calcite by Stone et al. (1998b), but considerable additional work will be needed before muon production can be applied to geological problems involving other lithologies or nuclides.

In addition to the potential application of muogenic nuclides to deeply eroded landforms, their effects must also be considered in situations where materials covered to moderate depth are brought to the surface by either steady or episodic erosion. For example, Stone et al. (1998b) have shown that in a limestone that has been rapidly eroding for a long period, up to 50% of the $^{36}$Cl at the surface can be a result of muon, rather than spallation, production. Similarly, if a relatively stable limestone surface has in the recent past suddenly had several meters of rock removed by an event that is assumed to have "reset the clock" for dating, a substantial background of muogenic $^{36}$Cl may be inherited from production prior to the erosion event. These examples demonstrate the importance of quantifying muon production.

#### 3.1.9. Factors limiting TCN applications

At this point, it is important to make a distinction between meteoric cosmogenic nuclides, which are produced in the atmosphere, and terrestrial cosmogenic nuclides that are produced in situ from nuclear transmutations in rock. The familiar radiocarbon dating method is based on the abundance of $^{14}$C, a cosmogenic nuclide produced in the atmosphere largely by thermal neutron absorption into $^{14}$N. Most of the commonly used TCN are produced in the atmosphere as well as within rocks. Some nuclides such as $^{10}$Be are produced in the atmosphere at a rate approximately $10^3$ times greater than the average rate of production in rocks on Earth, so it is necessary to take rigorous steps in sample preparation to ensure that the atmospheric component does not contaminate the terrestrial component (cf. Kohl and Nishiizumi, 1992). Atmospherically produced TCN that are highly reactive with mineral surfaces (e.g., $^{10}$Be) are more of a problem than those that react little with rocks (e.g., $^{3}$He and $^{36}$Cl).

Although there may be a very large number of nuclides that can be produced from cosmic-ray interactions with target atoms in rock, only six TCN have been commonly used for geologic applications: $^{3}$He, $^{10}$Be, $^{14}$C, $^{21}$Ne, $^{26}$Al, and $^{36}$Cl (Table 1, see Lal, 1988 for others). In addition, in situ produced cosmogenic $^{39}$Ar and $^{41}$Ca have been investigated (Looosli, 1983; Middleton et al., 1989), but not applied to any significant extent. Most other nuclides have not been used for one or a more of the following reasons: (i) the nuclide also exists naturally (from primordial or radiogenic sources) and the radiogenic contribution cannot be reliably determined (e.g., $^{7}$Li), (ii) the nuclide may decay too rapidly to be useful (e.g., $^{24}$Na, which has a half-life of 15 h), (iii) the cosmogenic production rate of the nuclide in rocks at the surface of the earth may be too low to have concentrations above the detection limits of existing analytical methods (e.g., TCN with $A > 56$ are rarely produced because of the low abundance of target elements), and (iv) other isotopes of the element may exist naturally in rocks in such abundance as to make measurement of the abundance of the cosmogenic nuclide difficult, even with state-of-the-art accelerator mass spectrometry with isotopic ratio limits of $10^{-15}$ (e.g., cosmogenic $^{41}$Ca in plagioclase).

### 3.2. Numerical simulation of low-energy neutron behavior

Knowledge of the depth-distribution of TCN production beneath the surface of the solid earth is necessary for surface exposure dating and erosion studies. As described above, production due to spallation reactions, mainly from energetic neutrons, follows a relatively simple exponential distribution (see also Sections 3.3.1 and 3.4). The distribution of low-energy neutrons, however, is more complex. (For the purposes of this paper, we consider "low-energy neutrons" to be those in the range where TCN production by simple neutron absorption reactions is significant, $\sim 10$ keV to 0.025 eV, corresponding to the epithermal and thermal energy regimes). This section and Section 3.3 describe approaches to quantifying the low-energy neutron distributions.

Low-energy neutrons are produced as the result of a complex cascade of nuclear reactions propagated down through the atmosphere and solid earth. The production distribution of cosmogenic nuclides depends on nuclear reactions at a wide range of energy levels within this cascade. The most satisfactory approach to simulating the cosmogenic nuclide production is to comprehensively model the chain of reactions. Critically important early efforts in this direction were described by Lal and Peters (1967). Later, O'Brien et al. (1978) focused on neutron fluxes, down to thermal energies, over a range of atmosphere/surface interfaces. More recently, Dep (1995) has applied linked high- and low-energy neutron transport codes to simulating neutron flux distributions and resultant $^{36}$Cl production rates at the atmosphere/land surface interface. Dep et al. (1994a) compared the calculated thermal neutron flux distribution with experimental results and Dep et al. (1994c) compared the calculated $^{36}$Cl distribution with that in a natural rock, both with very favorable results.

A significant proportion of the $^{36}$Cl is produced by absorption of epithermal neutrons (those with energies

Table 1
Important reactions and advantages and disadvantages due to physical and chemical attributes for common TCN

| Nuclide | Lifetime | Reaction types and primary targets | Primary target minerals | Advantages | Disadvantages |
|---|---|---|---|---|---|
| $^{3}$He | stable | *Spallation on:* O, Mg, Si, Ca, Fe, Al $^{6}Li(n,\alpha)^{3}H \rightarrow {}^{3}He$ | Ol, Pyx, Hbl, Gnt | $^{3}$He has the highest production rate of all TCN and low detection limit on a conventional mass spectrometer (blanks $<$ 50,000 atoms $^{3}$He, background $\sim$ 20,000 atoms) so it can be used to date young surfaces ($<$ 3000 kyr). Extremely long exposures can be investigated because it is stable. Presently there is more known about production rate for $^{3}$He than the other TCN noble gas $^{21}$Ne. | $^{3}$He appears to diffuse too rapidly from quartz and fine grained groundmass in aphanitic rocks (Brook and Kurz, 1993). Correction for radiogenic /nucleogenic /magmatic $^{3}$He is necessary, particular on rocks with old crystallization ages. Greater opportunity for inheritance of stable cosmogenic $^{3}$He if the mineral grains have ever been exposed previously. Interference from $^{1}H^{2}H$ molecules. |
| $^{10}$Be | 2.2 Ma | $^{16}O(n,4p3n)^{10}Be$ $^{28}Si(n, x)^{10}Be$ $^{16}O(\mu^{-},\alpha pn)^{10}Be$ $^{28}Si(\mu^{-},x)^{10}Be$ $^{7}Be^{7}Li(\alpha,p)^{10}Be$ $^{9}Be(n,\gamma)^{10}Be$ $^{10}B(n,p)^{10}Be$ $^{13}C(n,\alpha)^{10}Be$ | Qtz, Ol, Mgnt, Plag? | Simple, stoichiometric chemistry of target mineral. Quartz is resistant to chemical weathering and is almost ubiquitous. Mostly produced through spallation and muon reactions on O and Si. $^{10}$Be samples can be prepared simultaneously with $^{26}$Al, $^{14}$C, and $^{21}$Ne in quartz. Olivine is fairly resistant to weathering and may be a suitable alternative where quartz is absent. Its long half life make it useful for long exposures. Not a gas, relatively immobile. | Atmospheric $^{10}$Be is potentially a significant source of contamination. The isobar $^{10}$B is difficult to remove during AMS analysis. Little work has been done to determine the production rate of $^{10}$Be in the olivine solid-solution series and other targets. $^{10}$Be has the lowest production rate in quartz of all TCN so young surfaces require large samples or not possible. |
| $^{14}$C | 0.82 kyr | $^{16}O(n,2pn)^{14}C$ $^{28}Si(n, x)^{14}C$ $^{16}O(\mu^{-},2p)^{14}C$ $^{14}N(n,p)^{14}C$ $^{17}O(n,\alpha)^{14}C$ $^{11}B(\alpha,p)^{14}C$ | Qtz | Excellent for recent exposure histories because its short half life renders it insensitive to low erosion rates. Inherited concentrations will likely be minimal because of its fast decay. Higher production rate than $^{10}$Be. | Short half life precludes investigation of long ($>$ 30 kyr) exposure histories. Although whole rock analyses were attempted, quartz has been the only reliable target. Probability of contamination makes sample preparation and analysis difficult and expensive. |
| $^{21}$Ne | stable | *spallation:* Mg, Na, Al, Fe, and Si $^{16}O(\alpha,n)^{21}Ne$ $^{19}F(\alpha,pn)^{21}Ne$ | Qtz, Ol, Gnt. Plag? | Extremely long exposures can be investigated because it is stable. $^{21}$Ne does not diffuse as rapidly through quartz as $^{3}$He does (Brook and Kurz, 1993; Brown et al., 1991; Staudacher and Allegre, 1991). Higher production rate than $^{10}$Be. | Correction for radiogenic / nucleogenic $^{21}$Ne is necessary, particularly in old rocks (worse if exposure time is short). Greater opportunity for inheritance of stable $^{21}$Ne if the mineral grains have ever been exposed previously. Interference for Ne isotopes from $H_2{}^{18}O^{+}$ and $^{40}Ar^{2+}$. |
| $^{26}$Al | 1.0 Ma | $^{28}Si(n,p2n)^{26}Al$ $^{28}Si(\mu^{-},2n)^{26}Al$ $^{23}Na(\alpha,n)^{26}Al$ | Qtz | Simple, stoichiometric chemistry of target mineral, low stable Al abundances ($<$ 1%). Production rate of $^{26}$Al is higher than $^{10}$Be. | Mostly restricted to quartz. $^{26}$Mg is an isobar; AMS is required. Difficult to measure low $^{26}Al/^{27}Al$ in quartz with high Al contents. |
| $^{36}$Cl | 430 kyr | $^{40}Ca(n,2n3p)^{36}Cl$ $^{39}K(\mu^{-},p2n)^{36}Cl$ $^{40}Ca(\mu^{-},\alpha)^{36}Cl$ $^{35}Cl(n,\mu)^{36}Cl$ $^{39}K(n,\alpha)^{36}Cl$ | Spallation tgt: K-spar, Plag, Calcite Thermal neutron activation tg: $^{35}$Cl in Chlorite, fluid inclusions in qtz | Has multiple production pathways ($n$, $n_f$, $\mu$) so it is possible to use just $^{36}$Cl for erosion and burial investigations. Atmospheric production is not as important as it is for $^{10}$Be, so whole rock chemistry is possible, and therefore wide range of lithologies. AMS sensitivity higher for Cl isotopic analysis than Be and Al. Production rate higher than $^{10}$Be. | Has multiple pathways on multiple elements, so production rates from individual pathways are currently difficult to decipher. Exposures greater than $\sim$ 1 Ma cannot be determined. Complicated system unless pathways are isolated when erosion is slow but non zero. Thermal neutron leakage is significant factor in variable moisture conditions, snow cover. Radiogenic and nucleogenic pathways limit low-level applications. AMS required for analysis. |

reactions: target(reacting particle, emitted particle)product; negative muon capture reactions also produce $\nu_{\mu}$

between approximately10 keV and 0.5 eV) and numerical simulations can accurately model the transport of neutrons in this energy range. In addition to a realistic simulation of cosmic-ray physics, the numerical modeling approach allows for the incorporation of complex boundary conditions into neutron-flux computations, for example, a high water-content soil over a layer of non-porous rock.

The main limitation of the numerical simulation approach is the complexity and the relatively large computational demands of the programs employed. Another is the sensitivity of the results to small variations in input parameters. An alternative to full-scale neutron transport simulation is to use simplified analytical solutions.

### 3.3. Analytical equations for TCN production

Analytical expressions for neutron behavior offer a simpler alternative approach to full-scale neutron transport numerical modeling. In this approach, the energy-dependent aspects of neutron transport are condensed into a limited number of energy categories and the transport properties are computed from bulk material composition. Although less flexible and comprehensive than first-principle transport codes, this approach has the advantage that solutions can be obtained in a few minutes on standard personal computers.

For purposes of computing cosmogenic nuclide production, we divide the equations governing neutron production and transport into three discrete energy ranges:

1. *High energy or "fast" range.* This range extends from maximum cosmic-ray energies ($\gg$TeV) to $\sim$ 10 MeV. In this energy range, the cosmic-ray particles are assumed to act as a beam. The cosmic-ray flux is attenuated exponentially with mass depth ($g\,cm^{-2}$). Cosmogenic nuclides are assumed to be produced by spallation reactions, with the production rate independent of the energy spectrum.
2. *Thermal energy range.* In the thermal energy range ($< 0.5$ eV), the neutrons can be assumed to be moving in a Brownian fashion and hence a diffusion-equation approximation can be used to model their behavior. Similar approaches have long been employed in nuclear reactor theory (Stephenson, 1954). In this range, cosmogenic nuclide production is assumed to be solely due to thermal neutron absorption. The production of thermal neutrons is assumed to be derived from the epithermal neutron flux, less some fraction of neutrons absorbed in the epithermal energy range. Thermal neutrons are, by definition, at the lowest energy possible in their environment, and hence can be removed from the thermal energy population only by absorption into the nuclei of atoms with which they collide.
3. *Epithermal energy range.* In the epithermal range (between $\sim$0.1 MeV and 0.5 eV) neutrons behave in a diffusive manner, similar to that of thermal neutrons. However, epithermal neutrons can be "lost" (i.e., drop out of the epithermal energy range) by energy loss due to kinetic energy transfer during collisions as well as due to absorption. Single-valued epithermal neutron absorption cross sections ($I_{\mathrm{eff}}$) are assumed to describe cosmogenic nuclide production in this range and the resonance escape probability ($p(E_{\mathrm{th}})$) is used to calculate the likelihood that a neutron will pass through the epithermal energy range without being absorbed in some nucleus. The resonance escape probability is given by

$$p(E_{\mathrm{th}}) = \exp\left[ -\frac{I_{\mathrm{eff},i}}{\Sigma_k \xi_k N_{k,i} \sigma_{\mathrm{sc},k}} \right], \tag{3.8}$$

where $\xi_k$ is the average log decrement of energy per collision for element $k$ (dimensionless) and $\sigma_{\mathrm{sc},k}$ is the cross section of element $k$ for scattering of neutrons, and $i$ identifies the material for which the property is calculated. If $i = \mathrm{a}$, the atmosphere is indicated and $i = \mathrm{ss}$ indicates the subsurface. $N_{k,i}$ is the atomic concentration of element $k$ in the atmosphere or subsurface. $I_{\mathrm{eff},i}$ is the effective resonance integral for absorption of epithermal neutrons and is given by

$$I_{\mathrm{eff},i} = \sum_k I_{\mathrm{a},k} N_{k,i}, \tag{3.9}$$

where $I_{\mathrm{a},k}$ is the dilute resonance integral for element $k$ (commonly expressed in barns, where one barn equals$10^{-24}\,cm^2\,atom^{-1}$). (Note that the "a" subscript in $I_{\mathrm{a},k}$ refers to "absorption", not "atmosphere"). Values for these and other elemental constants used below are provided in Table 2 (see Fabryka-Martin (1988) and Phillips et al. (2000)for discussion).

Given the simplifications described above, the production of a particular cosmogenic nuclide, $m$, formed by nucleons in all three energy ranges and by muons, in a sample of finite thickness at a specified geographical location is given by

$$P_{t,m} = S_{\mathrm{el}} S_{\mathrm{T}} (Q_{\mathrm{s}} P_{\mathrm{s,m}} + S_{\mathrm{L,th}} Q_{\mathrm{th}} P_{\mathrm{th,m}} + S_{\mathrm{L,eth}} Q_{\mathrm{eth}} P_{\mathrm{eth,m}}) + S_\mu S_{\mathrm{T},\mu} Q_\mu P_{\mu,m}, \tag{3.10}$$

where $S_{\mathrm{el}}$ is the scaling factor for the dependence of the nucleonic component of the cosmic-ray flux on elevation and latitude, as described in Section 3.7.1 below and $S_\mu$ is the same scaling factor for the muonic component. $S_{\mathrm{T}}$ is the scaling factor for shielding of the nucleonic component of the cosmic radiation due to rock geometry and surrounding topography, described in Section 3.7.2 below, and $S_{\mathrm{T},\mu}$ is the same scaling factor for the muonic component. $P_{\mathrm{q},m}$ is the production rate of cosmogenic nuclide $m$ for the type of reaction $q$, where $q = \mathrm{s}$ indicates fast neutron (spallation) reactions, $q = \mathrm{th}$ indicates thermal neutron absorption reactions, $q = \mathrm{eth}$

Table 2
Elemental values for low-energy neutron transport parameters, from Fabryka-Martin (1988). Parameters are defined in text and in Section 2.2

| k | $A_i$ ($g\,mol^{-1}$) | $\xi_i$ (unitless) | $\sigma_{sc,i}$ ($10^{-24}\,cm^2\,atom^{-1}$) | $\sigma_{th,i}$ ($10^{-24}\,cm^2\,atom^{-1}$) | $I_{a,i}$ ($10^{-24}\,cm^2\,atom^{-1}$) |
|---|---|---|---|---|---|
| **O** | 16 | 0.12 | 3.76 | 0.0002 | 0.0004 |
| **H** | 1 | 1 | 20.5 | 0.33 | 0 |
| **C** | 12 | 0.158 | 4.74 | 0.0034 | 0.0016 |
| **Na** | 23 | 0.084 | 3.025 | 0.53 | 0.311 |
| **Mg** | 24.3 | 0.08 | 3.42 | 0.063 | 0.038 |
| **Al** | 27 | 0.072 | 1.41 | 0.23 | 0.17 |
| **Si** | 28.1 | 0.07 | 2.04 | 0.17 | 0.127 |
| **P** | 31 | — | 5 | 0.2 | — |
| **K** | 39.1 | 0.05 | 2.04 | 2.15 | 1 |
| **Ca** | 40.1 | 0.049 | 2.53 | 0.43 | 0.235 |
| **Ti** | 47.9 | 0.041 | 4.09 | 6.1 | 3.1 |
| **Mn** | 54.9 | 0.036 | 2.2 | 13.3 | 14 |
| **Fe** | 55.8 | 0.035 | 11.35 | 2.56 | 1.39 |
| **Cl** | 35.5 | 0.055 | 15.8 | 33.5 | 13.7 |
| **B** | 10.8 | 0.174 | 4.27 | 767 | 1722 |
| **Sm** | 150.4 | 0.013 | 38 | 9640 | 1400 |
| **Gd** | 157.3 | 0.013 | 172 | 41560 | 390 |

indicates epithermal neutron absorption reactions, $q = \mu$ indicates muon reactions, and $q = t$ indicates total production. $S_{L,eth}$ is a scaling factor to account for the net diffusion ("leakage") of epithermal neutrons, in excess of the standard flat geometry, out of rocks that project into the air (Section 3.7.3), and $S_{L,th}$ is the same for thermal neutrons . $Q_q$ accounts for the variation in the depth-integrated production rate as a function of sample thickness. It is the ratio of the average production over the actual thickness of the sample to the production at the surface. The method for calculating $Q_q$ is given in Section 3.7.4. In general, for near-surface samples the muonic component of production is much smaller than the nucleonic and is often neglected.

This section of paper derives in detail the equations that describe the depth-dependence of TCN production for the various types of nuclear reactions. All of the material may not be of interest for all readers. For readers interested only in purely spallogenic nuclides (e.g., $^3$He and $^{21}$Ne) we recommend reading Sections 3.3.1 and 3.3.5. For readers interested in $^{10}$Be, $^{14}$C, and $^{26}$Al, we recommend Sections 3.3.1, 3.3.4 and 3.3.5. For readers interested in $^{36}$Cl and $^{41}$Ca we recommend all subsections of Section 3.3.

### 3.3.1. *Fast neutron (spallation) production*

The mechanics of spallation production have been described above in Section 3.1.2. If only a small sector of the sky area is considered, the cosmic radiation responsible for spallation reactions can be visualized as a linear beam of high-velocity particles. It is an important principle that the rate of reaction of cosmic-ray particles with the medium through which the beam passes depends on the number of nucleons in the medium, per unit path length, and not on the atomic arrangement of those nucleons. In other words, the rate of interaction is proportional to the density of the medium without regard to the elemental composition. This property allows the attenuation of the cosmic radiation with distance in any material to be characterized by a single constant, so long as the path length is given in units of cumulative mass traversed, or mass length, $Z$ ($g\,cm^{-2}$):

$$Z(z) = \int_0^z \rho(z)\,dz, \tag{3.11}$$

where $z$ is ordinary linear distance (cm). With distance expressed in mass units, the rate of particle interception will simply be proportional to the flux of particles passing through the medium:

$$\frac{dF}{dZ} = \frac{F}{\Lambda_{f,p}}, \tag{3.12}$$

where $F$ is the cosmic-ray intensity (particles $cm^{-2}\,s^{-1}$ from a single direction) and $\Lambda_{f,p}$, the constant of proportionality, is termed the particle attenuation length ($g\,cm^{-2}$): the path length that is required to attenuate the intensity by a factor of $e^{-1}$. This equation may be solved for the boundary condition that $F = F_{ref}$ at some reference point to yield:

$$F = F_{ref}\exp\left(-\frac{Z}{\Lambda_{f,p}}\right). \tag{3.13}$$

To obtain the total cosmic-ray flux, the intensity must be integrated over the entire sky. This produces the resulting analogous expression:

$$\Phi_f(Z) = \Phi_f(0)\exp\left(-\frac{Z}{\Lambda_f}\right), \tag{3.14}$$

where $\Phi_f$ is the annual cosmic-ray flux integrated over the entire sky assuming a horizontal land surface and horizontal horizon (particles $cm^{-2}\,yr^{-1}$), $\Phi_f$ (0) is the integrated cosmic-ray flux at zero depth (land surface), and $\Lambda_f$ is the apparent attenuation length of the energetic cosmic-ray particles for the integrated flux. The relation between $\Lambda_{f,p}$ and $\Lambda_f$ is derived in Section 3.4.

The spallation production rate for nuclide $m$, $P_{s,m}$ (atoms (g target material)$^{-1}\,yr^{-1}$), is proportional to the cosmic-ray flux, to the cross section of the target element for production of nuclide $m$, and to the abundance of the target element in the target material. $P_{s,m}$ is also a function of the cosmic-ray energy spectrum, because reaction cross-sections depend on the incident particle energy. Because the energy spectrum does not vary significantly over the surface of the earth or with depth, the cross sections can be treated as constants. Inasmuch as the target element cross sections are generally poorly known and the production equation therefore empirically calibrated, the production equation is usually parameterized in terms of the product of the flux and the cross section: $\Psi_{m,k}(0)$, the production rate of species $m$ by spallation of element $k$, per unit mass of $k$, at the reference position (land surface ($z = 0$), sea level, and high latitude) (atoms (g target element)$^{-1}\,yr^{-1}$):

$$P_{s,m}(Z) = \Psi_{m,k}(0) C_k \exp\left(-\frac{Z}{\Lambda_f}\right), \tag{3.15}$$

where $C_k$ is the concentration of element $k$ (g of $k$ (g material)$^{-1}$).

### 3.3.2. Production by epithermal neutrons

Production of cosmogenic nuclides by epithermal neutron absorption is given by

$$P_{eth,m,ss} = f_{eth,m,ss} \Gamma_{eth,ss} = \frac{f_{eth,m,ss}}{\Lambda_{eth,ss}} \Phi_{eth,ss}, \tag{3.16}$$

where

$$f_{eth,m,ss} = \frac{N_{k,ss} I_{a,k}}{I_{eff,ss}} \tag{3.17}$$

is the fraction of the total epithermal neutrons absorbed that are taken up by target element $k$ (e.g., $^{35}Cl$ or $^{40}Ca$) to produce nuclide $m$ (e.g., $^{36}Cl$ or $^{41}Ca$). In general, we will omit the material subscript (i.e., "ss") in production terms, since in this paper we are only concerned with in situ cosmogenic nuclide production.

$\Gamma_{eth}$ is the total rate of epithermal neutron absorption ($n\,g^{-1}\,yr^{-1}$). $\Phi_{eth}$ is the epithermal neutron flux ($n\,cm^{-2}\,yr^{-1}$) and $\Lambda_{eth}$ is the effective epithermal neutron attenuation length ($g\,cm^{-2}$). Note that the epithermal and thermal neutron fluxes are independent of the direction of individual neutrons and are therefore the equivalent of neutron concentration rather than a net directional transport in the usual sense of a flux. $\Lambda_{eth,i}$ is given by

$$\Lambda_{eth,t} = \left[\xi_i\left(I_{eff,i} + \sum_{sc,i}\right)\right]^{-1} = \sum_{eth,i}^{-1}. \tag{3.18}$$

$\Lambda_{eth,i}$ is a measure of the propensity of material $i$ for epithermal neutron absorption (the length of penetration of the epithermal neutrons decreases as the propensity for absorption grows). $\sum_{eth,i}$ is the effective epithermal loss (by both absorption and energy moderation) cross section ($cm^2\,g^{-1}$). $\bar{\xi}_i$ is the macroscopic (average) log decrement energy loss per neutron collision:

$$\bar{\xi}_i = \frac{\sum_k \xi_k \sigma_{sc,k} N_{k,i}}{\sum_k \sigma_{sc,k} N_{k,i}}. \tag{3.19}$$

When neutrons have reached the epithermal energy regime, such that there is very little net directional transfer of momentum, the spatial distribution of the epithermal neutron flux can be described by a diffusion equation (e.g., Glasstone, 1955) that balances the epithermal neutron sources (moderation of energetic neutrons) and sinks (moderation into the thermal range or absorption into atomic nuclei). The formulation that we present here assumes that all epithermal neutrons are derived from moderated spallation and evaporation neutrons produced by high-energy cosmic-ray nucleons, and that other sources of neutrons, such as nucleogenic reactions (originating from radioactive decay), muon capture-produced neutrons, and neutrons derived from photodisintegration reactions, are neglected. The epithermal neutron flux is assumed to be in temporal equilibrium with the high-energy flux.

$$D_{eth,i}\frac{d^2\Phi_{eth,i}}{dZ^2} = \frac{\Phi_{eth,i}}{\Lambda_{eth,i}} - R_{eth,i} P_f, \tag{3.20}$$

$D_{eth,i}$ is the epithermal neutron diffusion coefficient ($g\,cm^{-2}$), calculated according to

$$D_{eth,i} = \left[3\sum_{sc,i}(1 - 2(3A_i)^{-1})\right]^{-1}, \tag{3.21}$$

where

$$\sum_{sc,i} = \sum_k \sigma_{sc,k} N_{k,i} \tag{3.22}$$

is the macroscopic neutron scattering cross section ($cm^2\,g^{-1}$) in material $i$. $A_i$ is the average atomic weight of material i. $\overline{A_i}$ is given by

$$\overline{A_i} = \frac{\sum_k A_k N_{k,i}}{\sum_k N_{k,i}} \tag{3.23}$$

where $A_k$ is the atomic mass of element $k$. For this derivation the datum is the land surface; positive is downward and negative upward.

$P_f$ is the production rate ($n\,g^{-1}\,yr^{-1}$) of epithermal neutrons from fast (i.e., energetic: $\sim$ 1–10 MeV) secondary cosmogenic neutrons, given as a function of $Z$ by Eq. (3.9) and $P_f(0)$ is the production rate of epithermal neutrons from fast neutrons in the atmosphere at the land/atmosphere interface. $R_{eth,i}$ dimensionless) is the normalization factor for the epithermal neutron production rate and according to Dep et al. (1994b) is given by

$$_{eth,i} = \left(\frac{A_i}{A_a}\right)^{1/2}, \tag{3.24}$$

where $A_a$ is the average atomic weight of the atmosphere, equal to $14.5\,g\,mol^{-1}$. $R_{eth,a}$ is equal to unity.

As described in Phillips et al. (2000), coupled differential equations for atmosphere and for subsurface, of the form of Eq. (3.20), can be solved subject to the boundary conditions (Eq. (3.25)) below:

(i) $\Phi_{eth,ss}(\infty) = 0$ (the cosmic-ray flux is completely attenuated at an infinite depth)

(ii) $\Phi_{eth,ss}(\infty) = \Phi_{eth,a}(0)$ continuity of concentration [commonly referred to as epithermal neutron flux] across the atmosphere/subsurface boundary)

(iii) $D_{eth,ss}\,d\Phi_{eth,ss}(0)/dZ = D_{eth,a}\,d\Phi_{eth,a}(0)/dZ$ (continuity of [true] epithermal neutron flux across the boundary)

(iv)
$$\Phi_{eth,a}(Z) = P_f(0)\Lambda_{eth,a}\exp\left(-\frac{Z}{\Lambda_f}\right) \quad z \ll 0$$
(at large distances above the boundary the epithermal neutron flux is in spatial equilibrium with the atmospheric energetic neutron flux).

The solutions for the subsurface and atmospheric epithermal neutron fluxes are given by

$$\Phi_{eth,i}(Z) = \left[\Phi^*_{eth,i}\exp\left(-\frac{Z}{\Lambda_f}\right) + \frac{(D_{eth,j}/L_{eth,j})(\Phi^*_{eth,j} - \Phi^*_{eth,i}) - \frac{D_{eth,ss}}{\Lambda_f}(\Phi^*_{eth,ss} - \frac{D_{eth,a}}{D_{eth,ss}}\Phi^*_{eth,a})}{D_{eth,a}/L_{eth,a} - D_{eth,ss}/L_{eth,ss}} \times \exp\left(\frac{|Z|}{L_{eth,i}}\right)\right], \tag{3.25}$$

where $L_{eth,i}$ is the epithermal neutron diffusion length ($g\,cm^{-2}$), equal to $(D_{eth,i}/\sum_{eth,i})^{1/2}$. The epithermal neutron diffusion length is equal to approximately 0.4 times the net mean distance traveled by a neutron between production and absorption.

$$\Phi^*_{eth,i} = P_f(0)\frac{R_{eth,i}}{\Sigma_{eth,i} - D_{eth,i}/\Lambda_f^2}. \tag{3.26}$$

Eq. (3.25) can be expressed as

$$\Phi_{eth,i} = \Phi^*_{eth,i}\exp\left(-\frac{Z}{\Lambda_f}\right) + (F\,\Delta\Phi)^*_{eth,i}\exp\left(-\frac{|Z|}{L_{eth,i}}\right), \tag{3.27}$$

where

$$(F\,\Delta\Phi)^*_{eth,i} = \frac{(D_{eth,j}/L_{eth,j})\Delta\Phi^*_{eth,i} - (D_{eth,ss}/\Lambda_f)\Delta\Phi^{**}_{eth,a}}{D_{eth,a}/L_{eth,a} - D_{eth,ss}/L_{eth,ss}} \tag{3.28}$$

and

$$\Delta\Phi^*_{eth,i} = \Phi^*_{eth,j} - \Phi^*_{eth,i}, \tag{3.29}$$

$$\Delta\Phi^{**}_{eth,a} = \Phi^*_{eth,ss} - \frac{D_{eth,a}}{D_{eth,ss}}\Phi^*_{eth,a}, \tag{3.30}$$

where $i$ is the environment of interest (a or ss) and $j$ is the other environment (i.e., if $i$ = a, then $j$ = ss). Physically, $\Phi^*_{eth,ss}$ represents the epithermal neutron flux ($n\,cm^{-2}\,yr^{-1}$) that would be observed at the position of the land surface if the atmosphere had the same epithermal neutron transport properties as the subsurface and $\Delta\Phi^*_{eth}$ is the difference between the equilibrium epithermal neutron fluxes in a medium with the properties of the atmosphere and one with the properties of the subsurface. $(F\Delta\Phi)_{eth,i}$ represents the difference between the flux that would be observed at $Z = 0$ if only medium $i$ were present and that actually observed in the presence of an interface.

### 3.3.3. Production by thermal neutrons

Production of cosmogenic nuclides by thermal neutron absorption is given by

$$P_{th,m} = f_{th,m}\Gamma_{th,m} = \frac{f_{th,m}}{\Lambda_{th}}\Phi_{th}(Z), \tag{3.31}$$

where

$$f_{th,m} = \frac{\sigma_{th,k}N_k}{\sum_{th}} \tag{3.32}$$

is the fraction of thermal neutrons absorbed that are taken up by target element $k$ to form the nuclide of interest, $m$. The distribution of the thermal neutron flux with depth is assumed to be governed by an equation similar to that for epithermal neutrons, but with the epithermal neutron distribution as the source term, rather than the fast neutron distribution:

$$D_{th,i}\frac{d_2\Phi_{th,i}}{dZ^2} = \frac{\Phi_{th,i}}{\Lambda_{th,i}} - R_{th,i}\frac{p(E_{th})_a}{\Lambda_{eth,i}}\left[\Phi^*_{eth,i}\exp\left(\frac{-Z}{\Lambda_f}\right) + (F\,\Delta\Phi)^*_{eth,i}\exp\left(\frac{-|Z|}{L_{eth,i}}\right)\right], \tag{3.33}$$

where

$$R_{\mathrm{th},i} = \frac{p(E_{\mathrm{th}})_i}{p(E_{\mathrm{th}})_{\mathrm{a}}}, \tag{3.34}$$

$$\Lambda_{\mathrm{th},i} = \sum_{\mathrm{th},i}^{-1}, \tag{3.35}$$

$$D_{\mathrm{th},i} = \left[ 3\sum_{\mathrm{sc},i} (1 - 2(3A_{\mathrm{i}})^{-1}) \right]^{-1}. \tag{3.36}$$

Eq. (3.35) applies to both the atmosphere and the subsurface, with the substitution of "a" and "ss" for "$i$". These equations can be solved together, subject to the same boundary conditions listed under Eq. (3.24), except that "th" is substituted for "eth". The solutions are of the form

$$\Phi_{\mathrm{th},i} = \Phi^*_{\mathrm{th},i}\exp\left(\frac{-Z}{\Lambda_{\mathrm{f}}}\right) + (\Im\Delta\Phi)^*_{\mathrm{eth},i}\exp\left(\frac{-|Z|}{L_{\mathrm{eth},i}}\right) + (\Im\Delta\Phi)^*_{\mathrm{th},i}\exp\left(\frac{-|Z|}{L_{\mathrm{th},i}}\right), \tag{3.37}$$

where

$$\Phi^*_{\mathrm{th},i} = \frac{p(E_{\mathrm{th}})_{\mathrm{a}} R_{\mathrm{th},i}\Phi^*_{\mathrm{eth},i}}{\Lambda_{\mathrm{eth},i}(\Sigma_{\mathrm{th},i} - D_{\mathrm{th},i}/\Lambda_{\mathrm{f}}^2)}, \tag{3.38}$$

$$(\Im\Delta\Phi)^*_{\mathrm{eth},i} = \frac{p(E_{\mathrm{th}})_{\mathrm{a}} R_{\mathrm{th},i}(F\Delta\Phi)^*_{\mathrm{eth},i}}{\Lambda_{\mathrm{eth},i}(\Sigma_{\mathrm{th},i} - D_{\mathrm{th},i}/L^2_{\mathrm{eth},i})}, \tag{3.39}$$

$$\begin{aligned}(\Im\Delta\Phi)^*_{\mathrm{th},i} = {} & [D_{\mathrm{th,a}}(\Phi^*_{\mathrm{th,a}}\Lambda_{\mathrm{f}}^{-1} - (\Im\Delta\Phi)^*_{\mathrm{eth,a}}L^{-1}_{\mathrm{eth,a}}) \\ & - D_{\mathrm{th,ss}}(\Phi^*_{\mathrm{th,ss}}\Lambda^{-1}_{\mathrm{th,ss}} + (\Im\Delta\Phi)^*_{\mathrm{eth,ss}}L^{-1}_{\mathrm{eth,ss}}) \\ & + \frac{D_{\mathrm{th},j}}{L_{\mathrm{th},j}}(\Delta\Phi^*_{\mathrm{th},i} + \Delta(\Im\Delta\Phi)^*_{\mathrm{eth},i})\Big] \\ & \times \left[\frac{D_{\mathrm{th,ss}}}{L_{\mathrm{th,ss}}} + \frac{D_{\mathrm{th,a}}}{L_{\mathrm{th,a}}}\right]^{-1}.\end{aligned} \tag{3.40}$$

The terms $(\Im\Delta\Phi)^*_{\mathrm{eth},i}$ and $(\Im\Delta\Phi)^*_{\mathrm{th},i}$ quantify the deviations of the thermal neutron profile at the atmosphere/subsurface interface from one in the atmosphere only, due to, respectively, the shape of the parent epithermal neutron profile and the subsequent diffusion of the thermalized neutrons across the interface. The other parameters in Eq. (3.40) are as follows:

$$\Delta\Phi^*_{\mathrm{th},i} = \Phi^*_{\mathrm{th},j} - \Phi^*_{\mathrm{th},i}, \tag{3.41}$$

$$\Delta(\Im\Delta\Phi)^*_{\mathrm{eth},i} = (\Im\Delta\Phi)^*_{\mathrm{eth},j} - (\Im\Delta\Phi)^*_{\mathrm{eth},i}. \tag{3.42}$$

Phillips et al. (2000) compared the epithermal and thermal neutron profiles with depth computed from Eqs. (3.27) and (3.37) with measurements performed within a concrete slab, with very favorable results. Fig. 3a illustrates epithermal and thermal neutron depth profiles for a variety of common rock types, calculated by means of Eqs. (3.27) and (3.37). These curves illustrate the effects of elemental composition on both the magnitude of the neutron fluxes and the depth of its maximum. One important advantage of the expanded derivations of Phillips et al. (2000) over the earlier ones of Liu et al. (1994) is that by deriving the source term for the thermal neutron production from the epithermal neutron flux, rather than directly from the fast neutron flux, enables the dependence of the epithermal and thermal neutron fluxes on water content to be described. Figs. 3b and c show how these fluxes vary in a shale as a function of water content.

One significant effect of the epithermal neutron production is that it tends to counter the steep thermal neutron flux gradient near the interface. The steep gradient of thermal neutron flux at the interface can make the inventory of thermal-neutron-produced nuclides at the surface very sensitive to small amounts of erosion. Since the epithermal neutrons are also absorbed by the same target elements, the combined production varies less steeply at the interface and hence is less sensitive to erosion than thermal-neutron production alone.

### *3.3.4. Production by muons and muon-derived neutrons*

The calculation of cosmogenic nuclide production by muons differs considerably from the calculations for production by the nucleonic component, presented above. This is because the mean transport length of the lower-energy components of the nucleonic radiation are short enough that they can be assumed to be in quasi-equilibrium with the high-energy component. Muons are tertiary products of the high-energy component (produced by decay of secondary charged pions and K mesons, Fig. 1b) and are less reactive and hence have much longer mean transport lengths. As a consequence, the muon flux is generally not in equilibrium with the local high-energy flux and separate scaling factors, angular distributions, and attenuation lengths must be used.

Muons can produce TCN by a variety of mechanisms, discussed in Section 3.1.8. Following Stone et al. (1998b), they can be summarized as follows:

$$P_{\mathrm{t},\mu} = S_\mu S_{\mathrm{t},\mu} Q_\mu (P_\mu + P_{\mathrm{n,s}\mu} + P_{\mathrm{n,f}\mu}) \tag{3.43}$$

where $P_{\mathrm{t}\mu}$ is the total nuclide production by muons (atoms $\mathrm{g}^{-1}\,\mathrm{yr}^{-1}$), $P_\mu$ is direct production by capture of slow negative muons (atoms $\mathrm{g}^{-1}\,\mathrm{yr}^{-1}$), $P_{\mathrm{n,s}\mu}$ is production by absorption of neutrons emitted following slow negative muon capture (atoms $\mathrm{g}^{-1}\,\mathrm{yr}^{-1}$), and $P_{\mathrm{n,f}\mu}$ is production by absorption of neutrons emitted due to photodisintegration reactions initiated by fast muons. The other terms are defined above.

Of these reactions, slow negative muon capture is generally the most important. It is given by

$$P_{\mu,m}(Z) = \sum_k \psi_{\mu^-}(Z) f_{\mathrm{c},k} f_{i,k} f_{\mathrm{d},k} f_{\mathrm{n},k,m} = Y_{\Sigma k,m}\psi_{\mu^-}(z) \tag{3.44}$$

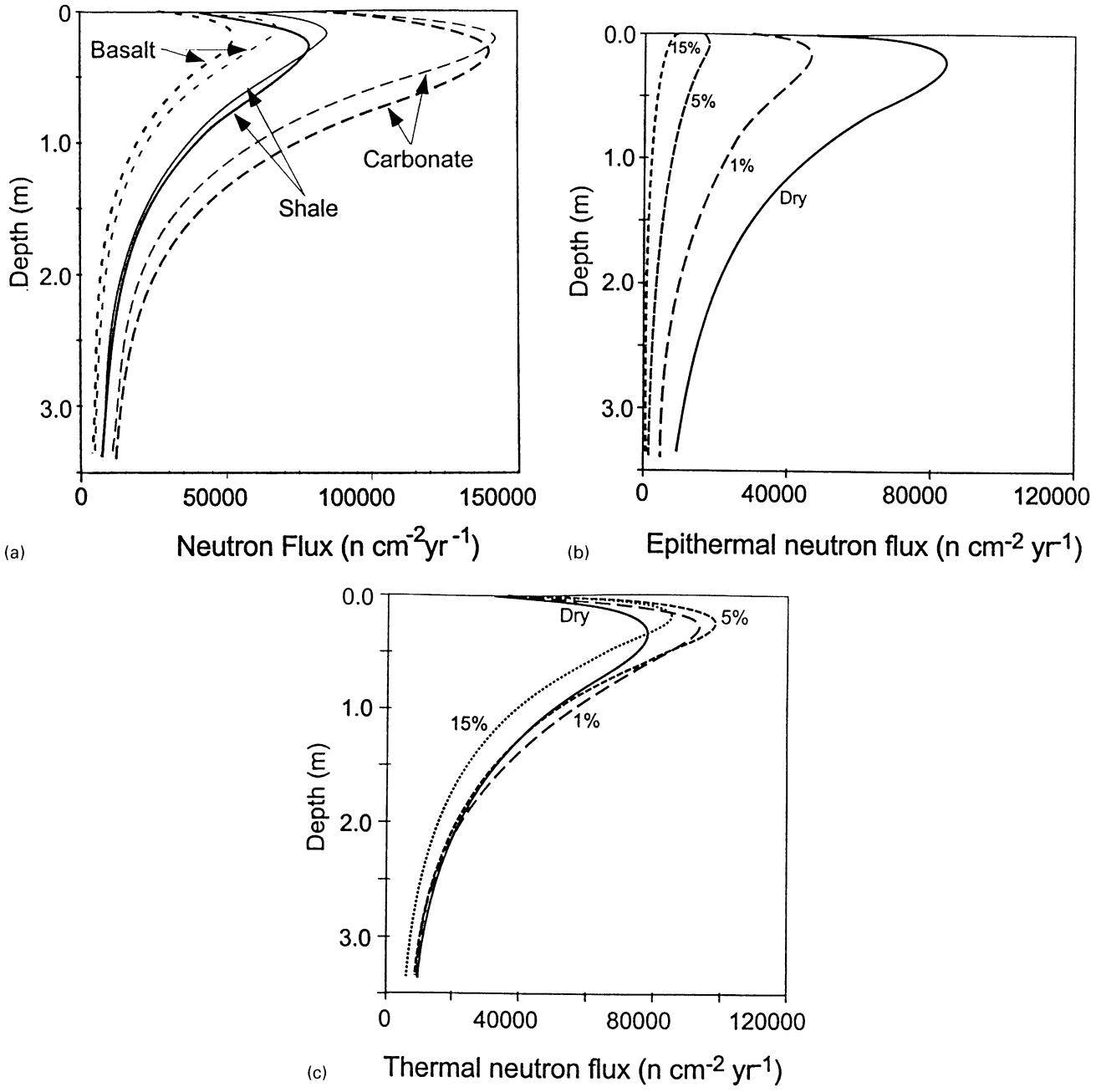


Fig. 3. (a) Profiles of the thermal and epithermal neutron fluxes with depth in a variety of rock types. Rock compositions were taken from average values given by Fabryka-Martin (1988) and rocks were assumed to be at sea level, high latitude and to be dry. Heavy lines indicate thermal neutron fluxes and thin lines epithermal fluxes. (b) Epithermal neutron flux as a function of depth and water content in an average shale (Fabryka-Martin, 1988). Shale was assumed to have 30% porosity. Numbers beside curves refer to volumetric water content. (c) Thermal neutron flux as a function of depth and water content in same shale.

where $k$ refers to all elements that may produce the nuclide of interest, $m$, by negative muon capture, $\psi_{\mu^-}(z)$ is the muon stopping rate as a function of depth ((stopped $\mu^-$) $g^{-1}\,yr^{-1}$), $f_{c,k}$ is the fraction of stopped negative muons that are captured by element $k$ (unitless; known as the "chemical compound factor" and dependent upon the chemistry of the material), $f_{i,k}$ is the abundance of the isotope that produces nuclide m after negative muon capture (unitless), $f_{d,k}$ is the fraction of the captured negative muons that are absorbed by the nucleus of element $k$ before they decay (unitless), and $f_{n,k}$ is the probability that the nucleus of the particular isotope of element $k$ will produce nuclide $m$ after it has absorbed the negative muon (unitless). $Y_{\sum k,m}$ is the (composition dependent) total production constant for nuclide $m$ from slow negative muon absorption reactions.

Of the parameters in Eq. (3.44), some are fairly well determined (the scaling factors, $\psi_{\mu-}(z)$, $f_{i,j}$, and $f_{d,j}$). However, $f_{c,j}$ and $f_{n,j}$ are in most cases poorly known. The chemical compound factor, $f_{c,j}$, in particular, is difficult to estimate. It can be crudely ($\pm 25\%$) calculated based on the Fermi–Teller $Z$-law (Charalambus, 1971):

$$f_{c,j} = \frac{N_j z_j}{\sum_k N_k z_k}, \tag{3.45}$$

where $z_j$ and $z_k$ are the proton numbers of elements $j$ and $k$, and $k$ refers to all elements in the material. This formulation is only approximate because it neglects interactions of the slow muons with the electron shells of the atoms comprising the material. The probability that the muon absorption will result in production of the nuclide of interest, $f_{n,j}$, can be obtained from muon irradiation experiments, but with regard to reactions of significance for TCN production, $f_{c,j}$ is fairly well known only for $^{40}Ca(\mu^-,\alpha)^{36}Cl$, for which it has a value of $0.062 \pm 0.02$ (Dockhorn et al., 1991), and for $^{16}O(\mu^-,\alpha pn)^{10}Be$ and $^{28}Si(\mu^-,2n)^{26}Al$ for which the values are $\sim 0.704$ and $\sim 0.296$, respectively (Heisinger et al., 1997).

The slow negative muon stopping rate is always much larger than the production rate of the nuclide of interest by direct muon capture (i.e., most of the slow muon captures do not result in production of the nuclide of interest). Most of the muon captures, however, do result in the ejection of one or more neutrons from the nucleus. These "muogenic neutrons" are then thermalized and can produce $^{36}Cl$ or $^{41}Ca$ (or other TCN to a much lesser extent) by thermal or epithermal neutron absorption reactions. The production distribution of neutrons by this reaction is given by

$$P_{n,s\mu}(Z) = Y_s \psi_{\mu^-}(Z), \tag{3.46}$$

where $Y_s$ is the average neutron yield per stopped negative muon. This parameter is dependent on the composition of the material (Fabryka-Martin, 1988) and is subject to a moderate degree of uncertainty. This formulation depends on the assumption that the muogenic thermal neutron flux is in equilibrium with the muogenic neutron production rate. Given the long attenuation length for stopping muons, this should generally be valid, except near the atmosphere/subsurface interface, but there the muogenic thermal neutron flux is small compared to that derived from the nucleonic component. In the case of limestone close to sea level, Stone et al. (1998b) found that the production rate from muogenic neutron absorption was about one order of magnitude less than production by absorption of spallogenic neutrons.

In addition to direct emission of neutrons as a result of muon capture, muons also can indirectly produce neutrons by means of photodisintegration reactions initiated by the deceleration of the fast component of the muon flux. As fast muons are slowed by collisions with atoms, bremsstrahlung (gamma rays, some highly energetic) is produced. Absorption of the energetic bremsstrahlung gammas by nuclei can cause photo-disintegration reactions that result in the release of a neutron. Thermalization and absorption of these neutrons can then produce TCN. The parameters governing the production of bremsstrahlung and the release of photodisintegration neutrons are reasonably independent of rock type, and such neutrons are only a minor source of TCN production (except at great depth), therefore Fabryka-Martin (1988) has presented a generalized formulation for neutron production from photodisintegration reactions:

$$P_{n,f\mu,m}(Z) = 8 \times 10^{-6} \ln(0.1Z) \varphi_{f\mu\pm}(Z), \tag{3.47}$$

where $\phi_{f\mu\pm}(Z)$ is the fast muon (both positive and negative) flux as a function of depth. This formulation assumes that the average neutron yield per photodisintegration is equal to unity. Due to the very long penetration length of fast muons, this production reaction tends to become the dominant one at depths below 10–20 m of rock.

Total muon-induced neutron production is given by combining the individual terms above:

$$P_{\mu,m}(Z) = Y_{s,m} \psi_{\mu^-}(Z) + 8 \times 10^{-6} \ln(0.1Z) \phi_{f\mu\pm}(Z). \tag{3.48}$$

Neither the slow muon stopping rate nor the fast muon flux follow an exponential distribution with depth. Due to the nature of the reactions producing muons in the atmosphere, the energy spectrum of the muon flux has a strong angular dependence, resulting in a decrease with depth that is slower than an exponential function. Stone et al. (1998b) have presented polynomial formulas for these distributions. However, in the top $\sim 3000\,g\,cm^{-2}$ of rock (equal to $\sim 10$ m linear depth), the slow muon stopping rate does fairly closely follow an exponential distribution with an attenuation length ($\Lambda_\mu$) of $\sim 1500\,g\,cm^{-2}$. The fast muon flux decreases even more slowly than the slow muon stopping rate, but the function $\ln(0.1Z)\phi_{\mu\pm}(Z)$ is also approximately proportional to $\exp(-Z/1500\,g\,cm^{-2})$ in the upper $3000\,g\,cm^{-2}$. Given these approximations, the total muon-induced neutron production as a function of depth can be given by

$$P_{n,\mu} = (Y_s \psi_{\mu 0} + 5.8 \times 10^{-6} \phi_{\mu f 0}) \exp\left(-\frac{Z}{\Lambda_\mu}\right) \tag{3.49}$$

where $\psi_{\mu_0}$ is the slow negative muon stopping rate at the land surface at high latitude and sea level, equal to $175\,\mu\,cm^{-2}\,yr^{-1}$, and $\phi_{\mu f 0}$ is the fast muon flux at land surface at high latitude and sea level, equal to

$7.9 \times 10^5\ \mu\,\mathrm{cm}^{-2}\,\mathrm{yr}^{-1}$. The approximations above should be adequate for typical surface exposure dating studies, and most erosion studies. However, studies of very deep profiles, or samples from very rapidly eroding terrains ($> 10\,\mathrm{mm/kyr}^{-1}$) should employ the full muon flux formulations from Stone et al. (1998b) due to the possibility of significant influence of production from $> 3000\,\mathrm{g\,cm}^{-2}$ depth.

Close to the land/atmosphere boundary the muon-induced neutron flux cannot be assumed to be in equilibrium with the production rate because neutrons diffuse in proportion to the total neutron concentration, and at the interface the neutron concentration difference is dominated by the spallation-induced neutrons, as described above in this section and Section 3.3.1. We therefore assume that the muon-induced low-energy neutrons follow the same distribution as the spallation-induced neutrons at shallow subsurface depths. Given this assumption, the total subsurface epithermal and thermal neutron distributions are given by

$$\Phi_{\mathrm{eth,ss,total}}(Z) = S_{\mathrm{el}}\Bigg[\Phi^{*}_{\mathrm{eth,ss}}\exp\!\left(-\frac{Z}{\Lambda_{\mathrm{f}}}\right) + (1 + R_{\mu}R_{\mathrm{eth}})(F\,\Delta\Phi)^{*}_{\mathrm{eth,ss}} \times \exp\!\left(-\frac{Z}{L_{\mathrm{eth,ss}}}\right) + R_{\mu}\Phi^{*}_{\mathrm{eth,ss}}\exp\!\left(-\frac{Z}{\Lambda_{\mu}}\right)\Bigg], \tag{3.50}$$

$$\Phi_{\mathrm{th,ss,total}} = S_{\mathrm{el}}\Bigg[\Phi^{*}_{\mathrm{th,ss}}\exp\!\left(-\frac{Z}{\Lambda_{\mathrm{f}}}\right) + (1 + R'_{\mu})(\Im\,\Delta\Phi)^{*}_{\mathrm{eth,ss}}\exp\!\left(-\frac{Z}{L_{\mathrm{th,ss}}}\right) + (1 + R'_{\mu}R_{\mathrm{th}})(\Im\,\Delta\Phi)^{*}_{\mathrm{th,ss}}\exp\!\left(-\frac{Z}{L_{\mathrm{th,ss}}}\right) + R'_{\mu}\Phi^{*}_{\mathrm{th,ss}}\exp\!\left(-\frac{Z}{\Lambda_{\mu}}\right)\Bigg], \tag{3.51}$$

where

$$R_{\mu} = \frac{S_{\mu}P_{\mu n0}}{S_{\mathrm{el}}P_{\mathrm{f}}(0)R_{\mathrm{eth,ss}}} \quad \text{and} \quad R'_{\mu} = \frac{p(E_{\mathrm{th}})_{\mathrm{a}}}{p(E_{\mathrm{th}})_{\mathrm{ss}}}R_{\mu}. \tag{3.52}$$

### 3.3.5. Total nuclide production

The results from the sections above enable the production terms in Eq. (3.10) to be calculated. Spallation production is given by

$$P_{\mathrm{s,m}}(Z) = \Psi_{\mathrm{m,k}}(0)C_{\mathrm{k}}\exp\!\left(-\frac{Z}{\Lambda_{\mathrm{f}}}\right) \tag{3.53}$$

Epithermal neutron production can be obtained by combining Eqs (3.16), (3.25), and (3.50):

$$P_{\mathrm{eth,m}} = \frac{f_{\mathrm{eth}}\Phi_{\mathrm{eth,ss,total}}(Z)}{\Lambda_{\mathrm{eth,ss}}} = \frac{f_{\mathrm{eth}}}{\Lambda_{\mathrm{eth,ss}}}\Bigg\{\Phi^{*}_{\mathrm{eth,ss}}\exp\!\left(-\frac{Z}{\Lambda_{\mathrm{f}}}\right) + (1 + R_{\mu}R_{\mathrm{eth}})(F\,\Delta\Phi)^{*}_{\mathrm{eth,ss}}\exp\!\left(-\frac{Z}{L_{\mathrm{eth,ss}}}\right) + R_{\mu}\Phi^{*}_{\mathrm{eth,ss}}\exp\!\left(-\frac{Z}{\Lambda_{\mu}}\right)\Bigg\}, \tag{3.54}$$

where $f_{\mathrm{eth}}$ is the fraction of epithermal neutrons that are absorbed by element $k$ to produce cosmogenic nuclide m, and is given by Eq. (3.17). Similarly, thermal neutron production is given by

$$P_{\mathrm{th,m}} = \frac{f_{\mathrm{th}}\Phi_{\mathrm{th,ss,total}}}{\Lambda_{\mathrm{th,ss}}} = \frac{f_{\mathrm{th}}}{\Lambda_{\mathrm{th,ss}}}\Bigg\{\Phi^{*}_{\mathrm{th,ss}}\exp\!\left(-\frac{Z}{\Lambda_{\mathrm{f}}}\right) + (1 + R'_{\mu})(\Im\,\Delta\Phi)^{*}_{\mathrm{eth,ss}}\exp\!\left(-\frac{Z}{L_{\mathrm{eth,ss}}}\right) + (1 + R'_{\mu}R_{\mathrm{th}})(\Im\,\Delta\Phi)^{*}_{\mathrm{th,ss}}\exp\!\left(-\frac{Z}{L_{\mathrm{th,ss}}}\right) + R'_{\mu}\Phi^{*}_{\mathrm{th,ss}}\exp\!\left(-\frac{Z}{\Lambda_{\mu}}\right)\Bigg\}. \tag{3.55}$$

Muon production, $P_{\mu,m}$, is given by Eq. (3.44).

## 3.4. Energetic neutron attenuation length

Shielding measurements and calculations, describing the relative flux of cosmic rays from varying incident angles, are made in the spherical coordinate system. Here we choose a system consistent with the terrestrial physics convention, where the origin for the angle of inclination, $\phi$, is vertically upward and the azimuth ($\theta$) origin is north (Fig. 4a).

The atmospheric depth through which incoming radiation must pass is thickest for rays that are close to horizontal and thinnest vertically overhead. The cosmic radiation flux is therefore greatest in the vertical and decreases toward the horizon. The angular distribution of cosmic radiation is given by

$$F(\phi) = F_0\cos^{m}\phi, \tag{3.56}$$

where $F(\phi)$ is the intensity of the cosmic radiation in any particular direction, $F_0$ is the maximum intensity (which is in the vertical direction), $\phi$ is the inclination angle, and commonly cited values of $m$ vary from 2.3 (Lal, 1958) to 3.5 (Heidbreder et al., 1971). The value $m = 2.3$ is generally used in cosmogenic nuclide applications (Nishiizumi et al., 1989). The effect of the difference is not large (Fig. 5).

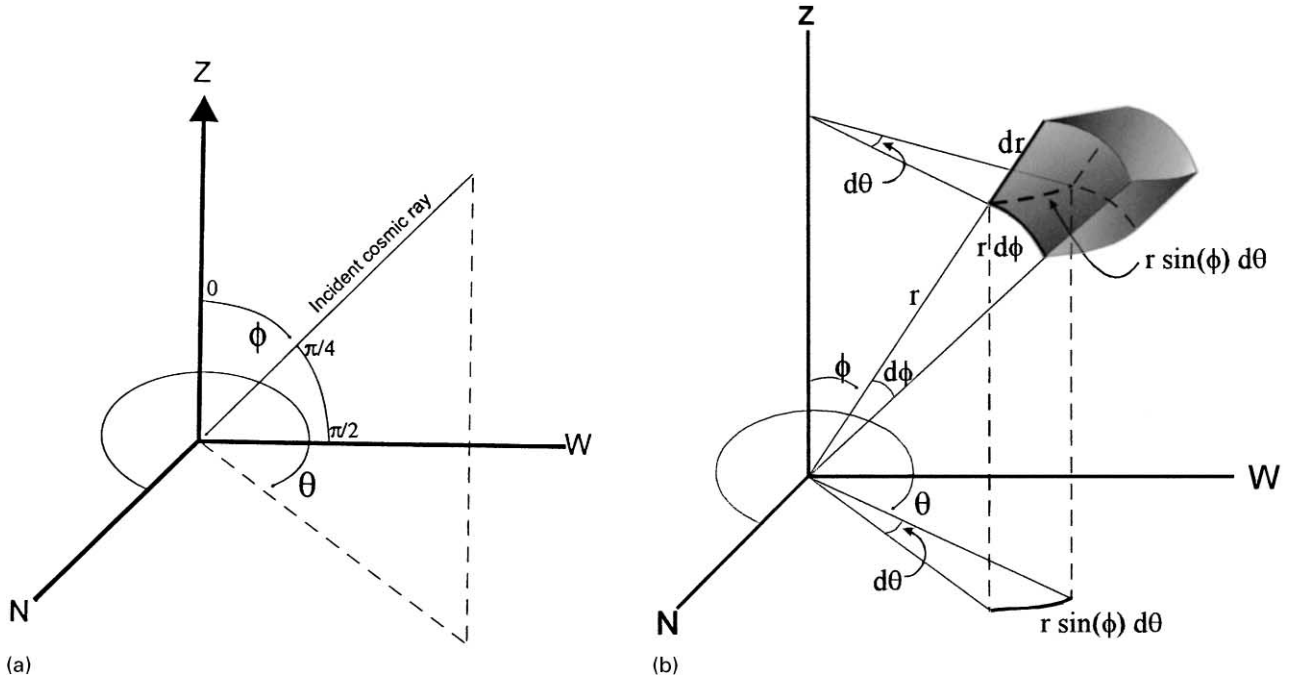


Fig. 4. (a) Coordinate system for computations involving cosmic-ray distributions. The origin for the angle of inclination, $\phi$, is toward the zenith and the origin for the azimuth, $\theta$, is north. (b) Illustration of solid geometry used in integration of the cosmic-ray flux.

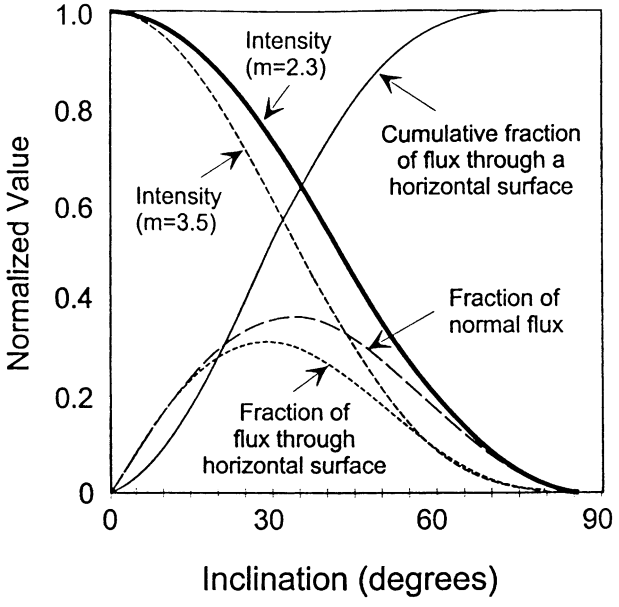


Fig. 5. Variation of the cosmic-ray intensity ($F(\phi)$) with inclination angle ($\phi$).The variation of the intensity is shown for both $F(\phi) = F_0 \cos^{2\cdot3} \phi$ and $F(\phi) = F_0 \cos^{3\cdot5}\phi$. The fraction of the total flux passing through a surface rotated so as to be always normal to the flux, the fraction of the total flux passing through a horizontal surface, and the cumulative fraction of the total flux passing through a horizontal surface are also illustrated, based on $F(\phi) = \mathrm{F}_0 \cos^{2\cdot3}\phi$.

The total incoming cosmic radiation will then be given by

$$F = \int_{\theta=0}^{2\pi} \int_{\phi=0}^{\pi/2} F(\phi) \sin\phi \, \mathrm{d}\phi \, \mathrm{d}\theta, \tag{3.57}$$

where the sin $\phi$ term accounts for convergence of the spherical coordinate system toward the origin (Fig. 4b).

However, the cosmic-ray flux impinging on a horizontal surface from inclinations greater than zero (i.e., toward the horizon) will be distributed over a larger surface area as the inclination increases. When calculating the cosmic-ray flux through a unit surface area, this "foreshortening" effect is proportional to cos $\gamma$, where $\gamma(\phi)$ is the angle between the normal to the surface, $N$, and the incident ray, $\phi$.

$$\Phi_{\mathrm{f}}(\phi,\theta) = \int_{\theta=0}^{2\pi} \int_{\phi=0}^{\pi/2} F(\phi) \sin\phi \cos\gamma(\phi) \, \mathrm{d}\phi \, \mathrm{d}\theta \tag{3.58}$$

$\Phi_f(\phi,\theta)$ is the flux of the energetic component of the cosmic radiation through the horizontal surface. For a horizontal surface, $\gamma(\phi) = \phi$ and, including the inclination-dependence of the cosmic-ray flux in Eq. (3.56), the expression for the cosmic-ray flux through a unit surface area becomes

$$\Phi_{\mathrm{f}}(\varphi,\theta) = \int_{\theta=0}^{2\pi} \int_{\phi=0}^{\pi/2} F_0 \cos^m \phi \sin\phi \cos\phi \, \mathrm{d}\phi \, \mathrm{d}\theta. \tag{3.59}$$

Integration with $\phi = 0$ as the lower limit yields

$$\Phi_{\mathrm{f}}(\max) = \frac{2\pi F_0}{m+1}. \tag{3.60}$$

As shown in Section 3.3.1, the high-energy component of the cosmic radiation is generally considered to follow an exponential decrease as a function of the cumulative mass penetrated perpendicular to the surface of the rock.

Because a large component of the incoming flux arrives at non-vertical angles, the attenuation depth of the integrated flux is generally shorter than the true particle attenuation length. For a horizontal surface the vertical penetration depth of a particle, $z_p$, as a function of the angle of incidence, $\phi$, and the true particle attenuation length, $\Lambda_{f,p}$, is given by

$$z_p = \Lambda_{f,p} \cos\phi. \tag{3.61}$$

The attenuation length that is usually cited is obtained by fitting an exponential function to cosmogenic nuclide concentrations (e.g., Kurz, 1986b; Brown et al., 1992a or neutron counts (e.g., Liu et al., 1994) measured beneath horizontal, unshielded surfaces. These profiles integrate production from all angles of exposure. The resulting parameter is commonly termed the apparent attenuation length, $\Lambda_f$ and values range from 121 to $> 170\,g\,cm^{-2}$ (Table 3, Fig. 6; see discussion in Dunai, 2000). The apparent attenuation length, $\Lambda_f$, can be calculated from the flux-weighted integral of the average attenuation depth:

$$\Lambda_f = \frac{\int_0^{\pi/2} z_p(\phi)\cos^{2.3}\phi \sin\phi\, d\phi}{\int_0^{\pi/2}\cos^{2.3}\phi \sin\phi\, d\phi} = \frac{\Lambda_{f,p}\int_0^{\pi/2}\cos^{3.3}\phi \sin\phi\, d\phi}{\int_0^{\pi/2}\cos^{2.3}\phi \sin\varphi\, d\phi}$$

$$= \frac{3.3}{4.3}\Lambda_{f,p}. \tag{3.62}$$

If $\Lambda_f$ can be taken to be about $160\,g\,cm^{-2}$, then $\Lambda_{f,p}$ is about $208\,g\,cm^{-2}$. In the atmosphere, the attenuation length decreases approximately with geomagnetic latitude (Fig. 6) until latitude 60°. At higher latitudes the secondary nucleon flux is invariant with latitude. The effect at latitudes less than 60° results from the change in the energy spectrum of the cosmic-ray secondaries. The average spectrum is harder at lower latitudes (because the vertical cutoff rigidity is higher), so the average attenuation length is greater (e.g. Lingenfelter, 1963). However, at atmospheric depths below $600\,g\,cm^{-2}$, (approximately 4400 m asl) the latitudinal dependence on attenuation length may be insignificant (Simpson and Fagot, 1953).

As described above, the attenuation coefficient is generally expressed in units of mass length ($g\,cm^{-2}$) because the length depends on the total mass traversed. Length in units of cm can be determined for materials with constant or known densities (e.g. for $\Lambda = 160\,g\,cm^{-2}$, the depth that the production rate will decrease by a factor of $e^{-1}$ is 61.5 cm in granite [$\rho \sim 2.6\,g\,cm^{-3}$], 64.0 cm in basalt [$\rho \sim 2.5\,g\,cm^{-3}$], 80 cm in soil or tuff [$\rho \sim 2\,g\,cm^{-3}$], 160 cm in water, and 640 cm in snow [$\rho \sim 0.25\,g\,cm^{-3}$]).

Most attenuation lengths in air for fast nucleons have been measured directly with neutron and proton monitors during aircraft or balloon flights (e.g. Merker et al., 1973) or by measuring the abundance of TCN on rock surfaces at different elevations (e.g. Zreda et al., 1991). Attenuation lengths in rock have been measured by collecting rocks at discrete depths or from continuous rock cores. Estimates of the fast nucleon $\Lambda$ range from 125 to $213\,g\,cm^{-2}$ in the atmosphere and 145–190 $g\,cm^{-2}$ in rock (Table 3). The differences in fast nucleon attenuation data from rocks at the same latitude may be partly attributed to differences in the contribution of muogenic production of different nuclides. Attenuation lengths may also (i) increase with increasing atomic weight (Brown et al., 1992a), (ii) be larger in solids than in air because pions will decay in air before interacting (Lal, 1991) and muons have a greater attenuation length in solids than in the atmosphere (Lal and Peters, 1967), but this is likely to be $< 20\%$ effect. However, because the muonic contribution relative to nucleonic contribution increases with depth, apparent attenuation lengths will appear to be longer in deeper cores (i.e. for rock depth profiles approaching the cross over of the relative contribution to production, $800\,g\,cm^{-2}$ for $^{10}Be$ in New Zealand, Kim et al., 1999). Attenuation lengths do not appear to vary significantly due to changes in solar modulation (Lingenfelter, 1963; Merker et al., 1973). Despite these uncertainties and variations, values of $150 \leqslant \Lambda \leqslant 170\,g\,cm^{-2}$ are presently used for fast nucleon attenuation coefficients for rock samples within the upper 1 m of Earth's surface. In general, variation within this range has a small influence on the results of applied investigation of 'surface' exposures. For subsurface samples, the uncertainty becomes more important. Within the next few years a better constrained value for the nucleon and muon attenuation length in shallow rock worldwide will undoubtedly be determined.

The attenuation of negative muons at sea level is approximately exponential, similar to that of the high-energy neutron flux. Muon production is difficult to distinguish from the much larger fast nucleonic production near the Earth's surface, but the $\mu^-$ stopping rate exceeds the fast neutron disintegration rate at depths of $\sim 200$–$300\,g\,cm^{-2}$ (Kurz, 1986b; Lal, 1987a; Brown et al., 1995a) at sea level, deeper at higher elevations. Estimates of $\Lambda_{\mu^-}$ range from 800 to $1500\,g\,cm^{-2}$ (Table 3).

### 3.5. Temporal variations in production rates

Like their atmospheric counterparts, all in situ production rates vary over time. Early empirical production rate studies suggested evidence for temporal variations in the time-integrated production rate of TCN in rocks over the past 60 kyr (Kurz et al., 1990; Cerling and Craig, 1994a; Clark et al., 1995). Calculations employing estimates of cosmic-ray intensities at different sites based on dipole-induced variations in geomagnetic paleolatitudes have predicted that the integrated production rates may have varied more than 15% over that time period (Kurz et al., 1990; Bierman, 1996; Bierman et al., 1996; Clark et al., 1996). However, variation of terrestrial cosmogenic

Table 3
Attenuation lengths[a] Fast nucleon, thermal neutron, and muon attenuation lengths in stopping materials in the Earth's atmosphere, Earth rock, and Lunar rock. (Not an exhaustive list)

| Cosmogenic nuclide, material | $\lambda_{geo}$ (°) | $\Lambda_f$ (g cm$^{-2}$) | Reference |
|---|---|---|---|
| **Atmosphere** (elevation in km or mb) | | | |
| Protons | 50 | 150 | (Conversi, 1950) |
| Fast nucleons in 0–5000 m | 0 | 160 | compiled by Lal (1991) |
| Fast nucleons in 0–5000 m | 30 | 150 | compiled by Lal (1991) |
| Fast nucleons in 0–5000 m | > 60 | 140 | compiled by Lal (1991) |
| Fast neutrons between 200 and 700 mb | 58 | 163 ± 10 | (Merker et al., 1973) |
| Fast neutrons between 200 and 700 mb | 57 | 172 ± 13 | (Merker et al., 1973) |
| Fast neutrons between 200 and 700 mb | 31.5 | 181 ± 28 | (Merker et al., 1973) |
| Fast neutrons between 200 and 700 mb | 17.3 | 215 ± 15 | (Merker et al., 1973) |
| Fast Neutrons | 0 | 212 | (Lingenfelter, 1963) |
| Fast Neutrons | 10 | 213 | (Lingenfelter, 1963) |
| Fast Neutrons | 20 | 205 | (Lingenfelter, 1963) |
| Fast Neutrons | 30 | 196 | (Lingenfelter, 1963) |
| Fast Neutrons | 40 | 182 | (Lingenfelter, 1963) |
| Fast Neutrons | > 60 | 164 | (Lingenfelter, 1963) |
| > 35 MeV Neutrons, 1680–5960 m | 0 | 149 ± 2 | (Dixit, 1955) |
| > 35 MeV Neutrons, 2630–5350 m | 21 | 149 ± 2 | (Roederer, 1952) |
| > 35 MeV Neutrons, 150–3774 m | 47–50 | 127 ± 3 | (Teucher, 1952) |
| > 8 MeV Neutrons, 0–3230 m | 47–50 | 132 ± 4 | (Brown, 1954) |
| < 30 MeV Neutrons, 3000–4200 m | 0 | 145 ± 9 | (Simpson and Fagot, 1953) |
| < 30 MeV Neutrons, 3400–4400 m | 0 | 149 ± 9 | (Simpson et al., 1953) |
| < 30 MeV Neutrons, 260–4300 m | 42–45 | 132 ± 15 | (Tongiorgi, 1949) |
| < 30 MeV Neutrons, 260 m | 42 | 121 ± 7 | (Tongiorgi, 1949) |
| < 30 MeV Neutrons, 1900 m | 44 | 140 ± 2 | (Lockwood and Yingst, 1956) |
| < 30 MeV Neutrons, 2500–5000 m | 52 | 141 ± 2 | (Simpson and Fagot, 1953) |
| < 30 MeV Neutrons, 1000–7000 m | 60–65 | 130 | (Sandstrom, 1958) |
| < 30 MeV Neutrons, 4300–9000 m | 60–65 | 138 | (Sandstrom, 1958) |
| $^{7}$Be | 25 | 165 | (Nakamura et al., 1972) |
| $^{7}$Be | 50 | 158 | (Nakamura et al., 1972) |
| $^{10}$Be 1.3–1.7 m | 78 | 142 | (Brown et al., 1991) |
| $^{36}$Cl 280–4050 m | 20 | 152 | (Zreda et al., 1991) |
| Thermal neutrons | 0 | 220 | (Lal and Peters, 1967) |
| 1 eV neutrons | 10.1 | 212 | (Soberman, 1956) |
| Thermal neutrons | 39.5 | 165 | (Boella et al., 1968) |
| < 0.5 eV neutrons, 1900 m | 44 | 125 | (Lockwood and Yingst, 1956) |
| 1 eV neutrons | 55.1 | 164 | (Soberman, 1956) |
| Thermal neutrons | > 60 | 150 | (Lal and Peters, 1967) |
| 1 eV neutrons | 88.6 | 164 | (Soberman, 1956) |
| $\mu$ | | 247 | (Lal et al., 1958); (Rossi, 1948) |
| **Earth rocks** | | | |
| $\mu$ in deep saprolite | 4 | ~ 800 | (Brown et al., 1995) |
| $\mu$ at depth > 170 g cm$^{-2}$ in Hawaiian basalt | 37 | ~ 1000 | (Kurz, 1986a) |
| $\mu$ at depth 2650 g cm$^{-2}$ | — | 1500 | (Middleton and Klein, 1987) |
| Fast nucleons in $SiO_2$, CaO, and $FO_{81}$ | — | 157–167 | (Masarik and Reedy, 1995) |
| $^{3}$He in Reunion basalt | 21 | 159 ± 10 | (Sarda et al., 1993) |
| $^{3}$He in Hawaiian basalt | 37 | 164–170 | (Kurz, 1986a) |
| $^{3}$He in Antarctic sandstone | 78 | 150, 227 ± 14 | (Brook et al., 1996b) |
| $^{10}$Be to depth 200 g cm$^{-2}$ saprolite | 4 | ~ 150 | (Brown et al., 1995) |
| $^{10}$Be in laterite | 12 | 190 | (Bourlès et al., 1992) |
| $^{10}$Be in Bandelier Tuff, NM | 36 | 172 | (Olinger et al., 1992) |
| $^{10}$Be in Bandelier Tuff, NM | 36 | 159 | (Nishiizumi et al., 1994) |
| $^{10}$Be in Antarctic sandstone | 78 | 145 ± 7, 152 ± 5 | (Brook et al., 1996b; Brown et al., 1992) |
| $^{21}$Ne in Reunion lava | 21 | 165 ± 6.2 | (Sarda et al., 1993) |
| $^{21}$Ne in Bandelier Tuff, NM | 36 | 178 | (Olinger et al., 1992) |
| $^{26}$Al in Antarctica quartz sandstone | 78 | 156 ± 13, 152 ± 5 | (Brook et al., 1996b; Brown et al., 1992) |
| $^{26}$Al in laterite | 12 | 190 | (Bourlès et al., 1992) |
| $^{26}$Al in Bandelier Tuff, NM | 36 | 166 | (Nishiizumi et al., 1994) |
| $^{26}$Al in Bandelier Tuff, NM | 36 | 173 | (Olinger et al., 1992) |
| **Lunar rocks**[b] | | | |
| $^{10}$Be in Lunar basalt | — | 163 | (Nishiizumi et al., 1984) |
| $^{10}$Be in Lunar basalt | — | 120 | (Middleton and Klein, 1987) |
| $^{26}$Al in Lunar basalt | — | 165 | (Nishiizumi et al., 1984) |
| $^{26}$Al in Lunar basalt | — | 122 | (Middleton and Klein, 1987) |
| $^{36}$Cl in Lunar basalt | — | 180 | (Nishiizumi et al., 1984) |

[a]Thermal neutron attenuation in the upper 200 g cm$^{-2}$ of rock cannot be described by a simple exponential function (Dep, 1995; Dep et al., 1997; Liu et al., 1994; O'Brien et al, 1978; Zreda et al., 1994). Atmospheric estimates are for equilibrium depths (below Pfotzer Maximum, i.e. > 200 g cm$^{-2}$). For other estimates see discussion in Dunai (2000).

[b]The latitudes for some of these sites are *geographic* latitudes because we cannot assume the dipole was geocentric over the short time of TCN accumulation.

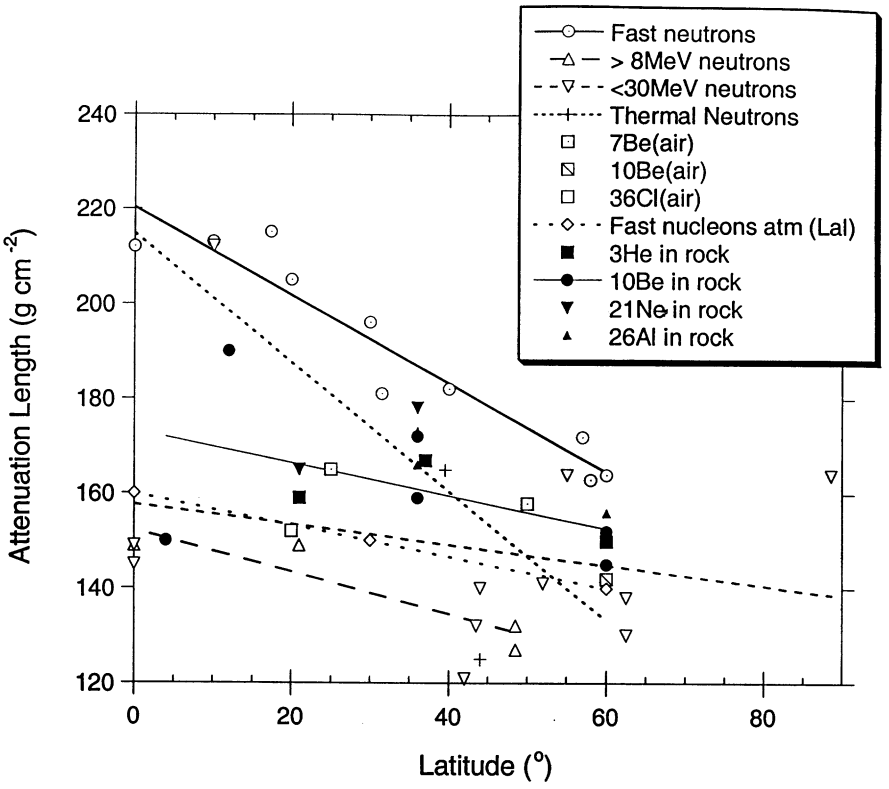


Fig. 6. Apparent attenuation length $\Lambda_f$) versus latitude ($\lambda_{geo}$). Solid symbols are rock depth profiles in upper 300 g cm$^{-2}$, open symbols are from measurements in or at the bottom of the atmosphere. All other curves are linear fits on $\Lambda_f$ with at least 3 measurements. High latitude sites are assigned to latitude 60°, above which $\Lambda_f$ is invariant. Refer to Table 3.

nuclide production with time has not been unequivocally documented and uncertainties in the chronological constraints used in these early empirical studies may explain the observed apparent temporal variations. More recently, using 33 in situ $^{36}$Cl measurements for rocks with independent exposure ages ranging from 2.1 to 55 kyr, Phillips et al. (1996a) found that incorporation of secular variation of production, based on the paleointensity record, did not improve the agreement of calculated ages with independently determined ages. Although this result may be also in large part due to errors in the independent age constraints, it does indicate that the effects of paleomagnetic intensity variations have not been profound. Licciardi et al. (1999) also indicate that the magnitude of the influence of paleointensity variations for mid-latitude sites is low (within $2\sigma$ experimental uncertainty and error of the results) based on the consistency of recent and recalculated published $^{3}$He production rates. More recently, Stone (1999) showed that the $^{10}$Be production rate may not have varied more than the precision of the empirical production rate estimates between 20 and 10 kyr. He re-scaled production rates of $^{10}$Be to sea level at high latitude with a lower muonic component. However, because increased precision in TCN methods is allowing finer resolution of geological events (e.g. correlation of Dansgaard–Oeschger cycles or multiple movements along a single fault scarp), we need to establish the temporal variations in order to reduce the uncertainty due to this second-order source of systematic error (Section 6).

The flux of cosmic radiation reaching the surface of the earth determines the rate at which cosmogenic nuclides are produced in exposed rocks. The surface flux varies temporally according to (i) variations in the intensity of the primary cosmic radiation; (ii) changes in the interplanetary magnetic field and solar modulation of GCR; (iii) changes in the geomagnetic field effect on the GCR and secondary radiation due to variations in dipole intensity, dipole axis position (dipole wobble), and variations in the presence and strength of non-dipole components of the geomagnetic field; (iv) variations in atmospheric shielding; and (v) variations in the character of the landform surface over time.

### 3.5.1. *Variations in the primary GCR flux*

All applications of TCN have assumed that the primary GCR flux has been constant over the exposure durations of interest ( $< 10$ Myr). Vogt et al. (1990) and Caffee et al. (1988) provided summaries of the use of meteorites to determine the history of extra-terrestrial cosmogenic nuclide production, but more meteorites analyzed for radionuclides of appropriate half life are

needed to substantiate this assumption. Lavielle et al. (1999) measured cosmogenic radionuclides in meteorites to determine the difference between recent ( $< 10$ Myr) and long-term cosmic-ray fluxes (150–700 Myr). Using a multiple-nuclide approach, they measured $^{10}$Be, $^{26}$Al, $^{36}$Cl, and the cosmogenic noble gases Ne, He, and Ar, to select meteorites that were uncomplicated by erosion or other effects and to adjust for atmospheric shielding during residence on earth. They showed that the average cosmic-ray flux for the last 10 Myr is 38% higher than the long-term average flux based on published $^{40}$K/$^{41}$K exposure ages of the same meteorites, in agreement with previous estimates (e.g. Hampel and Schaeffer, 1979).

The growing cosmochemical database from meteorites and other sources have successfully limited the number of possible explanations for long-term changes in the primary GCR flux to our solar system and earth. Hampel and Schaeffer (1979) concluded that a decrease in the cosmic ray flux in the inner solar system was the only explanation for $^{26}$Al/$^{21}$Ne exposure ages of iron meteorites being two-thirds younger than $^{40}$K/$^{41}$K exposure ages. They suggested that the recent decrease may have been caused by a change in the galactic cosmic-ray intensity, although solar modulations were also proposed (see Section 3.5.2). Alternatively, Earth could pass through different static interstellar fluxes during its motion relative to nearby interstellar medium, although it can be shown that Earth would not likely feel such variation in cosmic ray flux over $> 10^5$ yr periods (Jokipii, 1991).

Earth has also received GCR shock waves, e.g. from a nearby supernova. The effect would be felt over short time scales ( $< 10^5$ yr). However, these are generally isolated, non-recurring, short-lived events which would have only a small effect on integrated TCN production rates. Significant variations in primaries result from supernovae explosions and although such events are rare, they may be important for the time scales of 1 Myr (Reedy et al., 1983; Raisbeck et al., 1985; Lal, 1987a; Kocharov et al., 1989).

### 3.5.2. Variations due to solar modulation of the magnetic field

Solar particles have only minor effects on atmospheric cosmogenic nuclide production and are inconsequential for TCN production at the surface of the earth (cf. Masarik and Reedy, 1995). On the other hand, solar modulation of the interplanetary magnetic field can influence TCN production rates. The interplanetary magnetic field, generated mainly by the sun and transported by the solar wind, serves to deflect some portion of the primary GCR. The resulting GCR-flux variation with 11- and 22-year solar sun spot variations is well documented with atmospheric cosmogenic nuclides (e.g. $^{10}$Be and $^{14}$C) and significant in magnitude (Beer et al., 1991). However, even the 200-year period of solar activity (for instance, that creating the Maunder Minimum from 1645 to 1715 AD) is too short to be an influence on TCN production integrated over $10^3$–$10^7$ years. Direct measurements of flux or production rates (e.g. from waterbed experiments) need to be evaluated in terms of the specific time of a solar cycle over which the data were collected, if they have not been averaged over multiple cycles (e.g. Nishiizumi et al., 1996). Although longer-period solar cycles may exist, they are difficult to isolate from signals in prehistoric records that are also influenced by climate or the geomagnetic field. The solar modulation effect is thus assumed to integrate to a stationary mean value over the periods of interest for geological applications. Until more is known about low-frequency solar modulation of the GCR cosmic ray flux, models for TCN dating must perforce ignore this potential (probably minor) source of variation.

### 3.5.3. Effects of the geomagnetic field

The low latitude flux is dominated by relatively particles that are relatively more energetic than those at high latitude (the low latitude flux is said to be 'harder'), as documented by empirical measurements. The incident secondary flux of particles generated in the atmosphere, and therefore production rates of TCN, will also increase with geomagnetic latitude. The mean absorption free path with decrease with latitude. This generalization is true for long exposure durations because the time-averaged ( $> 10^4$ years) geomagnetic field is predominantly *dipolar* (Acton et al., 1996; McElhinny et al., 1996; Merrill et al., 1996; McElhinny and McFadden, 1997). As shown in Section 3.1 and Eq. (3.3) the geomagnetic cutoff rigidity is strongly latitude-dependent. To calculate the effect of a change in the magnetic dipole intensity on the cutoff rigidity of vertical particles at some time in the past, Eq. (3.3) can be expressed as

$$\Re = \Re_o \frac{M}{M_o} \cos^4(\lambda_{geo}), \tag{3.63}$$

where $R_0$ is the present cutoff rigidity on the geomagnetic equator, $M/M_o$ is the ratio of the geomagnetic paleodipole moment to its modern value, and $\lambda_{geo}$ is the geomagnetic latitude of the site (Quenby and Webber, 1959; Quenby and Wenk, 1962; Shea et al., 1965, 1987; Quenby, 1966; Lal and Peters, 1967; Bland and Cioni, 1968; Shea and Smart, 1983; Kocharov et al., 1989; Nishiizumi et al., 1989; Kurz et al., 1990; Lal, 1991). As the dipole field lines become steeper near the magnetic poles, the permitted particle rigidity decreases and becomes less than the threshold energy required to produced cosmogenic nuclides at the surface of the earth. In this region (geomagnetic latitudes above approximately 58° for the present dipole field, slightly lower for higher elevations), the cosmogenic nuclide production rate is insensitive to variations in the terrestrial magnetic field

strength (Lal, 1991; Lal and Peters, 1967). Below this latitude, changes in $M$ may result in a significant change in the cosmic-ray flux to a site at a given time (depending on the total exposure duration and the magnitude and duration of the intensity change). The following sections examine how $M$ may change over time at a given geographic latitude.

*3.5.3.1. Paleointensity variations.* Another way to express the relationship between geomagnetic field intensity and cosmic-ray flux above a site is that a change in $M$ will result in an apparent change in the effective geomagnetic latitude of a site relative to the present geomagnetic latitude:

$$\cos \lambda_{\mathrm{geo}} = \left[\frac{M}{M_{\mathrm{o}}}\right]^{1/4} \cos \lambda_{\mathrm{pdgeo}}, \tag{3.64}$$

where $\lambda_{\mathrm{pdgeo}}$ is the present-day site geomagnetic latitude (Clark et al., 1995; Nishiizumi et al., 1989). Eq. (3.64) allows us to predict the effect of dipole intensity changes on production rate by calculating the apparent geomagnetic latitude for any site (without considering the effects on rigidity). This approximation is most appropriate for latitudes above 30° because it does not consider the accompanying variations in the higher-order field components that will influence the effective cutoff rigidity for a given site. Furthermore, changes in dipole field strength may cause changes in the size of allowed and forbidden trajectory cones (for more discussion see Lifton et al., submitted). Based on relative paleointensity records, over the past 200 kyr $M/M_{\mathrm{o}}$ has ranged between 0.35 and 2.0 (Guyodo and Valet, 1996). This range is probably a minimum, as the true amplitudes of intensity variations may have been attenuated by the stacking of multiple relative paleointensity records with variable age control in the Guyodo and Valet (1996) compilation record.

In addition to paleointensity records (discussed in more detail below), variations in magnetic field strength are also evident from the change in accumulation rate of atmospherically produced cosmogenic nuclides. The changes are apparent in measurements of $^{10}$Be, $^{14}$C, and $^{36}$Cl accumulations in archives such as Barbados corals, polar ice cores, fossil rat urine, and marine and terrestrial sediments, although other factors such as climatically induced disequilibrium among carbon reservoirs may also play an important role in the temporal variation of $^{14}$C (Elsasser et al., 1956; Lal et al., 1985; Beer et al., 1988; Peng, 1989; Bard et al., 1990a,b; Mazaud et al., 1991; Stuiver et al., 1995; Plummer et al., 1997; Kitagawa and van der Plicht, 1998). It has been proposed that increases in the atmospheric production rates were a result of a weaker geomagnetic field. Evidence for a strong correlation between the Earth's geomagnetic field intensity and atmospheric $^{10}$Be accumulation in marine sediments and polar ice has been repeatedly documented (McHargue et al., 1995; Henken–Mellies et al., 1990; Morris et al., submitted; Raisbeck et al., 1985; Raisbeck et al., 1992).

Like atmospheric cosmogenic nuclide production rates, in situ TCN production rates are controlled by variations in the geomagnetic dipole field strength. If the history of the geomagnetic field intensity were known accurately, it would be possible to calculate the apparent rigidities or geomagnetic latitudes by integrating Eqs. (3.62 and 3.63) over the exposure duration and then adjusting the TCN production rate accordingly. Alternatively, numerical simulations could be performed to assess the time-integrated production rate change. Although paleointensity fluctuations have certainly had some influence on TCN production rates, the reader should be aware that the magnitude of the influence is still largely unknown and no agreement as to the amount of production rate adjustment needed, if any, has been reached. Unlike the near-instantaneous influence that intensity fluctuations have on the production of atmospheric cosmogenic nuclides (which have short atmospheric residence times relative to their half lives), and hence the necessity for independent calibration of organic radiocarbon dating, the influence on terrestrial production is subdued because the effect is integrated over the entire exposure time. Instantaneous in situ production rates may change due to paleointensity-induced changes in the cosmic-ray flux, but when averaged over the entire exposure duration the rates will approach a constant value, depending on the duration of exposure. The first published attempts to show the relationship between measured TCN production rates and an integrated time-varying production rate modeled from estimates of paleointensity indicated that a small adjustment may be useful (e.g. factor of 1.15 for a short $\sim$11 kyr exposure; Nishiizumi et al., 1989). Others indicated that the influence (assumed minor) of paleointensity variations may be recorded by $^{3}$He and $^{21}$Ne in lavas (Kurz et al., 1990; Sarda et al., 1993; Cerling and Craig, 1994a, b). However, they recognized that non-cosmogenic production and surface erosion and burial effects could also cause anomalies in in situ TCN concentrations. The necessity for calibration of the TCN timescales with other timescales, and the lack of highly reliable empirical calibrations led to the use of '$^{10}$Be years' (analogous to $^{14}$C-years) to distinguish non-calibrated exposure dates until a reliable calibration was attained (Gosse et al., 1995a; Brown et al., 1998a). Others proposed refinements to the cosmogenic nuclide chronometers based on the paleointensity records available and Eq. (3.64) (Bierman, 1996; Bierman et al., 1996; Clark et al., 1996). More recently, Lifton et al (submitted) have suggested that trajectory modeling of particles at cutoff rigidities should be modeled using existing paleointensity data.

Unfortunately, the geomagnetic paleointensity history of the Quaternary was poorly known in the early to

mid-1990s. Only a limited number of records were compiled (McElhinny and Senanayake, 1982; Meynadier et al., 1992; Tric et al., 1992; Mankinen and Champion, 1993; Tauxe, 1993; Valet and Meynadier, 1993; Roberts et al., 1994), and estimates of the $1\sigma$ uncertainty in the available combined relative and absolute paleointensity records were approximately 25% (Gosse et al., 1996a, d). Accurate pre-historic *absolute* paleointensity records are difficult to attain for a variety of reasons. Paleointensity curves based on direct measurements from volcanic rocks and fired archeological materials commonly have large uncertainties due to non-ideal magnetic properties (e.g., multidomain magnetizations), empirically irreproducible cooling histories of lavas, and the discontinuous nature of the record. The absolute records are produced by interpolating between paleointensities measured for single short time intervals which are often poorly dated and therefore are not truly continuous records and are often difficult to correlate to other records because of dating uncertainties. Continuous relative records from sedimentary paleointensity studies may be unreliable due to difficulties in dating and a lack of a sound explanation for the acquisition of detrital remanence, considering the effects of inclination-shallowing and other depositional and post-depositional grain reorientation processes. Furthermore, it is extremely difficult to remove the contribution of the non-dipole fields from both sedimentary– and volcanic/archeological–based paleointensity records for the past 15 kyr, until multiple sites with sufficient geographic distribution can be correlated. Attempts to reconstruct high-resolution paleointensities from measurements of atmospherically produced cosmogenic nuclides such as $^{14}C$, $^{10}Be$, (which are produced predominantly from $N_2$ and $O_2$) and $^{36}Cl$ (produced from Ar) in polar ice (Raisbeck et al., 1987; Raisbeck et al., 1992) and marine and terrestrial sediments (Raisbeck et al., 1994; Robinson et al., 1995; Frank et al., 1997) have also been made. The results have generally been ambiguous because, unlike in situ produced nuclides, the accumulation of these atmospheric nuclides in ice or sediment can depend on environmental conditions (e.g., temperature, precipitation, circulation in the oceans and atmosphere), and because age constraints may have large uncertainties due to errors in snow accumulation, incorrect ice flow models, or poorly known sedimentation rates. However, the coupling of $^{10}Be$ with other records for deciphering paleointensity is becoming significantly more useful (cf. Morris et al., submitted).

To make any reliable conclusion about the effects of paleointensity on the secondary cosmic-ray flux, we need (i) a record with sufficient resolution to capture the paleointensity variations that affect production rates over different exposure durations; i.e. for the past 30 kyr we need to resolve paleointensity variations with periods of 1 kyr, but for longer exposure times the resolution can be coarser. (ii) We require that the paleointensity record has accurate temporal control to some uniform timescale. (iii) For exposure durations less than 30 kyr, the amplitudes of the paleointensity variations need to be well constrained; older exposures are more forgiving, particularly if the paleointensity fluctuation is short lived (see below). Since the mid-1990s, the paleomagnetism community has made significant progress in acquiring records that meet experimental criteria (King et al., 1983) for developing and testing a reliable paleointensity record for the late Quaternary (Stoner et al., 1995; Yamazakia et al., 1995; Constable and Tauxe, 1996; Guyodo and Valet, 1996; Kok and Tauxe, 1996a, b; Kono and Hiroi, 1996; McClelland and Briden, 1996; Meynadier and Valet, 1996; Peck et al., 1996; Valet et al., 1996; Verosub, 1996; Brassart et al., 1997; Channell et al., 1997; Lanci and Lowrie, 1997; Roberts et al., 1997; Guyodo and Valet, 1999).

However, total uncertainties in recent absolute and relative paleointensity records are still too large to permit reliable adjustments of TCN production rates for shorter ($< 10^5$ kyr) exposures. For instance, $2\sigma$ standard errors of the mean relative intensities from multiple records often exceed $3 \times 10^{22}$ Am$^2$ (40% of the present intensity), and this does not account for systematic uncertainties in the chronology or the attenuation of amplitudes that results from the stacking of multiple records with different chronology quality (Guyodo and Valet, 1996, 1999; Schneider and Mello, 1996; Roberts et al., 1997). The present magnetic moment of the earth is approximately $8 \times 10^{22}$ Am$^2$. Standard deviations about weighted means of multiple measurements on single TRM events for absolute paleointensities are also greater than $2 \times 10^{22}$ Am$^2$ (Brassart et al., 1997) especially magnetic moments before 5 kyr BP (McElhinny and Senanayake, 1982). This standard deviation does not account for the error in interpolating between dated events to construct a continuous record or for non-dipole field effects due to the lack of sufficient geographic averaging of coeval magnetic acquisitions. As the paleointensity record improves, we can use accepted existing data to evaluate the potential magnitude of the second-order influence of paleointensity on production rates.

The Sint-200 relative paleointensity curve (Guyodo and Valet, 1996) arguably provided a reasonable estimate of the relative change in magnetic field strength over the past 200 kyr (there is also a compiled record for the past 800 kyr (Guyodo and Valet, 1999). It is a low-resolution composite record of global relative paleointensity (Fig. 7) based on paleomagnetic measurements from 18 marine sediment cores with low sedimentation rates, stacked and correlated using the SPECMAP $\delta^{18}O$ timescale (Martinson et al., 1987). Relative paleointensity data are interpolated linearly by increments of 1 kyr (Fig 5a of Guyodo and Valet, 1996), with indication of standard deviation and the number of cores involved in each successive time

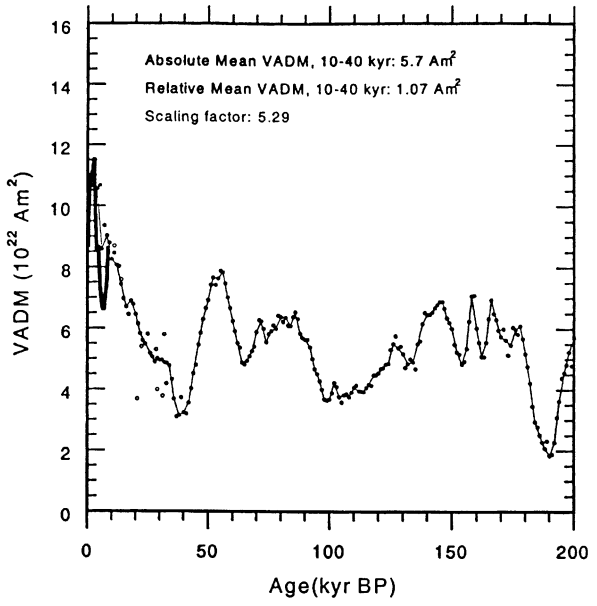


Fig. 7. The Sint 200 record (dots and thin curve). The relative record was normalized for absolute mean VADM as discussed in text using the absolute paleointensity data (open circles) from (Coe, 1978; Barbetti and Flude, 1979; Kovacheva, 1980, 1982; McElhinny and Senanayake, 1982; Chauvin et al., 1989, 1991; Brassart et al., 1997). Thick solid curve is the Holocene absolute paleointensity from McElhinny and Senanayake (1982). The last 2000 yr is based on archeomagnetic data from McElhinny and Senanayake (1982) and a modern moment of 8.0 $Am^2$. The error bars represent standard deviations.

period. The curve has sufficient resolution for modeling the effects of paleointensity variations on exposure ages between 50 and 200 kyr. However, higher resolution paleointensity records from sites with higher sedimentary rates and less attenuation of the intensity variation are necessary for exposure durations less than 50 kyr (Meynadier et al., 1992; Tric et al., 1992; Stoner et al., 1995; Peck et al., 1996; Schneider and Mello, 1996; Channell et al., 1997). Notwithstanding these shortcomings, because the Sint-200 composite record has been shown to be reasonably consistent with more recent relative (Channell et al., 1997; Roberts et al., 1997) and scaled absolute paleointensity records (Brassart et al., 1997) (with most misalignments attributed to chronology differences), we will use it to analyze the influence of paleointensity on terrestrial production rates.

To calibrate the Sint-200 curve to absolute paleointensity, we assumed that the curve should have the same mean dipole intensity when averaged over 30 kyr as volcanic data with reliable chronologies for the same time period (Brassart et al., 1997). We selected the time period between 10 and 40 kyr for our calibration interval because (i) there are a large number of volcanic paleointensity data available for this time period; (ii) all 17 core records used in the Sint-200 curve overlap during this time; and (iii) it is the time in which much existing TCN research has been conducted. We used the original references of the volcanic data, ignored the anomalous paleointensities derived for transition periods (e.g. Laschamp excursion), and recalibrated radiocarbon dates based on Calib 3.0.3c (Bard et al., 1993; Stuiver and Reimer, 1993) and the recent varve chronology for radiocarbon ages greater than 18.4 ka (Kitagawa and van der Plicht, 1998). Using a Sint-200 scaling factor of $5.04 \times 10^{22}$ $Am^2$ (amplitudes were not increased) the resulting dipole moment record is reasonably consistent with recent absolute intensities of Brassart et al. (1997) and the original volcanic data used for scaling. However, the Holocene record of McElhinny and Senanayake (1982) shows higher amplitude variation than the Sint-200 record, and the Holocene average paleointensity from the archeomagnetic data is less than the Sint-200 average. We attempted no further calibration to accommodate this inconsistency because of the significant differences in the nature of the two curves. Because there are no Sint-200 data for the last 2000 years, we extrapolated the Sint-200 curve through the absolute paleointensity for 1200 cal. yr BP (500-year average from McElhinny and Senanyake, 1982, age calibrated with Clark (1975) to the present dipole moment of $8 \times 10^{22}$ $Am^2$ (Fig. 7). Results of modeling with the Sint-200 record were found to be consistently within about 1.5% of the results modeled only with the McElhinny and Senanayake (1982) record for the last 10 kyr.

Recognizing the uncertainties associated with the paleointensity data we used and the manner in which we calibrated the curve, we are not recommending any adjustments in TCN production rates. An assumption of constant production rate is reasonable for middle and high latitude sites ($\lambda > 30^\circ$) because the resulting (inversely modeled) variations in integrated production rate are less than the variation in production rates empirically measured for exposure periods ranging from 2 to 55 kyr (e.g. Phillips et al., 1996b; Licciardi et al., 1999). Nevertheless, several observations can be made which may be important for sites at lower latitudes where there is greater sensitivity to changes in geomagnetic intensity. The intensity of the field reached its maximum only 3 kyr ago, so all TCN exposure applications will be influenced by this paleointensity maximum. Between 40 ka and 2 ka the field intensified from approximately $3 \times 10^{22}$ $Am^2$ to $10.2 \times 10^{22}$ $Am^2$ (even higher according to McElhinny and Senanayake, 1982). The lower field strength may have permitted a higher cosmic-ray flux and therefore relatively higher production rates for the late Pleistocene than in the Holocene. Between 200 and 50 ka, the mean intensity was $5.0 \times 10^{22}$ $Am^2$ ($\sigma 1.2 \times 10^{22}$ $Am^2$) but for the entire 200 to 2 ka record the mean is $5.2 \times 10^{22}$ $Am^2$ ($\sigma 1.5\ 10^{22}$ $Am^2$), indicating the past 50 kyr may have experienced greater fluctuation.

If we assume that the geomagnetic field can be described as an axial dipole (e.g. we ignore any paleosecular variation of the dipole axis and any non-dipole effects),

we can examine the paleointensity-induced variation in TCN production rate for a given geographic latitude. For comparison, we assume under a geocentric dipole field that the geographic latitude is equivalent to the geomagnetic latitude of the site under the current field strength ($8 \times 10^{22}$ Am$^2$). During times of higher (or lower) paleointensities, the geomagnetic latitude of the site will appear lower (or higher) than the current geomagnetic latitude. We represent the effects of varying production rates as the ratio of the time-averaged production rates integrated over the exposure duration, $P(t)$, to the production rate for the present geographic latitude assuming a geocentric dipole field and the present dipole moment, $P$(geog). We consider the effects of a non-geocentric dipole field below.

We have calculated the time-averaged production rates over the range of exposure times between 0.1 and 100 ka for 0–60° latitude (Fig. 8). The scaling factors of Lal (1991, his Table 1) were used for 3 km elevation (the variation is greater at higher elevations, Fig. 8 inset B). The first-order trends indicate that the time-averaged production rates during the Holocene were significantly lower (for site geographic latitudes between 15 and 60°) than during the late Pleistocene (Fig. 8). Sites above geographic latitude 35° have always been within 12° of their geomagnetic latitude for the past 100 kyr. This may explain why Phillips et al. (1996a) did not see a significant variation attributable to paleointensity variations in $^{36}$Cl production rates over 2.1–55 kyr time period, considering all except one of the 33 rock samples they analyzed were collected at or above 35° geographic latitude. Production rate variation is greatest for latitude 20° (see Fig. 8 inset A), which may explain why Kurz et al. (1990) observed the effects of paleointensity variation from Holocene $^3$He

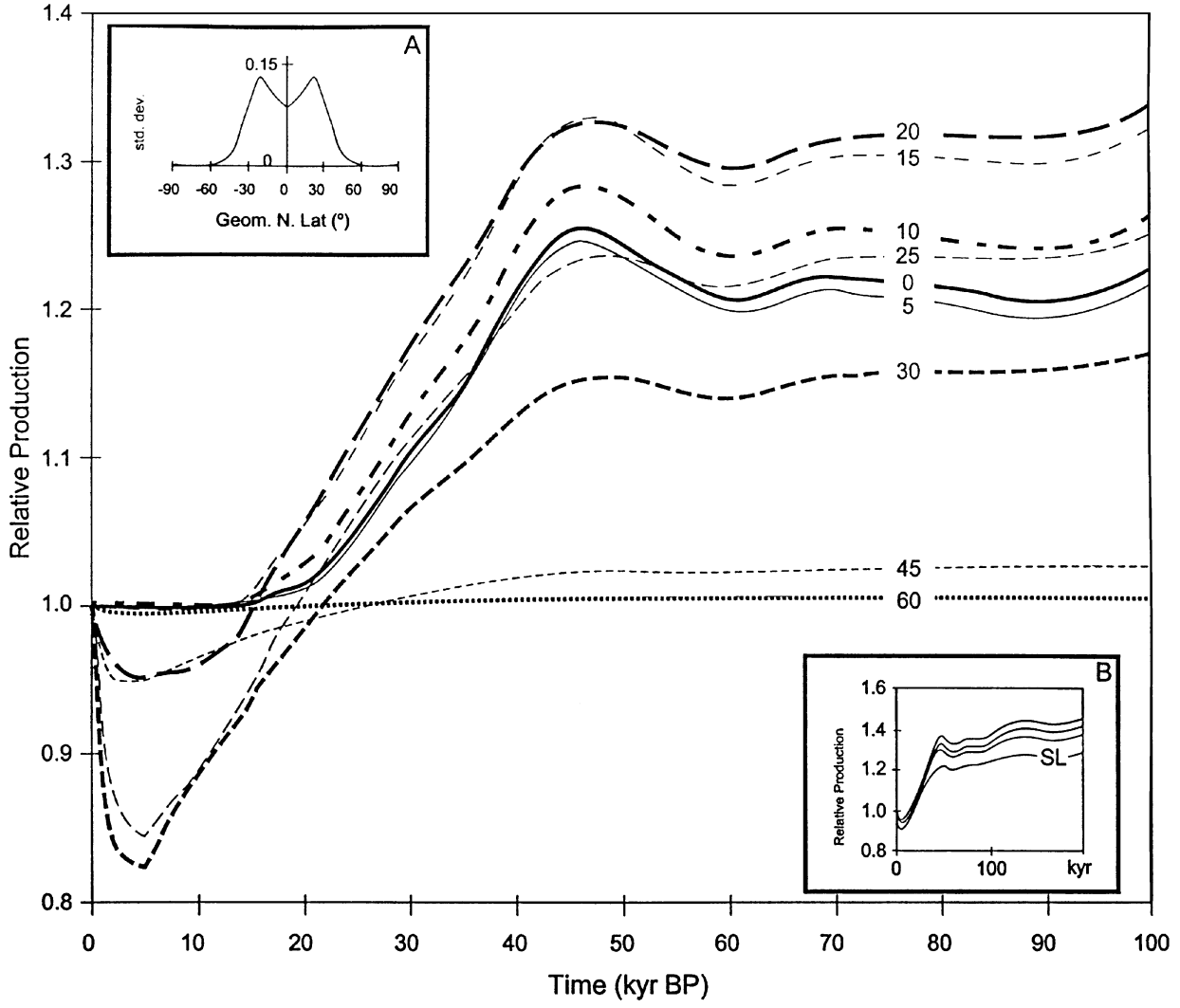


Fig. 8. Effects of paleointensity on TCN production rates at different latitudes and altitudes, using the Sint-200 relative paleointensity record (Fig. 7) to estimate dipole moment. The effect is expressed as the ratio of time-averaged production rate, $P(t)$, to the present production rate at the geographic site latitudes (0 to 60°) at 2000 m elevation. Inset A shows the standard deviation in time-averaged production rates over the past 200 kyr, one way of showing that the greatest variability is felt at 20° latitude (negative latitude represents south). Inset B shows the effect of paleointensity variation at different elevations (sea level, 1, 2 and 3 km) at 20° latitude. All spatial scaling was done using Table 1 in Lal (1991).

calibration samples collected at Hawaii (although we show in the following section that wobble of the dipole axis will decrease this effect at Hawaii). Sites at geographic latitude above 60° have not experienced an apparent geomagnetic latitude of less than 57° during the past 200 kyr, even if modeled with paleointensities from McElhinny and Senanayake (1982), so these sites are invariant with paleointensity variations because they remained above the cutoff rigidity.

*3.5.3.2. Effects of reversals and excursions.* When averaged over long exposure periods ($>5\times10^5$ yr) even large amplitude paleointensity variations associated with transition events such as the Brunhes–Matuyama reversal 780 kyr ago (Baski et al., 1992) do not significantly influence the time-averaged TCN production rates (cf. O'Brien, 1979). This is true even considering that although it may take only 5 kyr for the directional change (Merrill et al., 1996) intensity fluctuations last more than three times that duration (Raisbeck et al., 1985; Valet and Meynadier, 1993). Using Eq. (3.64) and paleointensity data from Valet and Meynadier (1993) which show a $>10\times$ increase in relative intensity immediately after the low intensity associated with the reversal, time-averaged production rates for exposures beginning during the reversal would be at most 3% higher than the lowest production rates after the reversal (for a site with the worst-case scenario, at 20° latitude, 3 km elevation, Fig. 9). The actual affect is difficult to determine from the Valet and Meynadier (1993) paleointensity because the duration of the reversal is difficult to deduce. However, if a simplified model is used by assuming a constant paleointensity interrupted between 790 and 770 kyr with an intensity of only 20% of the constant strength, the production rate for this worse-case site averaged at 791 kyr would be approximately 3% higher than at 769 kyr, and exposures much longer than 1000 kyr would be required to return to the normal rate (Fig. 9). The simulation overestimates the actual effect because the actual paleointensity appears to have increased immediately before and after the transition (Raisbeck et al., 1985; Valet and Meynadier, 1993), which reduces the affect of the reversal on production rates. It is clear that even in the worst-case scenario, TCN production rates for long ($>10^5$ kyr) exposures are essentially indistinguishable from a constant long-term integrated production rate for the same period, a point made earlier by Sarda et al. (1993).

*3.5.3.3. Secular variations in the dipole axis position.* In addition to changes in the geomagnetic paleointensity variations discussed above, the effective geomagnetic latitude of a sample site may also vary with secular changes in the geomagnetic field geometry over short (i.e. $<10^4$ yr) exposure durations. There are two ways that the averaged geomagnetic field geometry may not be

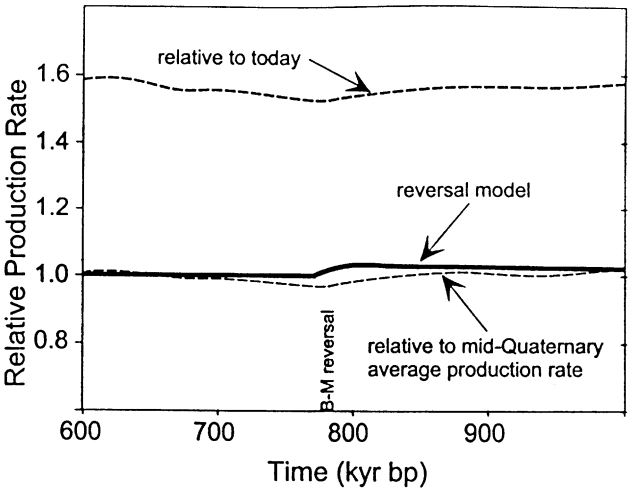


Fig. 9. Impact of a short-lived high amplitude geomagnetic intensity change on TCN production rates. The thick solid line shows the effect on production rates if the magnetic field was constant except during the Brunhes–Matuyama transition. The curve show the effect of decreasing a intensity to 20% of the modern intensity between 790 and 770 kyr. The effect reaches 3% for exposures that began within a few 100 kyr before the reversal. The upper dashed curve is the $P(t)/P$(today) based on Valet and Meynadier (1993) paleointensity for exposure times between 1000 and 600 kyr. For comparison, the thin dashed line is the same data, but relative to an average production rate (today's magnetic field appears to be almost 1.5 times stronger than the average intensity over the past 1 Myr).

symmetric about the Earth's spin axis: (1) variations in the position of the dipole moment axis; and (2) significant contributions of (asymmetric) non-dipole field components over long time periods (discussed below). It has been shown that the axial dipole component of the geomagnetic field can be considered approximately geocentric when averaged over the last 780 kyr (Negrini et al., 1987; Acton et al., 1996; Constable and Tauxe, 1996). Gubbins and Kelly (1993) have shown that for the past 2.5 Myr there is a strong resemblance of the morphology of the paleomagnetic and modern field and that paleosecular variation of the magnetic field has been similarly intense as today. Virtual geomagnetic poles (VGP), the position of the equivalent geomagnetic pole calculated for an instant in time from multiple geographically spaced concurrent readings of the paleomagnetic field, have been calculated with the greatest reliability for the past 10,000 years by Ohno and Hamano (1992) and Merrill and McElhinny (1983) from archeomagnetic and sediment paleomagnetic data. The reader is directed to recent discussion regarding the selection criteria of paleomagnetic data for VGPs over the past 5 Myr (Quidelleur et al., 1994; Johnson and Constable, 1995; McElhinny and McFadden, 1997). The mean position of the geomagnetic pole over the past 10,000 years is 88.2°N, 84.6°E, with approximately 1° uncertainty (Ohno and Hamano, 1992). When averaged over 5 Myr, the dipole position is not exactly geocentric but lies at

approximately 87°N 144°E ($\alpha_{95} \sim 1°$), depending on the method (e.g. average including far-sided effect or common-site longitude) and dataset used to calculate it (Merrill et al., 1996, p. 220). However, for most TCN applications this is sufficiently geocentric that time-integrated pre-Holocene production rates will not be affected. For shorter timescales the VGP are not consistent with the geographic north pole. Single VGP (excluding transition periods) have been measured below 80°N latitude (e.g. the modern geomagnetic north pole, and for around 2.8 kyr ago (Ohno and Hamano, 1992)).

With the exception of Sternberg(1996), Klein and Gosse (1996), and Licciardi et al. (1999) the effects of dipole wobble on TCN production rates have not been considered. Does the variation in the position of the dipole axis significantly affect TCN production rates? Klein and Gosse (1996) showed that for geomagnetic latitudes above 20°, dipole axis position variation may contribute a greater influence on production rates than paleointensity variations, although their estimate of possible pole position changes (20°) is double the average deviations for the Holocene. Using the 500-year averaged Holocene VGP positions ($\lambda_p$, $\phi_p$) of Ohno and Hamano (1992), we recalculated the site geomagnetic paleolatitude for sites specified by means of geographic position ($\lambda_p$, $\phi_p$) by subtracting the paleocolatitude ($\lambda_{paleo}$) from 90°, where

$$\cos\lambda_{paleo} = \sin\lambda_s \sin\lambda_p + \cos\lambda_s \cos\lambda_p \cos(\phi_p - \phi_s). \quad (3.65)$$

The production rate scaling factors for the geomagnetic paleolatitudes were then integrated over the exposure time (as done previously for paleointensity effects) to calculate the time-averaged production rates for different locations. Note that because the longitude of the VGP has also varied with time, geographic site locations will have lower or higher magnetic fields depending on whether the longitude of the VGP is far-sided or near-sided.

Based on the Ohno and Hamano (1992) record, it appears the variation in geomagnetic latitude induced by secular variation in the dipole axis position is of a similar magnitude to the paleointensity-induced variations for low latitude sites (Fig. 10). It was shown in Fig. 8 that geocentric dipole paleointensity variations would not influence sites with geographic latitude above 60°. However, if we consider the Holocene history of the dipole axis position, some high latitude sites (again, depending on longitude) dropped below the cutoff rigidity for TCN production. Their record for polar motion over the past 2 kyr is consistent with archaeomagnetically derived pole positions (Merrill and McElhinny, 1983). Unfortunately, the Ohno and Hamano (1992) data may not be sufficiently reliable to warrant corrections of the integrated TCN production rate for the rest of the Holocene. Their

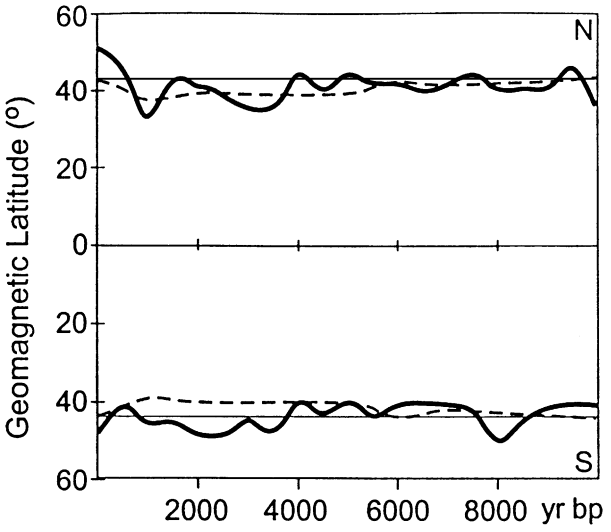


Fig. 10. Comparison of the effects on geomagnetic latitude of variation in intensity (long dashes) and dipole axis position (thick solid curve). Upper curves for the Wind River Range, United States (geographic latitude 43°N). Lower curves for Southern Alps, New Zealand (geographic latitude 44°S). Paleointensity effects based on Sint-200 curve (Figs. 5 and 6). Dipole wobble effects modeled from VGPs of Ohno and Hamano (1992). Fine dashed line is geographic latitude.

model is based on relative magnetic records from sediment at up to 11 sites, but only one site had an archaeomagnetic record close enough to allow correction of the core timescale (e.g. due to fluctuating sedimentation rates and marine reservoir effects), adjustments for inclination shallowing, and calibration of the relative declinations to absolution values. They were forced to construct a second-degree spherical harmonic global expansion anchored with only six suitable archaeomagnetic records. We cannot evaluate the uncertainty of the pole positions because their global geomagnetic field variation model was insufficiently constrained (Merrill et al., 1996), and because the pole positions for sites older than 7 kyr are based on only half the number of sites used to constrain the past 2 kyr record. Nevertheless, Fig. 10 (c.f. also Fig. 11) shows that for exposures greater than 7 kyr, the effect of polar wobble is less important on an integrated production rate, but that the consequent changes in geomagnetic latitudes for the late Holocene can have large ($> 15\%$) influences at certain sites. The true effects of dipole axis wobble (and non-dipole field effects discussed below) will become increasingly important issues to resolve as the analytical and chemical precisions improve to allow finer ($10^2$ yr) resolution of late Holocene exposure histories.

*3.5.3.4. Non-axial dipole field.* Despite early recognition of the influence of the non-axial dipole field components on atmospheric secondary nucleon production rates (Section 3.1.2), they have been largely ignored at ground level (however, see O'Brien (1996; Dunai, 2000; Lifton

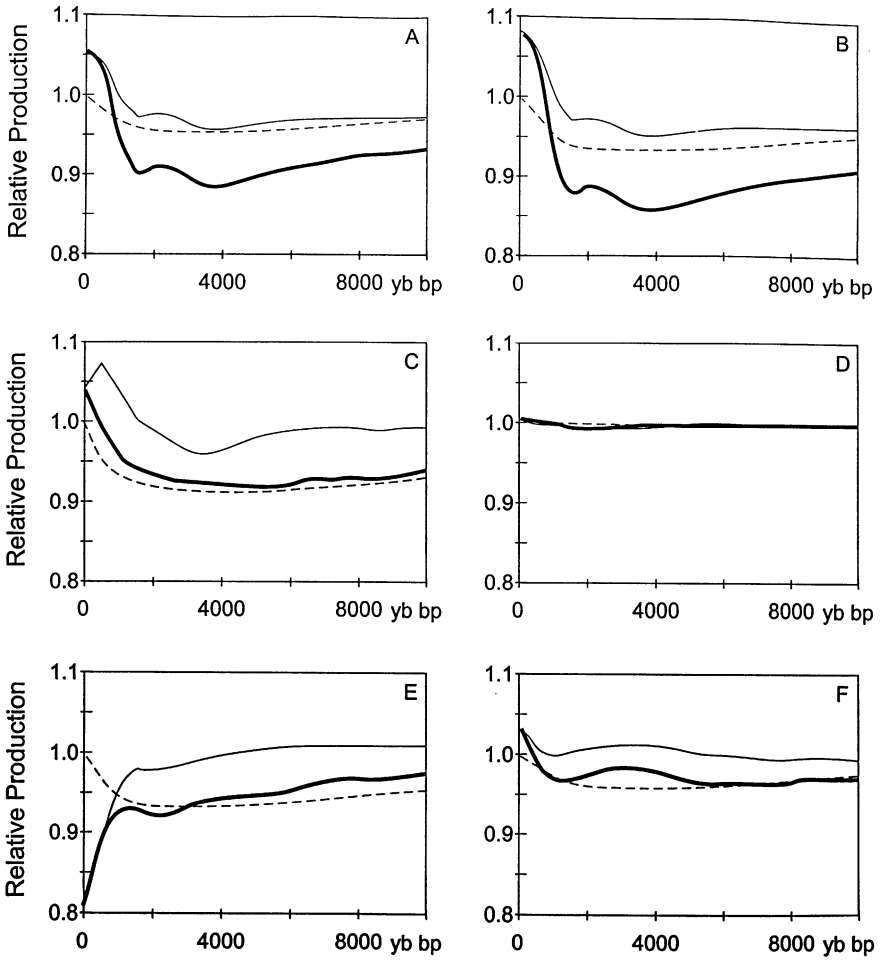


Fig. 11. Effects of variations in the geomagnetic field on TCN production rates, expressed as relative production rate. Dashed line is the change in time averaged production rate due to paleointensity variation according to the Sint-200 data (Fig. 7). Thin solid line is the effect on production rate due to secular variations in the dipole axis position. Thick line is the net geomagnetic field effect, calculated as described in the text. All graphs are for 1 km elevation for comparison. (A) Wind River Range, Wyoming, USA, 43°N, 251°E. (B) Echo Lake, Sierra Nevada, California, USA (39.7°N, 286°E). (C) Hawaii, Pacific Ocean (21°N, 209°E). (D) Prescott Island, Central Arctic, Canada (74°N, 263°E). (E). Southern Alps, New Zealand (44°S, 169°E). (F) Gobi Desert, China (41°N, 113°E).

et al., submitted). Using deviations in Holocene archeomagnetic intensity data, McElhinny and Senanayake (1982) showed that the variation in magnetic moments due to the non-axial dipole field contributions (plus experimental errors) account for about 20% of the total field, and that this proportion has been relatively consistent throughout the Holocene. Acton et al. (1996) have shown that over 90% of the paleomagnetic field can be explained with an axial dipole field (fitted to be geocentric) with a quadrapole field approximately $6.2 \pm 4.7\%$ of the dipole field when averaged over 780 kyr. Their field geometry, constrained by means of skewness tests on global magnetic data for a ubiquitous magnetic anomaly (Central marine magnetic anomaly after the B/M reversal) is consistent with other predictions of dipolar geocentricity (Kono and Hiroi, 1996). More recently, Fang et al. (1997) obtained antipodal VGP data in loess above and below the Blake Event, leading them to suggest that the field was dipolar and approximately geocentric between 120 and 114 ka BP. Thus, the general thinking was that because most of the magnetic field effects on TCN production rates can be attributed to an axial dipole field (and essentially all of it after 20 kyr) any effects of non-axial dipole components would be relatively small, if not negligible, over exposure periods greater than a few thousand years.

More investigation of these non-axial dipole field effects is clearly needed for a more complete appreciation of the influences of the magnetic field on TCN production rates.

*3.5.3.5. Net geomagnetic effects.* The effects of variations in dipole axis position cannot be evaluated for exposures greater than 10 ka until better estimates of the location of the geomagnetic north pole are established. For exposures greater than 100 ka, it is likely that the field is geocentric, so the net geomagnetic effect would be the production rate variation due only to paleointensity

variations, and we have demonstrated the low sensitivity of TCN production rates to paleointensity variation over such long exposure durations. The net geomagnetic effect for the Holocene should be modeled for any geographic site by first calculating the variations in geomagnetic latitude due to secular variation of the dipole axis position, then recalculating the effects of paleointensity variations on these geomagnetic latitudes, and integrating the production rate scaling factors over the exposure time (i.e., the net effect is not simply determined by taking the sum of the deviations in the magnetic latitudes from both paleomagnetic and paleosecular variation effects).

Net changes in production rates are site specific (latitude, longitude, and altitude, Fig. 11). As an example, we have modeled the Sierra Nevada $^{10}$Be production rates of Nishiizumi et al. (1989)and Nishiizumi et al. (1996) for the geographic site location 38°N, 241°E, 3.32 km elevation, assuming 13 kyr of exposure (Clark and Gillespie, 1997), and using the Sint-200 paleointensity record, correcting the last 10 kyr for dipolar wobble and assuming geocentric dipole before 10 ka BP to provide an estimate of the net geomagnetic effect. The time-averaged production rate over 13 kyr of exposure at the geographic location is 52.4 atoms g$^{-1}$ $SiO_2$ yr$^{-1}$, corresponding to a high latitude sea level production rate of approximately 5.6 atoms g$^{-1}$ $SiO_2$ yr$^{-1}$ (muonic and spallogenic components scaled in the same manner as Lal, 1991). Scaled today, the production rate would be 54.2 atoms g$^{-1}$ $SiO_2$ yr$^{-1}$ at the geographic site and 5.8 atoms g$^{-1}$ $SiO_2$ yr$^{-1}$ at high latitude and sea level. We also scaled the Sierra Nevada production rate for longer time periods (50–1000 kyr), assuming no change in position due to tectonic or isostatic effects, and using Valet and Meynadier (1993) data for the first 800 kyr. At the geographic site, the long time-averaged production rate is 61.6 atoms g$^{-1}$ $SiO_2$ yr$^{-1}$ ($\sigma = 1.2$, range = 58.4–65.5 atoms g$^{-1}$ $SiO_2$ yr$^{-1}$). At high latitudes and sea level, the long time-averaged production rate is 6.6 atoms g$^{-1}$ $SiO_2$ yr$^{-1}$ ($\sigma = 0.13$, range = 6.3–7.0 atoms g$^{-1}$ $SiO_2$ yr$^{-1}$).

### 3.5.4. Variations in atmospheric shielding

Changes in effective atmospheric depth can affect production rates over $10^2$–$10^4$ year periods. For example, atmospheric depth changes can result from changes in the crustal altitude of a sample by isostatic rebound. Fig. 12 shows effect on integrated production rate and ages of beaches on an emergent shoreline in the central Arctic. The emergence is due to isostatic rebound since about 10 kyr ago. The marine limit around Prescott Island is approximately 130 m. The emergence curve was determined with radiocarbon-dated driftwood around Prince of Wales Island and $^{10}$Be-dated boulders on beaches on Prescott Island. The figure expresses the difference in an calculated age that ignore the effect of uplift and the corrected age. In less than 10 kyr there is only a 1% difference. However, in the case of tectonic surface uplift that occurs over longer time periods (Brook et al., 1995a), the effect can be significant.

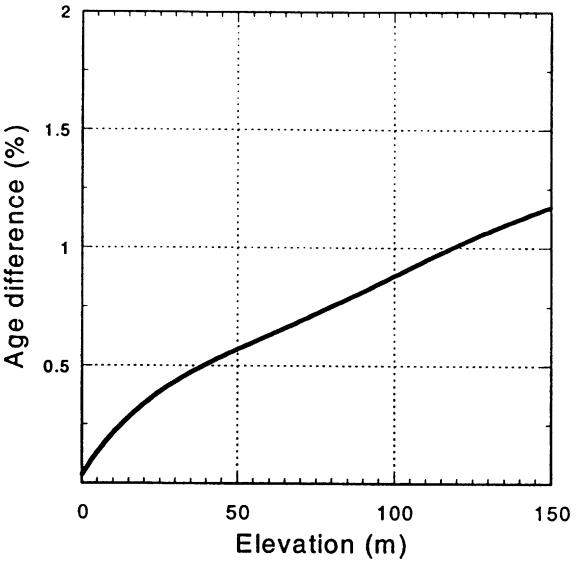


Fig. 12. Comparison of spallogenic production rates on a stationary surface in the central Arctic with those on surfaces that have been isostatically rebounding at an exponential rate (emergence rate from Dyke et al. (1991) based on 40 calibrated radiocarbon dated driftwood fragments on beaches around Prince of Wales island, with emergence history adjusted for eustatic sea level rise estimated from Fairbanks, 1989).

Production rate variations may also result from changes in atmospheric 'thickness' via the migration of persistent density anomalies due to climate change, although this is still speculative and has not been documented. Relatively fixed pressure deviations from the Standard Atmosphere have been proposed by Stone (in press) to offset production rates as much as 30% over Antarctica, less than 5% elsewhere, from production rates scaled with Lal (1991) and other published scaling models. To calculate this, it was necessary to assume that the annually averaged pressure anomalies were static over the Holocene. A model of sea surface and land paleotemperatures and adiabatic lapse rates could help verify the effects of Holocene climate change. Also, barometric changes due to fluctuations in sea level will need to be considered (albeit this is probably a third-order effect). For longer durations, the magnitude and location of the anomalies may have been significantly different (e.g. shifting and enlarging of the intertropical convergence zone).

### 3.5.5. Other sources of temporal variations in production

The above sources of variation deal with physical on the primary and secondary cosmic-ray flux before they reach the surface. Additional temporal variation can be expected with the changes in the surface exposure history. Although it is impractical to evaluate the potential

magnitude of the effect of such changes, we suggest a few common examples: (i) periodic snow cover (e.g. Gosse et al., 1995a), (ii) episodic loess cover, (iii) gradual erosion of a sediment (e.g. till) cover exposing a bedrock surface with little or no evidence of the cover, (iv) changes in vegetation shielding (should be a small effect, determined by the total mass of the organic molecules per area above the ground, but extremely dense forest may reduce the cosmic ray flux by up to 4% (Cerling and Craig, 1994b) and may also enhance thermalization of cosmic-ray neutrons), and (v) paleoaltimetry change (Brook et al., 1995a; Schaefer et al., 1999).

### 3.6. Estimation of production rates

Production rates have been determined by three general methods: (i) with geological calibration, by measuring the concentration of the nuclide in a natural rock surface with a known simple exposure history (stable, no erosion, no shielding) that has been exposed for an independently determined duration. In essence, this method is calibrating a particular nuclide time scale to another time scale, such as radiocarbon-, U–Th-, or dendro-years. A variant on this approach is to perform calibration measurements on stable surfaces that are known to have been exposed for long enough to reach saturation (attained secular equilibrium without erosion), either from independent geological data or through measurement of a longer-lived TCN (e.g., Nishiizumi et al., 1990; Jull et al., 1992; Brook et al., 1995b). (ii) Production rates can be determined experimentally, by laboratory measurements of the nuclide concentration in slabs of known composition that were placed in a nuclear accelerator beam line of particles with energy that can be extrapolated to the secondary radiation flux on the Earth or by exposing target materials to actual cosmic radiation at high altitudes for periods of years (e.g. Nishiizumi et al., 1996); and (iii) by numerical simulation of the nuclear interactions and other physical processes that would be responsible for the product nuclides (e.g. Masarik and Reedy, 1995). Although all three have been useful, spallogenic production rates used in most TCN applications have been derived from geological calibration. Table 4 gives a current list of production rate estimates for the six commonly used TCN. Where earlier estimates of a nuclide production rate has been revised by the same authors we only provide the latest estimate.

We emphasize that it is important for the reader to consult the original source of these rates in order to evaluate, for example, the suitability of the sample sites, the reliability of the time scale being calibrated against, the manner in which it was normalized to high latitude and sea level, or the accuracy of the transport code. Fortunately, most of the production rates measured this decade have used the scaling model by Lal (1991) even if they report results of other scaling models. Even if Lal's (1991) normalization method may not apply to all regions (e.g. Antarctica due to atmospheric affects (Stone, in press) or tropical regions due to magnetic and atmospheric deviations) it provides a uniform means of comparing production rates. All of the production rates reported below have been normalized (by the original or subsequent authors) to production at high latitude sea level with Lal's scaling model.

#### 3.6.1. Helium-3

Empirically derived production rates of the noble gas $^{3}$He have been mostly reported for olivine and pyroxene, although other phases have been attempted, including quartz (Hudson et al., 1991; Brook and Kurz, 1993). Although there was an apparent discrepancy among $^{3}$He production rate estimates recently Licciardi et al. (1999), recalibrated the independent lava ages and normalized the previously published production rates including their own for $^{3}$He data from Oregon basalts. At mid-latitudes (39°–46° N), Cerling and Craig (1994a) measured an average production rate of about $114 \pm 2$ atoms g$^{-1}$ yr$^{-1}$ over the past 17,500 years (calibrated), for olivine and pyroxene at sea level high latitude. This is slightly lower than earlier measurements on Hawaiian lava by Kurz et al. (1990) (approximately $125 \pm 3$ atoms g$^{-1}$ yr$^{-1}$ at sea level high latitude according to Licciadi et al., 1999). The average normalized production rate reported by Licciardi et al. is $119 \pm 1$ atoms g$^{-1}$ yr$^{-1}$ based on 44 measurements that span from about 600–17,500 yr. The precision and consistency of these measurements make the $^{3}$He system the best calibrated, and also suggests than any dipole or non-dipole field effects were not significant. However, because the low latitude Kurz et al. (1990) production rates have a large range ($55 \pm 9$–$231 \pm 101$ atoms g$^{-1}$ yr$^{-1}$) over the Holocene and are higher, it is possible that there was a magnetic (dipole or non-dipole) or surface effect on these data. Other recent estimates of $^{3}$He in pyroxene (Schaefer et al., 1999) agree with the Licciardi (1999) results.

#### 3.6.2. Beryllium-10

Considering that $^{10}$Be is largely produced by only one kind of nuclear reaction (spallation), the discrepancies in calculated production rates are large. Published values for production in quartz, based on empirical measurements range from 4.74 atoms g$^{-1}$ yr$^{-1}$ (Clark et al., 1995) to 6.4 atoms g$^{-1}$ yr$^{-1}$ (Brown et al., 1991), a range of nearly 40%. The discrepancies between the numerous $^{10}$Be production rate estimates may derive partially from uncertainties in the assumed exposure times of the calibration sites or unrecognized shielding by snow or sediment, and partially from temporal variations in production rate due magnetic and atmospheric effects. The standard $^{10}$Be production rate study was (and probably will continue to be) the measurements by Nishiizumi et al. (1989) on surfaces assumed to be 11,000 years old.

When scaled to sea level at high latitudes, the surfaces yielded an average rate of 6.03 atoms $g^{-1}$ $yr^{-1}$ (neutron and muon contribution combined, but scaled separately according to Lal, 1991). When the 11,000 $^{14}C$ yr BP age was calibrated to 11.5 cal kyr BP, the corresponding rate is 5.96 atoms $g^{-1}$ $yr^{-1}$.

However, in 1995 two studies led to the conclusion that these earlier production rate estimates were too high (Clark et al., 1995, 1996; Bierman et al., 1996). One study provided an improved glacial history for the Sierra Nevada (Clark and Gillespie, 1997) and indicated that the surfaces sampled by Nishiizumi et al. (1989) were exposed for at least 13.0 cal kyr BP and probably longer for some of the surfaces. This resulted in much lower $^{10}Be$ production rates (4.74 atoms $g^{-1}$ $yr^{-1}$ or lower, depending on scaling). Concurrently, Clark et al. (1995) reported the results of empirical measurements from the terminal moraines of the Laurentide Ice Sheet in New Jersey which supported lower production rates (maximum of 4.76 atoms $g^{-1}$ $yr^{-1}$). They also proposed that geomagnetic paleointensity could affect the production rates of $^{10}Be$, and could be invoked to explain a possible discrepancy between $^{10}Be$ ages and TL ages of Meteor Crater. Yet subsequent estimates of $^{10}Be$ production rate in quartz yielded high production rates (Gosse and Klein, 1996; Nishiizumi et al., 1996; Kubik et al., 1998) equivalent to the Nishiizumi et al. (1989) value. Additionally, it was recognized that the published Nishiizumi et al. (1989) production rate needed to be adjusted for an approximately geocentric dipole field, which returned the production rate to its original high value, even assuming the longer exposure duration of Clark and Gillespie (1997). The dilemma resulted in a loss of confidence in the applicability of TCN methods for high-resolution dating (e.g. Clark et al., 1995, p. 367).

Fortunately, Stone et al. (1998a) and Stone (1999) found an explanation for the discrepancy between the published production rates. They recognized that production rates derived from low elevation sites (e.g. Clark et al., 1995; Stone et al., 1998a) yielded lower normalized production rates relative to high elevation sites (e.g. Nishiizumi et al., 1989; Gosse and Klein, 1996; Kubik et al., 1998). If the muonic component of the total production at sea level and high latitudes is assumed to be 0–5% (cf. Strack et al., 1994; Brown et al., 1995a; Heisinger et al., 1997) instead of the 15.6% or higher used by Nishiizumi et al. (1989) and Lal (1991), then the scaled high production rates would accordingly be significantly reduced. By assuming a 3% contribution of muons to the production of $^{10}Be$ at sea level, the scaled production rates from the different sites worldwide converge to approximately $5.1 \pm 0.3$ $^{10}Be$ atoms $g^{-1}$ $yr^{-1}$ (Stone, 1999). Therefore, by modifying the way the site measurements were normalized to production at sea level and high latitudes, the discrepancy production rate of $^{10}Be$ can be eliminated and the dilemma is probably resolved.

### 3.6.3. Carbon-14

Although production rates for in situ $^{14}C$ have been estimated with numerical simulations (most recently and with very comparable results, by Masarik and Reedy, 1995), a few production rates have been determined empirically. Establishing the production rate of $^{14}C$ has lagged behind the other isotopes (with the arguable exception of $^{21}Ne$) mainly because of the difficulty in the extraction of cosmogenic $^{14}C$ with a low isotopic background. Recent improvements in the extraction procedure of $^{14}C$ from limestone (Handwerger et al., 1999) and quartz (Lifton et al., submitted) have demonstrated that the isotope can now be reliably measured routinely in these phases. The earliest empirical estimates of in situ $^{14}C$ production rate were derived from whole rock samples (similar to $^{36}Cl$, Section 3.6.6). From measurements on basalts (that had not reached saturation) from Tabernacle Hill, Utah at approximately 1500 m asl, Jull et al. (1994a) calculated a whole rock production rate corrected to $SiO_2$ composition of $55 \pm 10$ and $51 \pm 9$. When scaled to high latitude sea level using the approach of Lal (1991), the rate was $20 \pm 2$ atoms $g^{-1}$ $yr^{-1}$. This value agreed well with their earlier estimates based on whole rock samples that were assumed to have attained saturation (Donahue et al., 1990; Jull et al., 1992). Lifton et al. (submitted) recently determined with a much higher precision the production rate of $^{14}C$ in quartz to be $15.0 \pm 0.5$ atoms $g^{-1}$ $yr^{-1}$ (using Lal (1991) to scale to high latitude sea level). Handwerger et al. (1999) find a similar production rate of $18 \pm 3$ atoms $^{14}CO$ per g $CaCO_3$ from limestone at the same latitude, altitude, and exposure age (Provo Shoreline, scaled with Lal, 1991).

### 3.6.4. Neon-21

Neon-21 is a noble gas that has often been measured in the same samples as $^{3}He$. Production rates of $^{21}Ne$ from Mg and Al are 196 atoms $g^{-1}$ $yr^{-1}$ and 55 atoms $g^{-1}$ $yr^{-1}$ respectively (Schaefer et al., 1999), and 169 atoms $g^{-1}$ $yr^{-1}$ in olivine (Sarda et al., 1993). However there has been a number of measurements of $^{21}Ne$ in quartz, showing that unlike the more diffusive $^{3}He$, neon appears to be well contained in quartz (at least in the samples reported). The production rate in quartz has been determined to be approximately 21 atoms $g^{-1}$ $yr^{-1}$ (Niedermann et al., 1994). Reviews of the production systematics, including non-cosmogenic components have been included elsewhere (Marti and Craig, 1987; Graf et al., 1991, 1995; Poreda and Cerling, 1992; Niedermann et al., 1993; Phillips et al., 1998).

### 3.6.5. Aluminum-26

The production of $^{26}Al$ in quartz has been closely tied with the production rate of $^{10}Be$ (Section 3.6.2). The two are commonly measured in the same sample because the extraction chemistry is similar and can be done

simultaneously. The measured $^{26}Al/^{10}Be$ production ratio is approximately 6.0 to 6.1 (Nishiizumi et al., 1989; Bierman et al., 1996), although it has been reported as high as 6.5 (Brown et al., 1991; Kubik et al., 1998). The AMS measurement of the $^{26}Al/^{27}Al$ remains difficult relative to $^{10}Be/^{9}Be$ and the other radionuclides, so a significant part of the discrepancy among $^{26}Al$ production rate estimates may be attributed to analytical uncertainty.

#### 3.6.6. Chlorine-36

The difference in the estimates of production rates for three pathways of $^{36}Cl$ from different groups is large (Table 4). At least a part of the difference may be explained by the methods used in determining the rates. Stone et al. (1994, 1996, 1998b) worked with mineral separates (plagioclase and microcline) in different environments to isolate individual pathways and maximize target element abundance and Ca/Cl and K/Cl, and used high altitude sites for the spallation reactions and deep subsurface sites for muon reactions. They scaled spallogenic and muonic reactions separately. Phillips et al. (1996b) based their latest estimate on the measurement of $^{36}Cl$ in 33 whole-rock samples. In addition to production rates for the spallation of Ca and K, they indirectly determined the rate of $^{36}Cl$ production via the thermal neutron component by quantifying all other pertinent (Liu et al., 1994) chemical and physical parameters for each sample, then solving the age equation while maximizing the weighted $\chi^2$ function for the three unknowns. They demonstrated that accounting for temporal variations in geomagnetic paleointensity fluctuations did not improve the weighted $\chi^2$ function. They grouped the muonic component with the spallogenic component and ignored the different altitude-scaling of muons by using predominantly low altitude sites (the majority at 1300–1700 m asl), and calibrated against three different clocks: calibrated $^{14}C$, K/Ar, and thermoluminescence. Swanson (1996) estimated the contribution of the three $^{36}Cl$ production pathways in 64 radiocarbon-age-constrained glacierized rock surfaces near sea level at high latitude. The causes of the differences in the results of the three groups are not yet explained and are an area of active investigation. The most likely candidates are methodological differences (most likely in sample preparation) or problems with the independent age control.

The new formulation of epithermal neutron fluxes that was presented by Phillips et al. (2000) also requires that the production parameters be recalibrated. Phillips et al. (2000) used the same data set as Phillips et al. (1996) for the recalibration, but in addition to the new epithermal neutron equations, they also included muon production (Table 3). This recalibration resulted in a production rate by calcium spallation lower by about 10%. This is largely a result of including production due to slow muon absorption by calcium. The production rate from spallation of potassium also necessarily decreased since the calibration fixed the production ratios from these two elements. The 40% increase in $P_f(0)$ is almost entirely due to the new epithermal/thermal neutron equation.

### 3.7. Scaling and correction factors for production rates

The reference condition for the production of cosmogenic nuclides is a horizontal surface on a flat plain at high latitude and sea level. However, TCN samples may be collected at any latitude and elevation, and may be on sloping surfaces that have partially obstructed horizons. Some surfaces may be covered, perhaps temporarily, by snow or sand. These deviations from the standard reference situation can be addressed quantitatively by means of scaling factors and modified attenuation lengths.

#### 3.7.1. Spatial scaling

Recent models of the altitude and latitude variation in the global flux of secondary radiation (Section 3.1.4) have been based on experimental measurements of (i) slow and fast neutrons in the atmosphere, (ii) nuclear disintegrations (star production) in nuclear emulsions and cloud chambers, (iii) energy spectra of protons and the secondary component in the atmosphere, (iv) energy spectra of various charged particles at production in nuclear disintegrations at mountain latitudes (e.g. Lal et al., 1960; Yokoyama et al., 1977), and (v) physical processes controlling the flux and interactions. These measurements have been extrapolated in order to estimate the global distributions of the cosmic-ray flux of secondary thermal neutrons, muons, and fast nucleons responsible for TCN (Lal, 1958, 1991; Lal et al., 1960; Lal and Peters, 1967). The normalized spatial variation in rates of production from thermal neutrons and fast nucleons with $E < 400$ MeV is identical (Lal et al., 1958) which simplifies the scaling models. These scaling models are temporally invariant, use a simple model for spatial variations in atmospheric density, and do not account for non-dipole and other second-order affects on the cosmic-ray flux.

The most widely used scaling model is that by Lal (1991). It is difficult to evaluate the uncertainty in the Lal (1991) scaling factors (Fig. 13), although Lal suggests the total uncertainty is approximately 10–20%. The altitude scaling seems reasonably robust for mid- to high-latitude sites. Measurements of cosmogenic $^{36}Cl$ in independently dated Hawaiian lava flows and moraines over a range in elevations from 120 to 4090 m (Zreda et al., 1991) and measurements of $^{3}He$ over similar altitude and latitude range (Cerling and Craig, 1994a; Licciardi et al., 1999) suggest at least the altitude scaling of the 1991 model is a reasonable first order approximation. However, as discussed above (Section 3.6.2), the 1991 model scales from a 15.6% muonic contribution of the total production of $^{10}Be$ at sea level, which may be too large (Stone et al.,

Table 4
Production rates at the rock surface, (normalized where necessary by the authors using Lal, 1991) for production at sea level and high latitude

| Path–target–nuclide | Exposure time (ca sideral) | Rate (atom $g^{-1}$ target $a^{-1}$) | Reference |
|---|---|---|---|
| $P_{s,SiO_2}$ $^{3}$He | Calculated | 75 | (Lal, 1991) |
| $P_{s,SiO_2}$ $^{3}$He | Calculated | 124 | (Masarik and Reedy, 1995) |
| $P_{s,Olivine}$ $^{3}$He | Calculated | 64 | (Lal, 1991) |
| $P_{s,Olivine}$ $^{3}$He | Calculated | 105 | (Masarik and Reedy, 1995) |
| $P_{s,Olivine}$ $^{3}$He | Calculated | 115 | (Yokoyama et al., 1977) |
| $P_{s,Olivine}$ $^{3}$He | 0.6–13.5 ka | 47–50 | (Kurz, 1986b; Kurz et al., 1990) |
| $P_{s,Olivine}$ $^{3}$He | 2–17.5 ka | $115 \pm 4$ | (Cerling and Craig, 1994a) |
| $P_{s,Olivine}$ $^{3}$He | 2–7 ka | $116 \pm 3$ | (Licciardi et al., 1999) |
| $P_{s,Pyroxene}$ $^{3}$He | $< 11$ ka | $= P_{s,Olivine}$ $^{3}$He | (Laughlin et al., 1994) |
| $P_{s,SiO_2}$ $^{10}$Be | 4 solar cycles | $5.32 \pm 0.27$ | (Nishiizumi et al., 1996) |
| $P_{s,SiO_2}$ $^{10}$Be | $\sim 21.5$ ka | $5.17 \pm 0.15$ | (Bierman et al., 1996; Clark et al., 1995) |
| $P_{s,SiO_2}$ $^{10}$Be | 14.0 ka | 4.74 | (Clark et al., 1995) |
| $P_{s,SiO_2}$ $^{10}$Be | Calculated | 5.97 | (Masarik and Reedy, 1995) |
| $P_{s,SiO_2}$ $^{10}$Be | Calculated | 6.5 | (Lal and Peters, 1967) |
| $P_{s,SiO_2}$ $^{10}$Be | 2.5 Ma | 6.4 | (Brown et al., 1991) |
| $P_{s,SiO_2}$ $^{10}$Be | 7 Ma | 6.13 | (Nishiizumi et al., 1991a) |
| $P_{s,SiO_2}$ $^{10}$Be | 12.2 ka | 6.03 | (Ivy-Ochs, 1996; Nishiizumi et al., 1989) |
| $P_{s,SiO_2}$ $^{10}$Be | 12.9 ka | $5.5 \pm 0.7$ | (Gosse and Klein, 1996) |
| $P_{s,SiO_2}$ $^{10}$Be | 17.6 ka | $5.4 \pm 0.6$ | (Gosse and Klein, 1996) |
| $P_{s,SiO_2}$ $^{10}$Be | 10.0 ka | $5.75 \pm 0.24$ | (Kubik et al., 1998) |
| $P_{s,Olivine}$ $^{10}$Be | Calculated | 5.25 | (Nishiizumi et al., 1990) |
| $P_{s,Basalt}$ $^{10}$Be | Calculated | 1.83 | (Yokoyama et al., 1977) (using Lal, 1991) |
| $P_{s,SiO_2}$ $^{14}$C | 17.8 ka | $20 \pm 4$ | (Jull et al., 1994; Jull et al., 1992) |
| $P_{s,SiO_2}$ $^{14}$C | Calculated | 18.6 | (Masarik and Reedy, 1995) |
| $P_{s,SiO_2}$ $^{21}$Ne | Artificial target | 19.3 | (Graf et al., 1996) |
| $P_{s,SiO_2}$ $^{21}$Ne | Calculated | 8 | (Lal, 1991) |
| $P_{s,SiO_2}$ $^{21}$Ne | Calculated | 18.4 | (Masarik and Reedy, 1995) |
| $P_{s,SiO_2}$ $^{21}$Ne | $\sim 11$ ka | 21 | (Niedermann et al., 1994) |
| $P_{s,Olivine}$ $^{21}$Ne | Calculated | 32 | (Lal, 1991) |
| $P_{s,Olivine}$ $^{21}$Ne | Calculated | 38.7 | (Masarik and Reedy, 1995) |
| $P_{s,Olivine}$ $^{21}$Ne | 17.8 ka | 45 | (Poreda and Cerling, 1992) |
| $P_{s,SiO_2}$ $^{26}$Al | 14.0 ka | 28.9 | (Clark et al., 1995) |
| $P_{s,SiO_2}$ $^{26}$Al | 12.2 ka | 36.8 | (Nishiizumi et al., 1989) |
| $P_{s,SiO_2}$ $^{26}$Al | 7 Ma | 37 | (Nishiizumi et al., 1991a) |
| $P_{s,SiO_2}$ $^{26}$Al | 10.0 ka | $37.4 \pm 1.9$ | (Kubik et al., 1998) |
| $P_{s,SiO_2}$ $^{26}$Al | Calculated | 27.5 | (Lal, 1991) |
| $P_{s,SiO_2}$ $^{26}$Al | Calculated | 36.1 | (Masarik and Reedy, 1995) |
| $P_{s,Olivine}$ $^{26}$Al | Calculated | 15.4 | (Nishiizumi et al., 1990) |
| $P_{s,Basalt}$ $^{26}$Al | Calculated | 40.6 | (Yokoyama et al., 1977) (using Lal, 1991) |
| $P_{s,Ca}$ $^{36}$Cl | Calculated | $99 \pm 20$ | (Yokoyama et al., 1977) |
| $P_{s,Ca}$ $^{36}$Cl | Calculated | 64.6 | (Masarik and Reedy, 1995) |
| $P_{s,Ca}$ $^{36}$Cl | 2.1 to 55 ka | $73.6 \pm 5.0$ | (Phillips et al., 1996b) |
| $P_{s,Ca}$ $^{36}$Cl | 15.2 ka | $44.2 \pm 1.4$ | (Swanson, 1996) |
| $P_{s,Ca}$ $^{36}$Cl | 11 to 17 ka | $48.8 \pm 3.4$ | (Stone et al., 1996) |
| $P_{s,Ca}$ $^{36}$Cl | 2.1 to 55 ka | $66.8 \pm 6.8$ | (Phillips et al., 2000) |
| $P_{s,K}$ $^{36}$Cl | Calculated | $321 \pm 64$ | (Yokoyama et al., 1977) |
| $P_{s,K}$ $^{36}$Cl | 2.1 to 55 ka | $154 \pm 10$ | (Phillips et al., 1996b) |
| $P_{s,K}$ $^{36}$Cl | 15.2 ka | $73.8 \pm 5.0$ | (Swanson, 1996) |
| $P_{s,K}$ $^{36}$Cl | 11 to 17 ka | $185 \pm 15$ | (Stone et al., 1996) |
| $P_{s,K}$ $^{36}$Cl | 11 to 17 ka | $235 \pm 10$ | (Stone et al., 1996) |
| $P_{s,K}$ $^{36}$Cl | 2.1 to 55 ka | $137 \pm 60$ | (Phillips et al., 2000) |
| $P_{\mu,Ca}$ | 11 to 17 ka | $4.8 \pm 0.5$ | (Stone et al., 1996) |
| $P_{f,air}$ $^{36}$Cl[a] | 2.1 to 55 ka | $597 \pm 83$ | (Phillips et al., 1996b) |
| $P_{f,(0)}$ $^{36}$Cl | 2.1 to 55 ka | $626 \pm 105$ | (Phillips et al., 2000) |

[a]This value of the production rate of fast secondary neutrons per gram of air above the air-rock interface per year is used (Liu et al., 1994; Phillips et al., 1996b) in lieu of the more complicated parameterization of the thermal neutron capture component of $^{36}$Cl by determining the thermal neutron absorption rate per gram of rock per year.

Earlier published production rates by the same group are not included if a more recent interpretation of the same data is provided.

The calculated values are based on numerical simulations and models with different assumptions, nuclear cross sections, and reliability.

At the time of publication of this manuscript, J. Stone has proposed that a different scaling function be used to normalize production rates to sea level, high latitude by assuming a $3 \pm 1\%$ muon capture instead of 15.6% (the latter has been estimated by earlier work and used extensively through Lal's (1991) scaling equations). This proposed scaling will bring the majority of $^{10}$Be production rates in quartz to $5.06 \pm 0.29$ $^{10}$Be atoms $g^{-1}$ $yr^{-1}$, and explains most of the apparent discrepancy. Scaling with a lower muonic component will affect the production rates of other nuclides that have been scaled with the Lal (1991) model.

Licciardi et al. (1999) have recently improved the independent chronology of sites used in earlier $^{3}$He production rate determinations by recalibrating and re-dating some of the sites. For mid-latitude sites they calculate a (normalized) production rate of 115 atoms $g^{-1}$ olivine $yr^{-1}$.

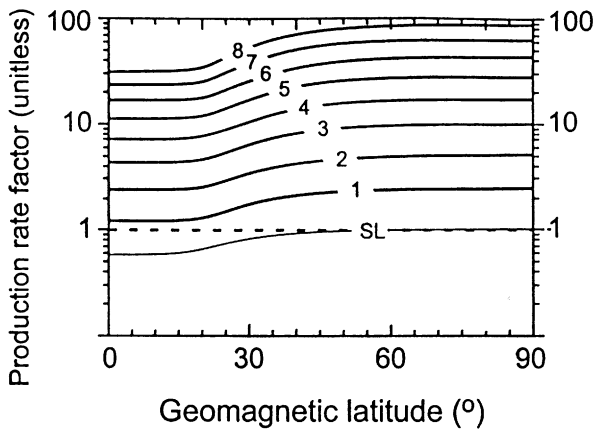


Fig. 13. Scaling factor for variation of production rates with elevation and latitude ($S_{el}$) based on Lal (1991). Contours are elevation in km.

1998a). Reducing the muon contribution most strongly affects the altitude scaling at low altitudes. Previously published dates on surfaces above 2500 m elevation based on the Nishiizumi et al. (1989) production rate and Lal (1991) scaling model will not change significantly. Other attempts are now being made to measure depth profiles to resolve the muonic contribution to production at different elevations and different rock types. For instance, initial results of Kim et al. (1999) show the transition from neutron-induced to muon-induced production of $^{10}$Be and $^{26}$Al at 800 g cm$^{-2}$ and show that the muon-dominated $^{26}$Al/$^{10}$Be less than 4.4 $\pm$ 0.1.

The horizontal scaling may not be so robust. Previously described atmospheric and longitudinal effects are not accounted for in the Lal (1991) model. Ongoing investigations (e.g. Graham, 1996) are attempting to more precisely evaluate Lal's scaling for latitude by measurements in natural and artificial samples at different latitudes in the Southern Hemisphere.

### 3.7.2. Topographic shielding

The standard model for calculating cosmogenic nuclide production assumes that the production is taking place below a horizontal planar surface. In actuality, many samples are collected from sloping surfaces, and many samples are in the vicinity of topographic irregularities that may block part of the otherwise incident cosmic radiation. The effects of these factors are usually termed "shielding". In this section we describe approaches to calculating the appropriate correction factors for topographic shielding. Our approach is derived somewhat differently, but yields results similar to the equations presented by Dunne et al. (1999).

*3.7.2.1. Shielding of horizontal surface.* The effect of topographic obstructions on the cosmic-ray flux through horizontal surfaces is accounted for by means of a scaling factor, $S_t$,. This scaling factor is the ratio of the actual radiation flux through the surface to the flux that would be present if the entire horizon were horizontal. It is given by the following relation:

$$S_t = \frac{\Phi_f(\phi,\theta)}{\Phi_f(\max)} = \frac{\int_{\theta=0}^{2\pi}\int_{\phi=0}^{\min\{\phi_s,\phi_t(\theta)\}} F_0 \cos^{2.3}\phi \sin\phi \cos\phi \, d\phi \, d\theta}{\Phi_f(\max)}, \quad (3.66)$$

where $\phi_s$ is the inclination of the surface itself (equal to 90° in all directions for a horizontal surface) and $\phi_t(\theta)$ is the inclination angle in direction $\theta$ dictated by the surrounding topography.

In general, as illustrated in Fig. 5, the effect of typical topographic obstructions is small because the incoming cosmic radiation is strongly concentrated near the vertical. For example, a flat surface on the bottom of a conical pit with 45° walls would still receive 80% of the radiation incident upon an unobstructed surface. However, the shielding effect may be accentuated if the sampled surface is sloped toward a major topographic obstruction.

*3.7.2.2. Shielding of sloping surface.* When the surface sampled is sloped, several factors act to increase the effective shielding. One is that, since the preponderance of the cosmic radiation is from close to the vertical, the foreshortening effect will tend to reduce the radiation flux. A second is that the effective surface area in the direction parallel to the axis of rotation will also be foreshortened (e.g., a surface on a vertical cliff face will receive no radiation from any inclination along the azimuth parallel to the cliff face). Finally, the portion of the slope above the sample point will topographically block incoming radiation (e.g., the upper portions of a vertical cliff will block one-half of the radiation potentially reaching a sample site in the middle of the cliff face). In this case, the angle between the normal to the surface, $N$, and the incident ray, $\gamma$, is a function of both $\phi$ and $\theta$, i.e. $\gamma(\phi,\theta)$ (Fig. 14). The normal to the sample surface is defined by an inclination $\phi_n$ and an azimuth $\theta_n$, in the spherical

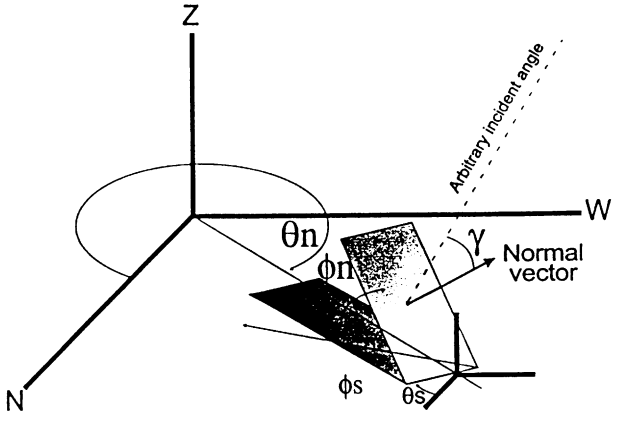


Fig. 14. Illustration of geometrical quantities used in derivation of the shielding factor for sloping surfaces.

coordinate system (Figs. 4a and b). Geological surface measurements however, are usually taken as strike ($\theta_s$, the azimuth of the intersection of the surface with a horizontal plane) and dip ($\phi_d$, downward slope of the surface below the horizontal). Given these conventions, $\phi_n = \phi_d$ and $\theta_n = \theta_s \pm 90^\circ$, using " + " if the dip is reported north to east and " − " if it is reported south to west, if the normal geological convention of reporting strike only in the northern half of the compass is followed (Compton, 1962). In order to avoid ambiguity, for cosmogenic nuclide measurements it is generally preferable to report "direction of dip" rather than strike, where the direction of dip is equal to $\theta_n$. Given a description of the orientation of the normal to the surface, the required cosine of $\gamma(\phi,\theta)$ (again, the angle between the normal and an arbitrary spherical orientation) can be derived using the spherical law of cosines

$$\cos(\gamma(\phi,\theta)) = \cos\phi_n\cos\phi + \sin\phi_n\sin\phi\cos(\theta_n - \theta). \tag{3.67}$$

For a field sample, the lower limit on the inclination of exposure, for a particular azimuth, may be limited either by a topographic obstruction, $\phi_t(\theta)$, or by the projection of the slope of the sampled surface. For a sloping surface, that projection, $\phi_s(\theta)$, is given by

$$\phi_s(\theta) = 90^\circ + \tan^{-1}(\cos(\theta - \theta_n)\tan\phi_n). \tag{3.68}$$

The equation describing the flux of the energetic component of the cosmic radiation through the surface thus becomes

$$\Phi_f(\phi,\theta) = \int_{\theta=0}^{2\pi}\int_{\phi=0}^{\min\left\{\begin{matrix}\phi_s(\theta)\\ \phi_t(\theta)\end{matrix}\right.} F_0\cos^{2.3}\phi\sin\phi \times\cos(\gamma(\phi,\theta))\,d\phi\,d\theta. \tag{3.69}$$

The scaling factor for a sloping surface surrounded by irregular topography is then given by

$$S_t = \frac{\int_{\theta=0}^{2\pi}\int_{\phi=0}^{\min\left\{\begin{matrix}\phi_s(\theta)\\ \phi_i(\theta)\end{matrix}\right.} F_0\cos^{2.3}\phi\sin\phi(\cos\phi_n\cos\phi + \sin\phi_n\sin\phi\cos(\theta_n - \theta))\,d\phi\,d\theta}{\Phi_f(\max)}, \tag{3.70}$$

where $\Phi_f(\max)$ is obtained from Eq. (3.60).

Increasing the obliquity of the angle between incident radiation and the sample surface has another effect besides altering the attenuation length (Fig. 15b). A more oblique angle creates a longer path-length through the sample, thereby slightly increasing production over a given depth, $Z$ (this effect in fact exactly counteracts the foreshortening effect previously described so that, in some formulations of the production equations (e.g., Dunne et al., 1999), both terms may be neglected). Thus, even for the case in which the cosmic-ray flux through a horizontal surface is the same as through a steeply

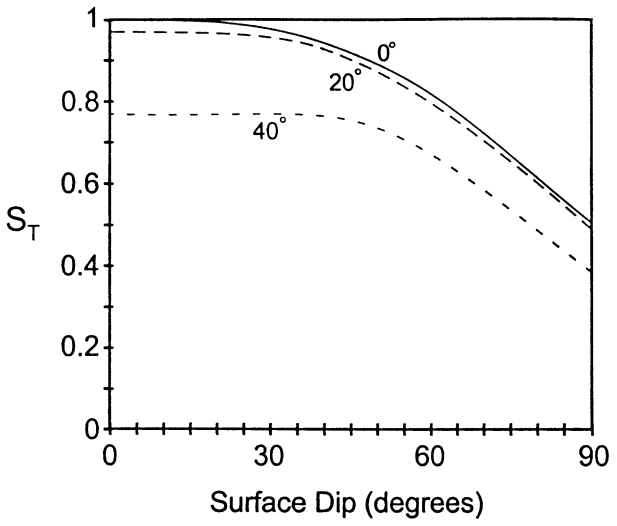


Fig. 15. Total topographic scaling ($S_T$) as a function of surface dip angle and topographic shielding. Degree labels on curves refer to the angle of shielding by surrounding, axially symmetric, topographic features.

dipping one, the surface production rate, $P_{t,m}(0)$ (atoms $g^{-1}\,yr^{-1}$), will be slightly greater for the dipping surface because, as indicated by the shorter effective attenuation length, the same amount of production is concentrated in a shorter thickness (measured perpendicular to the surface). This can be accounted for by equating the vertically integrated production beneath a horizontal surface to the production integrated perpendicular to a dipping surface

$$S_T\int_0^\infty P_0\exp\left(-\frac{\lambda}{\Lambda_{f,e}}\right)d\lambda = S_t\int_0^\infty P_0\exp\left(-\frac{Z}{\Lambda_f}\right)dZ, \tag{3.72}$$

where $l$ is the perpendicular to the dipping surface and $S_T$ is the complete (total) scaling factor for topographic obstructions, dipping surfaces, and changes in effective attenuation length. Integration yields the scaling factor for changes in effective attenuation length.

$$S_T = \frac{\Lambda_f}{\Lambda_{f,e}}S_t = S_\Lambda S_t. \tag{3.73}$$

The total shielding, as a function of slope of surface, for varying topographical geometry is shown in Fig. 15.

*3.7.2.3. Effects of shielding and slope on attenuation length.* For a surface penetrated by cosmic rays from

a range of incidence angles, an effective attenuation length, $\Lambda_{f,e}$, can be defined from the weighted average of all penetration depths. This attenuation length, like that for a horizontal surface, is defined as being perpendicular to the rock surface. The effective attenuation length, $\Lambda_{f,e}$, is calculated by combining Eq. (3.66) and (3.54)

$$\Lambda_{f,e} = \Lambda_{f,p}\frac{\int_{\theta=0}^{2\pi}\int_{\phi=0}^{\min\{\phi s,\phi i(\theta)\}} F_o \cos^{2.3}\phi \sin\phi \cos(\gamma(\phi,\theta))\,d\phi\,d\theta}{\int_{\theta=0}^{2\pi}\int_{\phi=0}^{\min\{\phi s,\phi i(\theta)\}} F_o \cos^{2.3}\phi \sin\phi\,d\phi\,d\theta}. \quad (3.74)$$

Although the apparent attenuation length, $\Lambda_f$, is often treated as a constant, it approximates such only for horizontal, unshielded surfaces. A dipping surface will have a shorter effective attenuation length because more of the particles will enter at oblique angles and a strongly shielded horizontal surface will have a longer effective attenuation length because fewer of the particles will be entering from oblique angles. Fig. 16 illustrates the variation of the effective attenuation length with surface dip and topographic shielding.

### 3.7.3. Surface coverage

One relatively common type of shielding is that due to cover by winter snow, or possibly sand, soil, or peat. Snow is the most common cause for surface coverage corrections and the discussion below will be framed in terms of snow corrections. However, the equations and principles are applicable to coverage by any other material, with suitable modifications for density and timing of the coverage. At any time when snow is present on the surface the energetic component $f$ the cosmic radiation is reduced according to the exponential attenuation equation

$$\Phi_{f,cover} = \Phi_f e^{(-Z_{cover}/\Lambda_f)}, \quad (3.75)$$

where $Z_{cover}$ is the mass of cover per unit area over the rock sampled. The correction for the cover must also include any temporal variation in depth. For instance, snow survey data of average snow depth and average snow water content can be used to construct distribution curves (as a function of time of the year) of snow water content overhead at various heights above the surface. The temporal distribution of snow water shielding is needed because the relationship between water content and shielding is not linear. Using these water content curves and Eq. (3.70), the shielding at different heights as a function of time of the year can be computed. Finally, these can be averaged over the year and divided by the computed flux without snow cover to yield curves of annual snow shielding ($S_{snow}$) as a function of height of the sampling point above the land surface. A typical annual snow shielding formulations is given in Eq. (3.76), using monthly snow depths as an example.

$$S_{snow} = \frac{1}{12}\sum_{i}^{12} e^{-((z_{snow,i} - z_{sample})\rho_{snow,i}/\Lambda_{f,e})}, \quad (3.76)$$

where $z_{snow,i}$ is the monthly average snow height (cm) above the land surface, $\rho_{snow,i}$ is the average monthly snow density, and $z_{sample}$ is the height (cm) of the boulder or other sampling point above the land surface. In this case, monthly intervals were used because snow depth data is the most commonly available in monthly means. However, the effect could be integrated over different time periods appropriate for the cover. This type of analysis can be generalized by computing curves of $S_{snow}$ as a function of height above land surface (i.e., as a function of $z_{sample}$) so that snow cover can quickly be estimated for a number of boulders of varying height.

Typical corrections for 4 months of shielding by snow of different depths and densities are shown for a spallogenic nuclide in Fig. 17 (cf. Gosse et al., 1995a; Licciardi et al., 1999). Onuchin and Burenina (1996) used a database of 2456 snow density observations in northern Eurasia to show a relationship between snow density variation and three other parameters: snow thickness, air temperature, and snow cover period. The range of densities they measured was 0.16–0.48 g cm$^{-3}$ while the average range was 0.16–0.33 g cm$^3$. Their model may be useful for estimating snow densities where historical records of the other parameters are available.

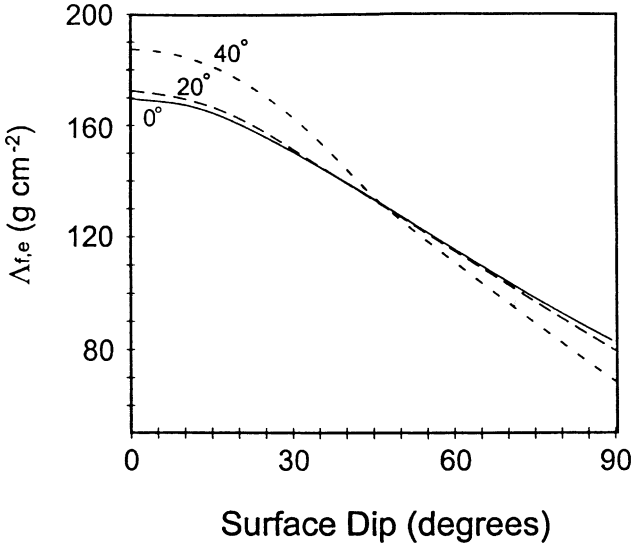


Fig. 16. Effective attenuation length ($\Lambda_{f,e}$) as a function of surface dip angle and topographic shielding. Degree labels on curves refer to the angle of shielding by surrounding, radially symmetric, topographic features.

### 3.7.4. Sample thickness

Cosmogenic nuclide production rates are specified at the rock surface. However, the production profile varies continuously with depth and samples are collected over finite depth intervals. The production rate must therefore be integrated over the actual sample thickness and

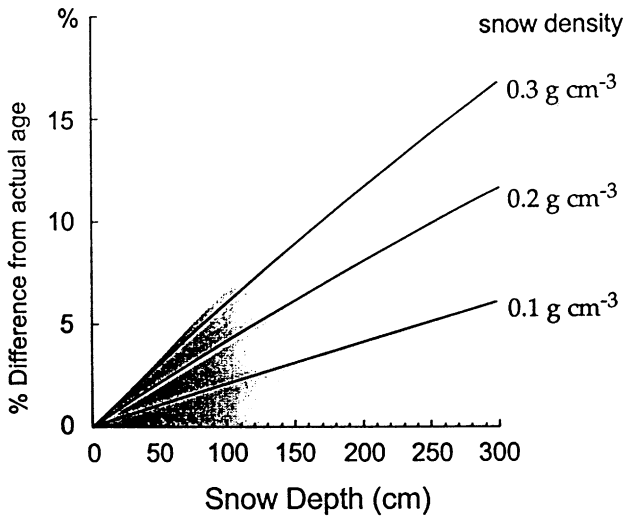


Fig. 17. Effects of shielding by snow of common densities and thicknesses. Calculated for a spallogenic nuclide, assuming an otherwise simple exposure, with snow shielding instantaneously applied for 4 months each year. This is a multiplicative effect so the deviation can apply to any exposure age.

divided by the surface production to yield the thickness correction factor $Q_i$

$$Q_{i,m} = \frac{\overline{P_{i,m}}}{P_{i,m}(0)} = \frac{\int_0^{Z_s} P_{i,m}\,\mathrm{d}Z}{Z_s P_{i,m}(0)}, \tag{3.77}$$

where $Q_{i,m}$ refers to the $i$th reaction producing the $m$th nuclide and $Z_s$ is the thickness of the sample (assuming that the top of the sample is the surface). The production terms in the numerator and denominator of Eq. (3.77) cancel and hence the correction factor depends only on the type of reaction and not on the nuclide produced. Substituting Eqs. (3.53)–(3.55), and (3.48) into Eq. (3.77) and solving yields

$$Q_s = \frac{\Lambda_{f,e}}{Z_s}\left(1 - \exp\left[-\frac{Z_s}{\Lambda_{f,e}}\right]\right), \tag{3.78}$$

$$\begin{aligned} Q_{eth} = \Bigg\{ & \left[\Phi^*_{eth,ss}\Lambda_{f,e}\left[1 - \exp\left(-\frac{Z_s}{\Lambda_{f,e}}\right)\right]\right. \\ & + (1 + R_\mu R_{eth})(F\,\Delta\Phi)^*_{eth,ss} L_{eth,ss} \\ & \times\left[1 - \exp\left(-\frac{Z_s}{L_{eth,ss}}\right)\right] \\ & \left. + R_\mu \Phi^*_{eth,ss}\Lambda_\mu\left[1 - \exp\left(-\frac{Z_s}{\Lambda_\mu}\right)\right]\right] \\ & \times [Z_s(\Phi^*_{eth,ss} + (1 + R_\mu)(F\,\Delta\Phi)^*_{eth,ss} \\ & + R_\mu \Phi^*_{eth,ss})]^{-1}\Bigg\}, \end{aligned} \tag{3.79}$$

$$\begin{aligned} Q_{th} = \Bigg\{ & \Phi^*_{th,ss}\Lambda_{f,e}\left[1 - \exp\left(-\frac{Z_s}{\Lambda_{f,e}}\right)\right] \\ & + (1 + R'_\mu)(\Im\,\Delta\Phi)^*_{eth,ss} L_{eth,ss} \\ & \times\left[1 - \exp\left(-\frac{Z_s}{L_{eth,ss}}\right)\right] \\ & + (1 + R'_\mu R_{th})(\Im\,\Delta\Phi)^*_{th} L_{th,ss} \\ & \times\left[1 - \exp\left(-\frac{Z_s}{L_{th,ss}}\right)\right] \\ & + R'_\mu \Phi^*_{th,ss}\Lambda_\mu\left[1 - \exp\left(-\frac{Z_s}{\Lambda_\mu}\right)\right]\Bigg\} \\ & \times \{Z_s[\Phi^*_{th,ss} + (1 + R'_\mu)((\Im\,\Delta\Phi)^*_{eth,ss} \\ & + (\Im\,\Delta\Phi)^*_{th,ss}) + R'_\mu \Phi^*_{th,ss}]\}^{-1}, \end{aligned} \tag{3.80}$$

$$Q_\mu = \frac{\Lambda_\mu[1 - \exp(-Z_s/\Lambda_\mu)]}{Z_s}. \tag{3.81}$$

The effect of sample thickness on the correction factor for $^{36}$Cl produced in a quartz arenite is shown in Fig. 18a. In general, the sensitivity of calculated ages to normal errors in estimation of sample thickness or bulk density is small, on the order of 1 or 2%, as illustrated in Fig. 18b.

### 3.7.5. Thermal neutron leakage

Eq. (3.10) contains correction terms for epithermal and thermal neutron leakage. This refers to the enhanced diffusion (due to greater surface area) of low-energy neutrons out of the corners and edges of objects that project into the air, relative to the "standard" diffusion out of flat surfaces. This effect has unfortunately never been adequately quantified, although it is probably generally small. For a very unfavorable geometry (the top of a thin, spine-like basalt pressure ridge) Zreda et al. (1993) estimated a minimum value for the thermal neutron leakage scaling factor of 0.7. The effect will be largest for sample sites with significant three-dimensional geometry (e.g., the top of an acute-angle pyramid), less for a more regular three-dimensional point such as the corner of a cube, and less yet for a two-dimensional geometry such as the edge of a cube. Epithermal and thermal neutron diffusion lengths are such that the low-energy neutron fluxes typically return to near-equilibrium values within $\sim 25$ cm below the rock surface. Given these characteristics, the simplest method of dealing with the neutron leakage problem is to sample flat surfaces at least 30 cm back from the edges of boulders, and to avoid sample sites consisting of acute vertices.

## 3.8. Exposure dating with a single TCN

Eqs. (3.10), (3.47) and (3.53)–(3.55) can be combined to obtain the total cosmogenic nuclide production rate (by spallation reactions, epithermal and thermal neutron

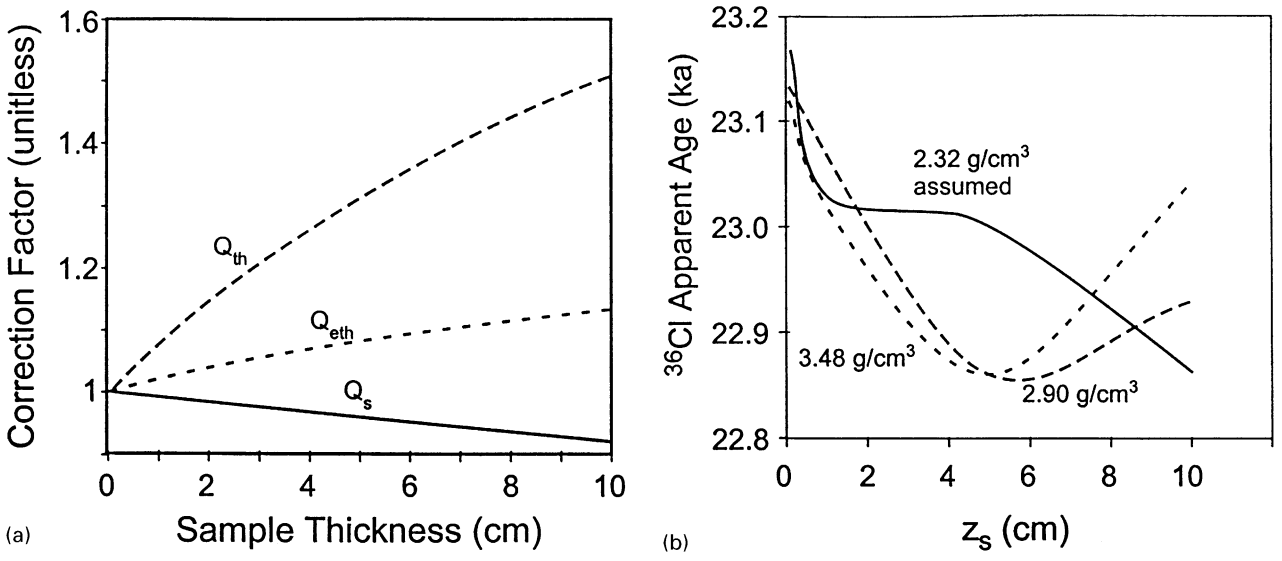


Fig. 18. (a) Variation of sample thickness scaling factor with sample thickness for spallation scaling factor ($Q_s$), thermal neutron scaling factor ($Q_{th}$), and epithermal scaling factor ($Q_{eth}$). Calculations are for an average low-Ca granite (Fabryka-Martin, 1988) with 1% volumetric water content and bulk density of 2.7 g cm$^{-2}$. (b) Variation in apparent age as a function of assumed rock density and sample thickness. Rock was a quartz arenite with actual density of 2.7 g cm$^{-3}$ and actual sample thickness of 5 cm.

absorption, and production from muons) as a function of depth

$$P_{t,m} = S_{el}S_T S_s\left\{J_f \exp\left(-\frac{Z}{\Lambda_{f,e}}\right) + J_{eth}\exp\left(-\frac{Z}{L_{eth,ss}}\right) + J_{th}\exp\left(-\frac{Z}{L_{th,ss}}\right) + J_\mu \exp\left(-\frac{Z}{\Lambda_\mu}\right)\right\}, \quad (3.82)$$

where

$$J_f = \sum_k \Psi_{m,k}(0)C_k + S_{L,eth}(1 - p(E_{th}))_{ss} \times f_{eth}\Lambda_{eth,ss}^{-1}\Phi_{eth,ss}^{*} + S_{L,th}\Lambda_{th,ss}^{-1}\Phi_{th,ss}^{*} \quad (3.83)$$

$$J_{eth} = (F\,\Delta\Phi)_{eth,ss}^{*}[(1 - p(E_{th})_{ss})S_{L,eth} \times f_{eth}\Lambda_{eth,ss}^{-1}(1 + R_\mu R_{eth}) + S_{L,th}f_{th}\Lambda_{th,ss}^{-1}(1 + R'_\mu)] \quad (3.84)$$

$$J_{th} = S_{L,th}(1 + R'_\mu R_{th})(\Im\Delta\Phi)_{th}^{*}\Lambda_{th,ss}^{-1} \quad (3.85)$$

$$J_\mu = S_{L,eth}R_\mu(1 - p(E_{th})_{ss})f_{eth}\Lambda_{eth,ss}^{-1}\Phi_{eth,ss}^{*} + S_{L,th}R'_\mu f_{th}\Lambda_{th,ss}^{-1}\Phi_{th,ss}^{*} + \frac{S_\mu}{S_{el}}\sum_k Y_{\Sigma k,m}\psi_{\mu^-}(0) \quad (3.86)$$

If the land surface is not stable, but rather is eroding at a constant rate, then the sample depth will be a function of time:

$$\frac{dZ}{dt} = -\varepsilon, \quad (3.87)$$

where $\varepsilon$ is the erosion rate (g cm$^{-2}$ yr$^{-1}$). Eq. (3.87) can be integrated to yield

$$Z = Z_0 - \varepsilon t, \quad (3.88)$$

where $Z_0$ is the depth of the sample at the time the sample material was first exposed ($t = 0$).

The dependence of the cosmogenic nuclide concentration in the rock, $N_m$ (atoms g$^{-1}$), on time is given by

$$\frac{dN_m}{dt} = P_{t,m}(Z) - \lambda_m N_m. \quad (3.89)$$

Substituting Eqs. (3.82) and (3.88) into Eq. (3.89) and solving for the initial condition $N_m = 0$ at $t = 0$ yields

$$N_m(Z,t,\varepsilon) = S_{el}S_T S_s\sum_q \frac{J_q}{\varepsilon/(AL)_q + \lambda_m}\left[\exp\left(-\frac{Z_0 - \varepsilon t}{(AL)_q}\right) - \exp\left(-\lambda_m t - \frac{Z_0}{(AL)_q}\right)\right], \quad (3.90)$$

where $q$ refers to the production reaction and $(AL)_q$ to the attenuation length pertaining to it, as follows: $(q,(AL)_q) = (f,\Lambda_{f,e}),(eth,L_{eth,ss}),(th,L_{th,ss}),(\mu,\Lambda_\mu)$.

Frequently cosmogenic nuclide samples (of finite thickness) are collected from the land surface position ($Z = 0$). In this case $Z_0 = \varepsilon t$ and, if the thickness corrections are included, Eq. (3.90) becomes

$$N_m(t,\varepsilon) = S_{el}S_T S_s\sum_q \frac{J_q^Q}{\varepsilon/(AL)_q + \lambda_m} \times\left[1 - \exp\left(-\left(\lambda_m + \frac{\varepsilon}{(AL)_q}\right)t\right)\right], \quad (3.91)$$

where

$$J_f^Q = Q_s\sum_k \Psi_{m,k}(0)C_k + Q_{eth}S_{L,eth}(1 - p(E_{th}))_{ss} \times f_{eth}\Lambda_{eth,ss}^{-1}\Phi_{eth,ss}^{*} + Q_{th}S_{L,th}\Lambda_{th,ss}^{-1}\Phi_{th,ss}^{*} \quad (3.92)$$

$$J^{Q}_{\mathrm{eth}} = (\Im\Delta\Phi)^{*}_{\mathrm{eth,ss}}[Q_{\mathrm{eth}}(1 + R_{\mu}R_{\mathrm{eth}})(1 - p(E_{\mathrm{th}})_{\mathrm{ss}}) \times S_{\mathrm{L,eth}}f_{\mathrm{eth}}\Lambda^{-1}_{\mathrm{eth,ss}}R_{\mathrm{th}} + Q_{\mathrm{th}}S_{\mathrm{L,th}}f_{\mathrm{th}}\Lambda^{-1}_{\mathrm{th,ss}}(1 + R'_{\mu})], \tag{3.93}$$

$$J^{Q}_{\mathrm{th}} = Q_{\mathrm{th}}S_{\mathrm{L,th}}(1 + R'_{\mu}R_{\mathrm{th}})(\Im\Delta\Phi)^{*}_{\mathrm{th,ss}}\Lambda^{-1}_{\mathrm{th,ss}}, \tag{3.94}$$

$$J^{Q}_{\mu} = Q_{\mathrm{eth}}S_{\mathrm{L,eth}}R_{\mu}(1 - p(E_{\mathrm{th}})_{\mathrm{ss}})f_{\mathrm{eth}}\Lambda^{-1}_{\mathrm{eth,ss}}\Phi^{*}_{\mathrm{eth,ss}} + Q_{\mathrm{th}}S_{\mathrm{L,th}}R'_{\mu}f_{\mathrm{th}}\Lambda^{-1}_{\mathrm{th,ss}}\Phi^{*}_{\mathrm{th,ss}} \tag{3.95}$$

Two special cases allow simplification of Eq. (3.91). One is the case where the surface has been exposed for a very long time so that the cosmogenic nuclide profile has reached equilibrium with the erosion rate. In this case the surface nuclide concentration will be given by

$$N_{m}(\varepsilon) = S_{\mathrm{el}}S_{\mathrm{T}}S_{\mathrm{s}}\sum_{q}\frac{J^{Q}_{q}}{\varepsilon/(AL)_{q} + \lambda_{m}}. \tag{3.96}$$

The second is the case where the surface is stable ($\varepsilon = 0$):

$$N_{m}(t) = S_{\mathrm{el}}S_{\mathrm{T}}S_{\mathrm{s}}\lambda_{m}^{-1}\sum_{q}J^{Q}_{q}[1 - \exp(-\lambda_{m}t)]. \tag{3.97}$$

Eqs. (3.96) and (3.97) can be further simplified for several additional special considerations. If the nuclide of interest is produced only by spallation, its abundance as a function of time and erosion will be given by

$$N_{\mathrm{m,s}}(t,\varepsilon) = S_{\mathrm{el}}S_{\mathrm{T}}S_{\mathrm{s}}Q_{\mathrm{s}} \times\left\{\frac{\sum_{k}\Psi_{k,m}(0)C_{k}(1 - \exp(-(\lambda_{m} + \varepsilon\Lambda^{-1}_{\mathrm{f,e}})t))}{\lambda_{m} + \varepsilon\Lambda^{-1}_{\mathrm{f,e}}}\right\}. \tag{3.98}$$

After a time that is large compared to $\lambda_{m} + \varepsilon\Lambda^{-1}_{t,\mathrm{e}}$, Eq. (3.98) will further simplify to

$$N_{m,s}(\varepsilon) = \frac{S_{\mathrm{el}}S_{\mathrm{T}}S_{\mathrm{s}}Q_{\mathrm{s}}P_{\mathrm{s},m}}{\lambda_{m} + \varepsilon\Lambda^{-1}_{t,\mathrm{e}}}, \tag{3.99}$$

where $P_{\mathrm{s},m}$ is the total spallation production rate (usually expressed per unit mass for a particular mineral). This is often refereed to as the "steady-state erosion model" for a spallogenic nuclide. If a large age can be justified and constant erosion assumed, the erosion rate may be directly obtained.

A further simplification of Eq. (3.99) is possible if the cosmogenic nuclide is stable (i.e., the half-life is infinite), since both of the commonly used stable nuclides ($^{3}$He and $^{21}$Ne) are produced by spallation reactions. In this case, Eq. (3.99) reduces to

$$N_{m,s}(t,\varepsilon) = S_{\mathrm{el}}S_{\mathrm{T}}S_{\mathrm{s}}Q_{\mathrm{s}}\Lambda_{t,\mathrm{e}}\varepsilon^{-1}P_{\mathrm{s},m}[1 - \exp(-\varepsilon\Lambda^{-1}_{t,\mathrm{e}}t)]. \tag{3.100}$$

If the surface is also stable, the accumulation rate for a stable cosmogenic nuclide becomes linear with time

$$N_{m,\mathrm{s}}(t) = S_{\mathrm{el}}S_{\mathrm{T}}S_{\mathrm{s}}Q_{\mathrm{s}}P_{m,\mathrm{s}}t. \tag{3.101}$$

In general, applications of single nuclides are limited by the pervasiveness of erosion, inasmuch as both age and erosion rate cannot be obtained by a single nuclide measurement. As discussed above, a spallogenic cosmogenic nuclide concentration (e.g. all except for $^{36}$Cl, see (iv) below) will provide a minimum age estimate of the total exposure duration of a surface that has been eroding.

However, under some circumstances a single nuclide can provide adequate information. Those circumstances include the following:

(i) *Geological evidence of negligible erosion*. In some cases surface textures provide strong evidence that surfaces considered for dating have not suffered significant erosion since the event intended to be dated. Examples include the preservation of glacial polish (Nishiizumi et al., 1989; Clark et al., 1995), fluvially smoothed textures (Burbank et al., 1996), and diagnostic textures on the surfaces of lava flows (Anderson et al., 1994; Cerling, 1990; Phillips et al., 1996b).

(ii) *Reasonable inference of negligible erosion*. The effect of erosion on cosmogenic nuclide accumulation does not depend on the erosion rate, but rather on the total erosion depth. As illustrated in Fig. 19, high rates of erosion have little effect on nuclide concentrations until the exposure time is long enough for significant erosion to have occurred, but relatively low erosion rates can have significant effects on the cosmogenic inventory as secular equilibrium is approached. Significant erosion can be defined as an appreciable fraction of the apparent attenuation length, on the order of 15 or 20 cm rock depth. In many cases, it may be possible to argue that total erosion depths are relatively shallow, even in the

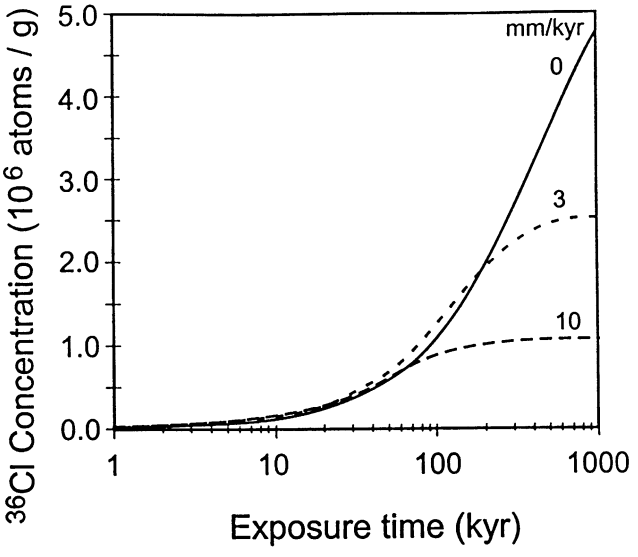


Fig. 19. Chlorine-36 concentration in Fabryka-Martin (1988) average low-Ca granite at sea level and high latitude as a function of surface exposure age and surface erosion rate.

absence of direct evidence such as preserved diagnostic surface textures. A variety of both conventional and cosmogenic nuclide studies on denudation rates (Bierman, 1994; Summerfield and Hulton, 1994; Brown et al., 1995b, 1998b; Bierman and Steig, 1996; Gosse et al., 1997; Fleming et al., 1999; Summerfield et al., 1999) indicates that total bare-rock surface loss rates typically lie in the range of $< 1$ to $20\,\mathrm{mm\,kyr^{-1}}$, except in basins with unusually steep topography or dominated by hillslope processes or areas with incompetent rock. For carefully selected samples that are of relatively resistant lithology, this range is likely reduced to $< 1$–$5\,\mathrm{mm\,kyr^{-1}}$ (Phillips et al., 1997b). Even for erosion rates at the high end of this range, about 30 kyr will be required to effect significant erosion. Reasonable argument can therefore be made that single nuclides and assumptions of negligible erosion are probably generally adequate for surface-exposure dating studies in the late Quaternary age range (provided, of course, that significant inheritance a complex exposure histories can also be considered unlikely).

(iii) *Reasonable inference of great age.* Conversely to the case in (ii) above, in many cases it may be possible to argue that the rock surface being investigated has been exposed for a time that is long compared to the nuclide half-life, and that erosion is relatively incremental and steady. Examples include the famous inselbergs and bornhardts of Australia (Bierman and Turner, 1995), summit flats in mountain ranges of the western United States (Small et al., 1997), and nunataks and surfaces in the dry valleys of Antarctica (Nishiizumi et al., 1991a; Brook et al., 1995a; Bruno et al., 1997; Schaefer et al., 1999). In this case, the cosmogenic nuclide inventory can reasonably be inferred to be in secular equilibrium with the erosion rate, and the erosion rate calculated using Eq. (3.99). In cases where the surface sampled can neither be inferred to be of great age, nor to have had a negligible total depth of erosion, useful chronological estimates can still be obtained by placing reasonable constraints on the rock erosion rates. As discussed above, numerous studies are available to help bound the range of reasonable erosion rates, based on lithology, climate, and topography. Apparent ages can be calculated through this range and the extreme ages selected as chronological references (cf. Phillips et al., 1997b). This approach can provide useful results so long as the erosion rates are not high, nor the surface ages too old.

(iv) It is worthwhile to note that production of $^{36}$Cl by thermal neutron reactions, in addition to spallation reactions, can cause erosion to have effects on surface exposure dating that are markedly different than for spallation alone. In Fig. 20 apparent $^{36}$Cl age is illustrated as a function of assumed erosion rate for different proportions of spallation versus thermal and epithermal neutron production. For the case of spallation production only, apparent ages increase consistently with increasing assumed erosion rate. (As the assumed erosion rate increases, the time-integrated production rate decreases, hence a longer time is required to accumulate the measured amount of the cosmogenic nuclide.) In contrast, thermal neutron production increases with depth, down to about $50\,\mathrm{g\,cm^{-2}}$, and if the low-energy neutron production is sufficiently large the apparent age may decrease for low erosion rates.

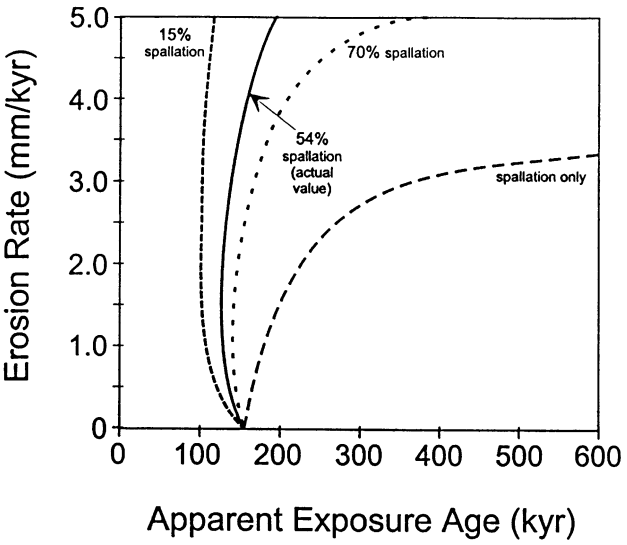


Fig. 20. Variation of apparent surface exposure age with erosion rate for different proportions of spallation and low-energy neutron production. The spallation-only curve would approximate the effects for $^{3}$He, $^{10}$Be, $^{14}$C, $^{21}$Ne, and $^{26}$Al for shallow samples or low erosion rates where muonic contributions were not significant. Hypothetical sample was Fabryka-Martin (1988) average low-Ca granite at sea level and high latitude. Chlorine concentration and $^{36}$Cl concentration were varied to maintain constant zero-erosion age while changing proportions of production reactions. 54% spallation production corresponds to 200 ppm Cl, the actual average value from Fabryka-Martin (1998).

The counteracting trends with depth of spallation and low-energy neutron production can be an advantage in some studies where only a single cosmogenic nuclide is measured. If the rate of change of the high- and low-energy production reactions with depth are approximately equal (as for the 70% spallation case, Fig. 20) then the total production rate will vary little with depth and the apparent age will be relatively insensitive to erosion. On the other hand, if production is strongly dominated by low-energy neutron absorption, the depth-dependence of the production will be even greater than for spallation alone and the apparent age will be very sensitive to erosion (Bierman et al., 1995a).

### 3.9. Exposure dating with multiple nuclides

Under the favorable circumstances listed in Section 3.8 a single nuclide may suffice to define the exposure age or erosion rate of a surface (see Gillespie and Bierman (1995) for discussion of precision). If an upper limit on erosion rate can be specified, a range of possible exposure ages can be determined. However, in the general case, the observed cosmogenic nuclide concentration in a sample will be a function of at least two independent variables, exposure age and erosion rate, and in order to uniquely determine both of them the concentrations of at least two nuclides must be measured. For example, a nuclide with the shorter half life such as $^{14}$C (Lifton et al., submitted) provides an estimate for the erosion rate of the surface because it reaches secular equilibrium (saturation) in about 25 kyr (even earlier for higher erosion rates). We must assume that the erosion rate was constant, continuous, and gradual (reasoning discussed below). Once the shorter half-life has been used to constrain the erosion rate $\varepsilon$, a stable nuclide (or a radionuclide with long half-life, e.g. $^{10}$Be, Fig. 21) can be used to determine the exposure age of the surface by compensating for any effects of erosion. Explicitly, Eq. (3.91) can be used to solve for exposure time as a function of $\varepsilon$.

In the absence of an isotope system that has reached equilibrium with erosion ($^{14}$C is not yet routinely measured in quartz), two nuclides can still be used to estimate total exposure duration, minimum total duration of burial, erosion rate, and style of erosion. Based on Eq. (3.91), the variation of the ratio of two spallation-produced radionuclides, $m$ and $n$, with time will be given by

$$R_{mn}(t) = \frac{N_m(t)}{N_n(t)} = \frac{P_m(0)(\lambda_n + \varepsilon/\Lambda_{f,e})\{1 - \exp[1 - \exp(-\lambda_m + \varepsilon/\Lambda_{f,e})t]\}}{P_n(0)(\lambda_m + \varepsilon/\Lambda_{f,e})\{1 - \exp[1 - \exp(-\lambda_n + \varepsilon/\Lambda_{f,e})t]\}}. \quad (3.102)$$

Note that the expressions for the two nuclides differ only in the half-life and production terms, and thus in order to be used for this purpose the two nuclides must exhibit some significant difference in either half-life or production profile (e.g., the ratio of two stable, spallogenic, noble gas nuclides will not vary with erosion rate or time).

The two-nuclide approach was first proposed by Lal and Arnold (1985). They proposed application of the $^{26}$Al/$^{10}$Be pair, since both can be readily measured in a single mineral separate (e.g. quartz), both have similar geochemical behavior, and they have half-lives that differ by a factor of two (Fig. 22a). The ratio $^{26}$Al/$^{10}$Be is customarily plotted against the log of measured $^{10}$Be concentration (scaled to production at sea level and high latitude) to evaluate age and erosion effects (Fig. 22b).

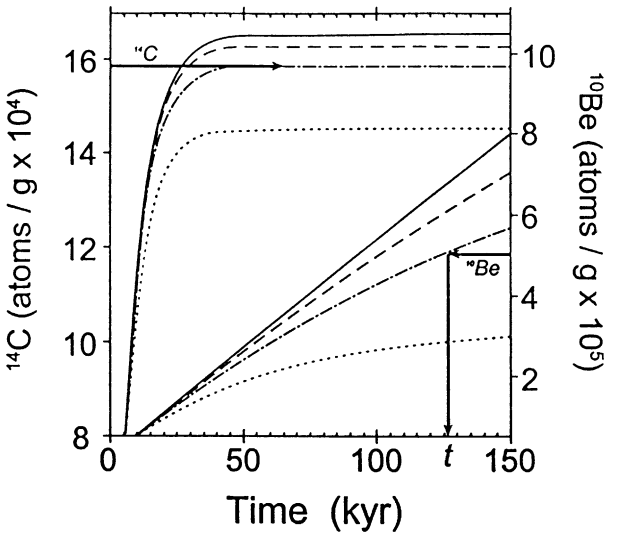


Fig. 21. Why use two isotopes? A single TCN measurement will at best provide a minimum estimate of an exposure age, because in most cases erosion reduces the concentration. After 30 kyr of exposure, in situ $^{14}$C at sea level high latitude ($P_{14C(Zo)} = 20$ atoms g$^{-1}$ yr$^{-1}$) is within 97% of the secular equilibrium concentration ($1.65 \times 10^5$ atoms g$^{-1}$, at $\varepsilon = 0$ mm k yr$^{-1}$). For higher erosion rates ($\varepsilon = 1$, 3, and 10 mm k yr$^{-1}$) the $^{14}$C saturation concentration is lower (respectively illustrated as long dash, dash-dot, and dot) and equilibrium is attained earlier. On a surface known to predate the last glacial maximum, a measurement of 'C' $= 1.59 \times 10^5$ atoms g$^{-1}$ would indicate that the erosion rate of the surface was 3 mm kyr$^{-1}$. Once the erosion rate is known it is possible to use a stable or longer-lived isotope (which has not reached saturation) to determine the actual exposure age. In this example, the measured concentration of $^{10}$Be ($P_{10Be(Zo)} = 5.5$ atoms g$^{-1}$ yr$^{-1}$) is 'Be' $= 5.05 \times 10^5$ atoms g$^{-1}$, which at $\varepsilon = 3$ mm kyr$^{-1}$ corresponds to an exposure age of 127 kyr (assuming ideal conditions as described in text).

Other spallogenic nuclides with sufficient half-life differences can be used, and we describe below the additional advantages of using the ratio of a thermal-neutron-derived nuclide with a spallogenic one.

The exposure/erosion history of a sample can be inferred from the position relative to the "steady-state erosion island" (Lal, 1991), as described in the caption of Fig. 23. This approach was first implemented by Klein et al. (1986b) and its advantages have been well illustrated, among others, by the work of Nishiizumi et al. (1991a) on glacially exposed rocks in Antarctica. A sample can plot in four fields (Fig. 22b) which yield different information about the age, erosion style and rate, and or history of surface burial.

(i) Samples with $^{26}$Al/$^{10}$Be greater than the initial production ratio (plot above the steady-state erosion island) cannot be explained by any combination of erosion, burial, exposure, or inheritance, and thus indicate sample preparation or measurement problems. (Another possible, although unlikely, explanation is nucleogenic production of both species.) Most existing studies in which the $^{26}$Al/$^{10}$Be was measured

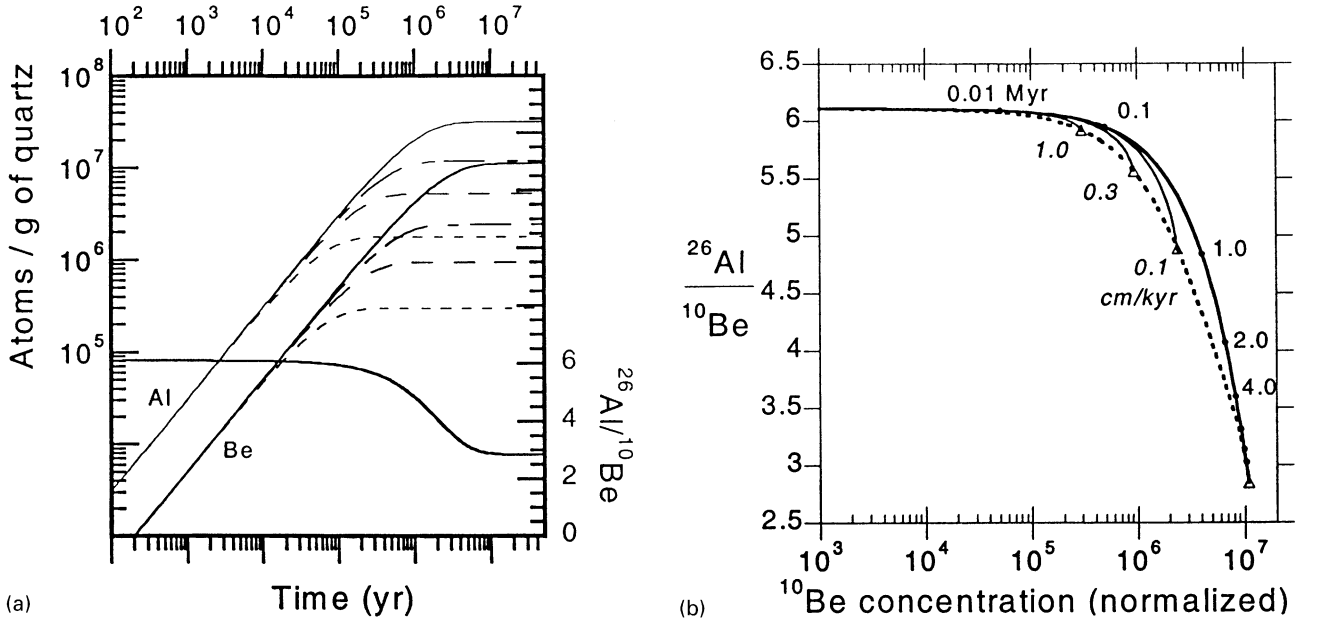


Fig. 22. TCN ratio diagram for $^{26}$Al and $^{10}$Be. (a) Production curves for $^{26}$Al ($P_{26\text{Al(Zo)}} = 33.6$ atoms g$^{-1}$ yr$^{-1}$) and $^{10}$Be ($P_{10\text{Be(Zo)}} = 5.5$ atoms g$^{-1}$ yr$^{-1}$), with production ratio of 6.1 (these production rates will vary with sites above sea level or $\lambda_m < 60°$). Additional curves for erosion rates of $\varepsilon = 1$, 3, and 10 mm kyr$^{-1}$ as in Fig. 21. The change in $^{26}$Al/$^{10}$Be also shown for $\varepsilon = 0$, 1, 3 and 10 mm kyr$^{-1}$. (b) As in (a), $^{26}$Al/$^{10}$Be shown for $\varepsilon = 0$, 1, 3, and 10 mm kyr$^{-1}$, but plotted (traditionally) against log $^{10}$Be concentration (normalized for production at sea level and high latitude). Samples with ratios plotting on the upper curve can be interpreted at have no erosion, and total exposure duration corresponds to distance along the $\varepsilon = 0$ ratio curve. Samples plotting on or between erosion curves have experienced the modeled erosion rate (assumed continuous, constant, and gradual), and the total exposure time corresponds to the distance along the erosion trajectory.

in a continuously exposed surface with negligible erosion simply assume that the initial production ratio is about 6.1. However, more reliable determinations of the production ratios of these and other isotopes are urgently needed (see Section 7 and Bierman et al., 1999). Although the ratios cannot plot above the production curve, a ratio can plot to the right of the curve if the assumed production rate (at its present location) is lower than the actual production rate that the surface recorded (e.g. in the case of subsidence or movement downslope).

(ii) Samples which plot on the production ratio curve probably have never been buried or eroded during the current exposure duration, and inheritance from an earlier exposure is unlikely. The distance along the production ratio curve corresponds to the exposure age of the sample. The $^{10}$Be or $^{26}$Al concentration can be interpreted directly as an exposure age. Both isotopes will yield the same exposure age.

(iii) Samples plotting within the steady-state erosion island have traditionally been interpreted to represent some combination of erosion and exposure. A unique production ratio curve for a constant, gradual, and continuous erosion rate can be fit through the sample, so the sample's erosion rate and age (distance along that erosion curve) can be calculated simultaneously. If the two nuclides were interpreted as ages separately, the shorter half-lived isotope will yield a younger age, and the disparity increases with exposure duration.

(iv) Samples plotting below the steady-state erosion island (under the curve that connects all of the end points of the erosion production ratio curves) have traditionally been interpreted as indicating that the exposure of the surface was interrupted by a shielding event (e.g. Granger et al., 1997; Bierman et al., 1999) (Fig. 23a). When a surface is completely or partially buried (e.g. by snow, sediment, glaciers, or water), the ratio will change due to the differences in the radioactive decay rates of the two isotopes. If the longer-lived or stable isotope is the denominator, the ratio will decrease during burial. Graphically, the pathway of the buried sample is vertical if the TCN denominator is stable, or slightly toward the origin if the TCN denominator is radioactive. The length of the path (or the distance below the steady-state erosion island) is proportional to the burial duration. Once the burial period is complete and the surface becomes exposed again, the ratio will increase (on a exponential pathway toward the production ratio curve). Therefore, ratios plotting below the island have been interpreted to have undergone complicated exposure histories, where the surface was shielded from cosmic rays at least once.

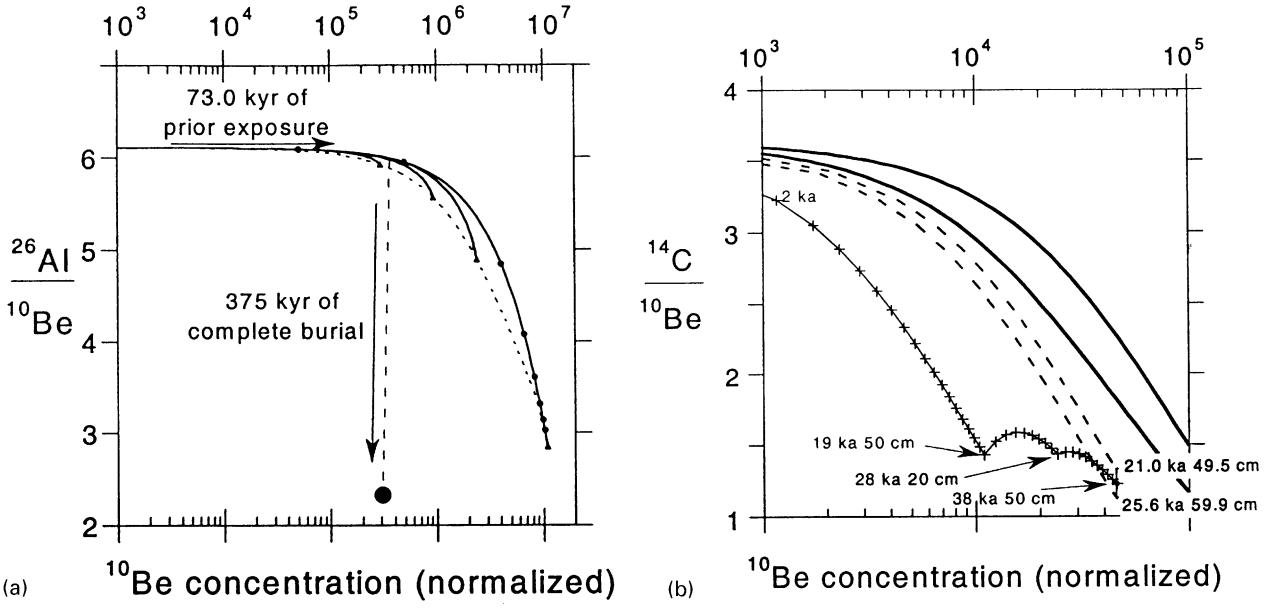


Fig. 23. TCN ratio diagrams. (a) $^{26}Al/^{10}Be$, as in Fig. 22b. Samples plotting below the steady state erosion island must have had experienced complicated exposure history (partial or complete shielding or plucking). The measured ratio could be explained by an infinite number of trajectories involving exposure, subaerial erosion, burial, or plucking. An example of complete shielding is given. If geological observations can decipher which surficial processes are likely, then the pathways illustrated can provide constraints on the minimum exposure age, minimum complete burial duration, and average plucking depth. Low ratios in allochthonous sediment also implies inheritance, so multiple nuclides are useful in depth profile studies. (b) $^{14}C/^{10}Be$ plot showing how the ratio behaves in the case of cliff retreat by block falls (i.e. erosion, not burial, caused the low ratios). If a cliff face was episodically retreating over the last 40 kyr, the ratios at any given time for the final surface are shown by the lowest curve ( + ). In this scenario, the cliff was exposed for 19 ka, then a 50 cm thick block fell, then the cliff was exposed for another 9 ka, then a 20 ka block fell, then another 10 ka, and finally another 50 cm block fell very recently (e.g. the block can be seen below the cliff, and the surface is very fresh). The average erosion rate is 120 cm over 38 kyr or $\varepsilon = 3.16\,cm\,kyr^{-1}$. In reality, we do not know this retreat history of the cliff. We can, however, provide an estimate of the minimum possible erosion rate to achieve the measured ratio. The dashed curves are calculated for the scenario that the cliff only underwent one block fall just before the sample was collected. The curves therefore provide the minimum possible erosion rate that could explain the measured ratio (considering $1\sigma$ uncertainty = 8%, AMS and ICP.OES measurements only, see Sections 6.1). In this case, the dashed curves bracket the minimum average erosion, $\varepsilon = 2.33–2.36\,cm\,kyr^{-1}$.

From the buried sample alone, there is no way to determine how many episodes of burial or the total duration of burial that a surface may have experienced, and without independent information there is no way to determine how long a surface was exposed since burial (e.g. Bierman et al., 1999). However, where a bracketing age can provide useful insight, estimates of the minimum exposure duration and minimum burial duration can be inversely modeled. The minimum exposure duration is determined by first assuming that the surface became instantaneously uncovered seconds before it was sampled. (If the actual post-emergence exposure duration is known independently, it could be modeled so that the ratio is returned (lowered) to the pre-exhumation value (Gosse et al., 1993; Granger et al., 1996)). The distance along the burial pathway corresponds to the minimum burial duration, and the distance along the zero-erosion production curve to the intersection with the burial pathway is the minimum duration of exposure before the single burial event. The three durations combined (pre-exposure, burial duration, and post-emergence exposure) provide the minimum total exposure duration.

There is a variant interpretation of ratios which plot below the island. The traditional interpretation described above considers that an unattached material is covering the surface, such as a glacier over a bedrock surface. A ratio will also plot below the steady-state erosion island if the surface has experienced episodic erosion in which thick layers of material are removed rapidly, such as during subglacial plucking or block erosion of a retreating vertical cliff face. For instance, a surface on a high tor that has recently lost a thick cap (say 60 cm) due to frost shattering or mass wasting will have a ratio that plots below a steady-state erosion island. With the exception of Macciaroli et al. (1994) and Gosse et al. (1995b), this possibility has not been widely considered, and may have resulted in misinterpretations of TCN ratios in glaciated regions. The distance that the zero-erosion production curve is displaced to the left is proportional to the thickness of the block removed (Fig. 23b). In this sense, we can use the ratio of two isotopes to help constrain the style and maximum rate of erosion on a surface that was not likely buried by another material (other than self-shielding).

Unfortunately, considering the uncertainty in the measurements involved and the non-unique causes for changes in the ratios, it is easy to make interpretations of multiple TCN measurements that are misleading, incomplete, or constitute over-interpretation. Here are some caveats to keep in mind when interpreting multiple ratios:

1. Analytical uncertainties are greatly enhanced when ratios of nuclides are considered. For example, even for optimal analyses the uncertainty is generally at least 7% for the $^{26}Al/^{10}Be$ ratio ($1\sigma$ ICP.AES and AMS experimental uncertainties only) (cf. Granger et al., 1996). Because of the shape of the island, this uncertainty will have significant implications for younger samples ($< 10^6$ kyr) because the $1\sigma$ range will cross a wider range of erosion production ratio curves and therefore a scenario of zero erosion cannot be distinguished from a scenario of very high erosion. On the other hand, samples with longer exposure durations ($> 10^6$ kyr) that plot along the subvertical portion of the production ratio curve will have $1\sigma$ uncertainties which cross only very low erosion rate production ratio curves. It is therefore important to minimize the consequences of measurement uncertainties and optimize the resolution of the erosion curves by selecting isotope pairs that provide the shape of island that is optimal for the specific study at hand. See below for the utility of using isotopic ratios that do not have the same production mechanisms.

2. The interpretation of low isotopic ratios (long-lived or stable denominator) is non-unique (multiple burial and exposure events are possible) and ambiguous — low ratios could be due to either burial or episodic rapid erosion unless there is an independent means to indicate burial (striae or till indicates at least partial shielding by ice) or lack of shielding (e.g., on top of a pedestal in a non-glaciated region, or on a high vertical face). In glaciated terrains, it will be difficult to resolve whether the resulting low ratio is due to ice shielding, plucking, or some combination of both. Depending on the question being addressed, in many cases it may not matter which process caused the low ratio. For example, Gosse et al. (1995b) argued that both plucking and shielding require that a glacier was present in a controversial area where geomorphic and biologic evidence has been adduced for the complete absence of any late Quaternary ice cover.

Although this approach to elucidating geomorphic histories of samples has proved to be powerful, it is limited by the precision of the nuclide analyses. The typical analytical uncertainty in the $^{26}Al/^{10}Be$ ratio is similar to the height of the steady-state erosion island, offering limited resolution of the erosion/exposure parameters. The narrow shape of the island is determined by the magnitude of the difference in half-lives, since $^{26}Al$ and $^{10}Be$ share the same spallogenic production profile. Liu et al. (1994) suggested that the resolution of the approach could be improved by combining a spallogenic nuclide with one that is also produced by thermal neutron absorption. The difference in production profiles for the high- and low-energy reactions will accentuate the difference in behavior on the plot.

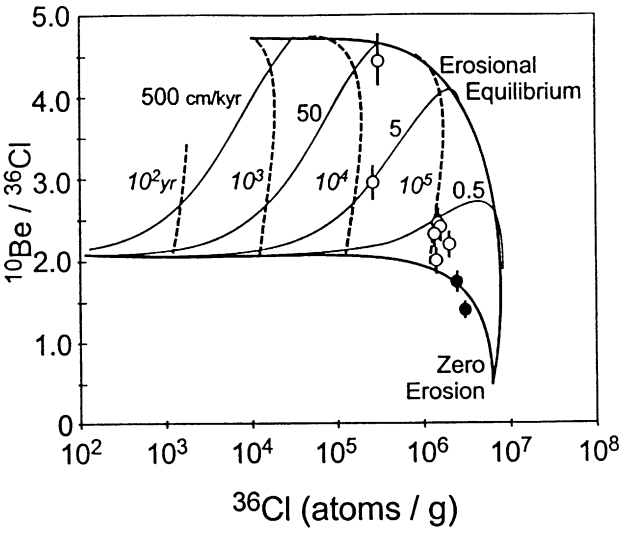


Fig. 24. Ratio diagram, $^{36}Cl/^{10}Be$ vs. $^{36}Cl$ (log concentration, normalized, as in previous figures) for boulder samples from moraines in the Wind River Range, Wyoming (from Phillips et al.,1997). Position of samples indicates generally very low erosion rates for boulder surfaces.

This effect is illustrated using $^{36}Cl$ and $^{10}Be$ data from boulders on moraines in the Wind River Range, Wyoming, from Phillips et al. (1997b) (Fig. 24). Due to the component of thermal neutron production in these samples (approximately 50%), the width of the erosion island is greatly increased, relative to the analytical accuracy of the ratio. The position of most of the data pairs on the plot indicates that surface erosion rates are very low.

In principle, it should be possible to tailor nuclide pairs for various specific applications. For example, the combination of $^{21}Ne$ and $^{10}Be$ should be very suitable to determining both the exposure age and erosion rate of very old ($> 1$ Ma) surfaces. However, the same pair would prove less informative for surfaces younger than 300 kyr because there would be insufficient time for decay of the $^{10}Be$ and thus the sensitivity to erosion would be low. Here, the $^{10}Be/^{36}Cl$ pair would prove more effective. For young surfaces ($< 100$ kyr), $^{14}C$ paired with a longer-lived nuclide would be optimal. Furthermore, such paired applications need not even involve two different nuclides. If one nuclide is produced by both spallation and low-energy neutron reactions, as is $^{36}Cl$, then mineral separates in which one or the other reaction predominates (e.g., a potassium feldspar separate in which spallation production off potassium predominates, paired with a quartz separate in which thermal neutron production from $^{35}Cl$ predominates) can be used in a similar fashion (Vogt et al., 1996). The main advantage of this approach is that it can greatly simplify the sample preparation and analysis.

### 3.10. Nuclide-specific considerations

The selection of the appropriate nuclide is controlled by the estimated exposure duration of the surface being investigated, the elevation of the surface, and the nature of the study. Conversely, the choice of lithologies can restrict the nuclides used.

The effective ranges of the various TCN depend on their half-lives and production rates, and spectrometry detection limits. If a surface has been continually exposed and negligibly eroded, it is possible to date pre-Quaternary landforms with stable and long-lived TCN ($^{3}$He, $^{10}$Be, $^{21}$Ne, $^{26}$Al). For instance, well-preserved rock surfaces in the Dry Valleys of Antarctica have yielded minimum exposure dates of $> 2.0$ Myr, with erosion rates of $< 1\,\mathrm{mm}^{-1}\,\mathrm{kyr}$ (Brown et al., 1991; Nishiizumi et al., 1991a; Brook et al., 1993, 1995a; Ivy-Ochs et al., 1995; Schaefer et al., 1999), although these ages may have considerable uncertainty due to an Antarctic atmosphere anomaly (Stone, in press). Rock surfaces in other climate regimes may undergo higher erosion rates, so the upper limit is truly geomorphic process. The shorter-lived nuclides $^{14}$C and $^{36}$Cl will reach saturation after 20 kyr and 1 Myr, respectively, so can provide minimum age estimates and valuable information regarding erosion (Sections 3.8 and 3.9).

The lower limit of exposure dating is controlled mainly by the combination of production rate and analytical detection limit (i.e. it is a function of nuclide and site location). For instance, $^{3}$He is ideal for dating young lavas because it has the highest relative production rate ($P_3 \sim 116\,\mathrm{atoms\,g^{-1}}$ olivine $\mathrm{yr^{-1}}$) and nucleogenic $^{3}$He has not become significant (Kurz, 1986a; Cerling and Craig, 1994a). Even $^{10}$Be ($P_{10\mathrm{Be,s.l.}} \sim 6\,\mathrm{atoms\,g^{-1}}$ quartz $\mathrm{yr^{-1}}$) has been used successfully to date late Holocene cirque moraines (Gosse, 1994) at high elevations ($P_{10}$ at 3500 m $\sim 60\,\mathrm{atoms\,g^{-1}}$ quartz $\mathrm{yr^{-1}}$). Shorter-lived TCN such as $^{14}$C and $^{36}$Cl will also have a shorter retention of inherited concentrations which may be advantageous for rocks expected to have been previously exposed.

#### 3.10.1. Helium-3

The selection of the $^{3}$He method over others requires two considerations: (i) like $^{21}$Ne, it can have a significant magmatic component that is contained mostly within melt and fluid inclusions; and (ii) because it is a gas, it can diffuse out of the target mineral. The (non-cosmogenic) magmatic (or trapped) $^{3}$He can either be primordial or from nucleogenic or radiogenic production after crystallization. Non-cosmogenic $^{3}$He may be produced from beta decay of $^{3}$H; indirectly from $\alpha$-induced n- and p-interactions (particularly radiogenic thermal neutrons on $^{6}$Li) and low-energy $\alpha$-particles on $^{11}$B (Morrison and Pine, 1955; Lal, 1987b, 1988); from primordial $^{3}$He (Craig and Poreda, 1986; Kurz, 1986a; Lal, 1987b; Cerling and Craig, 1994a); and atmospheric $^{3}$He. The magmatic component can be identified by analyzing the He isotopic composition of gas released upon crushing and during step heating (the inherited magmatic component, predominantly in melt and fluid inclusions, should be released first, whereas the cosmogenic $^{3}$He is mostly held inside the olivine lattice). The inherited $^{3}\mathrm{He}_{\mathrm{inh}}$ component is determined (Kurz, 1986a, b) using the $^{3}$He/$^{4}$He released during crushing, and the total $^{4}\mathrm{He}_{\mathrm{T}}$ measured:

$$^{3}\mathrm{He}_{\mathrm{inh}} = {}^{4}\mathrm{He}_{\mathrm{T}}\left(\frac{^{3}\mathrm{He}}{^{4}\mathrm{He}}\right)_{\mathrm{crushed}}. \tag{3.103}$$

Additional non-magmatic nucleogenic or radiogenic $^{3}$He accumulates in the olivine after crystallization. This will be important for old lavas with recent exposure ages, because the non-cosmogenic $^{3}$He will overwhelm the cosmogenic $^{3}$He. By measuring $^{3}$He in the same rock but at completely shielded depths it is possible to evaluate this difficulty (Cerling, 1990). The method clearly works best on rocks with young crystallization ages.

Retention of $^{3}$He is a more serious problem. Helium-3 is quantitatively retained in olivine, pyroxene, and diamond (Kurz, 1986a, b; Lal, 1987b; Lal et al., 1989; Cerling, 1990). Retention of $^{3}$He in quartz is poor when ambient temperatures are elevated (Cerling, 1990; Trull et al., 1991) and grain sizes are fine, although success at using $^{3}$He in cold regions has been reported (e.g. Brook and Kurz, 1993).

#### 3.10.2. Beryllium-10

In the last five years especially, cosmogenic $^{10}$Be has been used in a wider number of applications than any other TCN. This is partly due to the relatively well-constrained production rates (only $^{3}$He is better constrained) and partly due to the ability to measure $^{26}$Al in the same sample. (Although $^{26}$Al can provide a valuable internal check on the $^{10}$Be measurement, see above (Section 3.9) for a discussion on the perceived use of the $^{26}$Al/$^{10}$Be method). In situ production systematics have been discussed throughout Section 3. The most important of the non-cosmogenic (nucleogenic) $^{10}$Be reactions is from low-energy $\alpha$-particle interactions with $^{7}$Li. However, except in materials containing unusually high concentrations of Li, U, and Th, the nucleonic production rates are generally too low to produce significant background concentrations (Brown et al., 1991). Cosmogenic $^{10}$Be is abundantly produced in the atmosphere by spallation of oxygen and nitrogen and thence deposited on the land surface or in marine sediments (Brown et al., 1989, 1992b). Meteoric $^{10}$Be derived from recycling of marine sediment through subduction zones may be found in some island-arc volcanic rocks at significant levels (Brown et al., 1982; Morris, 1991). Meteoric $^{10}$Be can also infiltrate even dense rocks and adsorbs strongly to the surfaces of mineral grains. During sample preparation, mineral separates must undergo rigorous,

repeated partial dissolutions in HF in order to remove this meteoric component, which is often much larger than the cosmogenic component (Kohl and Nishiizumi, 1992; Klein et al., 1997). Stepped leaching experiments have been conducted to determine the amount of leaching required to remove the atmospheric $^{10}$Be (Brown et al., 1991; Kohl and Nishiizumi, 1992).

Attempts have been made to measure in situ $^{10}$Be in whole rock, or mineral phases other than quartz and olivine for $^{10}$Be measurement, but the results have not been encouraging. Klein et al. (1997) showed with incremental leaching of whole rock that granites, dissolved to the extent that more than 35% of the original mass was lost, still contained more than 3 times the concentration of $^{10}$Be measured in thoroughly treated pure quartz from the same rocks. Even after 90% leaching, the concentration of one rock never stabilized (a plateau was seldom obtained in whole rock basalts or tuffs, although based on comparative ages rocks with a significant desert varnish coating contained less meteoric $^{10}$Be). This experiment indicated that unless there is significant varnish cover that protects rocks susceptible to weathering, many felsic and mafic rocks can never be sufficiently cleaned of atmospheric $^{10}$Be. Ivy-Ochs et al. (1998) attempted to isolate in situ $^{10}$Be from pyroxene, but were unable to reliably remove the meteoric component. At least three non-quartz phases have been analyzed: olivine (Nishiizumi et al., 1990; Kong et al., 1999), one known instance of $^{10}$Be in feldspar (Graham, R., pers. comm.), and magnetite (Lal, D., pers. comm.).

### 3.10.3. Carbon-14

The ability to precisely extract in situ $^{14}$C from minerals has only recently been demonstrated (Handwerger et al., 1999; Lifton et al., submitted) although extraction from ice was made earlier (Jull et al., 1994b). In addition to the previously discussed in situ cosmogenic production, nucleogenic $^{14}$C can be produced from radiogenic neutrons interacting with $^{14}$Ni and $^{17}$O in rocks and from radiogenic $\alpha$-particles on $^{11}$B (Barker et al., 1985; Lal, 1987a), and radiogenic $^{14}$C has been detected from the $^{238}$U decay series (Barker et al., 1985). Nucleogenic production in rock, and hence subsurface background, of $^{14}$C is generally very low. However, $^{14}$C is produced at a very high rate in the atmosphere from neutron absorption by nitrogen (Libby et al., 1949). This meteoric $^{14}$C has proved very difficult to reliably isolate from mineral samples and this problem had inhibited routine measurement of in situ $^{14}$C (cf. Jull et al., 1994a). Much of this contaminating meteoric $^{14}$C may be introduced during sample processing, rather than contained within the sample. Initial applications of $^{14}$C were done in whole rock samples from lava (Section 3.6.3) but due to chemistry and production rate considerations, ongoing development of this method is focused on quartz (Lifton et al., submitted) and carbonate rocks (Handwerger et al., 1999).

Because of its short half-life, the use of in situ $^{14}$C decays quickly and therefore attains saturation faster than the other TCNs. This renders it useful to characterize average erosion rates for the short term, and offers the ability to effectively use TCN ratios for short exposure histories (Section 3.9).

### 3.10.4. Neon-21

The in situ cosmogenic $^{21}$Ne production has been discussed earlier (Sections 3.3.1 and 3.6.4). Its uses are similar to the other noble gas $^{3}$He, but its relatively lower diffusivity in quartz provides a significant advantage. When electing the use of $^{21}$Ne, its three non-cosmogenic sources should be considered: a component from the atmosphere and undegassed mantle (Niedermann et al., 1993; Sarda et al., 1993; Phillips et al., 1998); a primordial MORB-like component (Staudacher and Allégre, 1991, 1993; Niedermann et al., 1993; Sarda et al., 1993); and nucleogenic reactions on oxygen, sodium, and magnesium, especially in minerals with high U concentrations. Like $^{3}$He, even at common levels of U and Th concentration, sufficient nucleogenic $^{21}$Ne can accumulate over periods of millions of years to create major background problems in relatively old rocks even with short exposure histories (Niedermann et al., 1993, 1994). Neon-21 is therefore best suited for application to relatively young volcanic rocks, which have not had time to accumulate large amounts of nucleogenic $^{21}$Ne (e.g. Poreda and Cerling, 1992), or in rocks with very low U and Th concentrations, such as ultramafic volcanics (Staudacher and Allégre, 1991). Neon-21 does not appear to share with $^{3}$He the problem of rapid diffusive loss from most minerals and $^{21}$Ne is retained well by quartz (cf. Phillips et al., 1998). It also has the advantage that ratios of the three isotopes measured on sequential-heating steps can be combined on a single plot to help separate cosmogenic $^{21}$Ne from the non-cosmogenic contributions (Graf et al., 1991; Niedermann et al., 1994).

### 3.10.5. Aluminum-26

The major sample-related problem with $^{26}$Al is the stable element background. Aluminum has only one stable isotope ($^{27}$Al) which is abundant in most types of rock, swamping the $^{27}$Al/$^{26}$Al ratio to unmeasurably low levels unless the $^{27}$Al can be separated from virtually Al-free mineral separates. In situ $^{26}$Al is typically measured in tandem with $^{10}$Be in quartz because of the high native Al content in most other common silicates except olivine (Kong et al., 1999). Aluminum-26 has appreciably higher typical nucleogenic production rates than $^{10}$Be, especially due to reactions on sodium (Sharma and Middleton, 1989). This may create background problems for young (in terms of surface exposure age) samples with high U and Th. In contrast, meteoric $^{26}$Al production rates are quite low, due to lack of target elements in the atmosphere, and $^{26}$Al thus does not share the severe

potential meteoric contamination problem of $^{10}$Be. This may make it the isotope of choice for measurements in quartz of very young exposure ages or deep rocks.

### 3.10.6. Chlorine-36

Chlorine-36 is produced at moderate levels by nucleogenic neutron absorption by $^{35}$Cl, and also from $\alpha$-particle interaction with $^{33}$S and from nucleogenic neutrons with $^{39}$K (e.g., Bierman et al., 1995a; Fabryka-Martin, 1988). Cosmogenic production rates are much higher than other TCN (except $^{3}$He), so background levels are usually a problem only for very young samples. Nucleogenic $^{36}$Cl should routinely be accounted for in calculation of surface exposure ages, and the approach of Fabryka-Martin (1988) is usually followed for this purpose. Chlorine-36 is also abundantly produced in the atmosphere by spallation on argon. Fortunately, such meteoric $^{36}$Cl is strongly hydrophilic and can be removed from rock samples by simple grinding and water leaching (Zreda et al., 1991). This hydrophilic nature may possibly create problems by mobilizing $^{36}$Cl during weathering. No evidence of such mobilization has been found (Zreda et al., 1994), but further systematic investigation would be desirable.

## 3.11. TCN dating of sediment

A rapidly increasing number of studies are being published on use of TCN as a means of "calibrating" geomorphic process studies (e.g. Burbank et al., 1996; Small et al., 1997; Fleming et al., 1999). In many cases, the measurements are being made on sediments, not bedrock surfaces. These include application to geomorphic redistribution within soils (Anderson et al., 1996; Repka et al., 1997), relationships between rates of soil formation and morphology of landscapes (Heimsath et al., 1997, 1999; Small et al., 1999), rates of landscape denudation and quantification of erosion and deposition within drainage basins (Brown et al., 1995b, 1998b; Granger et al., 1996), and ages of fans, terraces, and beach sediment (Gosse, 1994; Bierman et al., 1995b; Trull et al., 1995; Siame et al., 1997; Ayarbe et al., 1998; Brown et al., 1998a; Gosse et al., 1998; Hancock et al., 1999). The work by Granger et al. (1997) using multiple nuclides in cave sediment to determine the duration that the sediment became shielded from cosmic rays ('burial age') was discussed in Section 3.9.

There has been a growing trend since the early-1990s to use TCN to date alluvial deposits and other allochthonous landforms. Originally there were two fascinations that drove this application. (1) Fluvial and glaciofluvial records in alpine environments older than the limits of radiocarbon dating lack anything but relative chronology with the rare exception of U-series travertine ages, luminescence dates on samples that were not completely reset, or some tenuous relationship with ash of known age (Gosse, 1994; Klein et al., 1995; Anderson et al., 1996; Repka et al., 1997; Hancock et al., 1999; Zentmire et al., 1999). (2) Alluvial fans in semiarid and arid environments are too dry for radiocarbon-datable material and too coarse for routine application of many other methods (Bierman et al., 1995b; Trull et al., 1995; Siame et al., 1997; Ayarbe et al., 1998; Brown et al., 1998a; Phillips et al., 1998). Since then, TCN experiments on hillslope deposits (Kubik et al., 1998; Small et al., 1999), beach sediments (Trull et al., 1995; Gosse et al., 1998) and soils (Heimsath et al., 1997, 1999) have been interpreted to have variable success. It has been demonstrated that desert pavement clasts provide exposure ages that are statistically similar to independent estimates of the landform age (see noteworthy paper by Wells et al. (1995), in which pavements on lava flows yielded ages similar to the Ar/Ar age of the lava flow). Moraines are also allochthonous landforms, but because they typically show little inheritance, and because large boulders are not subject to mixing processes (see discussion below), they are in practice more similar to bedrock outcrops.

Exposure models for *surface* clasts on depositional landforms are similar to models for bedrock surfaces if the sediment has not been vertically mixed. However, TCN measured in undisturbed *subsurface* sediments provide much more information about the exposure history of the sediments and can significantly improve the accuracy of the sediment chronology by minimizing the effects of surface processes (turbation, overturning, clast erosion) and inheritance. Gosse (1994) and Klein et al. (1995) used one or two subsurface samples composed of one to ten cobbles to date glacial outwash in the Wind River Range. Ages for the oldest terrace (Sacagewea Ridge Glaciation) were concordant with the exposure age of the Sacagewea Ridge moraine. However, a large concentration was inherited from previous exposure and resulted in ages that were too old for the ultimate (Pinedale) glaciation. Anderson et al. (1996) proposed a means of using more than two subsurface samples: concentration-depth profiles. Later they (Repka et al., 1997) showed numerically that at least 20 clasts per sample were needed to reduce the effects of inheritance.

Concentration-depth profiles are based on the predictable decrease in TCN concentration with depth due to attenuation of secondary fast and thermal neutrons. Muogenic production has been ignored unless depths approach about 800 g cm$^{-2}$ where muogenic production begins to dominate (Kim et al., 1999). The concentrations can be modeled to show the individual or combined influence of erosion, burial, hiatuses in sedimentation, changes in bulk density over time and depth (Fig. 25), and other factors for any Quaternary deposit (terraces, fans, beaches, colluvium, moraine). Curves can also be fit to more complicated profile models involving thermal neutron and muon production (Fig. 2a and b) (Ayarbe et al., 1998).

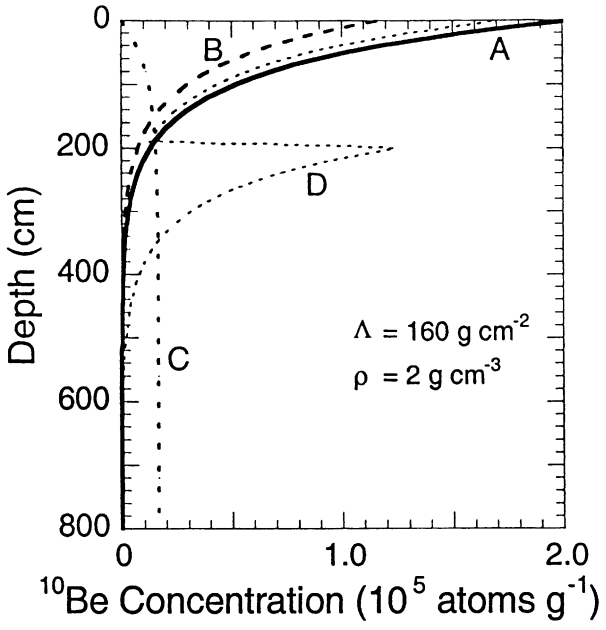


Fig. 25. Depth profiles for spallogenic $^{10}$Be showing the model concentration for exposure scenarios described in the text.

Accompanied with detailed interpretation of the soils and sediment stratigraphy, the concentration-depth profile method is a powerful means documenting the depositional history of an allochthonous landform (Fig. 25). Curve A (Fig. 25) is for the concentration of a spallogenic nuclide that is assumed to decrease exponentially (flattening in upper 20 g cm$^{-2}$ is ignored (Section 3.1.6) in an ideal deposit that has not experienced significant erosion or aggradation and that has been exposed during a single exposure event 18 kyr ago (Phillips et al., 1996c Type I). If the sediments had inherited concentrations of TCN from previous exposures (Sections 4.4 and 5.2), the concentrations would be higher (curve would be displaced to the right of a curve representing sediment of the same deposit without inheritance) and would not define a simple exponential equation unless the amount of inheritance was uniform with depth. Curve B is the model case where an 18 kyr old deposit was gradually eroded at a fast and constant rate (5 cm/kyr$^{-1}$), although non-constant episodic erosion can also be modeled (Section 3.9). The net effect of erosion is that the concentration will be proportionately lower at all depths. Curve C represents a deposit whose surface was continuously aggrading at a rate of 50 cm/kyr$^{-1}$ beginning 18 kyr ago (Phillips et al., 1996c Type II). The progressively more recent sediments on top are younger than the sediments below, and the linear depth profile is characteristic of a rapid constant aggradation rate. Below 9 m depth, the profile would again decrease exponentially. Curve D represents the situation where a fan was deposited 35 kyr ago, followed by 17 kyr of stability, then a rapid aggradation event which deposited 200 cm of sediment 18 kyr ago. Multiple significant episodic depositional events may therefore be identified in the profile record where normal exponential decrease in concentration is punctuated. Field evidence (such as buried soils our distinct fining upward units) should be sought to support an interpretation of separate depositional events within a single section. With the exception of constant erosion, each of these histories produce curves that are distinguishably different. Not shown is the uniform curve (Phillips et al., 1996c Type III) representing complete mixing of the sediments in a highly bioturbated or cryoturbated setting (but these areas can generally be recognized in the field and avoided, Section 4.4). Combinations of these processes will clearly complicate the depth profile. A detailed soil and sediment stratigraphic examination, higher TCN sampling frequency, additional independent ages, and Monte Carlo simulations of the possible models can help provide constraints for the interpretation of a compound scenario.

The work of Ayarbe et al. (1998)on eroding fault scarps provides an example of the advantages of the depth-profile approach. The scarp is located close to Socorro, New Mexico. It showed 3.5 m of offset and was about 15 m in width. Erosion and bioturbation had clearly disturbed the surface in many areas, so subsurface sampling was necessary. They measured $^{36}$Cl profiles down to 3.5 m depth from a medial position on a fault scarp (the profile was sampled from the footwall of the fault, about 1 m above the scarp itself). A profile was also measured at a point about 30 m above the position of the fault on the upthrown side, referred to as the "control profile". At this location, the topography was relatively flat and soil data indicated very little erosion. The samples were obtained by collecting several kilograms of sediment (consisting of coarse, poorly-sorted debris flow material) and amalgamating $>150$ individual clasts in the 1.5–0.5 cm size range. Two samples were collected as geological blanks from the deepest position on the control profile and were processed identically.

Several characteristics of their results are noteworthy (Fig. 26). First, the smoothness of the profiles indicates that a sufficient number of clasts have been homogenized to yield a consistent average inheritance for the deposit. This inference is strongly supported by the near-identical values for the replicate process samples from the deepest position on the control profile. Second, both profiles converge with depth to a consistent "baseline", which is the inherited component, equal in this case to $10^6$ atoms of $^{36}$Cl g$^{-1}$. This inheritance is quite substantial, equivalent to that which would accumulate from about 30 kyr of surface exposure. The control profile has a larger inventory of $^{36}$Cl and a smoothly exponential shape. Accounting for the inheritance, the exposure age for the terrace surface is 175 kyr. The footwall profile shows consistently lower inventories of $^{36}$Cl, as would be

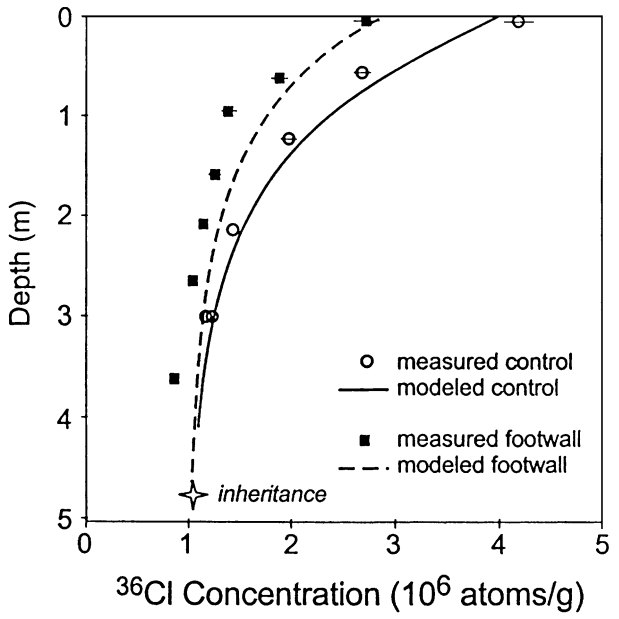


Fig. 26. Depth profiles of $^{36}$Cl concentration measured at two locations close to the Socorro Canyon Fault scarp. The control profile was sampled topographically above the scarp, in a location with little erosion. Continuous curve illustrates calculated $^{36}$Cl concentration after 140 ka of exposure. Star indicates average $^{36}$Cl inheritance of clasts in deposit. Footwall profile was sampled 1 m above fault plane, in location of maximum erosion. The effect of the erosion is seen in the lower $^{36}$Cl concentrations in this profile. The $^{36}$Cl accumulation under the eroding surface, shown by the dashed curve, was modeled using a topographic diffusion-equation approach.

expected in an eroding position. It is matched fairly well by a profile calculated assuming a steady 6 mm/kyr erosion rate. This model is not strictly accurate, inasmuch as geological evidence indicates multiple rupture episodes on the fault, but it clearly illustrates the sensitivity of depth profiles to erosion. The study demonstrates that with appropriate sample processing, TCN depth profiles can overcome the inheritance problem and can yield information about geomorphic history and processes that would otherwise be very difficult to obtain.

In addition to the advantage of avoiding problems such as turbation which affects surface clasts, subsurface profile sampling offers a powerful means of identifying and quantifying inheritance. Exposure of sediment prior to and during transportation will result in excess concentration of all TCNs proportional to the duration of pre-exposure on the hillslope or, in the case of a steady-state system, the rate of long-term hillslope erosion. As described above, fast neutrons and muons can penetrate regolith and bedrock on a hillslope and produce measurable TCN to depths of 5 m (deeper for the less significant muon flux). The total sediment volume containing inherited concentrations is essentially the catchment area × 5 m (plus the surface area of reworked older alluvial fans × 5 m). In steady-state cases, it is possible to predict the actual average concentration of inheritance. Where sedimentation rate (or hillslope erosion rate) is approximately constant over the duration of interest, the concentration of the inherited nuclides is simply proportional to the long term average catchment erosion rate ($E$), regardless of whether or not the regolith on the bedrock is being turbated, and regardless of the total exposure time after the steady state has been attained (Lal, 1991; Granger et al., 1996):

$$N = \frac{P\Lambda}{E}. \tag{3.104}$$

Unfortunately, in many circumstances stripping events are episodic over climate timescales of 20 kyr, so this simplification does not hold. For inheritance resulting from prior exposure on an old sedimentary surface before reworking, the sediment storage time may be too long ($\gg \Lambda/E$); and the total volume of stored sediment is too large. Because there is no simple model for a non-steady-state system, the significance of inheritance must be evaluated empirically by measuring the average TCN concentration integrated over the entire catchment basin (an expensive project) or by isolating the inheritance from in situ production in the deposits eroded from the catchment basin.

It may be possible to predict which sediment may carry high inherited components by studying the geomorphic processes prior to final deposition. For instance, catchment basin size, geometry, hypsometry, rock type and fracture density, weathering rate and style, and duration and frequency of precipitation events will influence sediment production on the hillslope. Zentmire et al. (1999) showed that modern outwash from the Matanuska glacier, Alaska, had no inheritance in five cobbles (all were indistinguishable from their chemical blank). This led them to suggest that it is favorable to sample sediment from glaciated catchments when possible, or at least seek to maximize the glaciogenic the component when sampling a bajada or terrace with multiple source basins. Their rationale was that because glaciers shield their substrate and are efficient at eroding their beds, glaciogenic sediment will have on average a lower probability of pre-exposure than most non-glaciogenic sediment in adjacent catchments. The observation that of more than 80 boulder measurements on moraines in the Wind River Range only two had indications of inheritance (Gosse, 1994) supports their conclusion. Furthermore, the variability of multiple TCN ages on alluvial surfaces with glaciogenic contributions appears to be lower when a significant portion of the alluvium is glacigenic (e.g. Bierman et al., 1995b) and higher where no glacigenic component is present (e.g. Trull et al., 1995).

## 4. Sampling strategies

The maxim that numerical ages are only as good as the samples upon which they are based holds particularly true for TCN studies. When stringent sampling strategies are invoked, fewer production rate adjustments and geometrical measurements will be necessary, and the resulting decrease in random errors will significantly improve the total precisions of the ages (Section 6, Fig. 27). The objective of sampling is to collect and describe the attributes of a sample that precisely represents the exposure history of a given landform (even if the landform is simply a narrow gully for which an erosion rate is sought). The following sections describe sampling strategies that are used in many TCN studies. Because the sample strategy used depends on the nuclide-target selected (e.g. $^{21}$Ne in quartz) a fundamental knowledge of the principles of each of the six TCN is also useful (Section 3.10).

### 4.1. Field sampling considerations

*Sample relevance*: TCN studies typically seek to relate cosmogenic nuclide concentrations to the timing of some geological event (e.g., a glacial advance (Gosse et al., 1995a; Phillips, 1996), mass wasting (Kubik et al., 1998; Cerling et al., 1999), flooding (Cerling, 1990) or to some geomorphological process rate (e.g., denudation rate or soil formation rate (Albrecht et al., 1993; Brown et al., 1995b, 1998b; Heimsath et al., 1997, 1999; Phillips et al., 1998; Small et al., 1997, 1999; Summerfield et al., 1999)). Depending on the nuclide used, many surficial processes can affect the TCN concentration during exposure (some nuclides are not as sensitive as others to certain processes) (Section 5.2). Many boulders may exist on the crest of a moraine, but only a few may have been continuously exposed and never buried since the initial deposition of the moraine. In addition to different exposure histories of surface on a single landform, Gosse et al. (1995c) demonstrated that on a single alpine moraine the TCN ages may reflect the timing of deposition. Boulders on the front of the crest of the Pinedale (22 kyr) terminal moraine were deposited almost 6 kyr before the boulders on the up-ice edge of the ridge. That trend shows that the age of a moraine may depend on the position of the sample relative to the leading edge of the moraine. Different strategies will be used when attempting to determine 'when the ice margin arrived at the moraine', or 'the average moraine age' or 'the timing of initial retreat'. This sample-specific nature of TCN stands in contrast with many types of dating (e.g. the position of a sample within an unaltered basalt flow should minimally affect its K–Ar age). Careful posing of the geological problem studied and consideration of the geomorphic processes are imperative to selecting relevant samples. Potential sample-to-sample variability provides a strong argument for collecting multiple samples (Section 6.2.3).

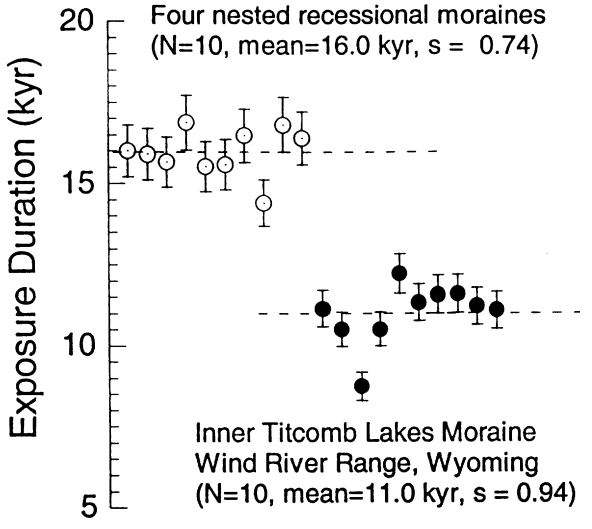


Fig. 27. TCN precision based on multiple ages on a single landform. Filled circles are $^{10}$Be measurements on fresh granitic boulders with heights above ground $>1.2$ m on a single moraine at 3200 m asl; coefficient of variation is 4.8% (Gosse et al., 1995a). Open circles are $^{10}$Be measurements on granodioritic boulders ($H > 2$ m) with varying degrees of weathering, on tightly nested recessional moraines of the Half Moon Lake Lobe near Pinedale, Wyoming, 2300 m asl; coefficient of variation is 4.6% (Gosse et al., 1995b). Measurements were done over two years with different but low chemical blanks ($^{10}$Be/$^{9}$Be averaged $< 2\times10^{-15}$), at the University of Pennsylvania.

*Surface geometry*: The ideal geometry of a rock or landform surface for TCN exposure sampling is one that can be characterized as sufficiently extensive, flat, and horizontal. Sufficiently extensive means that a sample can be collected at least 50 cm from an edge or second face. Edge effects are most significant for TCN that are produced in part through thermal neutron capture (such as $^{36}$Cl and $^{41}$Ca). Flatness is desired because complicated geometries require adjustments for self-shielding or changes in the effective cosmic ray flux (Section 3.7). Modeling the cosmic-ray flux on a horizontal surface is straightforward whereas dipping surfaces require adjustments for foreshortening effects because the total ray flux (particles m$^{-2}$) is less than that on a horizontal surface (Section 3.7.2). Each of these adjustments require additional measurements and calculations which have inherent uncertainties. The effort involved in finding an ideal surface geometry on a landform will be compensated by fewer required measurements and a greater precision and accuracy. Variance among multiple samples can help validate surface geometry corrections.

#### 4.1.1. Sample description

In addition to the considerations related to the history of a particular sample, cosmogenic nuclide results will also depend strongly on observations related to the setting of the sample, inasmuch as the cosmic-ray "dose" depends on the sample geometry and surrounding

topography. Unless accurate observations of these parameters are made the interpretation of the final results will be, at best, ambiguous. At a minimum, we suggest recording the following:

(1) *Rationale for sample selection*: Why was this particular piece of rock selected? What is its postulated connection to the event or process of interest? What evidence indicates that it is superior to alternative samples? What items raise doubts about its utility? How does it compare to other samples collected at the same site?

(2) *Description of object sampled*: Size, shape, color, other distinguishing or possibly significant characteristics. Note the height of the sample above surrounding ground level; this is important when shielding by snow or sediment is evaluated, and recent exhumation may explain why a surface has a lower-than-expected exposure age. Photographs and labeled sketches are useful when attempting to revisit a site and in interpreting the final results.

(3) *Description of sample material*: Surficial texture (e.g., presence or absence of glacial polish, fluvial rounding, projection of weathering-resistant inhomogeneities, dissolution features such as gnammas and rillen, granular disintegration or "case hardening" of the surface) is often an important clue to the history and stability of the sample. Note degree of weathering and lithology/mineralogy. Surface area covered by lichen may also be indicative of rate and style of erosion.

(4) *Location of sample*: Both the location within the geomorphic setting (e.g., "just below the crest of a slightly raised bed of gravel 20 m west of the bank of the paleoflood channel") and accurate geographic coordinates (in addition to latitude ($\pm 0.01^\circ$) and altitude ($\pm 3$ m), longitude ($\pm 0.01^\circ$) are also needed for exposures within the last 10 kyr to adjust for dipole wobble and non-dipole effects (Section 3.5.3) and to revisit the surface. Standard geographical latitude is used in calculating the geographical scaling factors ($S_{el}$ and $S_\mu$) for pre-Holocene exposures (longitude/latitude is thus the most convenient system of coordinates to use (Section 3.7.1). Longitude/latitude in decimal degrees is more convenient for calculations than deg/min/s. Accuracy in elevation is much more important for calculation of production rates than is accuracy in "$x$–$y$" coordinates.

(5) *Orientation of sample*: Dip and dip direction can be measured ($\pm 5^o$) with a standard geological hand transit.

(6) *Sample thickness*: In order to maximize the concentration of the TCN and minimize the uncertainty due to integrating the cosmic ray flux through thick samples, most TCN strategies use samples collected within the upper 2 cm of the surface. Note the sample thickness ($\pm 1$ cm) and whether it is variable or if it needs to be trimmed in the laboratory. An exception is when depth profiling is conducted.

(7) *Shielding geometry*: To record sample shielding above the $2\pi$ horizon, set up a table (or circle) with azimuthal intervals (e.g., 230–290°) of major features on the skyline and the corresponding angle ($\pm 3^\circ$) above the horizontal to the skyline. Alternatively, J. Klein has used a camera equipped with a fisheye lens can be leveled (so that it is pointing vertically upwards) and the resulting image digitized and processed to yield a very detailed shielding profile. In general, shielding of less than 5° is of negligible importance. Also describe vegetation canopy (Section 3.5.5).

(8) *Subsurface profile samples*: In the case of depth profile sampling, describe the thickness of the layer sampled, the depth from the surface to the top of the layer, average bulk density above each sample (or integrated over multiple point measurements), average clast size and number of clasts sampled in each layer (agglomerates of pea-sized samples are favorable), average rooting depth, amplitude of relief by tree throw disturbance, sedimentary structures that allowed you to deduce that the sediment sampled was not turbated, soil characteristics that imply erosion, hiatuses, or burial (by eolian or fluvial processes), and estimate the possibility of periodic snow or loess cover.

#### *4.1.2. Sampling methodology*

Samples for TCN studies on rock surfaces are usually collected with a hammer and chisel (see below for sampling strategies in alluvium). The hammer and chisel has advantages of portability, simplicity, and reliability. The main disadvantage is that some desirable sampling sites on rock surfaces may not be amenable to this method (quartzite, in particular). The portable drill and cutoff saw can sample in nearly any location on any rock. We have successfully used an airless jackhammer on quartzites, which is an alternative to motorized equipment that requires fuel or lubricant. Unfortunately, the optimum least-weathered sites are often also the most difficult ones to sample!

Given the choice, samples with no shielding have higher priority over samples with shielding (topographic or otherwise). The likelihood of blockage of the cosmic radiation at some time in the past, even if the surface is bare at present, also should be considered (Section 3.7.3). In some cases, such as snow cover, reasonable estimates can be made of the degree of shielding over the long term. In general, sites that are located above the surrounding topography, such as the tops of high boulders, are more likely to have been wind swept and less likely to have experienced coverage than those in depressions.

Even after a particular location (e.g., boulder, outcrop, slab) has been chosen, the specific point of sampling must still be carefully considered. If possible, sites near edges or corners of outcrops or boulders should be avoided because of complications due to cosmic-ray penetration from multiple directions and, in the case of $^{36}$Cl and

$^{41}$Ca, possible thermal neutron leakage (Section 3.7.5). Other considerations include differences in rock weathering from point to point and the sampler's evaluation of the distribution of surface erosion processes over the rock surface, such as granular disintegration, spalling, and formation of dissolution pits. If possible, sample the rock as small chips rather than large chucks to avoid trimming and possible contamination in the laboratory.

### 4.2. Other lithological considerations

In addition to restrictions of lithology that the characteristics of a particular TCN may impose, the competency of the lithology must be considered when determining exposure ages. This is particularly true on surfaces expected to be exposed longer than about 50,000 years, on which even modest erosion rates of 1 mm kyr$^{-1}$ will begin to significantly affect precision (Gillespie and Bierman, 1995). Interpretation of the TCN will be more reliable if the effects of erosion can be minimized. With only a few exceptions, any rock type can have variable competency with respect to erosion, even in the same outcrop. For example, granites may be very resistant or nearly saprolitized, depending on hydrothermal activity, climatic regime, history of glaciation, slope, and other regional and local factors. Typically, the least erodable rocks tend to be more siliceous endmembers (e.g., aplites and quartzites, but not diorites) and finer grained. Grain size is perhaps more important than lithology. All attempts should be made to collect from the same resistant rock type unless other systematic uncertainties may arise (for example, the effects of inheritance may be reduced if multiple lithologies are used). The effects of slightly different lithologies on TCN exposure ages of 13 boulders on ca. 150 kyr-old moraines in the Wind River Range, Wyoming were shown by Gosse (1994) to be minor but distinguishable (Fig. 28). Although other factors including stratigraphic position and inheritance may contribute to the observed scatter, there is a clear but statistically weak trend. Due to the potential for variable meteoric contamination, whole rock samples and less resistant minerals exposed to prolonged weathering should be avoided if possible — a catch 22 situation if the objective is to determine the history of a weathered surface.

### 4.3. How much sample is needed?

Rarely does the field sampling situation afford an endless supply of ideal samples characterized by suitable lithology and ideal geometry. Although extra sample is useful for replicate analyses or sharing with other investigators, time, availability of suitable surfaces, and limitations on transport of samples usually limit the collection of excess sample. The goal is to collect enough mass so that sufficient nuclides can be extracted or released to

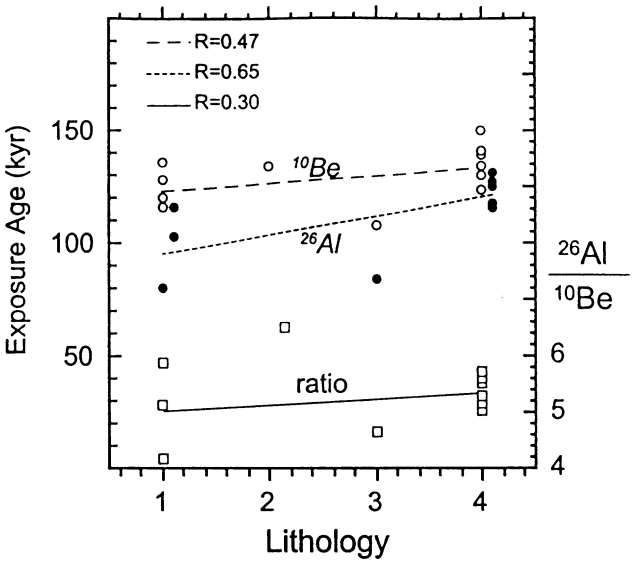


Fig. 28. Possible effects of lithology on exposure dating. Measurements of $^{10}$Be and $^{26}$Al on 13 boulders ($H > 2$ m) on the crests of broad Bull Lake-age moraine ridges of the Fremont Lake Lobe, Wind River Range, Wyoming. Lithology numbers are ranked in order of increasing resistance to erosion and difficulty in sampling [(1) weathered plagioclase porphyroblastic granodiorite; (2) plagioclase porphyroblastic granodiorite; (3) weathered granite; (4) fresh, unweathered granite]. These Bull Lake moraines are believed to approximately coincide with Oxygen Isotope Stage 6 glaciation. The correlations are weak, but the positive trends in the $^{26}$Al and $^{10}$Be ages indicate that the more resistant lithologies tend to erode less. The measured $^{26}$Al/$^{10}$Be also decrease with decreasing resistance to erosion. With the exception of inheritance, other geological factors that may cause variability should be constant. Although samples were collected from different recessional moraines of the same glaciation, there is no correlation between age and stratigraphic position.

enable measurement at the desired level of confidence. The minimum amount of sample required is not fixed and varies depending on TCN used, exposure duration, site effective production rate, proportion of the mineral phases sought, and nature of the analysis. A detailed review of the latter is beyond the scope of this paper. The reader is directed to reviews of AMS and gas mass spectrometry published elsewhere (Litherland, 1987; Tuniz and Klein, 1989; Tuniz et al., 1991; Finkel and Suter, 1993).

Before sampling, it is useful to calculate approximately how much sample will be needed. Consult with the analytical facility to determine the detection limits for geological samples. It is also necessary to determine what level of reliability is required to address the question being posed. If the goal is to distinguish between a lava that was emplaced 1 Myr ago and 50 kyr ago, or if it is only necessary to determine the relative ages of two or more samples, then lower precision may be tolerated and a smaller sample mass may suffice. However, if, for example, the goal is to distinguish between moraines of 15 kyr and 12 kyr, larger samples are needed to attain the required level of precision. In the case of $^{10}$Be, most of the

Table 5
How much sample is needed?[a]

| An example for cosmogenic $^{10}$Be from an estimated 20 kyr-old granitic surface on an Arctic shoreline | |
|---|---|
| Estimated surface exposure age | 20,000 yr |
| Site production rate (adjust for shielding, uplift, erosion) | 5.1 atoms $^{10}$Be per g qtz / yr |
| Est. conc. of $^{10}$Be in quartz (ignore decay if sample age $< 0.03T_{1/2}$ ) | 102000 atoms $^{10}$Be per g qtz |
| Desired minimum AMS $^{10}$Be/$^{9}$Be | $5\times10^{-14}$ atoms $^{10}$Be / atoms $^{9}$Be |
| Desired mass BeO used (for 1hour analysis) | 1 mg |
| Number $^{9}$Be atoms in 1 mg BeO (assuming pure BeO): | |
| (0.001 g BeO · 9/25 g Be/g BeO) / 9.0 g/mol · $6\times10^{23}$ atom/mol = | $2.4\times10^{19}$ atoms $^{9}$Be /in 1 mg BeO |
| Number $^{10}$Be atoms needed for desired ratio: | |
| $5\times10^{-14}$ $^{10}$Be/$^{9}$Be $2.4\times10^{19}$ atoms $^{9}$Be /mg BeO = | $1.2\times10^{6}$ atoms $^{10}$Be from the qtz |
| Mass of pure quartz to dissolve: | |
| $1.2\times10^{6}$ atoms $^{10}$Be / 102000 atoms $^{10}$Be per g qtz = | 11.8 g pure qtz |
| 40% of the quartz is lost to remove meteoric $^{10}$Be | |
| 11.8 / 60% = | 19.7 g qtz |
| Rock only contained 10% quartz | |
| 19.7 / 10% = | 197 g rock |
| Only 40% of crushed rock has the proper grain size | |
| 197 / 40% = | 500 g rock from site |

[a]These are minimum estimates. Additional sample will be needed for thin section and duplicate chemistry if necessary, and accidental wastage.

best chemical blanks have $^{10}$Be/$^{9}$Be that are equal or (typically) greater than $2\times10^{-15}$ (sources of $^{10}$Be include the carrier, solutions, and airborne particles added during chemistry). The detection limit for $^{10}$Be also varies with different accelerator mass spectrometer. Klein et al. (1982) indicated that their machine required on the order of $4\times10^{6}$ atoms of $^{10}$Be to be loaded (in order to get 400 counts for reasonable reliability, assuming detection of 1/10000 $^{10}$Be at a sputter rate of 1 mg$^{-1}$ and the willingness of the AMS facility to run for 1 h), but detection limits have improved since that time. Table 5 gives an example of how to calculate the amount of rock sample required to make a 1 mg BeO sample with a comfortable $^{10}$Be/$^{9}$Be of $5\times10^{-14}$. Alternatively, the forward approach can be useful to determine how much Be-carrier is needed when the mass of the sample is limited. If the required mass of rock sample is larger than permissible under stringent sampling strategies (i.e., you would have to sample on a steep slope), then a smaller AMS sample (e.g., 0.5 mg) can be produced by adding less carrier. However, a smaller sample means shorter run time before the sample is completely sputtered (and therefore increased Poisson error). A similar calculation can be made for other isotopes.

Nuclide-specific considerations can strongly affect the size of sample required. One of the most significant considerations is the abundance of particular mineral phases required for the analysis of specific nuclides. For example, 500 g of relatively pure quartzite may be pretreated for a $^{10}$Be analysis, whereas 5 kg of rock may be needed for the analysis of a fine-grained quartz-poor latite of the same age. Whole rock $^{36}$Cl analyses can routinely be performed on rock samples of 500 g or less because mineral separates are not required. The noble gas TCN have the significant advantage of requiring only a few grams of the target grains, although a few hundred grams of rock are often needed to obtain those grains.

### 4.4. Strategies for concentration-depth profiles

Much of the preceding discussion on sampling procedure applies to both autochthonous and allochthonous surfaces. However, there are two significant differences between sampling bedrock outcrops and sampling sediment: (1) the sediment is subject to vertical mixing near the surface by a variety of turbation mechanisms (cyroturbation, bioturbation, pedoturbation); (2) because sediment is allochthonous, it is possible that the individual clasts contain TCN inherited from previous exposure (much as incompletely reset luminescence dates have an inherited component). Sampling strategies for sediment have evolved to reduce the effects of these sources of error from pre- and post-depositional processes.

Samples are selected where sedimentary structures indicate there is no mixing (e.g., original fluvial bedding or imbrication is preserved). Where unambiguous sedimentary structures are absent, pedogenic features can be used to determine if mixing has occurred. The presence of buried or complicated soils can indicate if there has been accumulation or stripping, and these locations should be avoided if possible. The depth of the shallowest sample beneath a forested surface will be controlled by the average tree rooting depth and may be greater than $z = 100$ cm. Areas of high relief knoll and cradle topography from treethrow should be avoided because of the difficulty in establishing the long-term sample depth. If unavoidable, the temporally varying relief and bulk density (organic material, compaction) may contribute

significantly to the random error of a calculated age (Section 6.1.1).

There are several sampling approaches to estimate the amount of inheritance in the sediment. (1) One approach is to collect surface samples in proximal modern sediments (modern shoreline, active floodplain, active wash) that share the same catchment as the sediment being dated. If the concentrations are non-zero, the inherited concentration can be subtracted from the TCN concentration in the studied deposit. Unfortunately, in non-steady-state conditions the amount of inheritance will vary over time, depending on the frequency of the major aggradation events. (2) A second approach involves collecting samples that are well below the penetration depth of fast neutrons, where the sediment has remained shielded. This approach assumes that the shielded sediment was deposited approximately concurrently with the overlying sediment (i.e. it is the same depositional event). The amount of inheritance in the deeper sediment may also be systematically greater than the inheritance in the shallower sediments. This will occur if erosion proceeded in layers, so the deeper sediment in the section originally composed the top of the regolith and received a higher cosmic-ray dose. (3) Collecting multiple samples along a vertical transect in undisturbed sediment to measure the "concentration-depth" profile, constitutes a third approach (Anderson et al., 1996). Samples containing inherited components will have anomalously greater concentrations than the others for a given depth. A combination of (ii) and (iii) is useful in the case that all samples have an inherited component.

Ideally, a natural or anthropogenic vertical section beneath a stable flat surface should have sufficient depth to enable access to shielded sediment (e.g. $< 1\%$ production at the surface at 5 attenuation lengths, or approximately 3.3 m in gravel with $\rho = 2\,\mathrm{g\,cm^{-3}}$ assuming $\Lambda_f = 130\,\mathrm{g\,cm^{-2}}$). Subsurface sampling requires measurement of the bulk density of the shielding material above the samples. If the sample density varies significantly (e.g. due to differences in soil parent material such as loess and gravel, different grain sizes, or variable pedogenic carbonate development), multiple measurements of density will be needed to precisely compensate for the variability. The number of sample agglomerates collected will depend on the level of precision desired and on the complexity of the sediment exposure history. Based on numerical simulations (Repka et al., 1997) a minimum of 20 similarly sized clasts should compose each agglomerate in order to significantly improve precision. Ayarbe et al. (1998) showed that samples composed of $> 100$ pea-sized clasts have averaged the inherited component at each depth, and Phillips et al. (1996c) showed that sand-sized fragments may also be reliable.

Depth profiles of three or more samples are expensive and laborious means to estimate the age of an allochthonous landform. Notwithstanding the added insight into depositional history, the method remains prohibitively costly to determine the age of multiple surfaces of similar or different ages. In such instances, soil chronosequences tied to fan chronology may be the only means to date multiple surfaces of a large region. Recently, Gosse and McDonald (unpublished data) have shown in the Amargosa Valley that it may be possible to use just two aggregate samples (one surface sample on pavement and one subsurface sample below the mixing zone) to date alluvium older than about 50 kyr. (The inherited component will compose a larger proportion of the total measured concentration of younger and deeper sediment.) If the samples are in reasonable agreement, depending on the precision required, then these can be used as a maximum age estimate (of, if the inherited component is known or negligible that will represent an average age estimate). This method does require shallow burrow pits (generally $< 1.5$ m) but avoids the need for deeper pits and multiple analyses at one site, so that time and money can be spent analyzing multiple surfaces correlated on the basis of geomorphology and soils chronosequences.

## 5. Sample preparation and experimental data interpretation

### 5.1. TCN sample preparation

The goals of sample preparation are to purify the field specimen of materials not suitable for analysis, to concentrate the nuclide of interest sufficiently that it can be accurately analyzed, and to transform the sample material into a form suitable for analysis. The sample preparation consists of two parts: (1) a pretreatment phase in which target minerals are separated, concentrated, and purified; and (2) an isotope extraction phase in which the isotopes are isolated from the minerals and separated from non-in situ cosmogenic isotopes. From start to finish, the highest priorities must be given to safety, waste minimization, sample labeling and data recording, and the minimization of contamination.

The nuclide concentrations are measured using either gas mass spectrometry (for the noble gases) or accelerator mass spectrometry (AMS) (Litherland, 1987; Tuniz et al., 1991; Finkel and Suter, 1993; Synal, 1995). Ancillary analyses are necessary to determine the concentration of the rock matrix, the TCN element (e.g., Be or Al), the target elements, or the concentration of radioactive elements in the rock which may produce non-cosmogenic nuclides. These ancillary analyses are often done with ICP.AES (Moore, 1989), ICP.MS (Montaser, 1998), atomic absorption (Welz, 1999) or similar analytical methods. The detailed procedures required to prepare samples for the gas MS or AMS and ancillary analyses

are nuclide-specific and are too involved to include in this review article. However, this section provides a general survey of approaches and practical issues in TCN sample preparation.

*5.1.1. Preparation time*

The amount of time required in sample preparation varies widely, depending on the nuclide, its concentration, rock lithology, and the laboratory schedule. The noble gases $^{3}$He and $^{21}$Ne typically require careful isolation of specific mineral phases (e.g. olivine, pyroxene, or quartz) which can take weeks and may involve hand picking. Once isolated and cleaned, the samples do not require chemical preparation before analysis. The other TCN ( $^{10}$Be, $^{14}$C, $^{26}$Al, and $^{36}$Cl) can require more than four weeks for sample preparation because of the time necessary to concentrate the target mineral phases (quartz or other desired minerals) from the sample and the time to extract the radioisotopes from the minerals and prepare them in a form suitable for AMS analysis. The mineral concentrations for these TCN are usually never 100% pure because of the cost and time involved in separation of large masses (often $> 20$ g quartz is desired). Also, it is difficult to remove all of the feldspar content from myrmekite, poikilitic quartz, or ophitic pyroxene. However, the mineral purity can be verified to meet reasonable limits based on, for example, Al concentration, staining for Ca or K, petrography, and other qualitative tests. Samples for the analysis of some nuclides can be prepared in a week if mineral separation can be avoided (although presently only $^{36}$Cl is measured in whole rock samples). Samples with low TCN concentrations may require more mass which generally increases preparation time mostly due to the time it takes for dissolution. Low target mineral abundance (e.g. many basalts have $< 1\%$ olivine phenocrysts) will also increase preparation time because more of the original rock must be processed (Section 5.1.2).

*5.1.2. Physical and chemical pretreatment*

Samples are washed or brushed to remove undesirable organics, carbonate, and dust. If the samples were not reduced in size in the field, they are broken into fragments suitable for crushing (collecting chips ( $< 9\,\mathrm{cm}^3$) rather than large pieces in the field is recommended to avoid this step in the laboratory). The samples are crushed, ground, and/or pulverized and sieved to a predetermined grain size (sample- and nuclide-specific). Typical laboratory equipment for the physical preparation includes a jaw crusher, cone crusher, disc pulverizer, and/or shatter box, sieves and sieve shaker, and the cleaning equipment necessary to ensure safety and prevent cross contamination.

Mineral purification is a necessary pretreatment for most analyses (except whole rock $^{36}$Cl). This aspect of pretreatment involves two steps: (1) the isolation of a single mineral phase; (2) the removal of non-cosmogenic nuclides from that phase. Mineral separation can be completed with combinations of magnetic or electrostatic separation (Franz Magnetic Separator, or Carpco separators), heavy liquid separation (e.g. reusable lithium metatungstate in a 1 L separatory funnel), hand picking to cull grains or remove unwanted phases with tweezers under a dissecting binocular microscope, and selective chemical dissolution by differential leaching of silicates. The latter involves a mixture of HF and $HNO_3$ in hot ultrasonic baths (Kohl and Nishiizumi, 1992) or pyrophosphoric acid. These partial leaching methods offer the advantage of selectively dissolving the unwanted mineral phases while removing contaminating nuclides (such as atmospheric $^{10}$Be adhered to fracture surfaces in the quartz grains). Examples of equipment used for selective dissolution include an acid digestion fumehood, 25-gallon ultrasonic tank with heater and water level safety switch, and a means for acid neutralization. It has been demonstrated by partial leaching experiments that at least 30% of the quartz must be dissolved to sufficiently remove the atmospheric $^{10}$Be (Brown et al., 1991; Kohl and Nishiizumi, 1992; Klein et al., 1997). The optimum grain sizes of the minerals used depend on the isotope extraction procedure.

*5.1.3. Isotopic extraction*

Following mineral separation and purification, samples require chemical or thermal isotope extraction in preparation for analysis. The goal in extraction is to: (1) collect as much of the TCN as possible; (2) separate the TCN from non-cosmogenic nuclides (e.g. radiogenic or nucleogenic) or nuclides that were not produced in situ (e.g. atmospheric); (3) separate the TCN from any possible isobars (isotopes of the same mass, e.g. $^{10}$B is a significant isobar of $^{10}$Be which can make the mass spectrometry of $^{10}$Be difficult); and (4) transform the sample into a form that is suitable for analysis (e.g. $^{10}$Be and $^{26}$Al are precipitated as oxides, $^{36}$Cl as AgCl, $^{14}$C as graphite). Most of the samples have splits that are analysed for elemental concentrations (especially radioactive parents, native Al, Be, and Cl concentrations). Only simplified extraction procedures are outlined below and references to published procedures are provided.

The chemistry-intense extractions of $^{26}$Al and $^{10}$Be are similar and so are generally conducted concurrently (Nishiizumi et al., 1989; Brown et al., 1991; Nishiizumi et al., 1991a; Kohl and Nishiizumi, 1992; Ivy-Ochs, 1996; Ochs and Ivy-Ochs, 1997; Stone, 1998). A pre-determined mass (10–100 g, depending on the expected TCN concentration) and grain size (e.g. 250–350 μm fraction) of pretreated quartz is used. To the quartz or quartz solution is added a known mass of the native element with negligible or known TCN concentration. In some samples there is a sufficient amount of the native element naturally present so no spike is added. Elemental analysis of the Al

and Be by ICP.AES or similar means is necessary to determine the amount of native element present in each sample (in addition to any carrier added). The presence of a known concentration of native element allows for the undesirable but usually unavoidable case when less than 100% of the TCN is carried through the extraction chemistry, because only the ratio of the native element to TCN need to be determined by AMS. This isotope dilution strategy is similar to the addition of eucalyptus or other foreign pollen to subsamples collected for pollen counts. Next, selective precipitations are conducted to remove unwanted elements (e.g. Mg, Ca). Ion chromatography is conducted with anion and cation exchange resins, to separate solutions of Be and Al from Fe, Ti and other cations. Then $Al(OH)_3$ and $Be(OH)_2$ are precipitated (Be can be precipitated with anhydrous ammonia gas to preclude the introduction of boron from glass storage bottles). The hydroxides are oxidized and analysed by AMS.

The chemical extraction of $^{36}Cl$ is simpler and less time consuming then $^{10}Be$, but involves additional elemental analyses to determine the concentration of radioisotope sources of non-cosmogenic $^{36}Cl$ (Zreda, 1994; Bierman et al., 1995a; Ivy-Ochs, 1996; Stone et al., 1996). The procedure is slightly different for whole rock or mineral specific analysis. For the whole rock procedure, 50–100 g of sample can be used. In general, the chlorine is extracted by dissolving the pretreated sand-sized aliquot and precipitating as AgCl. Chlorine carrier may be added, and selective precipitation further separates undesirable hydroxides. The isobar $^{36}S$ is similarly separated by precipitating $BaSO_4$. The final AgCl precipitate is used for AMS analysis.

The noble gas samples are prepared differently than the other TCN (Craig and Poreda, 1986; Kurz, 1986a, b; Poreda and Cerling, 1992; Staudacher and Allégre, 1991, 1993; Laughlin et al., 1994; Niedermann et al., 1994; Bruno et al., 1997; Phillips et al., 1998). The pure mineral agglomerates bearing the cosmogenic $^{3}He$ and $^{21}Ne$ are split in two. One aliquot of the sample is prepared for analysis of the radioactive elements using standard procedures (e.g. for ICP analyses). The main aliquot of mineral grains is used for the gas mass spectrometry and requires no further chemistry. The samples are crushed in vacuo to release the inherited isotopes of He and Ne. By step-heating in a furnace attached to a gas mass spectrometer, the non-cosmogenic He or Ne in the crushed samples can be further separated from the in-situ cosmogenic gases by the low temperature heating because the former are generally weakly bound. However, there is generally some remaining component of the higher temperature volumes that is non-cosmogenic which must be subtracted from the total concentration measured by gas mass spectrometry.

Although experimental procedures for $^{14}C$ extraction from whole rock were attempted earlier (e.g. Jull et al., 1991), thermal isotope extraction method for $^{14}C$ in quartz has only recently been developed (Lifton et al., submitted). It does not involve the laborious chemistry of the other cosmogenic radioisotopes but does involve extensive care in keeping gas lines void of carbon contamination. Lifton et al. (submitted) used a step-heating method (analogous to the noble gas procedures) to remove the $^{14}C$ as $CO_2$. A $LiBO_2$ flux is used to facilitate melting. The more loosely bound non-in situ cosmogenic $^{14}CO_2$ is released at lower temperatures. The subsequent cosmogenic $^{14}CO_2$ is then graphitized and analysed by AMS. A new method of extracting in situ cosmogenic $^{14}C$ from carbonates uses cryogenic methods to separate cosmogenic $^{14}CO$ from $CO_3^{2-}$ and $CO_2$ (Handwerger et al., 1999). However, this method has the disadvantage that it requires an assumption of the $^{14}CO/^{14}CO_2$ production proportion, which they estimated from measurements in ice.

### 5.2. Experimental data interpretation

Unlike dating facilities for radiocarbon and Ar–Ar and most other dating methods, the laboratories that provide the TCN mass spectrometric measurements generally do not interpret the data. This is because in addition to the mass spectrometry data, the interpretation requires consideration of additional data, including sample site characteristics and sample geometry, ancillary elemental measurements, sample preparation procedures, adjustments for non-cosmogenic components, and the scaled production rate parameters described above for each individual sample. The normal model for cosmogenic nuclide applications is formulated under the assumption that the sample acts as a closed system, i.e., that the only source of the nuclide is from in situ cosmogenic production and that no cosmogenic nuclide is lost except through radioactive decay. Any concentration from non-cosmogenic sources needs to be taken into account and subtracted from the total measured concentration. This section provides a description of routine steps used to interpret cosmogenic nuclide data. Some common assumptions in interpreting TCN data are listed in Table 6.

The concentration ($N_m^{meas}$) of the nuclide of interest (such as $^{10}Be$) is calculated from the isotope ratio ($R$) of the stable and cosmogenic isotopes, as measured by AMS:

$$N_{10} = R_{10/9} m_c \left[\frac{N_A}{A_{Be}}\right] / m_{qtz}. \quad (5.1)$$

Once a measured concentration is calculated, the component of concentration that is produced in situ in the mineral phase during the geologic event (t) being dated needs to be determined. This can be involved, depending on the isotope-mineral system involved and the exposure

Table 6
Assumptions made for many applications of TCN

| Assumption | Basis of Validation | Consequences |
|---|---|---|
| 1. Primary GCR flux has been approximately constant over measured exposure durations | No known long term variations greater than $\sim 10\%$; supernovae explosions are short lived events | TCN production rates will vary if the primary GCR flux varied |
| 2. Secondary radiation flux is directed downward but azimuthally isotropic | Empirical measurements in the atmosphere and experimental observations and simulations of products of nuclear transmutations in uniform fields show that particle trajectories are azimuthally isotropic. | TCN production rates will vary with the orientation of the surface if the flux is azimuthally anisotropic. |
| 3. The concentration of the atmospheric cosmogenic nuclide in prepared sample is zero | For certain nuclides, $P_{TCN} \gg P_{atm}$, so $C_{atm}$ is negligible. Atoms of certain TCN are chemically mobile and do not readily adhere to mineral surfaces. Incremental measurements can be taken to determine if the TCN concentration decreases asymptotically with acid leaching as the $C_{atm}$ is removed. | $C_{meas} = C_{TCN} + C_{atm}$. If $C_{atm} > 0$, then the calculated ages will be higher than actual unless correction for the $C_{atm}$ is made. |
| 4. The concentration of radiogenic (magmatic) nuclides is known or is zero | Magmatic $^3He^*/^4He$ can be estimated; no significant radiogenic pathways exist for some nuclides, although most have at least a minor radiogenic component; the abundance of U, Th and other alpha emitters can be measured in the sample (Middleton and Klein, 1987). | $C_{meas} = C_{TCN} + C^*$. If $C^* > 0$, then the calculated ages will be higher than actual unless correction for the $C^*$ is made. |
| 5. The concentration of inherited TCN is known or is zero | No inheritance of TCN is possible if dating the time since formation of extrusive rocks (e.g. tuffs, rhyolite or basalt flows). Radionuclides will not be inherited from exposures that occur prior to $\sim 10 \times$ half life; inheritance can be estimated then subtracted from total $C_{meas}$ | $C_{meas} = C_{TCN} + C_{inherited}$. If $C_{inherited} > 0$, then the calculated ages will be higher than actual unless correction for the $C_{inherited}$ is made. |
| 6. Adjustments for spatial and temporal variations in $P_{TCN}$ are known and correct. | Computer simulations, empirical and experiment measurements to calculate production rates, comparison of TCN exposure ages with independent dates of the same event; empirical and experimental verification of Lal (1991) and other scaling factors. Geomagnetic paleointensity variations are less significant with longer exposure durations because they are integrated over longer time. Temporal variations in paleointensity do not affect sites $> 58^\circ$ geomagnetic latitude, corresponding to the cutoff rigidity of 0 GeV. | If corrections for spatial and temporal variations in TCN production rates are incorrect, all exposure history calculations will be systematically incorrect. |
| 7. Measured estimates of all parameters are correct within assumed uncertainty | Thermal neutron cross sections for $^{35}Cl$, decay constants for radionuclides, attenuation lengths for muons, high energy nucleons, and thermal neutrons, and the density of the atomic targets and the density of the rock can or have been estimated experimentally or empirically. | The magnitude and direction of the effects of error in these estimates will vary. |
| 8. Simple and ideal exposure history assumes no erosion continuous, uninterrupted exposure of a $2\pi$ surface. | Under some circumstances there has never been measurable erosion of the bedrock surface (e.g. very young lavas). Effects of low erosion rates may be insignificant if the exposure duration is short. It is possible to eliminate the possibility for burial or rolling in some circumstances, such as a high vertical face. | Snow, sediment, water, ice, and rocks that shield the surface and have subsequently been removed will cause the total long-term $P_i$ to be less than $P_s$, and therefore $N_i$ will be lower. If erosion is significant $N_{spal}$ will be lower and $N_{capt}$, depending on e, may be higher or lower than the $N_i$ if the surface is considered uneroded, i.e. it was not eroded to a depth of $\varepsilon T$. |

history of the sample. In general;

$$N_m^{meas} = N_m^t + \sum N_m^{inh} + N_m^* + N_m^n + N_m^{cont}, \quad (5.2)$$

where $N_m^t$ is the concentration of the cosmogenic isotope that is produced in situ in the target mineral during the geologic event being studied, minus any concentration lost due to radioactive decay. $\sum N_m^{inh}$ is the concentration inherited from all previous exposure events minus any concentration lost to radioactive decay. Examples of inheritance include exposures of rock on hill slopes before incorporated into beach sediment, till, or alluvial gravels; short-term storage near the surface during transportation of sediment before final deposition, and even

exposure of sand grains during the Cretaceous may be significant if the sediment is ultimately sampled in a Quaternary landform for analysis of a noble gas. Subaqueous exposure of sediments and bedrock before isostatic or tectonic emergence is another example of inheritance which should be considered when dating raised shorelines. Anderson et al. (1996) consider inheritance to include changes in sample depth during subsurface exposure due to bioturbation, pedogensis, or cryoturbation. However, we consider these mixing processes as factors that alter the production rate (increase or decrease) during the exposure event. This way inheritance will always increase the $N_m^t$.

An inherited component can be interpreted in three ways. (i) If there was a period of burial (e.g. by a glacier) between the inherited event and the final exposure event, the ratio of two isotopes in the same sample will plot below the exposure-erosion island. Although this method does not quantify the $\sum N_m^{inh}$, it does help to establish the presence of an inherited component. (ii) Using multiple TCN dates from a single landform surface, it may be possible to identity older 'statistical outliers' which may carry an inherited component. (iii) Single clast samples collected along depth profiles through sediment with no evidence of bioturbation, cryoturbation, erosion, or burial may show considerable scatter if there is a measurable inherited component in the clasts. (iv) Depth profiles consisting of numerous aggregated clasts may yield consistent values at depth that are in excess of that consistent with in situ production (Phillips et al., 1996c; Repka et al., 1997; Hancock et al., 1999). The magnitude of this excess quantifies the inherited component.

$N_m^*$ and $N_m^n$ are non-cosmogenic components, respectively, from radiogenic reactions (the nuclide is a direct daughter product of a radioactive decay) or nucleogenic interactions (nucleons produced from neighboring radioactive sources may interact with target atoms), and they are typically summed together. The radiogenic and nucleogenic contribution may be important for the noble gases if the rock age is older than the exposure age or for long exposures. Many sampling strategies tend to favor pegmatitic lithologies which carry higher concentrations of the large radioactive incompatible elements such as U and other important target elements such as Li and B. In addition to the in vacuo crushing method to determine the relatively loosely bound non-cosmogenic noble gas content (Kurz, 1986a, b), measuring completely shielded rock under the exposed surface can also determine the geological background of the isotopes.

$N_m^{cont}$ includes all concentrations of the nuclide that have been derived from any contamination of the sample with nuclides that have not been produced in the rock, including meteoric components. The potentially large atmospheric component in rocks limits the use of $^{10}$Be to mineral phases that are resistant to weathering, because the production rate (atoms $(g\,cm^{-2})^{-1}\,yr^{-1}$) for $^{10}Be_{atm}$ in the troposphere is a factor of about 1000 times greater than for in situ $^{10}Be_m^t$. This is partly why terrestrial $^{10}$Be measurements in multimineralogic samples is very difficult (Klein et al., 1997) and seldom attempted, but why $^{36}$Cl, with a much lower atmospheric production rate and relatively higher mobility, can be successfully measured in whole rock samples.

Eq. (5.2) assumes no loss of the nuclide other than by radioactive decay. This is important for the noble gases because the diffusivity is a function of mineral structure, size, and temperature.

## 6. Uncertainty and sources of error

Wiser sampling procedures, better chemical preparation and analytical methods, and a better understanding of the physical processes responsible for TCN production have significantly improved the reliability of TCN exposure methods since their conception. The technique is now being used to isolate short-lived surficial geology events (e.g. late Pleistocene glacial advances separated by a few thousand years, correlated to Heinrich events and the Younger Dryas epoch (Gosse et al., 1995a; Phillips, 1996; Ivy-Ochs et al., 1999). A few publications have explicitly dealt with aspects of uncertainty in TCN methods. For instance, Gillespie and Bierman (1995) calculated the total precision of single or multiple nuclide ages (and erosion rates) considering uncertainties in half-life, measurement precision, and the estimate of erosion (or exposure duration). They showed that while uncertainty in age increases with exposure duration, the uncertainty in erosion rate improves with duration. Finkel and Suter (1993) discuss uncertainty related to AMS and is a recommended reference. Other articles report uncertainty in production and erosion using Monte Carlo simulations of error (e.g. Phillips et al., 1996c; Stone et al., 1998b), describe treatment of blank subtraction for high blank proportions (Davis et al., 1999), and calculate total age uncertainty from multiple measurements on the same landform surface (Gosse et al., 1995a). However, no complete detailed evaluation of the sources of error and total uncertainty in the in situ TCN methods has been published. The following review outlines common error sources (Table 7) that influence the interpretation of TCN data and suggests how to treat uncertainty.

### 6.1. Sources of error

Error sources are classified as random or systematic errors. Measurement uncertainties and errors affecting *precision* are mostly random. Systematic errors affect the *accuracy* of the calculated ages and erosion rates. The uncertainty in accuracy continues to outweigh the uncertainty in precision, but when comparing ages determined with the same method (e.g. $^{21}$Ne dating), many of the

Table 7
Sources of error for TCN methods[a]

| 1. Random Errors (8%) | 2. Systematic Errors (10%) |
|---|---|
| 1.1 *Sample characteristics* (5%) | 2.1 *Radionuclide half life* (3%) |
| 1.1.1 Surface geometry correction (1%) | |
| 1.1.2 Shielding correction (1%) | 2.2 *Production rate* (9%) |
| 1.1.3 Thickness (2%) | 2.2.1 Basic calibration (5%) |
| 1.1.4 Meteoric contamination (0%) | 2.2.2 Whole rock theoretical estimates (na) |
| 1.1.5 Erosion rate and style (4%) | 2.2.3 Nuclear cross sections (na) |
| 1.1.6 Burial (0%) | 2.2.4 Attenuation lengths (rock and atmos.) (3%) |
| 1.1.7 Prior irradiation (inheritance) (0%) | 2.2.5 Altitude scaling, Standard Atmosphere (5%) |
| | 2.2.6 Latitude and longitude scaling (5%) |
| 1.2 *Sample preparation and analyses* (3%) | |
| 1.2.1 Sample interchange (0%) | 2.3 *Temporal variations* (3%) |
| 1.2.2 Contamination from physical processing (0%) | 2.3.1 Cosmic ray flux (0%) |
| 1.2.3 Weighing of sample (2%) | 2.3.2 Solar modulation (0%) |
| 1.2.4 Addition of carrier (2%) | 2.3.3 Geomagnetic polar wander (0%) |
| 1.2.5 Contamination with non-target minerals (na) | 2.3.4 Geomagnetic paleointensity (3%) |
| 1.2.6 Analysis of stable isotope (1%) | 2.3.5 Non-dipole uncertainties (0%) |
| 1.2.7 Other major & trace elemental analyses (na) | 2.3.6 Atmospheric thickness variations (0%) |
| 1.3 *Mass spectrometric measurement* (4%) | 2.4 *Stable element measurements* (2%) |
| 1.3.1 Poisson (3%) | |
| 1.3.2 Background subtraction (0%) | 2.5 *Carrier and standards* (2%) |
| 1.3.3 Blank correction (0%) | |
| 1.3.4 Sample reproducibility and normalization (3%) | 2.6 *Fractionation, spectrometry* (0%) |
| 1.3.5 Precision of standard (1%) | |
| 1.3.6 Correction for non-cosmogenic gases (na) | 2.7 *Other assigned constants* (0%) |
| | 2.8 *Calculation errors* (0%) |

[a]Error magnitudes ($1\sigma$) are based on estimates calculated by J. Klein (pers. comm., 2000) for fifteen $^{10}$Be exposure ages from quartz in boulders on a broad terminal moraine ridge approximately 22 kyr old, at 2250 m elevation, 43°N latitude, using carrier manufactured from a shielded beryl, with blank less than 5% of the measured ratio for the unknowns. Boulders average 1.8 m high, were probably not covered by significant snow or sediment, and rest on the crest of the moraines so are not shielded. Samples were less than 5 cm thick and were collected with chisel and hammer from the middle of flat-topped boulders. (na) indicates the error does not apply to $^{10}$Be TCN dating.

systematic errors can be ignored (i.e. 2.1–2.3 of Table 7). Although some error sources are common to all six TCNs (e.g. the uncertainty in spatial scaling for spallogenic production), there are uncertainties that are unique to individual nuclide systems and individual samples (e.g. the thermal neutron cross section for $^{35}$Cl, or the geometrical correction on a self-shielding surface). The magnitudes of errors (%) reported in Table 7 are based on $^{10}$Be measurements in 1993 and 1994 at the University of Pennsylvania but can be calculated for other nuclides, laboratories, and sites. Unless otherwise indicated, all uncertainties here are reported at the $1\sigma$ confidence level. The total uncertainty in the age reported in Table 7 can be represented as

$$\sqrt{\left(\sum \text{random}^2 + \sum \text{systematic}^2\right)} = 13\%. \quad (6.1)$$

*6.1.1. Sample characteristics*

The random sources of error associated with sample characteristics are calculated using equations provided throughout this review article (Table 7). With the exception of erosion, the contribution to the uncertainty in the calculated age due to sample attributes is low (e.g. error in measurement of surface slope, shielding, and thickness of the sample will unlikely contribute more than 2% uncertainty (Section 3.7). In some instances, a parameter assumed to be negligible may be non-zero (e.g. unrecognized burial, which will decrease $N_{\text{meas}}$, inheritance, and meteoric contamination of a weathered rock). In these cases, the error is guessed. Erosion rate and style (e.g. dissolution, grain-scale, block-scale, gradual, episodic) can significantly influence the reliability of calculated exposure ages if the amount eroded ($Z$) approaches the effective attenuation length ($\Lambda$) (e.g. for spallogenic nuclides, about 140 g cm$^{-2}$, but muogenic nuclides are not as sensitive) (Gillespie and Bierman, 1995; Lal, 1996). Estimates of inherited concentration of TCN from prior exposure have been attempted using deeply shielded samples, samples from modern wash (Brown et al., 1998a), and the depth profile method (Anderson et al., 1996; Phillips et al., 1996c; Repka et al., 1997; Hancock et al., 1999).

The effect of meteoric contamination will be different for each sample (Section 4.2). Significant concentrations of cosmogenic nuclides are produced in the atmosphere

(e.g., $^{14}C$ from $^{14}N$, 10Be from $^{14}N$ and $^{16}O$, and $^{36}Cl$ from $^{40}Ar$) at rates that in some cases are greater than $\sim 10^3$ times their terrestrial production (Brown et al., 1989; Morris, 1991). If pure quartz is used, meteoric contamination should be negligible. Less resistant minerals, especially clays, tend to be strong sinks of meteoric nuclides. Weathered olivines replaced with iddingsite yielded 36Cl exposure ages 30% older than unweathered samples from the same surface at Lathrop Wells, NV, probably reflecting the $^{36}Cl$ contribution from the meteoric water with relatively high $^{36}Cl/Cl$ (Zreda et al., 1993). Cosmogenic $^{10}Be$ ages based on whole rock granites and tuffs partially dissolved by 30% were as much as three times older than independent ages, whereas partially dissolved basalts with thick desert varnish layers tended to yield equivalent ages (Klein et al., 1997). These examples attest to the variable nature of meteoric contamination.

*6.1.2. Sample preparation and elemental analyses*

Sources of random error associated with the physical and chemical processing of each sample has been discussed previously (Section 5). Although potentially significant, these random sources of error generally do not contribute significantly to the total uncertainty of the method (average 3%, Table 7). The magnitudes of error assigned are based on experience and knowledge of the sample preparation procedure. Sample interchange occurs rarely but cross contamination will result if equipment (sieves, disc pulverizer, beakers) are not properly cleaned or during evaporation stages if samples are not adequately covered. Sample mass uncertainties are due to incomplete dissolution of the solid mineral, to loss of the minerals by static electricity (2% is probably generous), or to errors in weighing incompletely dried samples. In most cases, error due to analytical balance calibration is less than 0.2%. Analyses of the carrier element and other major and trace elements will each have errors associated with drift, linearity, and contamination of the machine used. With duplicate or triplicate measurements, typical $1\sigma$ total uncertainties in ICP or AA analyses of elemental concentrations at the 0.1–100 ppm levels are generally greater than 2%. This may become significant for whole rock samples (e.g. for $^{36}Cl$) but is not reported for $^{10}Be$ because elemental analyses are unnecessary if the $^{10}Be/^{9}Be$ in the carrier is well known.

*6.1.3. Mass spectrometry*

The principles of random errors are similar for both AMS and gas mass spectrometry. With the exception of blank corrections, random errors associated with the isotopic measurements tend to be small for most nuclides ratios (generally less than 5% for high precision measurements involving long run times or samples with high ratios to boost beam intensity). The uncertainty associated with Poisson counting statistics can be expressed as a function of the number of counts (cf. Eq. (6.3)). In AMS the number of counts for the cosmogenic isotope will vary considerably, depending on run time (8–60 min), beam current (10–20 μA of current is achieved for in situ Be) and most importantly, the concentration of cosmogenic nuclide in the sample. Poisson errors estimate the uncertainties in the ratio measurement itself, and therefore are good estimates of multiple runs on the same target (AMS) or mineral splits and step heating (gas MS). But they do not include uncertainty in the normalization of the ratio, which comes into play when comparing measurements with other AMS laboratories or other dating methods. They also do not include other sources of error (discussed above) that may arise during chemical preparation of completely separate samples. The estimates in Table 7 are generous; reproducibilities are often better than 0.5% and Poisson error can often be improved to better than 1% (10,000 counts) by longer run times.

The other sources of random error usually only make minor contributions to the total uncertainty. Small backgrounds after subtraction add linearly to the uncertainty, i.e. a background of 10% will increase the uncertainty by about 10%:

$$\sigma_{\text{Poisson}}^{\text{bkg}} = \frac{1}{\sqrt{N}}(1 + 2R_{\text{blk}})^{1/2} \tag{6.2}$$

with background subtraction, and

$$\sigma_{\text{Poisson}} = \frac{1}{\sqrt{N}} \tag{6.3}$$

without background subtraction, where $R_{\text{blk}}$ is the ratio of the background to the number of counts ($B/N$). The difference is therefore:

$$\sigma_{\text{Poisson}}^{\text{bkg}} - \sigma_{\text{Poisson}} = \frac{1}{\sqrt{N}}[(1 + 2R_{\text{blk}})^{1/2} - 1]$$

$$\approx \frac{1}{\sqrt{N}} R_{\text{blk}} = R_{\text{blk}}\sigma_{\text{Poisson}}. \tag{6.4}$$

Backgrounds are generally small for AMS and high precision gas MS. Uncertainties from blank subtraction are also small for most samples but can add significantly to the measurement uncertainty if the blank approaches the magnitude of the unknowns (Davis et al., 1999). In general, the formula is

$$\sigma_{\text{f}} = \frac{R_{\text{M}}}{R_{\text{f}}}\left(\sigma_{\text{M}}^2 + \frac{R_{\text{blank}}}{R_{\text{M}}}\sigma_{\text{blank}}^2\right)^{1/2}, \tag{6.5}$$

but as $R_{\text{f}}$ approaches 0, the 95% confidence limit is used for the upper limit of the ratio

$$R_{\text{f}}^{95\%} = 1.96\left(\sigma_{\text{M}}^2 + \frac{R_{\text{blank}}}{R_{\text{M}}}\sigma_{\text{blank}}^2\right)^{1/2}, \tag{6.6}$$

where $R_f$ is the final isotopic ratio, $R_M$ is the measured isotopic ratio, $R_{blank}$ is the isotopic ratio of the blank, $\sigma_M$ is the measurement uncertainty (e.g. $\sigma_{Poisson}$) and $\sigma_{blank}$ is the uncertainty of the isotopic ratio of the blank.In the case of $^{10}Be/^{9}Be$, blanks as low as $2\times10^{-15}$ can be achieved by using a Be carrier manufactured from shielded beryl (Middleton et al., 1984). Precision in the measurements of standards between analyses of unknown samples is generally better than 1%.

*6.1.4. Systematic errors*

Most of the systematic errors associated with sample preparation and mass spectrometry (e.g. fractionation, mass discrimination, variable sputter or melting rates, memory of previous sample) are eliminated by proper normalization. Uncorrected for systematic uncertainties associated with element and isotopic measurements vary, but are generally less than 2% after normalization. Uncertainty in carriers and standards may increase due to dilution or evaporation but can be verified with routine measurement. Uncertainties in assigned constants such as atomic masses are less than 0.01%. Calculation and rounding errors and other human errors are hopefully negligible. The weighted uncertainty (e.g. Holden, 1990) in radioactive half-lives (and thus decay constant and mean life) is 3% or lower (Table 8). The half-life of $^{10}Be$ has only recently reached an apparent consensus, so it deserves additional comment here. In 1987, the US National Institute of Standards and Technology (NIST) prepared a standard material with certified specific gravity and $^{10}Be/^{9}Be$ (Inn et al., 1987) and reported a value for the $^{10}Be$ half life of $1.34\pm0.07$ Myr (not included in the Holden (1990) evaluation). This was significantly lower than (not within $2\sigma$ limits of) the half-life reported earlier that year, $1.51\pm0.06$ Myr, by Hofmann et al. (1987). Middleton et al. (1993) compared the NIST SRM 4325 standard and a separate standard (A-N3.77) from ICN Biomedicals Inc. to their in-house AMS standard to estimate the $^{10}Be$ half-life. They reported 1.53 Myr $\pm$ 5% and 1.48 Myr $\pm$ 5%, respectively, as the half-lives from the relative comparison. Their measurements support the 1.52-Myr value (Holden, 1990).

The greatest sources of systematic error extend from estimates of time-integrated production rates. Unfortunately many of these errors are not independent of each other. However, the dependent errors may be combined before attempting error propagation. Production rate error sources that vary with site location should be included in total uncertainties calculated for each site, or should be at least described in text accompanying the data. By basic calibration (2.2.1 of Table 7) we mean the systematic uncertainty in the empirically derived production rates. Such uncertainties may derive from invalid assumptions regarding exposure history (e.g. no burial, Table 6), from incorrect exposure durations determined by independent timescales, and uncertainties in measurements of the cosmogenic nuclide. Table 7 indicates that the basic calibration for $^{10}Be$ (when scaled to sea level and high latitudes as suggested by Stone, 1999) is

Table 8
Half-lives of radioactive TCN

| TCN | Decay schemes[a] | Half-life[b] (yr) | Unc[c] (%) | Decay constant[d] ($yr^{-1}$) | Mean life[e] (yr) | References |
|---|---|---|---|---|---|---|
| $^{10}_{4}Be$ | $\beta^- \rightarrow {}^{10}_{5}B$ [100%] | $1.52\times10^6$ | 3.3 | $4.56\times10^{-7}$ | $2.19\times10^6$ | (Yiou and Raisbeck, 1972; Hofmann et al., 1987; Holden, 1990; Middleton et al., 1993) |
| $^{14}_{6}C$ | $\beta^- \rightarrow {}^{14}_{7}N$ [100%] | 5730 | 0.52 | $1.213\times10^{-4}$ | 8245 | (Hughes and Mann, 1964; Holden, 1990) |
| $^{26}_{13}Al$ | $\beta^+, EC \rightarrow {}^{26}_{12}Mg$ [82.1%,17.9%] | $7.1\times10^5$ | 2.8 | $9.8\times10^{-7}$ | $1.0\times10^6$ | (Rightmire et al., 1958; Endt and Van der Leun, 1973; Middleton et al., 1983; Holden, 1990; Norris et al., 1993) |
| $^{36}_{17}Cl$ | $\beta^- \rightarrow {}^{36}_{18}Ar$, $EC$, $\beta^+ \rightarrow {}^{36}_{16}S$ [98.1%,1.9%,0.2%] | $3.01\times10^5$ | 0.66 | $2.30\times10^{-6}$ | $4.3\times10^5$ | (Wu et al., 1949; Bartholomew et al., 1955; Goldstein, 1966; Endt and Van der Leun, 1973; Bentley et al., 1986) |

[a] Lederer and Shirley (1978); $\beta$, beta decay, $EC$, electron capture.

[b] Shirley (1998); and Holden (1990). The half life for $^{14}C$ from Holden (1990) is 5715 yr. However, the $^{14}C$ half life is more commonly reported as $5730\pm40$ yr (Lederer and Shirley, 1978).

[c] Uncertainty, as reported for half lives in Lederer and Shirley (1978) and Holden (1990).

[d] $\lambda_n = \dfrac{\ln 2}{T_{1/2}}$.

[e] $\tau = \dfrac{T_{1/2}}{\ln 2}$.

probably within 5%. Included in basic calibration is the uncertainty in the proportion of production components (spallation by fast neutron, thermal neutron capture, and muonic interactions). As discussed in Section 3.6.1, $^{3}$He is also well calibrated, but other nuclides may have higher systematic uncertainties. Uncertainties in theoretical estimates of production rates for whole rock samples (e.g. for $^{36}$Cl) depend on nuclear physics and the nuclear cross section data. Also, significant is the uncertainty in effective mean attenuation length of the different particles at different sites (function of magnetic field effects) in both atmosphere and rock (Table 3). However, the largest errors still originate from uncertainty in scaling the calibrated production rates to different positions (latitude, longitude, and elevation).

Systematic errors in the atmospheric scaling is caused by uncertainty in attenuation lengths, uncertainty in the model of atmospheric pressure over the range of possible altitudes, latitudes and longitude, and uncertainty in the global interpolation of incomplete star production or neutron and proton data at different altitudes. The Standard Atmosphere hydrostatic model (CRC Handbook: Lide, 1999, 2000) commonly used (Stone, in press) is the geopotential atmosphere with altitudinal pressure changes derived from

$$P_z = P_s \exp(-(M_a g/R_0 \xi)(\ln T_s - \ln(T_s - z\xi))), \qquad (6.7)$$

where $P_s$ is sea level pressure (1033.2 g cm$^{-2}$), $T_s$ is sea-level temperature (288.15 K), $\xi$ is the dry air adiabatic lapse rate ($dT/dz$, taken as 0.0065 K m$^{-1}$), $M_a$ is the mean molar mass of air (28.964 g mol$^{-1}$ at sea level), $R_0$ is the gas constant, $g$ is the acceleration due to gravity at sea level, and $z$ is altitude (Stone, in press). The International Civil Aviation Organization (ICAO) uses a similar approximation (see Dunai, 2000). The steady-state model represents mean annual atmospheric conditions of the atmosphere from sea level to 1000 km at latitude 45°N during a period of moderate solar activity. However, the fixed adiabatic lapse rate assumes dry air, and the model does not account for second-order pressure variations outside the mid-latitude region (e.g. anomalies over Antarctica may have caused a 30% underestimation in regional production rates (Stone, in press). More empirical studies are needed to evaluate these uncertainties.

The error in scaling the production rates for different latitudes (and longitudes) is still being evaluated, but agreement between TCN ages and independent ages at different sites (e.g. (Phillips et al., 1996b; Licciardi et al., 1999), see discussion in Sections 3.1, 3.5.3 and 3.6.6) suggests that at least for mid-latitude and arctic sites the scaling by models such as Lal (1991) is probably within 10%. For samples collected at elevations and latitudes similar to those of the original calibration sites (mostly 30–45°N, $>$ 1500 m asl), the scaling is less important (Table 7). As we improve the method of scaling production rates globally (e.g. with more robust rigidity-based transport codes that are constrained by empirical data Section 3.7), this error will decrease significantly.

Temporal variations in production rates contribute systematic errors when they are ignored. Most previous studies have calculated ages according to a single time-averaged production rate. This is generally appropriate when comparing TCN ages to other TCN ages, but when other timescales are involved the error may be significant. As described in Section 3.5.3, fluctuation of the primary GCR is probably negligible over the last Myr, and with the exception of late Holocene ages, the effect of high frequency ($< 10^3$ yr) solar modulation is probably balanced by integrating over the entire exposure duration. Likewise, the effects of secular variation in the position of the dipole axis and of non-dipole magnetic field effects will probably balance over long exposure periods. However, these latter effects are probably important for exposures less than 8 kyr when the time-averaged field axis is not geocentric (Section 3.5.3). The possible effects of temporal variations in the 'thickness of the atmosphere' (e.g. due to sea level change or isostatic rebound) have been calculated to be less than 1% over long exposure periods. Variations in geomagnetic intensity may produce systematic errors in ages for exposures as long as 50 kyr (Section 3.5.3). The effects can be modeled using available paleointensity data and integrating the 'apparent geomagnetic latitudes' or by using more robust transport code simulations that vary cutoff rigidity with the paleointensity. However, more investigation into the effects of paleointensity and better estimates of paleointensity are needed to evaluate the true error. Based on the agreements between independent empirical production rate calibrations for different exposure intervals (Phillips et al., 1996b; Licciardi et al., 1999; Stone, 1999) it appears that the error due to fluctuating paleointensity for the past 20 kyr may be within the precision of the individual production rates.

### 6.2. Reporting the uncertainty

When characterizing the age uncertainty from a radiometric dating method (e.g. U-series, $^{14}$C, $^{40}$Ar/$^{39}$Ar), it is common to report a 1$\sigma$ or 2$\sigma$ uncertainty that includes only an estimate of the precision of the analysis for that run. This is considered reasonable because dates from the same method will probably have the same systematic uncertainties (e.g., uncertainty in the half-life of $^{235}$U) if laboratory-specific errors are balanced by normalization. However, if dates from different methods are compared, it is necessary to report the total uncertainty in the method (i.e. the uncertainty in the accuracy and the precision). Error analysis of ages determined with a single method may also require more than simple experimental uncertainty. Calculation of production rates for any one of the TCN method involve

adjustments for spatial and temporal variations in production rates, and therefore may have different compound uncertainties for individual samples.

In any case, the approach used to report the total uncertainty should be explicitly described in the publication. At a minimum, the following information should be provided with any TCN data (Gosse et al., 1996d): magnitude and precision of chemical and analytical blank measurements; uncertainty in site and sample characteristics (position, density, snow cover, erosion); isotope ratio measurement uncertainty (specify if it includes the uncertainty due to normalization, or indicate systematic uncertainty too); and method of determining time-integrated site production rate, including geometrical and cover adjustments. Blank information should always be reported. When blank magnitudes are a significant portion of the magnitude of the unknown (e.g. $> 25\%$), it is crucial to report the magnitudes and analytical uncertainty in both values (Davis et al., 1999) to avoid underestimating the total uncertainty.

Total uncertainty can be reported in four ways. (1) A partial error propagation can be computed using the three or four most significant random error sources of known magnitude, and an error estimate that combines the error sources that are non independent. This provides an estimate of the precision of the method. Separate propagation of the most significant systemic errors will provide a means of evaluating the accuracy. (2) The accuracy of the ages can be evaluated by comparison with other dating methods. (3) The sensitivity to specific error sources can be reported. For instance, the maximum effect can be computed for a given source of error (e.g. the maximum thickness and density of snow possible) or a Monte Carlo error simulation can be used to evaluate the sensitivity of multiple influences (e.g. Stone et al., 1998b). (4) Variance in repeated measurements on multiple samples on the same surface provides another means of estimating precision.

### 6.2.1. Error propagation

As an example of error propagation, consider the variance ($\sigma^2$) analysis (cf Bierman and Gillespie, 1994) for a spallogenic $^{26}$Al exposure age ($t$) from a flat surface with simple exposure history using Eq. (3.89) from Section 3.8 that includes the uncertainty in the AMS and ICP.AES measurements, half-life, and site production rate. The age of the sample is

$$t = \frac{1}{\lambda_{26\mathrm{Al}}} \ln\left(1 - \frac{N_{26\mathrm{Al}}\lambda_{26\mathrm{Al}}}{P_{26\mathrm{Al}}(z_0)}\right). \tag{6.8}$$

Assuming that each of the errors is independent, we can propagate errors using partial derivatives:

$$\sigma_t^2 = \left(\frac{\partial t}{\partial P}\right)^2 \sigma_P^2 + \left(\frac{\partial t}{\partial \lambda}\right)^2 \sigma_\lambda^2 + \left(\frac{\partial t}{\partial N}\right)^2 \sigma_N^2, \tag{6.9}$$

which expands to

$$\begin{aligned}\sigma_t^2 = &\left[\frac{N}{(1-\lambda N/P)P^2}\right]^2 \sigma_P^2 \\ &+ \left[\frac{N}{\lambda(1-\lambda N/P)P} + \frac{\ln(1-\frac{\lambda N}{P})}{\lambda^2}\right]^2 \sigma_\lambda^2 \\ &+ \left[\frac{N}{(1-\lambda N/P)P^2}\right]^2 \left[\frac{\sigma_{\mathrm{AMS}}^2}{R_{26\mathrm{Al}/27\mathrm{Al}}^2} + \frac{\sigma_{\mathrm{ICP.AES}}^2}{C_{\mathrm{Al}}^2}\right].\end{aligned} \tag{6.10}$$

This calculation clearly ignores many significant uncertainties listed in Table 7. However, including many of the factors listed in Table 7 will not necessarily yield a more representative estimate of the measurement uncertainty because (i) it is pointless to under-estimate the true precision of the method by assigning maximum $1\sigma$ uncertainties to every variable; (ii) it is invalid to assume all uncertainties are independent; (iii) the uncertainties in some of the parameters are not well known (e.g., spatial scaling of the nucleon flux through the atmosphere) and our estimates might be too large; and (iv) many uncertainties are systematic rather than random (e.g., half-lives). When all possible errors are propagated through the equations used to derive exposure durations or erosion rates, the final uncertainties are usually much larger than comparisons with other dating methods imply. One reason for this discrepancy is that many of the uncertainties in Table 7 must be estimated, and these estimates are either too large or represent errors that only rarely contribute. It is necessary to consider how the date is going to be used to determine which factors should be included in the calculation of the measurement uncertainty. This is a second reason why error analyses including all error sources may be overestimates. In general, the uncertain effects of factors that affect all measurements in a comparison equally should not be included when the purpose is to combine or compare these measurements. For example, when comparing and combining dates from a single isotopic system, it is not appropriate to include uncertainties in half-life. When dates for a single landform are being compared or combined, it is not appropriate to include uncertainties due to factors that they share (e.g. analytical uncertainties, such as carrier concentration if all samples were prepared together, or snow cover, if all samples had similar burial histories). Only after the samples are combined and when it is necessary to compare the results to other systems, should other systematic (and sometimes random errors) be included in the quoted uncertainty of the measurement.

### 6.2.2. Evaluating accuracy by intercomparison

A comparison of TCN ages with reliable ages determined independently is one means of evaluating the accuracy of the TCN ages. As an example of such an intercomparison consider the results of Phillips (1997b),

who found that 8 out of 8 boulders on 100–150 kyr-old moraines in the Wind River Range yielded concordant $^{10}$Be and $^{36}$Cl ages. The agreement suggests: (i) the chemical procedures, calculations, and assumptions that are unique to each method are equally good (or equally poor) and (ii) different TCN methods can yield the same ages for boulders of this lithology and age in this environment. The agreement also sets limits on burial and erosion rates since erosion and burial affect different nuclides differently, and even on the secular constancy of the production rate since nuclides with different half-lives integrate changes in production rate differently. However, comparisons between two TCN ages do not test assumptions about systematic errors that are common to both methods (e.g. spatial scaling of nucleonic production rates for the boulder's latitude, longitude, and elevation). Comparisons with independent (non-TCN) dating methods such as varve chronologies, U-Th, and K-Ar provide more complete evaluations of accuracy (e.g. Gosse et al., 1999; Ivy-Ochs et al., 1999). For example, the uncertainty-weighted mean of 21 $^{36}$Cl age determinations from the Ashik Kol volcano in the Kun Lun Shan (northern Tibetan Plateau) was 66,000 $\pm$ 1000 years. The result of a $^{40}$Ar/$^{39}$Ar age determination on the same basaltic trachyandesite was 62,000 $\pm$ 1300 years (W. McIntosh, New Mexico Tech, person. comm., 1998). Unfortunately, there are very few locations with highly reliable independent estimates of exposure duration. Because of the continuous development of the TCN method, most sites with reliable independent age control and known simple exposure history are actually used to *calibrate* the TCN timescale.

#### 6.2.3. Multiple sample measurements

Multiple independent measurements of age on a single landform surface improve the precision of the determination of the mean age of the surface. Multiple measurements decrease the impact of an anomalous sample with an exposure history that does not represent the history of the entire surface. In two separate tests on nine boulders from late Pleistocene moraines from the Rocky Mountains, the coefficient of variation of individual measurements about the means of $^{10}$Be exposure ages were 3.8% and 4.1% (Gosse et al., 1995a; 1995c). A similar result was attained for $^{26}$Al. These apparent precisions are significantly better than the total random error of 8% predicted in Table 7. In another example, the coefficient of variation of $^{36}$Cl ages from ten boulders sampled on a similar-age moraine in the Sierra Nevada was 3.5%, compared to an average analytical uncertainty of 4.0% (F.M. Phillips, unpublished data). Unfortunately, due to the costs and time involved in sample preparation and measurement, this approach is seldom possible to the degree necessary to improve the reliability of the age.

#### 6.2.4. Sensitivity analysis

It is difficult to calculate the magnitude of some systematic errors. For instance, it is impossible to determine the duration, periodic thickness, and density of snow, ice, or loess cover over a surface for the past 100 kyr. A reasonable approach is to evaluate the sensitivity of the final age to a range of these factors. This may be done by using a wide range of parameter magnitudes in appropriate equations or statistically with Monte Carlo simulations of uncertainty (Phillips et al., 1996b; 1998; Stone et al., 1998b). The sensitivity of several factors has been treated in detail in this review: variation of the cosmic ray flux with surface inclination angle (Fig. 5) and shielding (Figs. 14 and 15); significance of post-glacial or tectonic emergence (Fig. 12); the most sensitive latitudes, longitudes, altitudes, and ages to geomagnetic changes (Figs. 8, 10 and 11); sensitivity of integrated production rates to short high-amplitude paleointensity changes during excursions or reversals (Fig. 9); significance of ignoring snow cover (Fig. 17) and erosion (Fig. 19) (see also Gillespie and Bierman, 1995for a thorough discussion). An advantage of sensitivity analysis is its capacity to determine before sampling if erosion rate or shielding by snow will be significant. For example, if bedrock or small boulders are being sampled, a simple calculation can reveal how much sediment cover could be tolerated while still being able to answer the question posed. A surface that was deglaciated 25 kyr ago but was covered under 5, 15, or 25 cm of sediment (2.0 g/cm$^3$) for the first 10 kyr, would yield respective ages that were 2.5, 7, and 11% too low if continuous exposure was assumed.

## 7. Directions of future contributions

If the past 15 years is any indication, we have surely not realized the full role of TCN exposure history characterization in Quaternary science. Developments in TCN methods are improving the reliability of landscape evolution, tectonic, and paleoclimate interpretations. We are expanding the ways in which the methods can be employed to assist in other field such as archeology and risk assessment. As more applications are discovered, Quaternary geologists are beginning to address questions that had never before been asked. Here we list examples of future advances in TCN methods that are inevitable or critical to technique development.

1. We need to improve estimates of terrestrial production rates of individual nuclides and better establish the production ratio of different nuclide pairs or triplets. A more rigid and complete numerical simulation model is needed for TCN production in shallow rocks. The transport code must account for aspects of the total (dipole and non-dipole field components) magnetic field influences on GCR and secondary cosmic rays, atmospheric affects, and terrestrial production. More

empirical calibrations at well-characterized sites are needed to establish temporal variations in production rates and place boundary conditions on the transport model. As recommended at two recent TCN workshops (Santa Fe, NM, in February 1996 (Gosse et al., 1996) and West Lafayette, IN, in February 1999), calibration site assessment should involve a group evaluation to prevent anomalous calibrations and to maximize the opportunity for measurement of multiple nuclides.

2. We need to have better control on important nuclear physics parameters that affect the nuclear interactions in rock. For instance, the muonic contribution of the nucleonic production of TCN at sea level must be more firmly determined. This directly affects the reliability of scaling production rates from one site to another and is an intricate and logical next step in future reducing uncertainties. Measurements in subsurface samples below four or five fast neutron attenuation lengths are needed to confirm that the muonic contribution to $^{10}$Be production is much less than assumed in the 1990s. Additionally, better resolution of the flattening of the attenuation of fast neutrons just below the air rock interface is needed. We also need to establish the absorption mean free path lengths in shallow rock depths for all cosmic radiation that is responsible for TCN production.

3. We must address systematic issues (e.g., spatial scaling, temporal variation, muonic contributions) so that the uncertainty in accuracy approaches our total random error. This will open the possibility of solving many new societal and geological problems using TCN. In additional to paleoclimate and neotectonic applications, at this level of accuracy the methods would be sufficiently reliable for many new risk assessments and environmental geology applications. For example, even at present accuracy levels, TCN have been instrumental in the characterization of the tectonic history of Yucca Mountain, the potential U.S. high level nuclear waste repository (Zreda et al., 1993; Gosse et al., 1996b).

4. We should continue to develop exposure techniques with different isotopes and mineral systems to further increase the universal applicability of the methods. For example, measurements of $^{10}$Be in magnetite (D. Lal, pers. comm.), $^{10}$Be in olivine (Kong et al., 1999), and $^{21}$Ne in garnet (W. Phillips, pers. comm.) are excellent prospects. In favorable instances other in situ cosmogenic nuclides, such as $^{41}$Ca, may be useful if the TCN : stable nuclide is sufficiently low for AMS analysis (Raisbeck and Yiou, 1979; Kubik et al., 1986; Klein et al., 1988; Middleton et al., 1989; Fink et al., 1990). As described in Sections 3.8 and 3.9, the short half-lives of $^{14}$C and $^{41}$Ca makes it the radionuclide of choice for establishing erosion rates of rock and sediment surfaces because (i) it will reach equilibrium within 25 kyr or less, and (ii) when expressed as a ratio with another spallogenic nuclide, the steady state erosion island is useful for younger exposure durations where other nuclide ratios are not. We need to support efforts at the U. Arizona (T. Jull and N. Lifton) and other institutions who are perfecting the extraction procedures for isolating cosmogenic $^{14}$C from quartz. The number of TCN applications and their reliability will increase significantly when this isotope system becomes routinely measured.

5. With improvements in chemistry and a reduction in required sample size, and a better understanding of production rates in the Holocene, cosmogenic nuclides can become more useful in paleoaltimetry, archeology, paleontology, and risk assessment. For instance, Phillips et al. (1997a) have used $^{36}$Cl to constrain the maximum exposure age of rock panels in Portugal that contain prehistoric engravings. With refinements in altitudinal scaling and the temporal variations in production, the technique will become important as a means to determine surface uplift history (for a precocious example see Brook et al., 1995a). Paleoaltimetry differs from rock uplift and denudation methods that are based on thermochronology or erosion rates, and does not depend on assumptions of paleowater depths that fossil-based paleoaltimetry methods require.

## Acknowledgements

Many of the experimental results and numerical simulations, as well as the time for the theoretical calculations, that are the basis for FMP's contributions to this paper were supported by the National Science Foundation through grants ATM-9117566, EAR-941780, and EAR-9206037. JCG was supported by NSF (OPP-9618844), DOE Yucca Mountain program at Los Alamos National Laboratory through C. Harrington, the Canada Geological Survey, and the University of Kansas Research Development Award (1996) and General Research Awards (1997 and 1998). JCG thanks Jeff Klein for clarifying many issues of the physics, mathematics, and uncertainty discussed in this review. Keran O'Brien gave useful suggestions for Sections 3.1–3.5. This manuscript benefited significantly from a thorough review by Bob Reedy. John Stone, Nat Lifton, Tom Davis, and Susan Ivy-Ochs are thanked for sharing preprints of submitted articles.

## References

Ackert, R.P.J., Barclay, D.J., Borns, H.W.J., Calkin, P.E., Kurz, M.D., Fastook, J.L., Steig, E.J., 1999. Measurements of past ice sheet elevations in interior West Antarctica. Science 286 (5438), 276–280.

Ackert, R.P.J., Singer, B.S., Guillou, H., Kurz, M.D., 1998. Cosmogenic $^{3}$He production rates over the last 125,000 years: calibration against $^{40}$Ar/$^{39}$Ar and unspiked K-Ar ages of lava flows. GSA Annual Meeting Abstracts with Programs 30 (7), A–299.

Acton, G.D., Petronotis, K.E., Cape, C.D., Rotto Ilg, S., Gordon, R.G., Bryan, P.C., 1996. A test of the geocentric axial dipole hypothesis

from an analysis of the skewness of the central marine magnetic anomaly. Earth and Planetary Science Letters 144, 337–346.

Albrecht, A., Herzog, G.F., Klein, J., Dezfouly-Arjomandy, B., Goff, F., 1993. Quaternary erosion and cosmic-ray-erosion history derived from $^{10}$Be and $^{26}$Al produced in situ-An example from Pajarito plateau, Valles caldera region. Geology 21, 551–554.

Allkofer, O.C. and Grieder, P.K.F., 1984. Cosmic rays on earth. Physics Data, 25-1. Fachinformationszentrum, Karlsruhe.

Anderson, R.S., Repka, J.L., Dick, G.S., 1996. Explicit treatment of inheritance in dating depositional surfaces using in situ $^{10}$Be and $^{26}$Al. Geology 24 (1), 47–51.

Anderson, S.W., Krinsley, D.H., Fink, J.H., 1994. Criteria for recognition of constructional silic lava flow surfaces. Earth Surface Processes and Landforms 19, 531–541.

Anthony, E.Y., Poths, J., 1992. $^{3}$He surface exposure dating and its implications for magma evolution in the Potrillo volcanic field, Rio Grande Rift, New Mexico, USA. Geochimica et Cosmochimica Acta 56, 4105–4108.

Armstrong, T.W., Chandler, K.C., Barish, J., 1973. Calculations of neutron flux spectra induced in the Earth's atmosphere by galactic cosmic rays. Journal of Geophysical Research 78 (16), 2715–2726.

Ayarbe, J.P., Phillips, F.M., Harrison, J.B.J., Elmore, D. and Sharma, P., 1998. Application of cosmogenic nuclides to fault-scarp chronology: Preliminary results from the Socorro Canyon Fault. In: Harrison, J.B.J. (Ed.), Soil, Water, and Earthquakes Around Socorro, New Mexico: Guidebook for the Rocky Mountain Cell of the Friends of the Pleistocene 1998 Field Conference, 10–13 September 1998, New Mexico Tech, Socorro, 12 pp.

Ballantyne, C., Stone, J.O.H., Fifield, L.K., 1998. Cosmogenic Cl-36 dating of postglacial landsliding at The Storr, Isle of Skye, Scotland. The Holocene 8 (3), 347–351.

Barbetti, M., Flude, K., 1979. Geomagnetic variation during the late Pleistocene period and changes in the radiocarbon time scale. Nature 279, 202–205.

Bard, E., Arnold, M., Fairbanks, R.G., Hamelin, B., 1993. $^{230}$Th-$^{234}$U and $^{14}$C ages obtained by mass spectrometry on corals. Radiocarbon 35, 191–195.

Bard, E., Hamelin, B., Fairbanks, R.G., Zindler, A., 1990a. Calibration of the $^{14}$C timescale over the past 30,000 years using mass spectrometric U-Th ages from Barbados corals. Nature 345, 405–410.

Bard, E., Hamelin, B., Fairbanks, R.G., Zindler, A., Mathieu, G., Arnold, M., 1990b. U/Th and $^{14}$C ages of corals from Barbados and their use for calibrating the $^{14}$C time scale beyond 9000 years BP. Nuclear Instruments and Methods in Physics B 52, 461–468.

Barker, D., Jull, A.T.J., Donahue, D.J., 1985. Excess Carbon-14 abundances in uranium ores: possible evidence for emission from uranium-series isotopes. Geophysical Research Letters 12 (10), 737–740.

Bartholomew, R.M., Boyd, A.W., Brown, F., Hawkings, R.C., Lounsbury, M., Merritt, W.F., 1955. The half-life of $^{36}$Cl. Canadian Journal of Physics 33, 43–48.

Baski, A.K., Hsu, V., McWilliams, M.O., Farrar, E., 1992. $^{40}$Ar/$^{39}$Ar dating of the Brunhes-Matuyama geomagnetic field reversal. Science 256, 356–357.

Beer, J., Raisbeck, G.M., Yiou, F. (Ed.), 1991. Time variations of 10Be and solar activity. The Sun in Time. The University of Arizona, Tucson, pp. 343–359.

Beer, J., Siegenthaler, U., Bonani, G., Finkel, R.C., Oeschger, H., Suter, M., Wölfli, W., 1988. Information on past solar activity and geomagnetism from $^{10}$Be in the Camp Century ice core. Nature 331, 675–679.

Bell, J.W., Brune, J.N., Liu, T., Zreda, M., Yount, J.C., 1998. Dating precariously balanced rocks in seismically active parts of California and Nevada. Geology 26 (6), 495–498.

Bentley, H.W., Phillips, F.M., Davis, S.N., 1986. Chlorine-36 in the terrestrial environment. In: Fritz, P., Fontes, J.-C. (Eds.), Handbook of Environmental Isotope Geochemistry. Elsevier, Amsterdam, pp. 427–480.

Bierman, P., 1996. Cosmocalibrate. Science 271, 1906.

Bierman, P., Gillespie, A., 1994. Continuing Education Manual on Geomorphic applications of in situ produced cosmogenic isotopes, Geological Society of America Annual Meeting, Seattle, Washington, pp. 100–102.

Bierman, P., Gillespie, A., Caffee, M., Elmore, D., 1995a. Estimating erosion rates and exposure ages with 36Cl produced by neutron activation. Geochimica et Cosmochimica Acta 59, 3779–3798.

Bierman, P., Larsen, P., Clapp, E., Clark, D., 1996. Refining estimates of $^{10}$Be and $^{26}$Al production rates. Radiocarbon 38 (1), 149.

Bierman, P., Turner, J., 1995. $^{10}$Be and $^{26}$Al evidence for exceptionally low rates of Australian bedrock erosion and the likely existence of pre-Pleistocene landscapes. Quaternary Research 44, 378–382.

Bierman, P.R., 1994. Using in situ produced cosmogenic isotopes to estimate rates of landscape evolution: A review from the geomorphic perspective. Journal of Geophysical Research 99 (B7), 13885–13896.

Bierman, P.R., Gillespie, A.R., Caffee, M.W., 1995b. Cosmogenic ages for earthquake recurrence intervals and debris flow fan deposition, Owens Valley, California. Science 270, 447–450.

Bierman, P.R., Marsella, K.A., Patterson, C., Davis, P.T., Caffee, M., 1999. Mid-Pleistocene cosmogenic minimum age limits for pre-Wisconsin glacial surfaces in southwestern Minnesota and southern Baffin Island: a multiple nuclide approach. Geomorphology 27, 25–40.

Bierman, P.R., Steig, E.J., 1996. Estimating rates of denudation using cosmogenic isotope abundances in sediment. Earth Surface Processes and Landforms 21, 125–139.

Bland, C.J., Cioni, G., 1968. Geomagnetic cut-off rigidities in non-vertical directions. Earth and Planetary Science Letters 4, 399–405.

Boella, G., Dilworth, C., Panetti, M., Scarsi, L., 1968. The atmospheric and leakage flux of neutrons produced in the atmosphere by cosmic ray interactions. Earth and Planetary Science Letters 4, 393–398.

Bourlès, D.L., Brown, E.T., Raisbeck, G.M., Yiou, F., Grandin, G. et al. 1992. Constraining the history of iron crust laterite systems using in situ produced cosmogenic $^{10}$Be and $^{26}$Al. EOS, Transactions of the American Geophysical Union 73, 173.

Brassart, J., Tric, E., Valet, J.-P., Herrero-Bervera, E., 1997. Absolute paleointensity between 60 and 40 ka from the Kohala Mountain (Hawaii). Earth and Planetary Science Letters 148, 141–156.

Briner, J.P., Swanson, T.W., 1998. Using inherited cosmogenic $^{36}$Cl to constrain glacial erosion rates of the Cordilleran ice sheet. Geology 26 (1), 3–6.

Brook, E.J., Brown, E.T., Kurz, M.D., Ackert, R.P., Raisbeck, G.M., Yiou, F., 1995a. Constraints on erosion and uplift rates of Pliocene glacial deposits in the Transantarctic Mountains using in situ-produced 10Be and 26Al. Geology 23, 1063–1066.

Brook, E.J., Kurz, M.D., 1993. Surface-exposure chronology using in situ $^{3}$He in Antarctic quartz sandstone boulders. Quaternary Research 39, 1–10.

Brook, E.J., Kurz, M.D., Achert, R.P.J., Denton, G.H., Brown, E.T., Raisbeck, G.M., Yiou, F., 1993. Chronology of Taylor Glacier advances in Arena Valley, Antarctica, using in situ cosmogenic $^{3}$He and $^{10}$Be. Quaternary Research 39, 11–23.

Brook, E.J., Kurz, M.D., Ackert, R.P., Raisbeck, G., Yiou, F., 1995b. Cosmogenic nuclide exposure ages and glacial history of late Quaternary Ross Sea drift in McMurdo Sound, Antarctica. Earth and Planetary Science Letters 131, 41–56.

Brook, E.J., Nesje, A., Lehman, S., Raisbeck, G., Yiou, F., 1996a. Cosmogenic nuclide exposure ages along a vertical transect in western Norway: implications for the height of the Fennoscandian Icesheet. Geology 24, 207–210.

Brook, J.E., Brown, E.T., Kurz, M.D., Raisbeck, G., Yiou, F., 1996b. An Antarctic perspective on in-situ cosmogenic nuclide production. Radiocarbon 38 (1), 150.

Brown, E.T., Bourles, D.L., Burchfiel, B.C., Oidong, D., Jun, L., Molnar, P., Raisbeck, G.M., Yiou, F., 1998a. Estimation of slip rates in the southern Tien Shan using cosmic ray exposure dates of abandoned alluvial fans. Geological Society of America Bulletin 110 (3), 377–386.

Brown, E.T., Bourles, D.L., Colin, F., Raisbeck, G.M., Yiou, F., Desgarceaux, S., 1995a. Evidence for muon-induced in situ production of $^{10}$Be in near-surface rocks from the Congo. Geophysical Research Letters 22, 703–706.

Brown, E.T., Brook, E.J., Raisbeck, G.M., Yiou, F., Kurz, M.D., 1992a. Effective attenuation lengths of cosmic rays producing $^{10}$Be and $^{26}$Al in quartz: Implications for surface exposure age dating. Geophysical Research Letters 19, 369–372.

Brown, E.T., Edmond, J.M., Raisbeck, G.M., Broules, D.L., Yiou, F., Measures, C.I., 1992b. Beryllium isotope geochemistry in tropical river basins. Geochimica et Cosmochimica Acta 56, 1607–1624.

Brown, E.T., Edmond, J.M., Raisbeck, G.M., Yiou, F., Kurz, M.D., Brook, E.J., 1991. Examination of surface exposure ages of Antarctic moraines using in situ produced $^{10}$Be and $^{26}$Al. Geochimica et Cosmochimica Acta 55, 2269–2283.

Brown, E.T., Stallard, R.F., Larsen, M.C., Bourles, D.L., Raisbeck, G.M., Yiou, F., 1998b. Determination fo predevelopment denudation rates of an agricultural watershed (Cayaguas River, Puerto Rico) using in-situ-produced $^{10}$Be in river-borne quartz. Earth and Planetary Science Letters 160 (3-4), 723–728.

Brown, E.T., Stallard, R.F., Larsen, M.C., Raisbeck, G.M., Yiou, F., 1995b. Denudation rates determined from the accumulation of in situ-produced $^{10}$Be in the Luquillo Experimental Forest, Puerto Rico. Earth and Planetary Science Letters 129, 193–202.

Brown, L., Klein, J., Middleton, R., Sacks, I.S., Tera, F., 1982. $^{10}$Be in island-arc volcanoes, and implications for subduction. Nature 299, 718–720.

Brown, L., Stensland, G.J., Klein, J., Middleton, R., 1989. Atmospheric deposition of $^{7}$Be and $^{10}$Be. Geochimica et Cosmochimica Acta 53, 135–142.

Brown, W.W., 1954. Cosmic-ray nuclear interactions in gases. Physical Reviews 93, 528–534.

Bruno, L.-A., Baur, H., Graf, T., Schluechter, C., Signer, P., Wieler, R., 1997. Dating of Sirius Group tillites in the Antarctic dry valleys with cosmogenic $^{3}$He and $^{21}$Ne. Earth and Planetary Science Letters 1–4 (1–4), 37–54.

Burbank, D.W., Leland, J., Fielding, E., Anderson, R.S., Brozovic, N., Reid, M.R., Duncan, C., 1996. Bedrock incision, rock uplift and threshold hillslopes in the northwestern Himalayas. Nature 379, 505–510.

Caffee, M.W., Goswami, J.N., Hohenberg, C.M., Marti, K., Reedy, R.C., 1988. Irradiation records in meteorites. In: Kerridge, J.F. (Ed.), Meteorites and the Early Solar System. University of Arizona Press, Tuscon, pp. 205–245.

Cerling, T.E., 1990. Dating geomorphic surfaces using cosmogenic $^{3}$He. Quaternary Research 33, 148–156.

Cerling, T.E., Craig, H., 1994a. Cosmogenic $^{3}$He production rates from 39°N to 46°N latitude, western USA and France. Geochimica et cosmochimica Acta 58, 249–255.

Cerling, T.E., Craig, H., 1994b. Geomorphology and in-situ cosmogenic isotopes. Annual Reviews of Earth and Planetary Sciences 22, 273–317.

Cerling, T.E., Webb, R.H., Poreda, R.J., Rigby, A.D., Melis, T.S., 1999. Cosmogenic $^{3}$He ages and frequency of late Holocene debris flows from Prospect Canyon, Grand Canyon, USA. Geomorphology 27 (1-2), 93–111.

Channell, J.E.T., Hodell, D.A., Lehman, B., 1997. Relative geomagnetic paleointensity and $^{18}$O at ODP site 983 (Gardar Drift, North Atlantic) since 350 ka. Earth and Planetary Science Letters 153, 103–118.

Charalambus, S., 1971. Nuclear transmutation by negative stopped muons and the activity induced by the cosmic-ray muons. Nuclear Physics A 166, 145–161.

Chauvin, A., Duncan, R.A., Bonhommet, N., Levi, S., 1989. Paleointensity of the Earth's magnetic field and K-Ar dating of the Louchadiere volcanic flow (Central France): New evidence for the Laschamp Excursion. Geophysical Research Letters 16 (10), 1189–1192.

Chauvin, A., Gillot, P.-Y., Bonhommet, N., 1991. Paleointensity of the Earth's magnetic field recorded by two late Quaternary volcanic sequences at the Island of La Réunion (Indian Ocean). Journal of Geophysical Research 96 (B2), 1981–2006.

Clark, D.H., Bierman, P., Gillespie, A.R., 1996. $^{10}$Be and $^{26}$Al production rates and a revised glacial chronology for the Sierra Nevada. Radiocarbon 38 (1), 152.

Clark, D.H., Bierman, P.R., Larsen, P., 1995. Improving in situ cosmogenic chronometers. Quaternary Research 44 (3), 366–376.

Clark, D.H., Gillespie, A.R., 1997. Timing and significance of late-glacial and holocene cirque glaciation in the Sierra Nevada, California. Quaternary International 38–39 (1), 21–38.

Clark, R.M., 1975. A calibration curve for radiocarbon dates. Antiquity 49, 251–266.

Coe, R.S., 1978. Geomagnetic paleointensities from radiocarbon-dated lava flows on Hawaii and the question of the Pacific Nondipole Low. Journal of Geophysical Research 83 (B4), 1740–1756.

Compton, A.H., 1933. A geographic study of cosmic rays. Physical Review 43 (6), 387–403.

Compton, R.R., 1962. Manual of Field Geology. Wiley, New York.

Constable, C., Tauxe, L., 1996. Towards absolute calibration of sedimentary paleointensity records. Earth and Planetary Science Letters 143, 269–274.

Conversi, M., 1950. Experiments on cosmic-ray mesons and protons at several altitudes and latitudes. Physical Reviews 79 (5), 749.

Craig, H., Poreda, R.J., 1986. Cosmogenic $^{3}$He in terrestrial rocks : The summit lavas of Maui. Proceedings of the National Academy of Science U.S.A., vol, 83, pp. 1970–1974.

Davis, P.T., Bierman, P.R., Marsella, K.A., Caffee, M.W., Southon, J.R., 1999. Cosmogenic analysis of glacial terrains in the eastern Canadian arctic: a test for inherited nuclides and the effectiveness of glacial erosion. Annals of Glacialogy 28.

Davis, R.J., Schaeffer, O.A., 1955. Chlorine-36 in nature. Annals New York Academy of Science 62, 105–122.

Dep, L., Elmore, D., Fabryka-Martin, J., Masarik, J., Reedy, R.C., 1994a. Numerical simulation of cosmogenic nuclide production in rocks for various exposure geometries, Abstracts of the 8th International Conference on Geochronology, Cosmochronology, and Isotope Geology, U.S. Geol. Surv. Bulletin 1107, pp. 80.

Dep, L., Elmore, D., Fabryka-Martin, J., Masarik, J., Reedy, R.C., 1994b. Production rate systematics of cosmogenic nuclides in terrestrial rocks: Monte Carlo approach of investigation $^{35}$Cl(n,g)$^{36}$Cl. Nuclear Instruments and Methods B 92, 321–325.

Dep, L., Elmore, D., Lipschutz, M., Vogt, S., Phillips, F.M., Zreda, M.G., 1994c. Depth dependence of cosmogenic neutron-capture-produced $^{36}$Cl in a terrestrial rock. Nuclear Instruments and Methods in Physics Research B 92, 301–307.

Dep, W.H.L., 1995. Cosmogenic radionuclide production in terrestrial rocks: Accelerator mass spectrometry measurements and Monte Carlo simulations. Ph.D. Thesis, Purdue University, West Lafayette, Indiana, 155 pp.

Dixit, K.R., 1955. The statistics of 29000 stars observed in nuclear emulsions in Kenya. Zeitschrift fur Naturforschung 10a, 339–341.

Dockhorn, B., Neumaier, S., Hartmann, F.J., Petitjean, C., Faestermann, H., Nolte, E., 1991. Determination of erosion rates with cosmic ray produced $^{36}$Cl. Zeitschrift Physik A 341, 117–119.

Donahue, D.J., Jull, A.J.T., Toolin, L.J., 1990. Radiocarbon measurements at the University of Arizona AMS Facility. Nuclear Instruments and Methods B52, 224–228.

Dunai, T.J., 2000. Scaling factors for production rates of in situ produced cosmogenic nuclides: a critical reevaluation. Earth and Planetary Science Letters 176, 157–169.

Dunne, J., Elmore, D., Muzikar, P., 1999. Scaling factors for the rates of production of cosmogenic nuclides for geometric shielding and attenuation at depth on sloped surfaces. Geomorphology 27 (1-2), 3–12.

Dyke, A.S., Morris, T.F., Green, D.E.C., 1991. Postglacial tectonic and sea level history of the central Canadian Arctic. Geological Survey of Canada Bulletin 397, 56.

Elmore, D., Phillips, F.M., 1987. Accelerator mass spectrometry for measurement of long-lived radioisotopes. Science 236, 543–550.

Elsasser, W., Ney, E.P., Winckler, J.R., 1956. Cosmic-ray intensity and geomagnetism. Nature 178 (4544), 1226–1227.

Endt, P.M., Van der Leun, C., 1973. Energy levels of $A = 21$–44 A-nuclei. V. Nuclear Physics A 214, 1–625.

Fabryka-Martin, J.T., 1988. Production of radionuclides in the earth and their hydrogeologic significance, with emphasis on chlorine-36 and iodine-129. Ph.D. Thesis, University of Arizona, Tucson, 400 pp.

Fairbanks, R.G., 1989. A 17,000-year glacio-eustatic sea level record: influence of glacial melting rates on the Younger Dryas event and deep-ocean circulation. Nature 342, 637–642.

Fang, X.-M., Li, J.J., Van der Voo, R., Niocaill, C.M., Dai, X.-R., Kemp, R.A., Derbyshire, E., Cao, J.X., Wang, J.-M., Wang, G., 1997. A record of the Blake Event during the last interglacial paleosol in the western Loess Plateau of China. Earth and Planetary Science Letters 146, 73–82.

Fink, D., Middleton, R., Klein, J., Sharma, P., 1990. $^{41}$Ca: Measurement by accelerator mass spectrometry and applications. Nuclear Instruments and Methods B 47, 79–96.

Finkel, R., Suter, M., 1993. AMS in the Earth Sciences: Technique and applications. Advances in Analytical Geochemistry 1, 1–114.

Fleming, A., Summerfield, M.A., Stone, J.O., Fifield, L.K., Cressweld, R.G., 1999. Denudation rates for the southern Drakensberg Escarpment, SE Africa, derived from in-situ-produced cosmogenic $^{36}$Cl; initial results. Journal of the Geological Society of London 156 (2), 209–212.

Frank, M., Schwarz, B., Baumann, S., Kubik, P.W., Suter, M., Mangini, A., 1997. A 200 kyr record of cosmogenic radionuclide production rate and geomagnetic field intensity from $^{10}$Be in globally stacked deep-sea sediments. Earth and Planetary Science Letters 149, 121–129.

Friedlander, M.W., 1989. Cosmic Rays. Harvard University Press, Cambridge, 160 pp.

Gaisser, T., 1990. Gamma rays and neutrinos as clues to the origin of high energy cosmic rays. Science 247, 1049–1056.

Gaisser, T.K., Stanev, T., 1998. Cosmic rays Review of Particle Physics. The European Physical Journal 3, 132–137.

Gall, R., 1960. The secular variation and the geomagnetic theory of cosmic radiation. Journal of Geophysical Research 65 (11), 3545–3558.

Gillespie, A.R., Bierman, P.R., 1995. Precision of terrestrial exposure ages and erosion rates estimated from analysis of cosmogenic isotopes produced in situ. Journal of Geophysical Research 100 (B12), 24,637–24,649.

Glasstone, S., 1955. Principles of Nuclear Reactor Engineering. D. Van Nostrand, Princeton, NJ.

Goldstein, G., 1966. Partial half-life for b-decay of $^{36}$Cl. Journal of Inorganic Nuclear Chemistry 28, 937–939.

Gosse, J., Dort, W., Sorenson, C., Steeples, D., Grimes, J., Hecht, G., 1997. Insights on the depositional age and rate of denudation of the pre-Illinioan till in Kansas from terrestrial cosmogenic nuclides. Geological Society of America Abstracts with Programs, North-Central Section 29 (4), A17.

Gosse, J., Klein, J., 1996. Production rate of in situ cosmogenic $^{10}$Be in quartz at high altitude and mid-latitude. Radiocarbon 38 (1), 154–155.

Gosse, J.C., 1994. Alpine glacial history reconstruction: 1. Application of the cosmogenic $^{10}$Be exposure age method to determine the glacial chronology of the Wind River Mountains, Wyoming, USA; 2. Relative dating of Quaternary deposits in the Rio Atuel Valley, Mendoza, Argentina. Dissertation Thesis, Lehigh University.

Gosse, J.C., Davis, P.T., Burr, G., Jull, A.T.J., Bozarth, S., Sorenson, C., Klein, J., Lawn, B., Dahms, D., 1999. Late Pleistocene/Holocene glacial and paleoclimate history of Titcomb Basin, Wind River Range, Wyoming based on lake sediments and cosmogenic nuclide dating. GSA Abstracts with Programs 31 (7), A–56.

Gosse, J.C., Evenson, E.B., Klein, J., Lawn, B., Middleton, R., 1995a. Precise cosmogenic $^{10}$Be measurements in western North America: Support for a global Younger Dryas cooling event. Geology 23 (10), 877–880.

Gosse, J.C., Gillespie, A.R., Harrington, C.D., Reedy, R.C., Poths, J., Klein, J., 1996a. Terrestrial cosmogenic nuclide dating: tested and ready for action. EOS, Transactions, American Geophysical Union 77 (29), 275–276.

Gosse, J.C., Grant, D.R., Klein, J., Klassen, R.A., Evenson, E.B., Lawn, B., Middleton, R., 1993. Significance of altitudinal weathering zones in Atlantic Canada, inferred from in situ produced cosmogenic radionuclides, Geological Society of America Annual Meeting, Boston, pp. A–394.

Gosse, J.C., Grant, D.R., Klein, J., Lawn, B., 1995b. Cosmogenic $^{10}$Be and $^{26}$Al constraints on weathering zone genesis, ice cap basal conditions, and Long Range Mountain (Newfoundland) glacial history. CANQUA-CGRG Conference Abstracts, Memorial University of Newfoundland, St. Johns, CA19.

Gosse, J.C., Harrington, C.D., Whitney, J.W., 1996b. Applications of in situ cosmogenic nuclides in the geologic site characterization of Yucca Mountain, Nevada, Materials Research Society Symposium Proceedings, pp. 799–806.

Gosse, J.C., Harrington, C.D., Whitney, J.W., 1996c. Applications of in situ cosmogenic nuclides in the geologic site characterization of Yucca Mountain, Nevada. Materials Research Society Symposium Proceedings 412, 799–806.

Gosse, J.C., Hecht, G., Mehring, N., Klein, J., Lawn, B., Dyke, A., 1998. Comparison of radiocarbon- and in situ cosmogenic nuclide-derived postglacial emergence curves for Prescott Island, Central Canadian Arctic. Geological Society of America Abstracts with Program 30 (7), 298.

Gosse, J.C., Klein, J., Evenson, E.B., Lawn, B., Middleton, R., 1995c. Beryllium-10 dating of the duration and retreat of the last Pinedale glacial sequence. Science 268, 1329–1333.

Gosse, J.C., Reedy, R., Harrington, C.D., Poths, J., 1996d. Overview of the Workshop on Secular Variations in the Production Rate of Cosmogenic Nuclides on Earth. Radiocarbon 38 (1), 135–147.

Gosse, J.C., Stone, J.O., submitted. Terrestrial cosmogenic nuclide methods passing milestones toward palaeo-altimetry. EOS.

Graf, T., Kim, J.S., Marti, K., Niedermann, S., 1995. Cosmic-ray-produced neon at the surface of the Earth in noble gas geochemistry and cosmochemistry. Terra Scientific Publishing Company, Tokyo, 115–123 pp.

Graf, T., Kohl, C.P., Marti, K., Nishiizumi, K., 1991. Cosmic-ray produced neon in Antarctic rocks. Geophysical Researc Letters 18, 203–206.

Graf, T., Marti, K., Wiens, R.C., 1996. The $^{21}$Ne production rate in a Si target at mountain altitudes. Radiocarbon 38 (1), 155.

Graham, I.J., 1996. Recent and planned research in cosmogenic isotopes at GNS. Radiocarbon 38 (1), 157.

Granger, D.E., Kirchner, J.W., Finkel, R., 1996. Spatially averaged long-term erosion rates measured from in-situ produced cosmogenic nuclides in alluvial sediment. Journal of Geology 104, 249–257.

Granger, D.E., Kirchner, J.W., Finkel, R.C., 1997. Quaternary downcutting rate of the New River, Virginia, measured from differential decay of cosmogenic $^{26}$Al and $^{10}$Be in cave-deposited alluvium. Geology 25 (2), 107–110.

Gubbins, D., Kelly, P., 1993. Persistent patterns in the geomagnetic field over the past 2.5 Myr. Nature 365, 829–832.

Guyodo, Y., Valet, J.-P., 1996. Relative variations in geomagnetic intensity from sedimentary records: the past 200,000 years. Earth and Planetary Science Letters 143, 23–36.

Guyodo, Y., Valet, J.-P., 1999. Global changes in intensity of the Earth's magnetic field during the past 800 kyr. Nature 399, 249–252.

Hampel, W., Schaeffer, O.A., 1979. $^{26}$Al in iron meteorites and the constancy of cosmic ray intensity in the past. Earth and Planetary Science Letters 42, 348–358.

Hampel, W., Takagi, J., Sakamoto, K., Tanaka, S., 1975. Measurement of muon-induced $^{26}$Al in terrestrial silicate rock. Journal of Geophysical Research 80 (26), 3757–3760.

Hancock, G.S., Anderson, R.S., Chadwick, O.A., Finkel, R.C., 1999. Dating fluvial terraces with $^{10}$Be and $^{26}$Al profiles: application to the Wind River, Wyoming. Geomorphology 27 (1-2), 41–60.

Handwerger, D.A., Cerling, T.E., Bruhn, R.L., 1999. Cosmogenic $^{14}$C in carbonate rocks. Geomorphology 27 (1-2), 13–24.

Hayakawa, S., 1969. Cosmic Ray Physics: Nuclear and Astrophysical Aspects. Wiley, New York.

Heidbreder, E., Pinkau, K., Reppin, C., Schönfelder, V., 1971. Measurement of the distribution in energy and angle of high-energy neutrons in the lower atmosphere. Journal of Geophysical Research 76, 2905–2916.

Heimsath, A.M., Dietrich, W.E., Nishiizumi, K., Finkel, R.C., 1997. The soil production function and landscape equilibrium. Nature 388 (6640), 358–361.

Heimsath, A.M., Dietrich, W.E., Nishiizumi, K., Finkel, R.C., 1999. Cosmogenic nuclides, topography, and the spatial variation of soil depth. Geomorphology 271, 2151–2172.

Heisinger, B., Niedermayer, M., Hartmann, J.F., Korschinek, G., Nolte, E., Morteani, G., Neumaier, S., Petitjean, C., Kubik, P., Synal, A., Ivy-Ochs, S., 1997. In-situ production of radionuclides at great depths. Nuclear Instruments and Methods in Physics Research B 123, 341–346.

Henken–Mellies, W.U., Beer, J., Heller, F., Hsü, K.J., Shen, C., Bonani, G., Hofmann, H.J., Suter, M., Wölfi, W., 1990. $^{10}$Be and $^{9}$Be in South Atlantic DSDP Site 519: Relation to geomagnetic reversals and to sediment composition. Earth and Planetary Science Letters 98, 267–276.

Hofmann, H.J., Beer, J., Bonani, G., von Gunten, H.R., Raman, S., Suter, M., Walker, R.L., Wölfli, W., Zimmermann, D., 1987. $^{10}$Be: Half-life and AMS-standards. Nuclear Instruments and Methods in Physics Research B 29, 32–36.

Holden, N.E., 1990. Total half-lives for selected nuclides. Pure and Applied Chemistry 62 (5), 941–958.

Hudson, G.B., Caffee, M.W., Beiringer, J., Ruiz, B., Kohl, C.P., Nishiizumi, K., 1991. Production rate and retention properties of cosmogenic $^{3}$He and $^{21}$Ne in quartz. EOS 72 (44), 575.

Hughes, E.E., Mann, W.B., 1964. The half-life of carbon-14: comments on the mass-spectrometic method. International Journal of Applied Radiation and Isotopes 15, 97–100.

Inn, K.G.W., Raman, S., Coursey, B.M., Fasset, J.D., Walker, R.I., 1987. Development of the NBS $^{10}$Be/$^{9}$Be isotopic standard reference material. Nuclear Instruments and Methods in Physics B 29, 27.

Ivy-Ochs, S., 1996. The dating of rock surfaces using in situ produced $^{10}$Be, $^{26}$Al, and $^{36}$Cl, with examples from Antarctica and the Swiss Alps. Ph. D. Thesis, Swiss Federal Institute of Technology Zurich, Zurich, 196 pp.

Ivy-Ochs, S., Kubik, P.W., Masarik, J., Wieler, R., Bruno, L., Schluechter, C., 1998. Preliminary results on the use of pyroxene for $^{10}$Be surface exposure dating. Schweizerische Mineralogische und Petrographische Mitteilungen 78 (3), 375–382.

Ivy-Ochs, S., Schlüchter, C., Kubik, P.W., Denton, G.H., 1999. Moraine exposure dates imply synchronous Younger Dryas glacier advance in the European Alps and in the Southern Alps of New Zealand. Geografiska Annaler, Series A: Physical Geography 81 (2), 313–323.

Ivy-Ochs, S., Schlüchter, C., Kubik, P.W., Dittrich-Hannen, B., Beer, J., 1995. Minimum $^{10}$Be exposure ages of early Pliocene for the Table Mountain Plateau and the Sirius Group at Mount Fleming, Dry Valleys, Antarctica. Geology 23, 1007–1010.

Jackson, L.E.J., Phillips, F.M., Shimamura, K., Little, E.C., 1997. Cosmogenic $^{36}$Cl dating of the Foothills Erratics train, Alberta, Canada. Geology 25 (3), 195–198.

Johnson, C.L., Constable, C.G., 1995. Paleosecular variation recorded by lavas over the last 5 Myr. Philosophical Transactions of the Royal Society of London A 354, 89–141.

Jokipii, J.R. (Ed.), 1991. Variations of the cosmic-ray flux with time. The Sun In Time. The University of Arizona, Tucson pp. 205–220.

Jull, A.J.T., Donahue, D.J., Linick, T.W., Wilson, G.C., 1991. Spallogenic $^{14}$C in high-altitude rocks and in Antarctic meteorites. Radiocarbon 31 (3), 719–724.

Jull, A.J.T., Lifton, N., Phillips, W.M., Quade, J., 1994a. Studies of the production rate of cosmic-ray produced $^{14}$C in rock surfaces. Nuclear Instruments and Methods in Physics Research B, 308-310.

Jull, A.T.J., Lal, D., Donahue, D.J., Mayewski, P., Lorius, C., Raynaud, D., Petit, J.R., 1994b. Measurements of cosmic-ray-produced $^{14}$C in firn and ice from Antartica. Nuclear Instruments and Methods B 92, 326–330.

Jull, A.T.J., Wilson, A.E., Donahue, D.J., Toolin, L.J., Burr, G.S., 1992. Measurements of cosmogenic $^{14}$C produced by spallation in high-altitude rocks. Radiocarbon 34, 737–744.

Kim, J., Englert, P.A.J., Finkel, R., Krofcheck, D., 1999. Cosmic-ray-induced $^{10}$Be and $^{26}$Al in subsurface samples from Macraes Flat, East Otago, New Zealand. EOS, Transactions American Geophysical Union 80 (17), F1166–F1167.

King, J.W., Banerjee, S.K., Marvin, J., 1983. A new rock-magnetic approach to selecting sediments for geomagnetic paleointensity studies: application to paleointensity for the last 4000 years. Journal of Geophysical Research 88 (B7), 5911–5921.

Kitagawa, H., van der Plicht, J., 1998. Atmospheric radiocarbon calibration to 45,000 yr B.P.: Late Glacial fluctuations and cosmogenic isotope production. Science 279, 1187–1190.

Klein, J., Evenson, E.B., Gosse, J.C., Lawn, B., Middleton, R., 1995. A preliminary attempt to date terraces using $^{10}$Be EOS, Trans. American Geophysical Union Annual Fall meeting 76, F684.

Klein, J., Giegengack, R., Middleton, R., Sharma, P., Underwood, J.R., Weeks, R.A., 1986a. Revealing histories of exposure using *in situ* produced $^{26}$Al and $^{10}$Be in Libyan Desert Glass. Radiocarbon 28 (2A), 547–555.

Klein, J., Giegengack, R., Middleton, R., Sharma, P., Underwood Jr.,, J.R., Weeks, W.A., 1986b. Revealing histories of exposure using in-situ produced $^{26}$Al and $^{10}$Be in Libyan desert glass. Radiocarbon 28, 547–555.

Klein, J., Gosse, J., 1996. Terrestrial factors that influence production rates. Radiocarbon 38 (1), 161–162.

Klein, J., Lawn, B., Gosse, J., Harrington, C., 1997. Can terrestrial cosmogenic Be-10 be measured in whole rock samples to decipher surface exposure histories. Geological Society of America Abstracts with Programs, 29(6).

Klein, J., Middleton, R., Fink, D., Sharma, P., 1988. $^{41}$Ca in terrestrial samples: applications in dating and geomorphology EOS, Transactions, American Geophysical Union, 1207.

Klein, J., Middleton, R., Tang, H.-Q., 1982. Modifications of an FN Tandem for Quantitative Measurements of $^{10}$Be. Nuclear Instruments and Methods 193, 601–616.

Kocharov, G.E., Blinov, A.V., Konstantinov, A.N., Levchenko, V.A., 1989. Temporal $^{10}$Be and $^{14}$C variations: a tool for paleomagnetic research. Radiocarbon 31 (2), 163–168.

Kohl, C.P., Nishiizumi, K., 1992. Chemical isolation of quartz for measurement of in situ-produced cosmogenic nuclides. Geochimica et Cosmochimica Acta 56, 3583–3587.

Kok, Y.S., Tauxe, L., 1996a. Saw-toothed pattern of relative paleointensity records and cumulative viscous remanence. Earth and Planetary Science Letters 137, 95–99.

Kok, Y.S., Tauxe, L., 1996b. Saw-toothed pattern of sedimentary paleointensity records explained by cumulative viscous remanence. Earth and Planetary Science Letters 144, E9–E14.

Kong, P., Nishiizumi, K., Finkel, R.C., Caffee, M.W., 1999. In situ produced cosmogenic $^{10}$Be and $^{26}$Al in olivine. Eos, Transactions, American Geophyisical Union 1999 Fall Meeting 80 (46), F1166.

Kono, M., Hiroi, O., 1996. Paleosecular variation of field intensities and dipole moments. Earth and Planetary Science Letters 139, 251–262.

Kovacheva, M., 1980. Summarized results of the archaeomagnetic investigation of the geomagnetic field variation for the last 8000 yr in south-eastern Europe. Geophysical Journal of the Royal Astronomical Society 61, 57–64.

Kovacheva, M., 1982. Archaeomagnetic investigations of geomagnetic secular variations. Philosophical Transactions of the Royal Society of London A 306, 79–86.

Kubik, P.W., Elmore, D., Conard, D., Nishiizumi, K., Arnold, J.R., 1986. Determination of cosmogenic $^{41}$Ca in a meteorite with tandem accelerator mass spectrometry. Nature 319, 568–570.

Kubik, P.W., Ivy-Ochs, S., Masarik, J., Frank, M., Schlüchter, C., 1998. $^{10}$Be and $^{26}$Al production rates deduced from an instantaneous event within the dendro-calibration curve, the landslide of Köfels Ötz, Valley Austria. Earth and Planetary Science Letters 161 (1–4), 231–241.

Kubik, P.W., Korschinek, G., Nolte, E., 1984. Accelerator mass spectrometry of $^{36}$Cl in limestone and some palaeontological samples using completely stripped ions. Nuclear Instruments and Methods B 5, 326–330.

Kurz, M.D., 1986a. Cosmogenic helium in a terrestrial igneous rock. Nature 320, 435–439.

Kurz, M.D., 1986b. In situ production of terrestrial cosmogenic helium and some applications to geochronology. Geochimica et Cosmochimica Acta 50, 2855–2862.

Kurz, M.D., Colodner, D., Trull, T.W., Moore, R.B., O'Brien, K., 1990. Cosmic ray exposure dating with in situ produced cosmogenic $^{3}$He : Results from young Hawaiian lava flows. Earth and Planetary Science Letters 97, 177–189.

Kurz, M.D., O'Brien, P., Garcia, M., Frey, F.A., 1985. Isotopic evolution of Haleakala volcano: Primordial, radiogenic and cosmogenic, helium. EOS 66, 1120.

Lal, D., 1958. Investigations of nuclear interactions produced by cosmic rays. Ph.D. Thesis, Tata Institute of Fundamental Research, Bombay.

Lal, D., 1987a. Cosmogenic nuclides produced in situ in terrestrial solids. Nuclear Instruments and Methods in Physics Research B 29, 238–245.

Lal, D., 1987b. Production of $^{3}$He in terrestrial rocks. Chemical Geology (Isotope Geoscience Section) 66, 89–98.

Lal, D., 1988. In situ-produced cosmogenic isotopes in terrestrial rocks. Annual Review of Earth and Planetary Sciences 16, 355–388.

Lal, D., 1991. Cosmic ray labeling of erosion surfaces: in situ nuclide production rates and erosion rates. Earth and Planetary Science Letters 104, 424–439.

Lal, D., 1996. On cosmic-ray exposure ages of terrestrial rocks: a suggestion. Radiocarbon 37 (3), 889–898.

Lal, D., Arnold, J.R., 1985. Tracing quartz through the environment. Proceedings of the Indian Academy of Science (Earth Planetary Science Section) 94, 1–5.

Lal, D., Arnold, J.R., Honda, M., 1960. Cosmic-ray production rates of $Be^{7}$ in oxygen, and $P^{32}$, $P^{33}$, $S^{35}$ in argon at mountain altitudes. Physics Reviews 118, 1626.

Lal, D., Arnold, J.R., Nishiizumi, K., 1985. Geophysical records of at tree: new application for studying geomagnetic field and solar activity changes during the past 104 years. Meteoritics 20, 403–414.

Lal, D., Craig, H., Wacker, F., Poreda, R., 1989. $^{3}$He in diamonds: The cosmogenic component. Geochimica et Cosmochimica Acta 53, 569–574.

Lal, D., Malhotra, P.K., Peters, B., 1958. On the production of radioisotopes in the atmosphere by cosmic radiation and their application to meteorology. Journal of Atmospheric and Terrestrial Physics 12, 306.

Lal, D., Peters, B., 1967. Cosmic ray produced radioactivity on the earth. In: Sitte, K. (Ed.), Handbuch der Physik. Springer, Berlin, pp. 551–612.

Lanci, L., Lowrie, W., 1997. Magnetostratigraphic evidence that 'tiny wiggles' in the oceanic magnetic anomaly record represent geomagnetic paleointensity variations. Earth and Planetary Science Letters 148, 581–592.

Larsen, P.L., Bierman, P.R., Caffee, M., 1995. Preliminary in situ production rates of cosmogenic $^{10}$Be and $^{26}$Al over the past 21.5 ky from the terminal moraine of the Laurentide ice sheet, north-central New Jersey. Geological Society of America Abstracts with Programs 27, A59.

Laughlin, A.W., Poths, J., Healey, H.A., Reneau, S., WoldeGabriel, G., 1994. Dating of Quaternary basalts using cosmogenic $^{3}$He and $^{14}$C methods with implications for excess $^{40}$Ar. Geology 22, 135–138.

Lavielle, B., Marti, K., Jeannot, J.-P., Nishiizumi, K., Caffee, M., 1999. The $^{36}$Cl–$^{36}$Ar–$^{40}$K–$^{41}$K records and cosmic ray production rates in iron meteorites. Earth and Planetary Science Letters 170, 93–104.

Lederer, C.M., Shirely, V.S., 1978. Table of Isotopes. 7th edition. Wiley, New York, 690 pp.

Leland, J., Reid, M.R., Burbank, D.W., Finkel, R., Caffee, M., 1998. Incision and differential bedrock uplift along the Indus River near Nanga Parbat, Pakistan Himalaya, from $^{10}$Be and $^{26}$Al exposure age dating of bedrock straths. Earth and Planetary Science Letters 154, 93–107.

Lemaitre, G., Vallarta, M.S., 1933. On Compton's latitude effect of cosmic radiation. Physical Review 43 (2), 87–91.

Libby, F., Anderson, E.C., Arnold, J.R., 1949. Age determination by radiocarbon content: World-wide assay of natural radiocarbon. Science 109, 227–228.

Licciardi, J.M., Kurz, M.D., Clark, P.U., Brook, E.J., 1999. Calibration of cosmogenic $^{3}$He production rates from Holocene lava flows in Oregon, USA, and effects of the Earth's magnetic field. Earth and Planetary Science Letters 172 (3-4), 261–271.

Lifton, N.A., Jull, A.J.T., Quade, J., submitted. A new extraction technique and production rate estimate for in situ cosmogenic $^{14}$C in quartz. Geochemica et Cosmochimica Acta.

Light, E.S., Merker, M., Verschell, H.J., Mendell, R.B., Korff, S.A., 1973. Time dependent worldwide distribution of atmospheric neutrons and of their products 2. Calculation. Journal of Geophysical Research 78 (16), 2741–2762.

Lingenfelter, R.E., 1963. Production of $^{14}$C by cosmic ray neutrons. Reviews of Geophysics 1 (1), 35–55.

Lingenfelter, R.E., Flamm, E.J., 1964. Solar neutrons and the earth radiation belts. Science 144, 292–294.

Litherland, A.E., 1987. Fundamentals of accelerator mass spectrometry. Philosophical Transactions of the Royal Society of London A 323, 5–21.

Liu, B., Phillips, F.M., Fabryka-Martin, J.T., Fowler, M.M., Stone, W.D., 1994. Cosmogenic $^{36}$Cl accumulation in unstable landforms, 1. Effects of the thermal neutron distribution. Water Resources Research 30, 3115–3125 (31, 1159).

Lockwood, J.A., Yingst, H.E., 1956. Correlation of meteorological parameters with cosmic-ray intensity. Physical Reviews 104, 1718–1722.

Looosli, H.H., 1983. A dating method with argon-39. Earth and Planetary Science Letters 63, 51–62.

Macciaroli, P., Giegengack, R., Klein, J., Middleton, R., Lawn, B., 1994. Late Quaternary glaciation of exposed rock surfaces along a ridge

of the Appalachian Mountains, dated using $^{26}$Al and $^{10}$Be produced in situ. Geological Society of America. Abstracts with Programs 26, A–125.

Mankinen, E.A., Champion, D.E., 1993. Latest Pleistocene and Holocene geomagnetic paleointensity on Hawaii, Science 412–416.

Marsella, K.A., Bierman, P.R., Davis, P.T., Caffee, M.W., in press. Cosmogenic $^{10}$Be and $^{26}$Al ages for the last glacial maximum, eastern Baffin Island, arctic Canada. Geological Society of America Bulletin.

Marti, K., Craig, H., 1987. Cosmic-ray produced neon and helium in the summit lavas of Maui. Nature 325, 335–337.

Martinson, D.G., Pisias, N.G., Hays, J.D., Imbrie, J., Moore, T.C.J., Shackleton, N.J., 1987. Age dating and the Orbital Theory of the Ice Ages: Development of a high-resolution 0 to 300000 year chronostratigraphy. Quaternary Research 27, 1–29.

Masarik, J., Beer, J., 1999. Simulation of particle flux and cosmogenic nuclide production in the Earth's atmosphere. Journal of Geophysical Research 104 (D10), 12,099–12,111.

Masarik, J., Reedy, R.C., 1995. Terrestrial cosmogenic-nuclide production systematics calculated from numerical simulations. Earth and Planetary Science Letters 136, 381–395.

Masarik, J., Reedy, R.C., 1996. Monte carlo simulation of in-situ produced cosmogenic nuclides. Radiocarbon 38 (1), 163–164.

Mazaud, A., Laj, C., Bard, E., Arnold, M., Tric, E., 1991. Geomagnetic field control of $^{14}$C production over the last 80 ka: implications for the radiocarbon time scale. Geophysical Research Letters 18, 1885–1888.

McCarroll, D., Nesje, A., 1993. The vertical extent of ice sheet in Nordfjord, western Norway: measuring degree of rock surface weathering. Boreas, pp. 255–265.

McClelland, E., Briden, J.C., 1996. An improved methodology for Thellier-type paleointensity determination in igneous rocks and its usefulness for verifying primary thermoremanence. Journal of Geophysical Research 101 (B10), 21,995–22,013.

McElhinny, M.W., McFadden, P.L., 1997. Palaeosecular variation over the past 5 Myr based on a new generalized database. Geophysical Journal International 131, 240–252.

McElhinny, M.W., McFadden, P.L., Merrill, R.T., 1996. The time-averaged paleomagnetic field 0-5 Ma. Journal of Geophysical Research 101 (B11), 25,007–25,027.

McElhinny, M.W., Senanayake, W.E., 1982. Variations in the geomagnetic dipole 1: the past 50,000 years. Journal of Geomagnetism and Geoelectricity 34, 39–51.

McHargue, L.R., Damon, P.E., 1991. The global beryllium 10 cycle. Reviews of Geophysics 29 (2), 141–158.

McHargue, L.R., Damon, P.E., Donahue, D.J., 1995. Enhanced cosmic-ray production of $^{10}$Be coincident with the Mono Lake and Laschamp geomagnetic excursions. Geophysical Research Letters 22 (5), 659–662.

Merker, M., Light, E.S., Verschell, H.J., Mendell, R.B., Korff, S.A., 1973. Time dependent worldwide distribution of atmospheric neutrons and of their products 1. Fast neutron observations. Journal of Geophysical Research 78, 2727–2740.

Merrill, R.T., McElhinny, M.W., 1983. In: The Earth's magnetic field, its history, origin, and planetary perspective International Geophysical Series, 32. Academic Press, New York, pp. 401.

Merrill, R.T., McElhinny, M.W., McFadden, P.L., 1996. The Magnetic Field of the Earth: Paleomagnetism, the Core, and the Deep Mantle. International Geophysics Series, 63. Academic Press, San Diego, 531 pp.

Meynadier, L., Valet, J.-P., 1996. Post-depositional realignment of magnetic grains and asymmetrical saw-tooth patterns of magentization intensity. Earth and Planetary Science Letters 140, 123–132.

Meynadier, L., Valet, J.-P., Weeks, R., Shackleton, N.J., Hagee, V.L., 1992. Relative geomagnetic intensity of the field during the last 140 ka. Earth and Planetary Science Letters 114, 39–57.

Middleton, R., Brown, L., Dezfouly-Arjomandy, B., Klein, J., 1993. On $^{10}$Be standards and the half life of $^{10}$Be. Nuclear Instruments and Methods in Physics Research B 82, 399–403.

Middleton, R., Fink, D., Klein, J., Sharma, P., 1989. $^{41}$Ca concentrations in modern bone and their implications for dating. Radiocarbon 31 (3), 305–309.

Middleton, R., Klein, J., 1987. $^{26}$Al: measurement and applications. Philosophical Transactions of the Royal Society of London A 323, 121–143.

Middleton, R., Klein, J., Brown, L., Tera, F., 1984. $^{10}$Be in Commercial Beryllium. Nuclear Instruments and Methods B 5, 511–513.

Middleton, R., Klein, J., Raisbeck, G.M., Yiou, F., 1983. Accelerator Mass Spectrometry with $^{26}$Al. Nuclear Instruments and Methods in Physics Research 218, 430–438.

Millikan, R.A., Neher, H.V., 1936. A precision world survey of sea-level cosmic-ray intensities. Physical Review 50, 15–24.

Montaser, A., 1998. In: Inductively coupled plasma mass spectrometry. Wiley, New York, pp. 964.

Moore, G.L., 1989. Introduction to Inductively Coupled Plasma Atomic Emission Spectrometry. Elsevier, Amsterdam, 340 pp.

Morris, J., Gosse, J.C., Brachfeld, S., submitted. Cosmogenic $^{10}$Be and the Solid Earth: Studies in Geomagnetism, Subduction Zone Processes, and Active Tectonics. Reviews of Mineralogy, Spec. Vol.

Morris, J.D., 1991. Applications of $^{10}$Be to problems in the earth sciences. Annual Review of Earth and Planetary Science 19, 313–350.

Morrison, P., Pine, J., 1955. Radiogenic origin of the Helium isotopes in rock. Annals of the New York Academy of Sciences 62, 71–92.

Moscariello, A., Pugin, A., Wildi, W., Beck, C., Chapron, E., de Batist, M., Girardclos, S., Ivy-Ochs, S., Rachoud-Schneider, A.-M., Signer, C., van Clauwenberghe, T., 1998. Deglaciation wuermienne dans des conditions lacustres a la terminaison occidentale du bassin lemanique. Eclogae Geologicae Helvetiae 91 (2), 185–201.

Negrini, R.M., Verosub, K.L., Davis, J.O., 1987. Long-term non-geocentric axial dipole directions and a geomagnetic excursion from the Middle Pleistocene sediments of the Humboldt River Canyon, Pershing County, Nevada, U.S.A. Journal of Geophysical Research 92, 10,617–10,628.

Niedermann, S., Graf, T., Kim, J.S., Kohl, C.P., Marti, K., Nishiizumi, K., 1994. Cosmic-ray produced $^{21}$Ne in terrestrial quartz: the neon inventory of Sierra Nevada quartz separates. Earth and Planetary Science Letters 125, 341–355.

Niedermann, S., Graf, T., Marti, K., 1993. Mass spectrometric identification of cosmic-ray-produced neon in terrestrial rocks with multiple neon components. Earth and Planetary Science Letters 118, 65–73.

Nishiizumi, K., Finkel, R.C., Caffee, M.W., Southon, J.R., Kohl, C.P., Arnold, J.R., Olinger, C.T., Poths, J. and Klein, J., 1994. Cosmogenic production of $^{10}$Be and $^{26}$Al on the surface of the earth and underground, Eighth International Conference on Geochronology, Cosmochronology and Isotope Geochemistry (U.S. Geol. Surv. Circular 1107), Berkeley, California, 234 pp.

Nishiizumi, K., Finkel, R.C., Klein, J., Kohl, C.P., 1996. Cosmogenic production of $^{7}$Be and $^{10}$Be in water targets. Journal of Geophysical Research 101, 22,225–22,232.

Nishiizumi, K., Kohl, C.P., Arnold, J.R., Klein, J., Fink, D., Middleton, R., 1991a. Cosmic ray produced $^{10}$Be and $^{26}$Al in Antarctic rocks: exposure and erosion history. Earth and Planetary Science Letters 104 (2/4), 440–454.

Nishiizumi, K., Kohl, C.P., Shoemaker, E.M., Arnold, J.R., Klein, J., Fink, D., Middleton, R., 1991c. In situ $^{10}$Be - $^{26}$Al exposure ages at Meteor Crater, Arizona. Geochimica et Cosmochimica Acta 55, 2699–2703.

Nishiizumi, K., Lal, D., Klein, J., Middleton, R., Arnold, J.R., 1986. Production of $^{10}$Be and $^{26}$Al by cosmic rays in terrestrial quartz in situ and implications for erosion rates. Nature 319, 134–135.

Nishiizumi, K., Elmore, D., Ma, X.Z., Arnold, J.R., 1984. $^{10}$Be and $^{26}$Cl depth profiles in an Apollo 15 drill core. Earth and Planetary Science Letters 70, 157–163.

Nishiizumi, K., Winterer, E.L., Kohl, C.P., Lal, D., Arnold, J.R., Klein, J., Middleton, R., 1989. Cosmic ray production rates of $^{10}$Be and $^{26}$Al in quartz from glacially polished rocks. Journal of Geophysical Research 94 (B12), 17,907–17,915.

Nishiizumi, N., Klein, J., Middleton, R., Craig, H., 1990. Cosmogenic $^{10}$Be, $^{26}$Al, and $^{3}$He in olivine from Maui lavas. Earth and Planetary Science Letters 98, 263–266.

Norris, T.L., Gancarz, A.J., Rokop, D.J., Thomas, K.W., 1993. Half-life of $^{26}$Al. Journal of Geophysical Research, Proceedings of the Fourteenth Lunar and Planetary Science Conference Part 1 (suppl. 88), pp. B331–333.

O'Brien, K., 1979. Secular variations in the production of cosmogenic isotopes in the earth's atmosphere. Journal of Geophysical Research 84 (A2), 423–431.

O'Brien, K., 1996. Cosmic-ray neutrons at ground level: temporal and geodetic variations. Radiocarbon 38 (1), 165.

O'Brien, K., Burke, G.D., 1973. Calculated cosmic ray neutron monitor response to solar modulation of galactic cosmic rays. Journal of Geophysical Research 78 (16), 3013–3019.

O'Brien, K., Sandmeier, H.A., Hansen, G.E., Campbell, J.E., 1978. Cosmic-ray-induced neutron background sources and fluxes for geometries of air over water, ground, iron, and aluminum. Journal of Geophysical Research 83, 114–120.

Ochs, M., Ivy-Ochs, S., 1997. The chemical behavior of Be, Al, Fe, Ca, and Mg during AMS target preparation from terrestrial silicates modeled with chemical speciation calculations. Nuclear Instruments and Methods in Physics Research B 123, 235–240.

Ohno, M., Hamano, Y., 1992,. Geomagnetic poles over the last 10,000 years. Geophysical Research Letters 19 (16), 1715–1718.

Onuchin, A.A., Burenina, T.A., 1996. Climatic and geographic patterns in snow density dynamics, Northern Eurasia. Arctic and Alpine Research 28 (1), 99–103.

Olinger, C.T., Poths, J., Nishiizumi, K., Kohl, C.P., Finkel, R.C., Caffee, M.W., Southon, J., Proctor, I., 1992. Attenuation lengths of cosmogenic production of $^{26}$Al, $^{10}$Be, and $^{21}$Ne in Bandelier Tuff. EOS 73 (14), 185.

Peck, J.A., King, J.W., Colman, S.M., Kravchinsky, V.A., 1996. An 84-kyr paleomagnetic record from the sediments of Lake Baikal, Siberia. Journal of Geophysical Research 101, 11,365–11,385.

Peng, T.-H., 1989. Changes in ocean ventilation rates over the last 7000 years based on $^{14}$C variations in the atmosphere and oceans. Radiocarbon 31 (3), 481–492.

Phillips, F.M., 1996. Chronology for fluctuations in Late Pleistocene Sierra Nevada glaciers and lakes. Science 274, 749–751.

Phillips, F.M., Flinsch, M., Elmore, D., Sharma, P., 1997a. Maximum ages of the Côa valley (Portugal) engravings measured with chlorine-36. Antiquity 71, 100–104.

Phillips, F.M., Leavy, B.D., Jannik, N.O., Elmore, D., Kubik, P.W., 1986. The accumulation of cosmogenic Chlorine- in rocks: a method for surface exposure dating. Science 231, 41–43.

Phillips, F.M., Stone, W.D., Fabryka-Martin, J., 2000. An improved approach to calculating low-energy cosmic ray neutron fluxes near the land/atmosphere interface. Chemical Geology submitted.

Phillips, F.M., Zreda, M.G., Elmore, D., Sharma, P., 1996a. A reevaluation of cosmogenic $^{36}$Cl production rates in terrestrial rocks. Geophysical Research Letters 23 (9), 949–952.

Phillips, F.M., Zreda, M.G., Gosse, J.C., Klein, J., Evenson, E.B., Hall, R.D., Chadwick, O.A., Sharma, P., 1997b. Cosmogenic $^{36}$Cl and $^{10}$Be ages of Quaternary glacial and fluvial deposits of the Wind River Range, Wyoming. Geological Society of America Bulletin 109 (11), 1453–1463.

Phillips, F.M., Zreda, M.G., Smith, S.S., Elmore, D., Kubik, P.W., Dorn, R.I., Roddy, D.J., 1991. Age and geomorphic history of Meteor Crater, Arizona, from cosmogenic $^{36}$Cl and $^{14}$C in rock varnish. Geochimica et Cosmochimica Acta 55 (9), 2695–2698.

Phillips, F.M., Zreda, M.G., Smith, S.S., Elmore, D., Kubik, P.W., Sharma, P., 1990. Cosmogenic chlorine-36 chronology for glacial deposits at Bloody Canyon, Eastern Sierra Nevada. Science 248, 1529–1532.

Phillips, W.M., Lifton, N.A., Quade, J., Jull, A.T.J., 1994. In situ produced $^{14}$C in late Quaternary lava flows of the Zuni–Bandera volcanic field, New Mexico, New Mexico Geological Society Ann Spring Mtg Proceeding VolNMIMT, Socorro, NM, 34 pp.

Phillips, W.M., McDonald, E.V., Reneau, S.L., Poths, J., 1996c. Resolving inherited cosmogenic nuclides in soils: a case study from the Pajarito Plateau: New Mexico, USA. Geological Society of America Abstracts with Programs 28 (7), A180.

Phillips, W.M., McDonald, E.V., Reneau, S.L., Poths, J., 1998. Dating soils and alluvium with cosmogenic $^{21}$Ne depth profiles: case studies from the Pajarito Plateau, New Mexico, USA. Earth and Planetary Science Letters 160, 209–223.

Plummer, M.A., Phillips, F.M., Fabryka-Martin, J., Turin, H.J., Wigand, P.E., Sharma, P., 1997. Chlorine-36 in fossil rat urine: An archive of cosmogenic nuclide deposition over the past 40,000 years. Science 277, 538–541.

Pomerantz, M.A., 1971. Cosmic Rays. Van Nostrand Reinhold, New York, 168 pp.

Pomerantz, M.A., Potnis, V.R., Sandstrom, A.E., 1960. The cosmic-ray equator and the Earth's magnetic field. Journal of Geophysical Research 65 (11), 3539–3543.

Poreda, R.J., Cerling, T.E., 1992. Cosmogenic neon in recent lavas from the western United States. Geophysical Research Letters 19, 1863–1866.

Poths, J., Anthony, E.Y., Williams, W.J., Heizler, M., McIntosh, W.C., 1996. Comparison of dates fror young basalts from the $^{40}$Ar/$^{39}$Ar and cosmogenic Helium techniques. Radiocarbon 38 (1), 167.

Quenby, J.J., 1966. The interaction of cosmic rays with the solar and terrestrial magnetic fields 415–426.

Quenby, J.J., Webber, W.R., 1959. Cosmic ray cut-off rigidities and the Earth's magnetic field. Philosphical Magazine 4, 90–113.

Quenby, J.J., Wenk, G.J., 1962. Cosmic ray threshold rigidities and the Earth's magnetic field. Philosophical Transactions 7, 1457–1485.

Quidelleur, X., Valet, J.-P., Courtillot, V., Hulot, G., 1994. Long-term geometry of the geomagnetic field for the last five million years: An updated secular variation database. Geophysical Research Letters 21 (15), 1639–1642.

Raisbeck, G.M., Yiou, F., 1979. Possible use of $^{41}$Ca for radioactive dating. Nature 277, 42–43.

Raisbeck, G.M., Yiou, F., Bourles, D., Kent, D.V., 1985. Evidence for an increase in cosmogenic $^{10}$Be during a geomagnetic reversal. Nature 315, 315–317.

Raisbeck, G.M., Yiou, F., Bourles, D., Lorins, C., Jouzel, J., Barkov, N.I., 1987. Evidence for two intervals of enhanced $^{10}$Be deposition in Antarctic ice during the last glacial period. Nature 326, 273–277.

Raisbeck, G.M., Yiou, F., Jouzel, J., Petit, J.R., Barkov, N.I., Bard, E., 1992. $^{10}$Be deposition at Vostok, Antarctica during the last 50,000 years and its relationship to possible cosmogenic production variations during this period. In: Bard, E., Broecker, W.S. (Eds.), Nato ASI Series: The Last Deglaciation: Absolute and Radiocarbon Chronologies. Springer, Berlin, pp. 127–139.

Raisbeck, G.M., Yiou, F., Zhou, S.Z., 1994. Paleointensity puzzle. Nature 371, 207–208.

Reedy, R.C., Arnold, J.R., Lal, D., 1983. Cosmic-ray record in solar system matter. Science 219 (4581), 127–134.

Reedy, R.C., Nishiizumi, K., Lal, D., Arnold, J.R., Englert, P.A.J., Klein, J., Middleton, R., Jull, A.J.T., Donahue, D.J., 1994a. Simulations of terrestrial in-situ cosmogenic-nuclide production. Nuclear Instruments and Methods in Physics Research B 92, 297–300.

Reedy, R.C., Tuniz, C., Fink, D., 1994b. Report on the Workshop on Production Rates of Terrestrial In-situ-produced cosmogenic nuclides. Nuclear Instruments and Methods B 92, 335–339.

Repka, J.L., Anderson, R.S., Finkel, R.C., 1997. Cosmogenic dating of fluvial terraces, Fremont River, Utah. Earth and Planetary Science Letters 152, 59–73.

Rightmire, V.R.A., Kohman, T.P., Hintenberger, H., 1958. Uber die Halbwertszeit des langlebigen $^{26}$Al. Zeitschrift fur Naturforschung 13A, 847–853.

Roberts, A.P., Lehman, B., Weeks, R.J., Verosub, K.L., Laj, C., 1997. Relative paleointensity of the geomagnetic field over the last 200,000 years from ODP sites 883 and 884, North Pacific Ocean. Earth and Planetary Science Letters 152, 11–23.

Roberts, A.P., Verosub, K.L., Negrini, R.M., 1994. Middle/Late Pleistocene relative paleointensity of the geomagnetic field from lacustrine sediments, Lake Chewaucan, western United States. Geophysical Journal International 118, 101–110.

Robinson, C., Raisbeck, G.M., Yiou, F., Lehman, B., Laj, C., 1995. The relationship between $^{10}$Be and geomagnetic field strength records in central North Atlantic sediments during the last 80 ka. Earth and Planetary Science Letters 136, 551–557.

Roederer, J.G., 1952. Uber die absorption der nukleonenkomponente der kosmischen strahlung in 21-o geomagnetischer breite. Zeitschrift fur Naturforschung 7A, 765–771.

Rossi, B.R., 1948. Interpretation of cosmic-ray phenomena. Reviews of Modern Physics 20, 537–583.

Rossi, B.R., 1964. Cosmic Rays. McGraw Hill Book Company, New York, 268 pp.

Sandstrom, A.E., 1958. Cosmic ray soft component measurements during a flight from Scandinavia across the North Pole and around Asia and Europe. Nuovo Cimento VIII (X, Suppl.), 263–276.

Sarda, P., Staudacher, T., Allegre, C.J., Lecomte, A., 1993. Cosmogenic neon and helium at Réunion: measurement of erosion rate. Earth and Planetary Science Letters 119, 405–417.

Schaefer, J., Ivy-Ochs, S., Wieler, R., Leya, I., Baur, H., Denton, G., Schluechter, C., 1999. Cosmogenic noble gas studies in the oldest landscape on Earth; surface exposure ages of the Dry Valleys, Antarctica. Earth and Planetary Science Letters 167 (3-4), 175–182.

Schneider, D.A., Mello, G.A., 1996. A high-resolution marine sedimentary record of geomagnetic intensity during the Brunhes Chron. Earth and Planetary Science Letters 144, 297–314.

Seidl, M.A., Finkel, R.C., Caffee, M.W., Hudson, G.B., Dietrich, W.E., 1997. Cosmogenic isotope analyses applied to river longitudinal profile evolution: problems and interpretations. Earth Surface Processes and Landforms 22, 195–209.

Sharma, P., Middleton, R., 1989. Radiogenic production of $^{10}$Be and $^{26}$Al in uranium and thorium ores: implications for studying terrestrial samples containing low levels of $^{10}$Be and $^{26}$Al. Geochimica et Cosmochimica Acta 53, 709–716.

Shea, M.A., Smart, D.F., 1983. A world grid of calculated cosmic ray vertical cutoff rigidities of 1980.0. 18th International Cosmic Ray Conference Conference Papers 3, 415–418.

Shea, M.A., Smart, D.F., Gentile, L.C., 1987. Estimating cosmic ray vertical cut-off rigidities as a function of the McIlwain L-parameter for different epochs of the geomagnetic field. Physics of the Earth and Planetary Interiors 48, 200–205.

Shea, M.A., Smart, D.F., McCracken, K.G., 1965. A study of vertical cutoff rigidities using sixth degree simulations of the geomagnetic field. Journal of Geophysical Research 70, 4117–4130.

Sheppard, M.K., Arvidson, R.E., Caffee, M., Finkel, R., Harris, L., 1995. Cosmogenic exposure ages of basalt flows: Lunar Crater volcanic field, Nevada. Geology 23, 21–24.

Shirley, V.S. (Ed.), 1998. Table of Isotopes, 1. Wiley, New York.

Siame, L.L., Bourlés, D.L., Sébrier, M., Bellier, O., Castano, J.C., Araujo, M., Perez, M., Raisbeck, G.M., Yiou, F., 1997. Cosmogenic dating ranging from 20 to 700 ka of a series of alluvial fan surfaces affected by the El Tigre fault, Argentina. Geology 25 (11), 975–978.

Simpson, J.A., Baldwin, H.W., Uretz, R.B., 1951. Nuclear bursts produced in the low energy nucleonic component of the cosmic radiations. Physical Review 84 (2), 332–339.

Simpson, J.A., Fagot, W.C., 1953. Properties of the low energy nucleonic component at large atmospheric depth. Physical Review 90, 1068–1072.

Simpson, J.A., Fenton, K.B., Katzman, J., Rose, D.C., 1956. Effective geomagnetic equator for cosmic radiation. Physical Review 102 (6), 1648–1653.

Simpson, J.A., Fonger, S.B., Treiman, S.B., 1953. Cosmic radiation intensity-time variations and their origin, 1. Neutron intensity variation method and meteorological factors. Physical Reviews 90, 934–950.

Small, E., Anderson, R.S., 1998. Pleistocene relief production in Laramide mountain ranges, western United States. Geology 26 (2), 123–126.

Small, E.E., Anderson, R.S., Hancock, G.S., 1999. Estimates of the rate of regolith production using $^{10}$Be and $^{26}$Al from an alpine hillslope. Geomorphology 27 (1-2), 131–150.

Small, E.E., Anderson, R.S., Repka, J.L., Finkel, R., 1997. Erosion rates of alpine bedrock summit surfaces deduced from in situ $^{10}$Be and $^{26}$Al. Earth and Planetary Science Letters 150, 413–425.

Smart, D.F., Shea, M.A. (Ed.), 1985. Galactic cosmic radiation and solar energetic particles. Handbook of Geophysics and the Space Environment. Air Force Geophysics Laboratory, 6-1–6-29 pp.

Soberman, R.K., 1956. High-altitude cosmic-ray neutron intensity variation. Physical Review 102 (5), 1399–1409.

Srinivasan, B., 1976. Barites: anomalous xenon from spallation and neutron-induced reactions. Earth and Planetary Science Letters 31 (6), 129–141.

Staudacher, T., Allégre, C.J., 1991. Cosmogenic Neon in ultramafic nodules from Asia and in quartzite from Antarctica. Earth and Planetary Science Letters 106, 87–102.

Staudacher, T., Allégre, C.J., 1993. Ages of the second caldera of Piton de la Fournaise volcano (Réunion) determined by cosmic ray produced $^{3}$He and $^{21}$Ne. Earth and Planetary Science Letters 119, 395–404.

Steig, E.J., Wolfe, A.P., Miller, G.H., 1998. Wisconsinan refugia and the glacial history of eastern Baffin Island, Arctic Canada: Coupled evidence from cosmogenic isotopes and lake sediments. Geology 26, 835–838.

Stephenson, R.M., 1954. Introduction to Nuclear Engineering. McGraw-Hill, New York.

Sternberg, R., 1996. Workshop on "The Secular Variations in the Production Rates of Cosmogenic Nuclides on Earth": paleomagnetic averages of geomagnetic latitude. Radiocarbon 38 (1), 169–170.

Stone, J., Allan, G.L., Fifield, L.K., Evans, J.M., Chivas, A.R., 1994. Limestone erosion measurements with cosmogenic chlorine-36 in calcite-preliminary results from Australia. Nuclear Instruments and Methods in Physics Research B 92, 311–316.

Stone, J., Evans, J., Fifield, K., Cresswell, R., Allan, G., 1996. Cosmogenic chlorine-36 production rates from calcium and potassium. Radiocarbon 38 (1), 170–171.

Stone, J.O., 1999. A consistent Be-10 production rate in quartz - muons and altitude scaling. AMS-8 Proceedings Abstract Volume, Vienna, Austria.

Stone, J.O., in press. Air pressure and cosmogenic isotope production. Journal of Geophysical Research.

Stone, J.O., Ballantyne, C.K., Fifield, L.K., 1998a. Exposure dating and validation of periglacial weathering limits, northwest Scotland. Geology 26, 587–590.

Stone, J.O.H., 1998. A rapid fusion method for separation of beryllium-10 from soils and silicates. Geochimica et Cosmochimica Acta 62 (3), 555–561.

Stone, J.O.H., Evans, J.M., Fifield, L.K., Allan, G.L., Cresswell, R.G., 1998b. Cosmogenic chlorine-36 production in calcite by muons. Geochimica et Cosmochimica Acta 62 (3), 433–454.

Stoner, J.S., Channell, J.E.T., Hillaire-Marcel, C., 1995. Late Pleistocene relative geomagnetic paleointensity from the deep Labrador Sea: Regional and global correlations. Earth and Planetary Science Letters 134, 237–252.

Stormer, C., 1934. On the trajectories of electric particles in the field of a magnetic dipole with applications to the theory of cosmic radiation: third communication. Astrophysica Norvegica 1 (1), 1–10.

Stormer, C., 1935. On the trajectories of electric particles in the field of a magnetic dipole with applications to the theory of cosmic radiation: fourth communication. Astrophysica Norvegica 1 (4), 115–184.

Strack, E., Heisinger, B., Dockhorn, B., Hartmann, F.J., Korschinek, G., Nolte, E., Morteani, G., Petitjean, C., Neumaier, S., 1994. Determination of erosion rates with cosmogenic $^{26}$Al. Nuclear Instruments and Methods B 92, 317–320.

Stuiver, M., Grootes, P.M., Braziunas, T.F., 1995. The GISP $\delta^{18}$O climate record of the past 16,500 years and the role of the sun, ocean, and volcanoes. Quaternary Research 44, 341–354.

Stuiver, M., Reimer, P.J., 1993. Extended $^{14}$C data base and revised CALIB 3.0 $^{14}$C age calibration program. Radiocarbon 35 (1), 215–230.

Summerfield, M.A., Hulton, N.J., 1994. Natural controls of fluvial denudation rates in major world drainage basins. Journal of Geophysical Research B 99 (7), 13,871–13,883.

Summerfield, M.A., Stuart, F.M., Cockburn, H.A.P., Sugden, D.E., Denton, G.H., Dunai, T., Marchant, D.R., 1999. Long-term rates of denudation in the Dry Valleys, Transantarctic Mountains, southern Victoria Land, Antarctica based on in-situ-produced cosmogenic $^{21}$Ne. Geomorphology 27 (1-2), 113–130.

Swanson, T., 1996. Determination of $^{36}$Cl production rates from the deglaciation history of Whidbey and Fidalgo Islands, Washington. Radiocarbon 38 (1), 172.

Synal, H.-A., 1995. Accelerator mass spectrometry: new applications. Applied Radiative Isotopes 46 (6/7), 457–466.

Tauxe, L., 1993. Sedimentary records of relative paleointensity of the geomagnetic field: theory and practice. Reviews of Geophysics 31 (3), 319–354.

Templeton, D.H., 1953. Nuclear reactions induced by high energy particles. Annual review of nuclear science 2, 93–104.

Teucher, M., 1952. Die absorption der nukleonenkomponente der kosmischen strahlung in luft zwischen seehohe und 4000 m. Zeitschrift fur Naturforschung 7A, 61–63.

Tongiorgi, V.C., 1949. On the mechanism of production of the neutron component of the cosmic radiation. Physical Review 76, 517–526.

Treiman, S.B., 1952. Analysis of the nucleonic component based on neutron latitude variation. Physical Review 86 (6), 917–923.

Tric, E., Valet, J.-P., Tucholka, P., Paterne, M., Labeyrie, L., Guichard, F., Tauxe, L., Fontugne, M., 1992. Paleointensity of the geomagnetic field during the last 80,000 years. Journal of Geophysical Research 97 (B6), 9337–9351.

Trull, T.W., Brown, E.T., Marty, B., Raisbeck, G.M., Yiou, F., 1995. Cosmogenic $^{10}$Be and $^{3}$He accumulation in Pleistocene beach terraces in Death Valley, California, U.S.A. Implications for cosmic-ray exposure dating of young surfaces in hot climates. Chemical Geology 119, 191–207.

Trull, T.W., Kurz, M.D., Jenkins, W.J., 1991. Diffusion of cosmogenic $^{3}$He in olivine and quartz: implications for surface exposure dating. Earth and Planetary Science Letters 103, 241–256.

Tuniz, C., Bird, R., Klein, J., Herzog, G., 1991. Accelerator Mass Spectrometry. CRC, Littleton, MA in preparation.

Tuniz, C., Klein, J., 1989. Ultra-high sensitivity mass spectrometry: Applications to rare nuclear and cosmological processes archived in geological samples. In: Cherubini, R., Dalpiaz, P., Minetti, B (Ed.), 3rd Winter School on HADRONIC PHYSICS. Elsevier Science Publishers, Folgaria (Trento), Italy, Feb 15–20, 1988, pp. 425–444.

Valet, J.-P., Brassart, J., Le Meur, I., Soler, V., Quidelleur, X., Tric, E., Gillot, P.Y., 1996. Absolute paleointensity and magnetomineralogical changes. Journal of Geophysical Research 101 (B11), 25,029–25,044.

Valet, J.-P., Meynadier, L., 1993. Geomagnetic field intensity and reversals during the past four million years. Nature 366, 234–238.

Van der Woerd, J., Ryerson, F.J., Tapponnier, P., Gaudemer, Y., Finkel, R., Meriaux, A.S., Caffee, M., Guaguang, Z., Qunlu, H., 1998. Holocene left-slip rate determined by cosmogenic surface dating on the Xidatan segment of the Kunlun fault (Qinghai, China). Geology 26 (8), 695–698.

Verosub, K.L., 1996. Recent advances in determining absolute and relative paleointensity variations of the geomagnetic field. Radiocarbon 38 (1), 173.

Vogt, S., Elmore, D., Sharma, P., Dunna, A., 1996. The $^{36}$Cl/$^{36}$Cl method for determining exposure time and erosion rates of surfaces. Radiocarbon 38, 122.

Vogt, S., Herzog, G.F., Reedy, R.C., 1990. Cosmogenic nuclides in extra-terrestrial materials. Reviews of Geophysics 28, 253–275.

Wells, S.G., McFadden, L.D., Poths, J., Olinger, C.T., 1995. Cosmogenic $^{3}$He surface exposure dating of stone pavements: Implications for landscape evolution in deserts. Geology 23 (7), 613–616.

Welz, B., 1999. Atomic absorption spectrometry. Wiley, New York, 941 pp.

Wolfendale, A.W., 1963. Cosmic Rays. Philosophical Library Inc, New York, 222 pp.

Wu, C.S., Townes, C.H., Feldman, L., 1949. Radioactivity of $^{36}$Cl. Physical Review 76, 692–693.

Yamashita, M., Stephens, L.D., Patterson, H.W., 1966. Cosmic-ray-produced neutrons at ground level: neutron production rate and flux distribution. Journal of Geophysical Research 71 (16), 3817–3834.

Yamazakia, T., Ioka, N., Eguchi, N., 1995. Relative paleointensity of the geomagnetic field during the Brunhes Chron. Earth and Planetary Science Letters 136, 525–540.

Yiou, F., Raisbeck, G.M., 1972. Half-life of $^{10}$Be. Physical Review Letters 29 (6), 372–375.

Yokoyama, Y., Reyss, J.-L., Guichard, F., 1977. Production of radionuclides by cosmic rays at mountain altitudes. Earth and Planetary Science Letters 36, 44–50.

Zentmire, K.N., Gosse, J.C., Baker, C., McDonald, E. and Wells, S., 1999. The problem of inheritance when dating alluvial fans and terraces with TCN: Insight from the Matanuska Glacier. GSA Abstracts and Programs, 31.

Zreda, M., England, J., Phillips, F., Elmore, D., Sharma, P., 1999. Unblocking of the Nares Strait by Greenland and Ellesmere ice-sheet retreat 10,000 years ago. Nature 398, 139–142.

Zreda, M., Noller, J.S., 1998. Ages of prehistoric earthquakes revealed by cosmogenic chlorine-36 in a bedrock fault scarp at Hebgen Lake. Science 292 (5391), 1097–1099.

Zreda, M., Phillips, F., Elmore, D., 1994. Cosmogenic $^{36}$Cl accumulation in unstable landforms Simulations and measurements on eroding moraines. Water Resources Research 30 (11), 3127–3136.

Zreda, M.G., 1994. Development and calibration of the cosmogenic $^{36}$Cl surface exposure dating method and its application to the chronology of late Quaternary glaciations. Ph.D. Thesis, New Mexico Institute of Mining and Technology, Socorro, 318 pp.

Zreda, M.G., Phillips, F.M., Elmore, D., Kubik, P.W., Sharma, P., Dorn, R.I., 1991. Cosmogenic $^{36}$Cl production in terrestrial rocks. Earth and Planetary Science Letters 105, 94–109.

Zreda, M.G., Phillips, F.M., Kubik, P.W., Sharma, P., Elmore, D., 1993. Cosmogenic $^{36}$Cl dating of a young basaltic eruption complex, Lathrop Wells, Nevada. Geology 21, 57–60.